Characterization and Vaccine Strategy Development for Circulating and Emerging Respiratory Viruses

Mariam Maltseva

This thesis is submitted to the University of Ottawa in partial fulfillment of the requirements for the degree of Doctorate in Philosophy with specialization in Microbiology & Immunology.

Department of Biochemistry, Microbiology and Immunology,
Faculty of Medicine,
University of Ottawa

Abstract

The ongoing evolution of severe acute respiratory syndrome coronavirus 2 (SARS-CoV-2) and the emergence of highly transmissible variants of this virus have significantly impacted the effectiveness of vaccines against infection, COVID-19 disease outcomes, and transmission. The decline in vaccine efficacy can be attributed to several factors, including immune evasion by new variants, waning immunity over time post-vaccination or infection-acquired immunity, and inadequate induction of protective mucosal immunity. While booster vaccinations have notably enhanced protection against severe disease, the continuous evolution of the virus necessitates a re-evaluation of current vaccine strategies due to their inherent limitations to prevent new infections.

To address these challenges effectively, it is crucial to consider the viral life cycle, accurately characterize viral phenotypes, and understand the interactions between the virus and the host, as well as the resulting immunological responses. This thesis explores virus-host interactions by characterizing viral phenotypes using flow virometry techniques and investigates viral kinetics, alongside the modulation of the host's immune response following viral infection. By analyzing these interactions, we aim to refine vaccine design and delivery, advancing the development of next-generation vaccines against SARS-CoV-2 and other respiratory viruses.

This doctoral thesis examines different immunization regimens and vaccine formulations, characterizing the humoral responses across various anatomical and immunological compartments. My research identifies immunogenic targets for intranasal vaccine design against SARS-CoV-2 and explores the impact of different vaccine formulations on induced humoral responses, providing insight into the development of a universal vaccine platform. Robust and durable mucosal immunity is crucial for neutralizing viruses and limiting infection at the point of

entry. Lastly, a plant-based expression platform for producing vaccine antigen candidates was evaluated, highlighting plant-produced proteins as advantageous candidates for use in protein subunit vaccines. Our data supports that the mucosal humoral response to SARS-CoV-2 intranasal vaccination is relevant to the development of more effective next-generation vaccine strategies to combat SARS-CoV-2 and other respiratory pathogens.

Acknowledgments

I owe the completion of this PhD to the mentors, colleagues, friends, and family who have supported me throughout this journey and helped me grow both as a scientist and as a person.

First, I would like to express my sincere gratitude to Dr. Marc-André Langlois. Your passion for science, perseverance, and work ethic have been truly inspiring. It has been a great privilege to complete my PhD in your lab. Thank you for your continued mentorship, support and for fostering an environment that allowed me to grow into an independent and creative scientist.

I would also like to extend my appreciation to my TAC members, Drs. Angela Crawley, Curtis Cooper, and Erin Mulvihill. Your guidance and insights throughout my PhD have not only improved the quality of my research but also provided me with essential external perspectives.
To Yannick, with whom I shared this PhD journey: through experiments, frustrations, conferences, and joyful moments, you have become a true friend. A heartfelt thanks to Pauline, who later joined our group and filled the lab with laughter and "tea." To Hiba, Nick, Matt, and Vinay: it was a pleasure working and laughing alongside you. I am also grateful to all members of the Langlois lab, past and present, including Corey, Anna, Andrew, Ricardo, Vera, Abisheck, Justino, Caroline, Negar, and Ziba, as well as the team at the high-throughput facility. Special thanks to Anthony and the ACVS team for your invaluable help, and entertaining conversations during long processing days. I also want to express my appreciation to Tyler for your guidance and continued friendship, even beyond your time at the Langlois lab.

To my parents, thank you for paving the way, believing in me, and supporting my dreams—this PhD is dedicated to you. Age, your unwavering resilience, perseverance, and infectious optimism have been a source of inspiration, and although you are not here to witness this, this is for you. To my brother and all of my extended family, thank you for your love, encouragement and support.
To my friends and Alena, Alexa, Sarah and Liliana thank you for your patience, support and for bringing much-needed laughter along the way. Yasha, Dasha and Dysia, the best cat researchers.
Finally, to Jean-Miguel, thank you for your love, support, patience (especially this last year) and for believing in my dreams. Here is a little reading material for bedtime stories.

Declaration of Academic Achievements

Chapter 2: Flow Virometry for Characterizing the Size, Concentration, and Surface Antigens of Viruses.

Maltseva M., and Langlois M-A. (2022), ***Current Protocols***, *2*(2), e368.
https://doi.org/10.1002/cpz1.368

- M.M. and M-A. L conceived and designed the study.
- M.M performed experiments.
- M.M. and M-A. L. analyzed data and prepared figures.
- M.M. and M-A. L wrote the manuscript.

Chapter 3: Influence of GlycoGag on the Incorporation of Host Membrane Proteins into the Envelope of the Moloney Murine Leukemia Virus.

Maltseva M., and Langlois M-A. (2021), ***Frontiers in Virology,*** *1*, 747253.
10.3389/fviro.2021.747253

- M.M. performed experiments.
- M.M. and M-A. L. analyzed data and prepared figures.
- M.M. and M-A. L wrote the manuscript.

Chapter 4: Seasonal human coronaviruses OC43, 229E, and NL63 induce cell surface modulation of entry receptors and display host cell-specific viral replication kinetics.
*****Siragam V., *****Maltseva M., Castonguay N., Galipeau Y., Srinivasan M., Soto J., Dankar S., Langlois M-A. (2024), ***Microbiology Spectrum***, 12:e04220-23.
https://doi.org/10.1128/spectrum.04220-23

*Equal contribution
V.S., M.M. and M-A. L conceived and designed the study.
V.S., M.M., N.C., M.M.S., J.H.S., and S.D. performed the experiments.
V.S., M.M. and M-A. L. analyzed data and prepared figures.
V.S., M.M., Y.G. and M-A. L wrote the manuscript.

Chapter 5: Characterization of systemic and mucosal humoral immune responses to an adjuvanted intranasal SARS-CoV-2 protein subunit vaccine candidate in mice.

Maltseva M., Galipeau Y., Renner T.M., Deschatelets L., Durocher Y., Akache B.. and Langlois M-A. (2022), ***Vaccines,*** *11*(1), p.30. **https://doi.org/10.3390/vaccines11010030**

- M.M., B.A., and M-A. L. conceived and designed the study.
- M.M. performed the experiments and prepared the figures.
- M.M., Y.G., T.R., B.A., and M-A. L. analyzed data.
- M.M., T.R., B.A and M-A. L. wrote the manuscript.

Chapter 6: Characterization of Systemic and Mucosal Humoral Responses to Variant-Specific SARS-CoV-2 Prime-Boost Vaccination: A Comparison of Intramuscular and Intranasal Administration in a Murine Model

Maltseva M., Galipeau, Y., McClauskie P., Castonguay N., Cooper C., and Langlois M-A. (2024). (Under Review)

- M.M., and M-A. L. conceived and designed the study.
- M.M., Y.G., N.C., and P.M. performed animal sample collection and processing.
- M.M performed *in vitro* experiments.
- M.M., Y.G., and M-A. L. analyzed data and prepared figures.
- M.M. and M-A.L wrote the manuscript.

Chapter 7: Immune imprinting: The persisting influence of the first antigenic encounter with rapidly evolving viruses

Maltseva M., Keeshan A., Cooper C. and Langlois M-A., (2024), ***Human Vaccines & Immunotherapeutics,*** *20*(1), p.2384192. **https://doi.org/10.1080/21645515.2024.2384192**

- M.M., A.K., C.C., and M-A. L. conceived and designed the study.
- M.M., and M-A. L. prepared figures.
- M.M., A.K., C.C. and M-A. L. wrote the manuscript.

Chapter 8: Plant-based production of SARS-CoV-2 antigens for use in a subunit vaccine.

*****Demone J., *****Maltseva M., Nourimand M., Nasr-Sharif M., Galipeau Y., Alarcon E.I., Langlois M-A., and MacLean, A.M. (2022), ***PLoS One*** 17.12 (2022): e0277668. **10.1101/2021.10.17.464700**

*****Equal contribution

- D.J., M.M., M-A. L., and A.M. conceived and designed the study.
- D.J., M.M., M.N., M.N., Y.G., and A.E. performed the experiments.
- D.J., M.M., M.N., A.E., M-A. L. and A.M analyzed data and prepared figures.
- D.J., M.M., M.N., M-A. L. and A.M wrote the manuscript

Abbreviations

ADCC: Antibody dependent cellular cytotoxicity
ADCP: Antibody dependent cellular phagocytosis

APC: Antigen presenting cell
APOBEC3: apolipoprotein B mRNA editing enzyme, catalytic polypeptide-like 3

BALF: Bronchoalveolar Lavage
BALT: Bronchial Associated Lymphoid Tissue

COVID-19: Coronavirus Disease 2019

DNA: Deoxyribonucleic acid

EBOV: Ebola virus
ELISA: enzyme linked immunosorbent assay
Env: Envelope glycoprotein
ESCRT: endosomal sorting complex required for transport
EVs: Extracellular vesicles

FBS: Fetal bovine serum
FCM: flow cytometry
FVM: flow virometry

GI.: Gastrointestinal
GlycoGag / gPr80: glycosylated Gag

HA: Hemagglutinin
HIV: human immunodeficiency virus

IgA: Immunoglobulin A
IgG: Immunoglobulin G
IgM: Immunoglobulin M
I.M.: Intramuscular
I.N.: Intranasal
IFN.: Interferon
IL.: Interleukin
J-chain: Joining chain

KBP: Kilobase pairs

LAIV: Live-attenuated influenza vaccine
LRT: Lower respiratory tract

MBC: Memory B cell

MERS: Middle east respiratory syndrome
MHC: Major histocompatibility complex
M. MLV: (Moloney) Murine leukemia virus

NALT: Nasal Associated Lymphoid Tissue
NHP: Nonhuman Primate
NK:Natural killer

PBS: Phosphate buffered saline
pIgR: Polymeric immunoglobulin receptor
Pol: polymerase

RNA: Ribonucleic acid
RNASeq: RNA Sequencing
RSV: Rous sarcoma virus

SARS-CoV: Severe acute respiratory syndrome coronavirus
SARS-CoV-2: Severe acute respiratory syndrome coronavirus 2
SD: Standard deviation
SDS-PAGE: sodium dodecyl sulphate polyacrylamide gel electrophoresis
sIgA: secretory IgA
SPG: Spike Glycoprotein

TB: Tuberculosis
Th1:T helper cell 1
Th2:T helper cell 2
TNFα.: Tumor necrosis factor alpha
Treg: Regulatory T cell
T_{CM}: Tissue central memory T cell
T_{RM}.: Tissue resident memory T cell

URT: Upper respiratory tract

WHO: World Health Organization

Table of Contents

List of Figures and Tables

1 Introduction

1.1 Respiratory Virus Pandemics and its Impact on Global Human Health

Respiratory viruses have long posed a significant threat to global health, causing substantial morbidity and mortality worldwide, with far-reaching public health, economic, and social consequences. The ability of respiratory viruses to rapidly spread through airborne transmission, combined with their high mutation rates and potential for zoonotic spillovers, allows them to trigger recurrent pandemics with varying severity. The 20th century witnessed several major viral outbreaks such as the 1918 Spanish influenza pandemic, which caused an estimated 50 million deaths globally (1). Influenza continues to circulate globally, causing recurrent seasonal epidemics and an estimated 300,000 to 650,000 deaths annually (2). Major outbreaks, such as the more recent 2009 H1N1 swine pandemic, highlight its pandemic potential and highlighting its persistent threat to public health (2, 3).

Coronaviruses have also been significant contributors to pandemics, with severe acute respiratory syndrome (SARS-CoV-1) emerging in 2002, Middle East respiratory syndrome (MERS-CoV) in 2012, and the most recently SARS-CoV-2, the causative agent of COVID-19. The COVID-19 pandemic, declared a Public Health Emergency by the World Health Organization in early 2020, has since resulted in over 776 million confirmed cases (4). The rapid transmission of SARS-CoV-2, its ability to spread asymptomatically and the emergence of highly transmissible variants of concern (VOCs) posed unprecedented challenges to traditional containment and therapeutic measures. The COVID-19 pandemic has thus become one of the most severe respiratory virus outbreaks in recent history, with over 7 million reported deaths globally - likely an underestimation of its true toll (5). Beyond its direct health impacts, the pandemic's response measures such as

lockdowns, social distancing, and travel restrictions, have had far-reaching economic repercussions. The economic toll of COVID-19 is estimated to be in the trillions of dollars, underscoring the global impact of respiratory viruses (6). Indeed, the annual economic burden of influenza alone in the United States is estimated to be approximately $11.2 billion, including both healthcare costs and indirect effects such as productivity losses (7).

Vaccination remains one of the most effective strategies for preventing infectious diseases. The development and widespread deployment of vaccines have eradicated or significantly reduced the prevalence of many pathogens worldwide, resulting in substantial decreases in mortality (8). In the case of COVID-19, vaccination was instrumental in reducing the total death toll. It is estimated that in the first year of the COVID-19 vaccine rollout, vaccination reduced global deaths by approximately 63%, preventing an estimated 19.8 million deaths (9). The majority of lives saved were among the most vulnerable populations, such as the elderly and immunocompromised individuals, who are at the highest risk of severe illness and death from SARS-CoV-2. In the European Union alone, the administration of the first booster dose is estimated to have saved an additional 700,000 lives (10).

The ongoing impact of circulating and emerging respiratory viruses on health, healthcare systems, and global economies highlights the urgent need for innovative strategies. A comprehensive understanding of a pathogen’s phenotypic characteristics, infection dynamics, and associated pathogenesis is essential for designing an effective vaccine. This knowledge provides the foundation for targeting key aspects of the pathogen's biology, enabling the development of vaccines that can effectively prevent infection or mitigate disease severity. This dissertation explores the development of rapid diagnostic tools for viral detection, characterization of virus-

host interactions, the investigation of next-generation vaccine strategies with increased breadth of protection—such as optimal antigen selection, administration routes, and the role of mucosal immunity in reducing viral infection and transmission. By integrating these insights, the goal of this dissertation is inform the design of next-generation vaccines to halt the circulation of SARS-CoV-2 and better prepare for future pandemics.

1.2 Flow Virometry: A Tool for Rapid Intact Virus Characterization

To develop an effective vaccine against an emerging infection, rapid identification and thorough characterization of the pathogen are essential. Understanding the virus's biology, including its structure and host interactions, is critical for informing vaccine and therapeutic strategies. Traditional methods, though informative, are limited in throughput and single-particle analysis.

1.2.1 Current Methods for Viral Characterization

Historically, viral characterization has relied on bulk analysis techniques such as ELISA**,** PCR**,** immunomagnetic capture assays, and mass spectrometry to analyze all virions within a sample, both defective and infectious particles. However, since viral stocks often contain both defective and infectious particles, this creates a significant confounding factor, as defective particles may have varying protein and genetic content that does not accurately represent infectious counterparts (11). However, these methods are limited in their sensitivity to discern variations among heterogenous viral populations, which are crucial for understanding virus-specific properties like antigen composition, population heterogeneity, and subpopulation characteristics that may influence pathogenicity and immune evasion. While immunoelectron microscopy has generated a wealth of knowledge on viral biology and phenotypic analysis at a single-virion scale, this technique is limited in its high-throughput capabilities (12).

1.2.2 Flow Virometry

Before the development of modern flow cytometers, cell heterogeneity was not well appreciated. Flow cytometry revolutionized immunology by enabling phenotypic analysis of extracellular and intracellular markers at the single-cell level**,** allowing researchers to characterize cell subsets, quantify different cell states, and understand disease mechanisms (13). Its high-throughput capability to measure multiple parameters simultaneously has been crucial for understanding disease pathogenesis and treatment. Flow cytometry principles have been adapted for the analysis of nanoscale particles, including viruses, giving rise to the field of flow virometry (FVM). FVM is a sensitive, multiparametric, and high-throughput technique that allows for the detection, quantification, and characterization of intact viral particles enabling rapid analysis of viral particles based on their biophysical properties **(Figure 1.1)** (14).

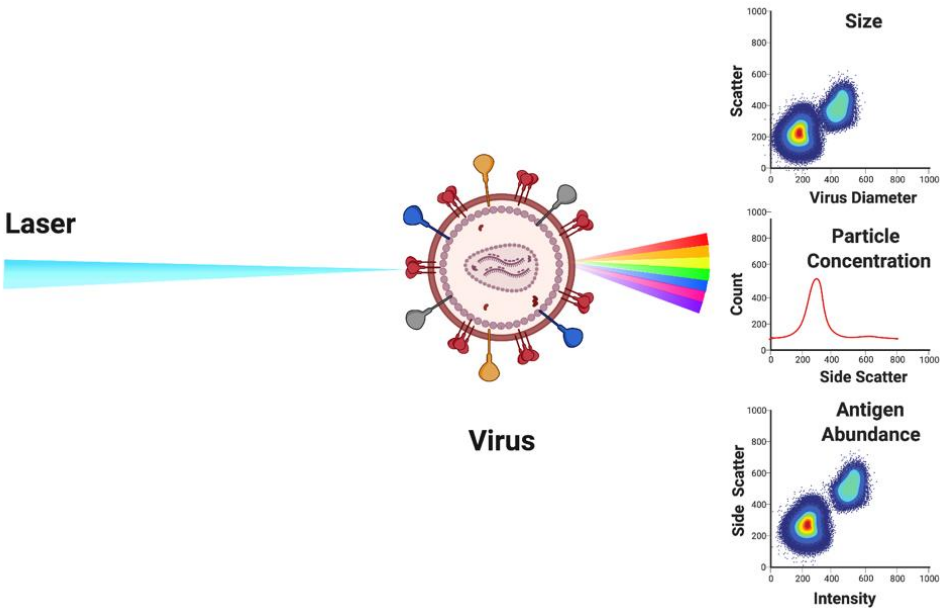

Figure 1.1: Schematic Illustration of Flow Virometry Applications.
Flow virometry (FVM) is a highly sensitive, multiparametric, and high-throughput technique for the detection, quantification, and characterization of intact viral particles. It facilitates rapid analysis by leveraging the biophysical properties of viruses, including size, structure, and surface protein expression.

In 1978, Hercher *et al.* developed the first custom cytometer, incorporating modifications that enabled the detection and discrimination of bacteriophages using light scattering(15). Initial viral staining targeting the genome allowed for the successful detection of larger DNA viruses(16, 17). The field further expanded with the increasing interest in extracellular vesicles (EVs)**,** which play important roles in both healthy and pathological processes (18). Using light scattering and fluorescence, FVM can measure the concentration of intact virions, assess antigen abundance, and detect specific host-derived proteins on viral surfaces (14). This single-particle analysis enhances our understanding of the full scope of viral heterogeneity and aides in the identification of subpopulations with increased infectivity or immune evasion potential.

1.2.3 Application of Flow Virometry in the Development of Vaccines

FVM shows potential promise as a complementary tool for evaluating viral-vectored vaccines during production. While not adopted for routine quality control, it has been explored during pilot manufacturing and preclinical processes to assess its feasibility alongside standard techniques.

For example, during the production of the Ebola vaccine ERVEBO**,** Ricci et al. used FVM alongside other analytical methods to monitor viral particle stability and antigen integrity in real time, enabling early detection of damaged virions to ensure vaccine consistency and quality(19). Indeed, FVM identified oncolytic vaccinia virus aggregation during handling, such as freeze-thaw cycles, demonstrating its usefulness for identifying process-related challenges and ensuring consistency in vaccine preparations (20). Recently, Prout et al. applied FVM to screen SARS-CoV-2 VSV viral-vector vaccine candidates during preclinical development stage, using it to characterize spike glycoprotein expression and conformation, while also assessing viral stability (21). These studies underscore the potential of FVM as a complementary tool for monitoring viral

particle integrity and stability, supporting vaccine development and production by enabling rapid and high-throughput evaluation of key parameters.

1.2.4 Flow Virometry: A Tool for Elucidating Viral-Host Interactions

Although originally intended for virus enumeration, FVM has been additionally employed for viral characterization, revealing significant insights into viral heterogeneity (14, 22-31). FVM not only allows for the detection and characterization of viral particles but also enables the sorting of viable viral particles. This capability is important for downstream applications, such as assessing the infectivity of specific viral particle subgroups.

Bilali *et al.* demonstrated by sorting herpes simplex virus 1 (HSV-1) particles, that while some viral proteins are incorporated consistently into viral particles, others exhibit significant variability (30). Notably, the tegument proteins VP16 and VP22 showed substantial variation among viral particles, with higher incorporation levels enhancing viral infectivity. These findings highlight the importance of both the presence and quantity of specific tegument proteins in viral fitness, as demonstrated by flow virometry's ability to detect, characterize, and sort viable viral particles for downstream applications, including the assessment of specific subgroups' infectivity (29-31). Similarly, Bonar *et al.* demonstrated the application of this technique by detecting and sorting fluorescently labeled HIV-1 particles for use in downstream infectivity assays (32). While Gaudin et al. showed that particle size and glycoprotein concentration on the surface of Junin virus particles correlate with differences in infectivity, as demonstrated by fluorescently sorting the viral particles by functional infectivity assays (25).

FVM was also used to study dengue virus, revealing subpopulations with varying maturation levels further demonstrating FVM's capability to monitor virion maturation and highlighting its broader

applications (24). Given that viral maturation impacts the virus's ability to interact with host receptors and immune evasion, identifying immature versus mature particles helped researchers understand their roles in disease severity, aiding targeted vaccine design against the most infectious form (14, 22, 24). Furthermore, Landowski et al. demonstrated receptor-induced conformational changes and differential incorporation of attachment and fusion glycoproteins, depending on the size of Nipah virus particles (26). This study underscores that differential incorporation of viral glycoproteins facilitates a more nuanced interpretation of viral kinetic assays and entry kinetic phenotype determination.

1.2.5 Murine Leukemia Virus

MLV is a simple, enveloped gammaretrovirus well studied as a model for more complex retroviruses like Human Immunodeficiency Virus-1 (HIV-1), with which it shares a similar diameter (~80-120 nm) (22, 33-38). The MLV genome encodes three essential genes for retroviral replication: group specific antigen (gag), polymerase (pol) and envelope glycoprotein (env) (39). Its straightforward structure and life cycle make MLV a valuable tool for studying retroviral biology and investigating viral protein interactions during assembly and release (22, 34, 36, 37). The number of Env varies across viral species. For example, HIV-1 has around 14-21 spikes per particle, Rous sarcoma virus (RSV) about 82, and MLV approximately 80-120 trimeric spikes(40-44). Furthermore, MLV expresses distinct cell-derived proteins along with Env on its surface, making it a valuable reference model for studying viral host interactions during assembly and release (34). Its use as a biological reference tool for glycoprotein quantification may offers insights into viral particle assembly, and host interactions of more complex viruses like HIV (33, 45). Overall, FVM provided detailed insights into viral heterogeneity, envelope glycoprotein abundance, and particle stability. FVM’s adaptability makes it a crucial tool for rapidly

characterizing viruses during emerging health crises and evaluating vaccine candidates, reinforcing its place in the virologist's toolkit.

1.3 Coronaviruses

Coronaviruses are a diverse group of enveloped, positive-sense, single-stranded RNA viruses from the *Coronaviridae* family, capable of causing a range of diseases in both animals and humans. Identified in the 1960s, they were initially linked to mild, self-limiting upper respiratory infections, such as the common cold (46, 47). The *Coronaviridae* family comprises three subfamilies: *Orthocoronavirinae***,** *Letovirinae***,** and *Pitovirinae***.** Orthocoronavirinae, the most relevant to human health, includes four genera: *Alphacoronavirus***,** *Betacoronavirus***,** *Gammacoronavirus***,** and *Deltacoronavirus* (**Figure 1.2**). While Gammacoronaviruses and Deltacoronaviruses primarily infect birds, occasionally crossing into mammals, Alphacoronaviruses and Betacoronaviruses predominantly infect mammals, including humans.

Of the seven known coronaviruses that infect humans, three betacoronaviruses—SARS-CoV, MERS-CoV, and SARS-CoV-2—are considered highly pathogenic **Figure 1.2**. In contrast, four coronaviruses circulate seasonally, causing mild upper respiratory infections associated with the common cold: two alphacoronaviruses (229E and NL63) and two betacoronaviruses (OC43 and HKU1) **Figure 1.2** (48). Studies have identified bats, rodents, and domestic animals as key reservoir species for these viruses, enabling occasional cross-species transmission and spillover events (48, 49).

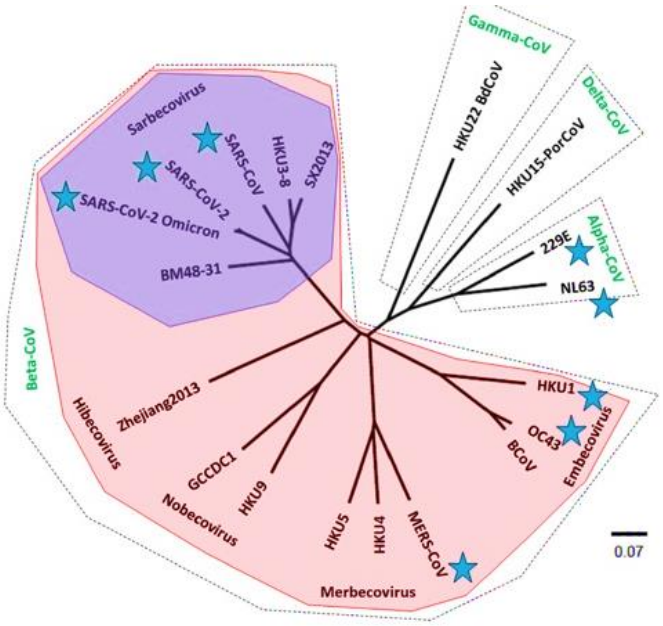

***Figure 1.2*: Evolutionary Relationships within Orthocoronavirinae.**
Phylogenetic Tree of the Orthocoronavirinae Based on Spike Protein Amino Acid Sequences. The tree illustrates the evolutionary relationships among orthocoronaviruses, with a scale bar representing a 7% amino acid change. It includes four genera: Alphacoronavirus (Alpha-CoV), Betacoronavirus (Beta-CoV), Gammacoronavirus (Gamma-CoV), and Deltacoronavirus (Delta-CoV). Viruses denoted by blue stars are either actively circulating in humans or have caused infections in the past. Figure adapted from Florian Krammer, 2024 (89) in accordance with the Creative Commons Attribution 4.0 International License (https://creativecommons.org/licenses/by/4.0/).

1.3.1 Common Cold Seasonal Coronaviruses

Human coronaviruses (HCoVs) OC43, 229E, NL63, and HKU1 are seasonal endemic viruses that primarily cause mild upper respiratory infections and are estimated to account for 15%–30% of common cold cases (46, 47). Epidemiological studies indicate that OC43 is the most prevalent strain, followed by NL63, 229E, and HKU1 (50, 51). While these HCoVs typically cause mild symptoms in healthy individuals, NL63 and 229E have been associated with severe respiratory issues, such as pneumonia and respiratory distress syndrome, in vulnerable populations (10, 11). Despite their widespread circulation, no vaccines exist for HCoVs, and treatment options for severe cases remain limited (23). Although the replication and pathogenesis of highly pathogenic

coronaviruses, such as SARS-CoV, MERS-CoV, and SARS-CoV-2, are well understood, less is known about the replication kinetics, immune modulation, and long-term effects of recurring infections with common HCoVs. Notably, HCoV-HKU1, was only identified in 2005 and its functional receptor only recently identified (52, 53). Given coronaviruses potential for zoonotic transmission and co-infection, which could lead to the emergence of recombinant strains, these viruses are of particular interest, especially in light of emerging pathogenic coronaviruses.

1.3.2 SARS-CoV and MERS

The first SARS epidemic, which occurred between 2002 and 2003, affected more than 26 countries, resulting in over 8,000 cases globally and approximately 774 deaths, with death rates significantly higher in vulnerable populations (54). SARS-CoV, believed to have originated from bats, spread to humans through an intermediate host, likely civet cats (55-57). However, few vaccine candidates reached clinical trials, as the outbreak was quickly contained and eradicated through non-pharmaceutical interventions (54). MERS, which emerged in 2012, is less transmissible but more lethal, with a case-fatality rate of about 35% (58). Outbreaks have been sporadic and largely confined to the Middle East, where transmission primarily occurs from camels to humans. Limited human-to-human transmission has been observed, mainly through close contact in healthcare settings (59, 60).

The emergence of both SARS-CoV and MERS-CoV underscore the potential for viruses to spill over from animal reservoirs, highlighting the persistent threat that cross-species transmission poses to human populations (55-57). While both SARS-CoV and MERS demonstrated epidemic potential, it was SARS-CoV-2 that triggered the first coronavirus pandemic, largely due to its increased transmissibility and ability to spread through asymptomatic carriers. However, all three

of these coronaviruses are listed in the WHO Blueprint for pathogen prioritization due to their pandemic potential and threat to global health security (61).

1.3.3 SARS-CoV-2

SARS-CoV-2 caused global turmoil following its emergence in Wuhan, China, in late 2019 (62-64). In December 2019, the World Health Organization was alerted to a cluster of pneumonia cases in Wuhan (65). Less than two weeks later, the virus' full genome was sequenced and shared, identifying it as a novel coronavirus closely related to SARS-CoV-1. The disease was named coronavirus disease 2019 (COVID-19). Case numbers in Wuhan surged due to community transmission, and soon after, cases were detected outside of China, linked to travel from Wuhan (66-71). Despite the implementation of various non-pharmaceutical interventions by different countries, such as lockdowns, travel restrictions, stay-at-home mandates, and mask-wearing, there were varying levels of success in reducing transmission rates (72). Within weeks, the virus spread globally, leading the WHO to declare COVID-19 a pandemic on March 11, 2020.

SARS-CoV-2 stood out from previous coronavirus outbreaks due to its highly efficient person-to-person transmission, with an estimated R_0 as high as 5.7 (73). The average incubation period from exposure to the ancestral SARS-CoV-2 to symptom onset was ~5-6 days (74, 75). In the first SARS-CoV-2 human challenge study, peak viral loads were observed before symptom onset, with the virus initially detected in the throat following inoculation but reaching significantly higher levels in the nose (74). Asymptomatic or presymptomatic transmission was estimated to account for 44% to 62% of cases, a major driver of the virus' rapid spread early on in the pandemic (76-78). The primary mode of transmission was through inhalation of virus-containing droplets and

aerosols (79). However, transmission through direct contact and contaminated surfaces (fomites) was also reported.

COVID-19 exhibited a wide range of symptoms and severity levels, with the majority of cases being mild, though a portion progress to severe or critical conditions. During the viral phase, typically within the first week, common symptoms included fever, dry cough, shortness of breath, nausea, vomiting, diarrhea, muscle pain, headache, fatigue, and rhinorrhea (74, 80, 81). Loss of smell (anosmia) and taste (ageusia) was frequently reported, and in mild cases, were sometimes the only symptoms(74). Most mild cases resolved without the need for hospitalization.

A large epidemiological study conducted in China in 2020, involving approximately 45,000 COVID-19 patients, reported that 81% presented with mild symptoms, 14% developed severe disease, and 5% experienced critical illness, characterized by complications such as respiratory failure, shock, or multiple organ failure (66). A study in the United Kingdom of approximately 20,000 hospitalized COVID-19 patients found that 17% were admitted to intensive care units, primarily due to respiratory failure (82). Lung damage in COVID-19 is linked to viral replication, immune cell infiltration, and elevated levels of proinflammatory cytokines and chemokines(80, 81, 83, 84). An excessive immune response, including cytokine storms, can lead to severe lung injury and increased mortality. Many COVID-19 survivors also experience long-term health issues, commonly referred to as long COVID (85, 86).

Despite variations in reported case fatality rates, initial estimates ranged from 1% to 4%, with age, sex, and underlying health conditions contributing to higher rates (81, 87). At-risk populations included the elderly, immunocompromised individuals, and those with comorbidities (such as heart disease, diabetes, obesity, hypertension, and kidney disease) were associated with a higher

risk of severe illness. In the United States, the case fatality rate varied significantly by age, from 0.3 deaths per 1,000 cases among children and adolescents to 210 deaths per 1,000 cases in individuals aged 75 and older (88). Among those hospitalized in intensive care, the case fatality rate reached as high as 40%.

1.4 Coronavirus structural overview

Coronaviruses are enveloped, positive-sense single-stranded RNA viruses, typically 120-160 nm in diameter, with a spherical structure (90, 91). The characteristic crown-like protrusions on their surface are formed by SGP, which plays a crucial role in viral entry by mediating attachment and fusion with host cell membranes (92, 93). Coronaviruses share a similar genome organization, with a size ranging from 26-32 kb in size (90, 91, 94). The 3' end encodes key structural proteins: nucleocapsid protein (N), the spike glycoprotein (SGP), envelope protein (E) and membrane protein (M), with the E and M proteins being particularly important in viral assembly (90, 91, 94). The 5' end contains two open reading frames (ORF1a and ORF1b), which encode non-structural proteins essential for viral replication. The SPG is a class I fusion homotrimeric protein divided into two subunits: S1 and S2 (92, 93). The S1 subunit contains the receptor-binding domain (RBD), which binds to host cell receptors such as angiotensin-converting enzyme 2 (ACE2) in the case of SARS-CoV, NL63 and SARS-CoV-2, determining viral tropism. Following receptor binding, the SPG is cleaved by host proteases, such as TMPRSS2, enabling the S2 subunit to mediate fusion between the viral envelope and the host cell membrane (92, 93). Once inside, the viral RNA is released into the cytoplasm, where it serves as a template for viral protein synthesis and genome replication.

Preclinical vaccine studies on SARS-CoV and MERS-CoV identified the SGP as the primary antigenic target. Since SARS-CoV-2 shares 79% of its genome with SARS-CoV and 50% with MERS-CoV, insights gained from these studies significantly accelerated the development of SARS-CoV-2 vaccines (94). Numerous studies have demonstrated that SGP-specific antibodies can neutralize both SARS-CoV-1 and MERS-CoV, providing protection in animal models (58, 95-98). As a result, the SGP was established as the key antigenic component in most SARS-CoV-2 vaccines, inducing robust neutralizing antibody and T cell responses, and offering protection in animal challenge models. Given the RBD's critical role in receptor binding and viral entry, it serves as the primary target for antibody binding and virus neutralization (99-105). Consequently, various forms of the S protein, including the full-length S protein, S1 domain, and RBD, have been utilized as vaccine antigens against SARS-CoV-2(106, 107).

Neutralizing antibodies serve as critical correlates of vaccine efficacy and protection against SARS-CoV-2 (108-110).These immune correlates facilitate immunobridging, enabling vaccine efficacy predictions based on immunogenicity, similar to the approach used for seasonal influenza vaccines. Anticipating changes due to waning immunity or the emergence of immune-evasive variants, particularly in vulnerable populations, can guide vaccine updates and other protective strategies (110). On a public health level, assessing neutralization capacity against current and future variants can help forecasting population immunity and assess infection risk.

1.5 Overview of Virus-Host Modulation

The immune response to SARS-CoV-2 is multifaceted, involving both innate and adaptive arms of the immune system. Upon infection, the innate immune system rapidly detects pathogen-associated molecular patterns (PAMPs) via pattern recognition receptors (PRRs) in immune cells

such as dendritic cells (DCs) and macrophages (111-114). This triggers activation and cytokine release, creating an inflammatory environment that recruits additional immune cells. Key innate cells, including natural killer (NK) cells, DCs, and macrophages help control viral replication and prime adaptive responses **Figure 1.3A**. DCs are central in this process as professional **a**ntigen-presenting cells (APCs). They internalize antigens through endocytosis, phagocytosis, or pinocytosis and present them to T cells to initiate adaptive immunity (115, 116). Upon activation, DCs upregulate major histocompatibility complex (MHC) molecules, enabling effective antigen presentation, and subsequently migrate to lymph nodes (LNs) **Figure 1.3A**.

These secondary lymphoid organs are strategically positioned within drainage areas throughout the body. Antigen acquisition of pathogens that breached the mucosal barrier through afferent lymphatics is essential for lymph node function, transporting antigens and activated APCs, including DCs, from mucosal tissues. Distinct draining lymph nodes, such as mesenteric LNs (intestinal tract), mediastinal LNs (lower respiratory tract, LRT), and cervical LNs (upper respiratory tract, URT), receive the components of the invading pathogen, allowing for efficient antigen presentation and initiation of adaptive immune responses (116-121). Peripheral lymph nodes are functionally interconnected with mucosal immunity, coordinating immune responses

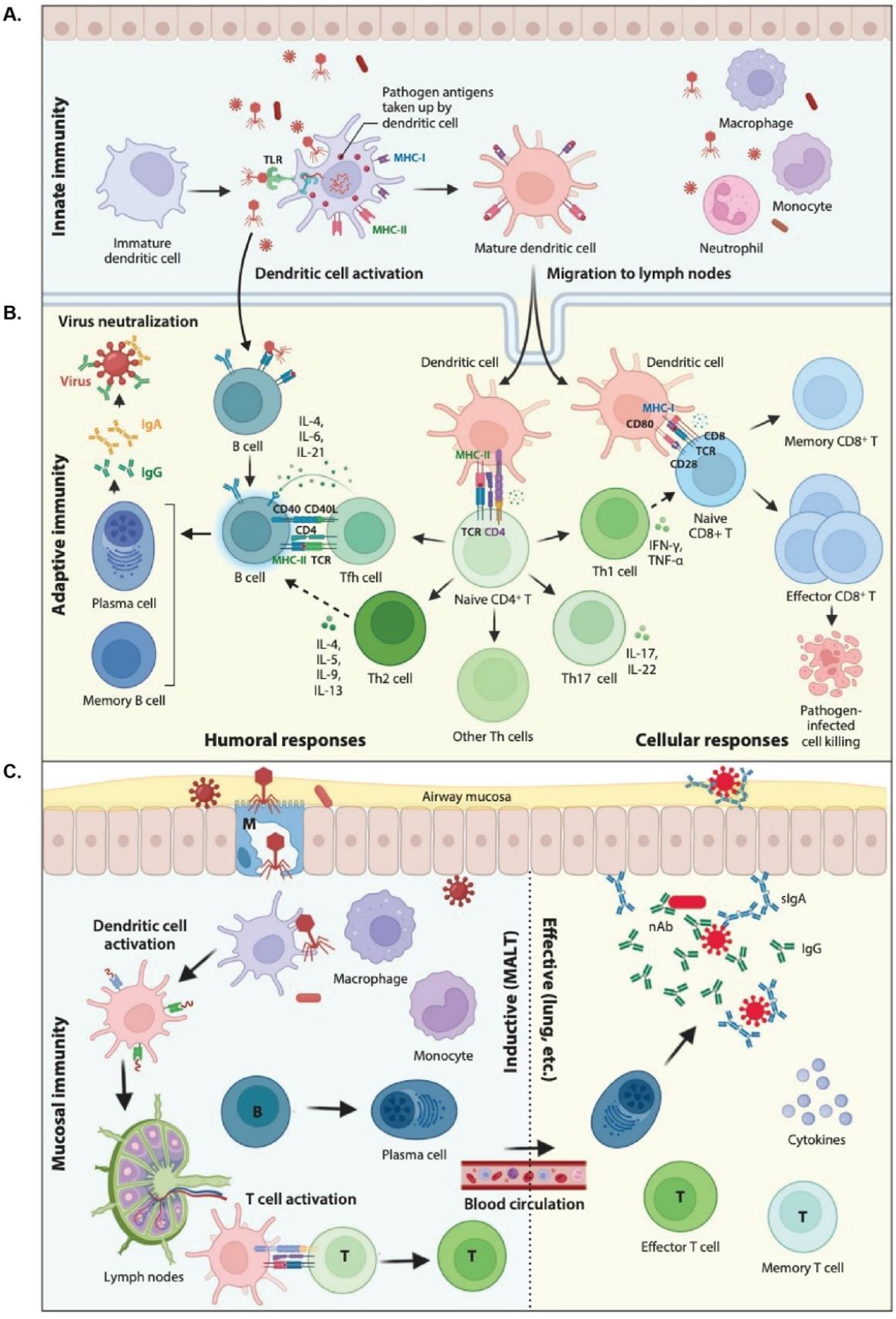
A.
Innate immunity
Pathogen antigens taken up by dendritic cell
TLR
MHC-I
MHC-II
Immature dendritic cell
Mature dendritic cell
Macrophage
Monocyte
Neutrophil
Dendritic cell activation
Migration to lymph nodes
B.
Virus neutralization
Virus
IgA
IgG
Adaptive immunity
B cell
IL-4, IL-6, IL-21
Dendritic cell
Dendritic cell
MHC-I
CD80
CD8
TCR
CD28
MHC-II
Memory CD8+ T
CD40 CD40L
CD4
MHC-II TCR
TCR CD4
Naive CD8+ T
IFN-γ, TNF-α
Th1 cell
Effector CD8+ T
Plasma cell
B cell
Tfh cell
Naive CD4+ T
Memory B cell
IL-4, IL-5, IL-9, IL-13
Th2 cell
Th17 cell
IL-17, IL-22
Pathogen-infected cell killing
Humoral responses
Other Th cells
Cellular responses
C.
Airway mucosa
M
Dendritic cell activation
Macrophage
Monocyte
Mucosal immunity
Inductive (MALT)
Effective (lung, etc.)
sIgA
nAb
IgG
B
Plasma cell
Cytokines
T cell activation
Blood circulation
T
Effector T cell
Memory T cell
Lymph nodes

Figure 1.3: Overview of Innate, Adaptive, and Mucosal Immune Responses Induced by Pathogen Exposure or Vaccination.

Activation of the immunological pathways by vaccines or pathogens, encompassing **A)** innate, **B)** adaptive, and **C)** mucosal immune responses. **A)** Innate immunity shows dendritic cell maturation and migration to lymph nodes. **B)** Adaptive immunity highlights humoral and cellular responses with B and T cells, cytokine release, and interactions. **C)** Mucosal immunity features dendritic cells, B cells, T cells, and secretory IgA production at the airway mucosa. Abbreviations: MALT (mucosa-associated lymphoid tissue), MHC (major histocompatibility complex), nAb (neutralizing antibody), TCR (T cell receptor), TLR (Toll-like receptor).

across mucosal and systemic compartments **Figure 1.3**. However, SARS-CoV-2, like other coronaviruses, has evolved immune evasion strategies. These include downregulating MHC class I molecules to impair cytotoxic T cell recognition and suppressing early interferon (IFN) responses, allowing unchecked viral replication in the early stages of infection (123-126).

CD8+ cytotoxic T cells play a crucial role in clearance of virus-infected cells. Since most T cell epitopes remain conserved across genetically distinct variants of SARS-CoV-2, memory cellular immunity is plays an important role in controlling infection severity, especially when these variants evade vaccine-induced humoral responses **Figure 1.3B** (127). Cross-reactive memory T cells correlate with protection against influenza A virus disease in humans (128-132). Central, effector, and tissue-resident memory T cells (T_{CM}, T_{EM}, T_{RM}) occupy distinct anatomical niches, each contributing uniquely to protective immunity (133). This pre-existing cellular immunity, whether from prior infection or vaccination, enables more rapid and effective responses upon re-exposure, with memory B and T cells facilitating swift neutralizing antibody production and T cell activation **Figure 1.3B** (128, 131, 133-135). This immunity can range from partial protection to

robust immune responses, depending on the individual's prior exposure, the specific vaccine used, and the variant of SARS-CoV-2 to which they are exposed.

1.5.1 SARS-CoV-2 evolution and the emergence of variants of concern

Since the emergence of SARS-CoV-2, the virus has undergone extensive genetic evolution, leading to the rise of variants with distinct characteristics, such as increased transmissibility, changes in disease virulence, and evasion from previously acquired immunity **(Figure 1.4)** (64, 136, 137). Natural selection favors mutations that increase transmissibility, enable viral immune escape and virulence in the host. SARS-CoV-2 initially exhibited gradual adaptation to humans, with limited viral diversity during the first eight months of the pandemic **(Figure 1.4)** (136, 137). Viral evolution occurs as mutations are introduced during each replication cycle, with beneficial mutations spreading through the population (138-140). Although coronaviruses possess a proofreading mechanism (nsp14 exonuclease) that reduces mutation rates compared to other RNA viruses, mutations still accumulate (141). The mutation rate for SARS-CoV-2 is estimated to be around 10^{-6} per base per replication cycle (142). The most notable early substitution was D614G in the SPG, which enhanced ACE2 receptor binding affinity and viral infectivity, resulting in an approximately 20% increase in transmissibility.

Approximately eight months into the COVID-19 pandemic, divergent SARS-CoV-2 lineages such as Alpha, Beta, Gamma, Delta, and Omicron began to emerge independently across different regions **(Figure 1.4A)** (64, 136, 137, 143). The discovery of the Omicron variant (BA.1) in November 2021, which was markedly antigenically distinct from earlier variants, marked a crucial turning point in the pandemic **(Figure 1.4B)**.

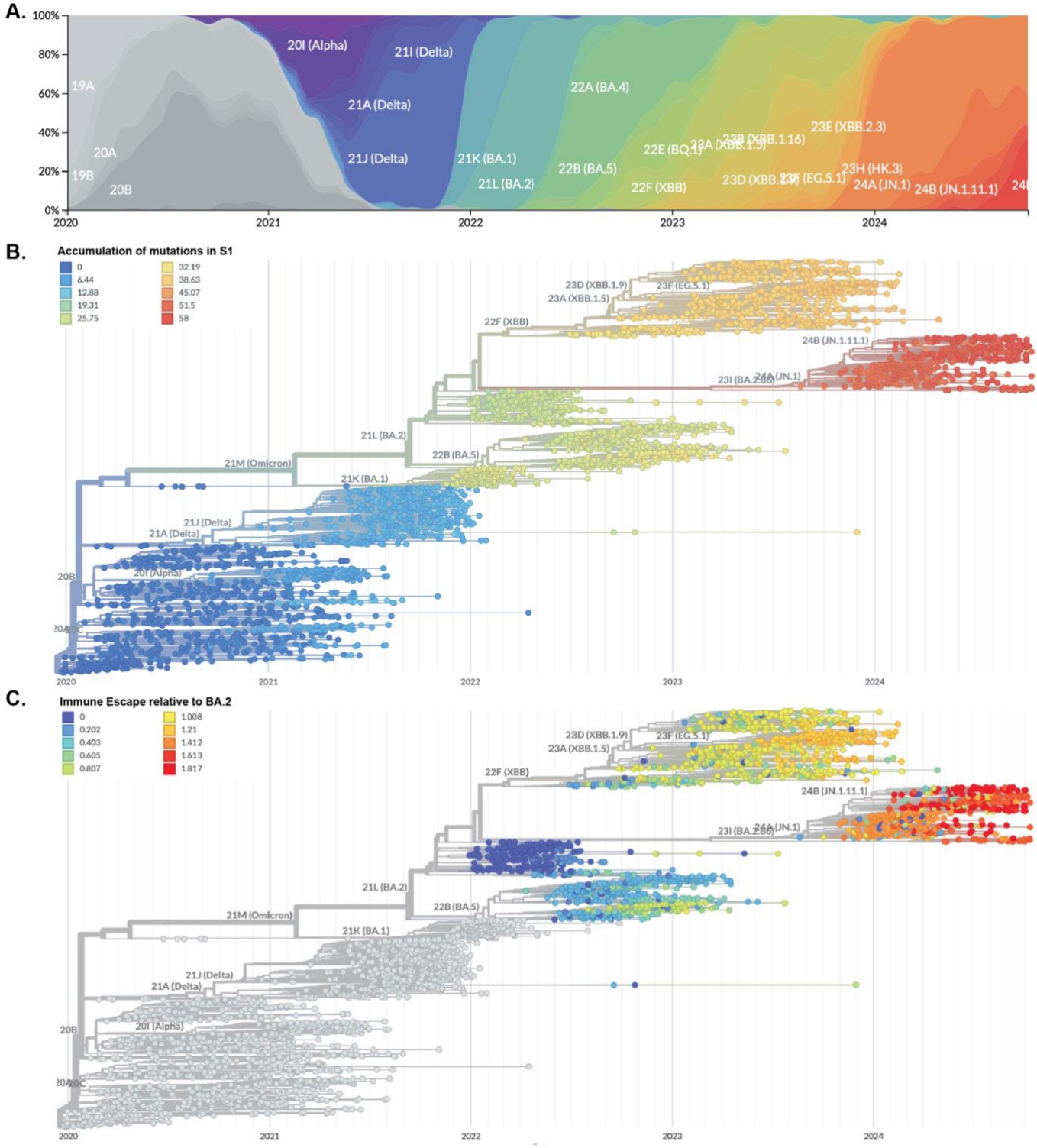
A.
100%
80%
60%
40%
20%
0%
2020
2021
2022
2023
2024
19A
19B
20A
20B
20I (Alpha)
21I (Delta)
21A (Delta)
21J (Delta)
21K (BA.1)
21L (BA.2)
22A (BA.4)
22B (BA.5)
22E (BQ.1)
22F (XBB)
23A (XBB.1.5)
23B (XBB.1.16)
23D (XBB.1.9)
23E (XBB.2.3)
23F (EG.5.1)
23H (HK.3)
24A (JN.1)
24B (JN.1.11.1)
B.
Accumulation of mutations in S1
0
6.44
12.88
19.31
25.75
32.19
38.63
45.07
51.5
58
21M (Omicron)
C.
Immune Escape relative to BA.2
0
0.202
0.403
0.605
0.807
1.008
1.21
1.412
1.613
1.817

Figure 1.4: SARS-CoV-2 Evolution Dynamics.
A) Phylogenetic Tree of the Orthocoronavirinae Based on Spike Protein Amino Acid Sequences. The tree illustrates the evolutionary relationships among orthocoronaviruses, with a scale bar representing a 7% amino acid change. It includes four genera: Alphacoronavirus (Alpha-CoV), Betacoronavirus (Beta-CoV), Gammacoronavirus (Gamma-CoV), and Deltacoronavirus (Delta-CoV). Viruses denoted by blue stars are either actively circulating in humans or have caused infections in the past. Figure adapted from Florian Krammer, 2024(89) in accordance with the Creative Commons Attribution 4.0 International License (https://creativecommons.org/licenses/by/4.0/). **B)** Frequency of SARS-CoV-2 lineages evolution from December 2019 to October 2024, with each Pango lineage labeled by WHO designation and Nextstrain clade, represented by a unique color, generated by nextstrain.org **C)** Accumulation of amino acid mutations in the S1 subunit of the SARS-CoV-2 spike glycoprotein and **D)** immune escape relative to the BA.2 variant over time, generated by nextstrain.org based on 3,338 globally sampled genomes. This image is Copyright nextstrain.org in accordance with the Creative Commons Attribution 4.0 International License (https://creativecommons.org/licenses/by/4.0/).

Omicron's enhanced transmissibility and its ability to evade immune responses contributed to its rapid global dominance, followed by successive waves driven by its subvariants (BA.2, BA.4, and BA.5) **(Figure 1.4B-C)** (136, 137, 144-146).Omicron and its subvariants carry over 30 mutations in the SPG, with a large proportion of these mutations clustered within RBD **(Figure 1.4B)** (80, 136, 137). These mutations allowed Omicron to partially evade the neutralizing antibody responses generated either by vaccines based on the ancestral Wuhan strain or by prior natural infections **(Figure 1.4C)** (144, 145, 147-158). Additional immune-evasive mutations in the RBD were observed in the BA.4 and BA.5 sub-lineages, leading to further reductions in neutralizing antibody titers, even in individuals who had received booster vaccinations (147, 159-163).

Recombination, a common mechanism in betacoronaviruses, accelerates viral adaptation by combining mutations from different variants during co-infection, leading to the creation of hybrid strains. The emergence of the BA.3 lineage has been suggested to result from a recombination

event between BA.1 and BA.2(143). Similarly, the Omicron subvariant XBB is thought to have emerged through the recombination of two co-circulating BA.2 descendants, enhancing its fitness primarily through recombination rather than through substitutions alone (164).

The continuous evolution of SARS-CoV-2 has led to the sequential emergence of highly immune evasive variants, including XBB1.5 EG.5.1, JN.1, KP.3, and KP.3.1.1 **(Figure 1.4C)** (147, 161, 165-172). Each new variant has progressively replaced its predecessor as the dominant strain, with KP.3.1.1 now prevailing in North America **(Figure 1.4A)** (173). These variants demonstrate increasingly enhanced immune evasion, infectivity and transmission, with greater resistance to neutralization in individuals with breakthrough infections or booster vaccinations(147, 161, 165-172).

Although SARS-CoV-2 can infect epithelial cells throughout the mucosal tract, Omicron and its subvariants demonstrate a preference for replication in the URT, providing a strategic advantage for viral entry and contributing to its increased transmissibility (174, 175). Interestingly, Omicron is associated with reduced pathogenicity in the LRT compared to earlier variants like Delta, though severe cases may still result in LRT involvement, particularly in vulnerable populations(174, 175). Additionally, Omicron exhibits a shorter incubation period, averaging around 3 days, compared to earlier variants(75, 176). This shortened period narrows the window of time for effective immune recall responses, thereby facilitating more rapid transmission.

Epitopes within the RBD are highly immunogenic, triggering strong humoral responses, which in turn creates selection pressure favoring the emergence of mutations (antigenic drift) and the development VOCs (153, 177, 178). Most T cell epitopes remain relatively conserved across VOCs, although certain mutations, such as the spike mutation P272L, have been reported to

potentially facilitate immune escape from dominant T cell epitopes (179-182). Additionally, several other mutations within T cell epitopes have been shown to reduce or entirely abrogate MHC class I presentation to evade CD8+ T cell responses (125). However, overall T cell epitopes have remained largely conserved, thus T cell immunity, critical in control severity of disease, is maintained and provides protection despite reductions in neutralization capacity of humoral responses.

Evolution of SARS-CoV-2 has been primarily driven by a combination of mutations that enhance viral entry, transmissibility, and immune evasion. Key mutations have resulted in increased affinity for the ACE2 receptor, a shift in replication preference to the upper respiratory tract, shorter incubation periods, and immune escape mutations in critical antigenic sites targeted by neutralizing antibodies. While T cell epitopes have remained largely conserved, the accumulation of mutations within the RBD has facilitated significant immune evasion from vaccine-induced humoral responses and has further enhanced transmissibility. This underscores the immunodominance of the RBD and the pivotal role of neutralizing antibodies in driving the evolutionary trajectory of SARS-CoV-2 **(Figure 1.4B-C)**.

1.6 Development of first-generation SARS- CoV-2 Vaccines

The rapid development and deployment of vaccines against SARS-CoV-2 stands as one of the most remarkable achievements in modern science. Multiple vaccine platforms, including messenger RNA-Lipid nanoparticle (mRNA-LNP) based vaccines (Pfizer-BioNTech, Moderna), adenoviral vector vaccines (AstraZeneca, Johnson & Johnson), and protein subunit vaccines (Novavax, Medicago), were developed, tested, and deployed in record time. By December 2020,

less than a year after the virus was identified, the first mRNA vaccines were granted emergency use authorization.

Vaccine design and the route of delivery are critical considerations in the development of an effective vaccine. The spike protein of SARS-CoV-2 is the primary antigenic target of current vaccines due to its high immunogenicity, which induces strong cellular and humoral responses (100, 101, 107, 183-185). Currently, all authorized vaccines in North America are administered intramuscularly (IM), which elicit strong systemic humoral and cellular responses and effectively prevent against severe disease.

The Pfizer-BioNTech and Moderna mRNA vaccines were the first COVID-19 vaccines authorized for emergency use in humans in North America. These vaccines use LNPs as carriers to deliver mRNA encoding the SARS-CoV-2 spike protein into host cells. Following IM administration, the mRNA-LNP is primarily taken up by local cells at the injection site and in the draining lymph nodes, where it is processed by APCs such as monocytes, macrophages, and dendritic cells (186-188). These APCs translate the mRNA, process and present the resulting antigen on the cell surface, driving both humoral and cytotoxic T-cell response (186, 188-191). Muscle cells can also take up mRNA and produce spike protein, either as a membrane-anchored or secreted form, depending on the mRNA design (192, 193). The initial mRNA-LNP vaccines were primarily designed to prevent severe disease and death, demonstrating up to 100% efficacy in preventing severe disease and hospitalization, and up to 90% effectiveness against symptomatic infection (185, 194-197).

The LNP component of the vaccine additionally contributes to the platform's impressive immunogenicity by acting as an intrinsic adjuvant. It promotes durable antibody responses by

inducing T follicular helper cells, long-lived plasma cells memory B cells, and prolonged germinal center reactions (188, 189, 198-205). Indeed, comparisons of mRNA-LNP vaccines with protein subunit vaccines adjuvanted with LNP further highlight the potent adjuvant effect of LNPs (189, 190, 203-208). While COVID-19 vaccines have generally been well-tolerated, with minor side effects such as reactogenicity reported, in rare cases, more notable side effects, such as an elevated risk of myocarditis, particularly in younger males following mRNA vaccination, have been observed (209-212). The biological mechanism behind the latter side effect is still under investigation, but it may be related to the immune response to the spike protein or to components of the lipid nanoparticle delivery system(212). The mRNA vaccine platform stands out for its speed, adaptability to drifting viruses, and potency, enabling development of strong and durable immune responses, making it a versatile tool for targeting a broad range of infectious diseases.

Adenoviral vector vaccines, such as AstraZeneca and Johnson & Johnson, use a modified adenovirus to deliver the spike protein gene into host cells. Although both vaccine platforms have been highly effective in preventing severe disease, they differ in their mechanisms of delivery and in the immune responses they generate. AstraZeneca vaccine demonstrated 100% efficacy in preventing severe disease and hospitalization, with around 70% efficacy against symptomatic infection (213). Similarly, Johnson & Johnson vaccine showed 94% efficacy against moderate to severe disease and 66% efficacy for symptomatic infection following the initial 2 dose vaccine regiment (214). The adenoviral vector vaccines have also been associated with rare but serious side effects, such as vaccine-induced thrombotic thrombocytopenia (VITT). Greinacher et al. demonstrate that VITT is driven by platelet-activating antibodies against PF4 following AstraZeneca administration, similarly to complications observed in heparin-induced thrombocytopenia disorder (215). Furthermore, other studies highlight that accidental

intravenous administration or leakage of the adenovirus vector into the bloodstream, has been linked to the potential development VITT (209, 216-218).

Protein subunit vaccines have a well-established safety record, with efficacy dependent on their adjuvant and antigen components. Novavax demonstrated around 90% efficacy against symptomatic infection and 100% efficacy against severe disease following a two dose primary vaccine regiment (219). In turn, Medicago's vaccine showed 71% efficacy against symptomatic infection and 100% efficacy against severe disease. Both vaccines offer strong protection, though efficacy was lower than mRNA vaccines, particularly against newer variants (220). Adjuvants are often crucial for directing antigen-specific immune responses and overcoming weak antigenicity of viral proteins. Due to adjuvants' intrinsic immunomodulatory properties, their combined administration with an antigen elicits superior and long-lasting immune responses (221, 222). In contrast, there are several advantages to a recombinant protein vaccine platform, including its expression and production in different systems ranging from insect cells to plants[46–49]. Indeed, transient transformation of *Nicotiana benthamiana* via agroinfiltration enables rapid and efficient expression of recombinant proteins for use in vaccines (223). Unlike traditional stable transformation, which takes months, transient transformation allows for the co-expression of multiple proteins simultaneously. This flexibility makes it an ideal platform for the rapid development of evolving vaccine targets (185, 224).

The vaccines used during the COVID-19 pandemic have been highly effective in preventing severe disease, hospitalization, and death. However, their efficacy in preventing asymptomatic infection and reducing transmission has been limited depending on the platform. This limitation was largely due to the inability of these IM vaccines to induce robust mucosal immunity in the respiratory

tract, where SARS-CoV-2 first establishes infection. Furthermore, the emergence of VOCs with significant antigenic divergence from the ancestral SARS-CoV-2 strain has necessitated vaccine adaptation to better match circulating variants, similar to the approach used in seasonal influenza (177, 178). Indeed, the accumulation of immune-evasive mutations within the RBD, has enabled these variants to partially evade immunity elicited by vaccines based on the ancestral strain (153, 177, 178). Indeed, breakthrough infections with both Delta and Omicron variants have been reported in fully vaccinated individuals, which showed viral shedding and onward transmission despite vaccination (225-227).

1.6.1 SARS-CoV-2 and role of mucosal immunity

SARS-CoV-2 infection primarily occurs via inhalation of aerosolized virus, with the upper respiratory mucosa (URT) serving as the main entry point. Furthermore, Omicron and its sub-lineages have evolved to preferentially replicate in the URT, increasing their transmissibility, and contributing to the persistence of infections despite parenteral vaccination.

Despite the strong systemic immune responses elicited by authorized IM vaccines in North America, these vaccines leave individuals vulnerable to infection in the URT, where local immune responses are crucial for controlling early viral replication, preventing systemic dissemination, and reducing onward transmission. Studies have demonstrated that mucosal humoral and cellular immunity, particularly IgA responses, are closely correlated with protection against breakthrough infections caused by variants (228-235). Individuals with hybrid immunity (from vaccination and breakthrough infection) exhibit higher levels of broadly neutralizing antibodies in bronchoalveolar lavage fluid (BALF) compared to vaccinated-only individuals, despite similar systemic IgG levels. Indeed, mucosal antibody responses have been shown to correlate with protection from

breakthrough infection with Omicron sub-lineages (228-233). Furthermore, these individuals demonstrate a lower incidence of subsequent breakthrough infections. This highlights the importance of incorporating mucosal immune stimulation into vaccine strategies to mitigate, or ideally prevent, the establishment of infection, a concept often referred to as sterilizing immunity. Achieving sterilizing immunity through intranasal vaccines would represent a major advance in controlling respiratory virus outbreaks.

1.6.2 Mucosal Immunity

Mucosal immunity is vital for defending against pathogens entering through mucosal surfaces such as the respiratory, gastrointestinal, and urogenital tracts, with approximately 70% of infections occurring via these routes (119, 120, 236). These surfaces are characterized by constant exposure to environmental substances, where specialized immune responses have evolved to protect the host against external threats while maintaining a balance between immune tolerance and activation. This balance ensures effective protection without excessive inflammation, preserving tissue homeostasis.

The mucosal immune system consists of an integrated network of tissues, lymphoid and non-lymphoid cells, and effector molecules—including antibodies, chemokines, and cytokines—that coordinate innate and adaptive responses to pathogens and vaccines (119, 121, 237, 238). Specialized mucosa-associated lymphoid tissues (MALT) include gut-associated lymphoid tissue (GALT), nasal-associated lymphoid tissue (NALT), and bronchus-associated lymphoid tissue (BALT). Mucosal surfaces are divided into type I (e.g., lung and gut) and type II mucosae (e.g., mouth, esophagus, cornea) (120, 121, 239).

In type I mucosal tissues, immune responses are organized into inductive and effector sites **(Figure 1.3C)**. Unlike peripheral LNs, which rely on migrating APCs for lymphocytes priming, inductive sites such as tonsils and Peyer's patches facilitate local antigen presentation and lymphocyte priming through mucosal DCs or microfold (M) epithelial cells **(Figure 1.3C)**. M cells allow for effective sampling and transcytosis of antigens on the lumen—including viruses and bacteria—to underlying mucosal DCs and immune cells (119, 240) which can then migrate to the draining LNs to further drive immune activation (116, 119, 241). This process activates adaptive immune responses, leading to lymphocyte proliferation and differentiation.

Effector sites are where activated immune cells carry out their protective functions. Organized lymphoid tissues beneath the mucosal epithelium resemble peripheral lymph nodes but have a higher proportion of B cells relative to T cells. These tissues are essential for the class switching of naïve IgM+ B cells to IgA-producing cells, highlighting their crucial role in mucosal immunity **(Figure 1.3C)** (242-244). IgA is among the most abundantly produced immunoglobulins in the body to ensure mucosal protection. Furthermore, the "common mucosal immune system" interconnects different MALT sites, enabling coordinated B lymphocyte trafficking and IgA secretion at mucosal sites distant from the initial antigen presentation and activation (245). In the respiratory and gastrointestinal tracts, secretory IgA (sIgA) acts as the first line of defense against pathogens, making potent IgA responses a key goal for mucosal vaccination (120, 237-239, 246-248).

1.6.2.1 IgA and its Role in Mucosal Immunity

Although IgA is the most abundant immunoglobulin at mucosal sites, particularly those lining the gastrointestinal, respiratory, and urogenital tracts, where it may account up to 70-80% of the total

immunoglobulin, it exists in various proportions and forms throughout the body (249-252). At type I mucosal surfaces, IgA primarily forms a dimer, linked by a J chain polypeptide, which facilitates the formation of multimeric IgA structures (253). While dimeric IgA is the predominant form, less common tetrameric and pentameric forms have also been observed (254, 255). Among the five human immunoglobulin isotypes, only IgA and IgM have the capacity to form these higher-order oligomeric structures. Dimeric IgA secreted by plasma cells in the lamina propria, binds to the polymeric immunoglobulin receptor (pIgR) at the basolateral surface of epithelial cells, and is transported across the epithelial layer into the lumen (249, 251). Upon reaching the lumen, the cleavage of pIgR releases secretory IgA (sIgA), with the secretory component which provides protection from enzymatic degradation in the mucosal environment (254, 256, 257). Type I epithelial cells also express the neonatal Fc receptor (FcRn), which can transport IgG across the epithelial cell layer (258).

IgG is generally less abundant at mucosal surfaces compared to IgA, however in some mucosal sites, IgG can account for 15-20% of the total immunoglobulins (252, 259). IgG has been shown to play a protective role in the lower respiratory tract, where it helped control infection through mechanisms like complement activation and antibody-dependent cellular cytotoxicity (ADCC) (260, 261).

In serum, IgA predominantly exists in a monomeric form, comprising approximately 15 % of total immunoglobins, being the second most abundant immunoglobulin after IgG (250, 251). Serum IgA contributes to immune defense by mediating mechanisms such as phagocytosis and ADCC, and, under specific conditions, can initiate the complement pathway(242, 249, 251, 262). Humans

possess two IgA isotypes: IgA1 and IgA2. IgA1 is the predominant isotype in serum, while IgA2 is more abundant in mucosal secretions (250, 251).

sIgA is highly efficient at neutralizing pathogens at mucosal entry points by binding to viral particles, thus limiting viral replication and making it a critical component of mucosal immunity (120, 242, 249, 251, 259, 263-265). This neutralization process involves both direct and indirect mechanisms. sIgA can directly bind to viral particles in the mucosal lumen, preventing their attachment to and entry into permissive epithelial cells. Neutralization is mediated through high-affinity interactions between sIgA and specific viral glycoproteins. For example, in SARS-CoV-2 and influenza, sIgA binds to the SPG and HA, respectively, preventing viral entry (235, 263, 266-270). Polymeric IgA proved to be more effective than monomeric IgA in preventing Clostridium difficile toxin A-induced damage to epithelial cells (271). The increased valency of multimeric IgA enhances its avidity, allowing it to robustly bind even lower-affinity antigens. This property contributes to its broad cross-reactivity against antigenically mismatched variants and enables it to bind multiple pathogens simultaneously. This "immune exclusion" process is efficient in containing pathogens within the mucosal lumen, thus preventing systemic dissemination and reducing the spread of infection.

Importantly, sIgA neutralizes pathogens without inducing inflammatory responses, unlike IgG, which may trigger inflammatory pathways such as complement fixation and ADCC. This non-inflammatory neutralization is crucial for preventing tissue damage in sensitive mucosal areas. Although Fc-mediated immunity is not the primary effector function of IgA at mucosal surfaces, IgA can activate neutrophils via its Fc receptor to mediate local ADCC, thereby contributing to the control of viral infections and limiting their transmission. Increasing evidence supports the

importance of mucosal sIgA in protection against respiratory pathogens, such as SARS-CoV-2 (229, 230, 233, 235, 236, 247, 248, 268, 272-283). Robust stimulation of respiratory mucosal immunity is thought to be critical in reducing infection at primary replication sites. The enhanced neutralizing capacity of sIgA, due to its multimeric structure and increased avidity, makes it more effective than systemic IgG in the respiratory tract.

1.6.2.2 The Cellular Arm of Mucosal Immunity

In addition to humoral immunity conferred by secretory IgA (sIgA), cellular immunity plays a critical role at mucosal sites, contributing substantially to the defense against invading pathogens. Tissue-resident memory cells represent a distinct population of long-lived memory cells that persist in mucosal tissues long after the clearance of an infection, thereby enabling rapid immune responses upon re-exposure and effectively limiting viral replication (128, 130, 135, 233, 248, 268, 275, 284-287). In contrast to circulating memory T cells, which provide protection but require time for antigen recognition, expansion, migration, and effector function at the site of infection, Trm cells are strategically poised within the tissue (288). This enables Trm cells to initiate immediate responses and tissue-wide protection against pathogens, thereby significantly expediting the recognition and clearance of pathogens that have been previously encountered at the same mucosal site (128, 135, 286, 287, 289, 290). Trm cells effectively limit viral replication through the release of IFN-γ, which induces interferon-stimulated genes, recruits leukocytes, and promotes local inflammation(135, 291). However, this response may come at a higher "cost" in inflammatory responses compared to sIgA, which neutralizes pathogens with minimal inflammation (248).

Studies on influenza and SARS-CoV-2 have shown that Trm and Brm cells are particularly effective at reducing viral load in the URT(130, 131, 133, 134, 247, 248, 268, 274, 275, 285-287, 289, 290, 292, 293). Importantly, mucosal tissue-resident memory T and B cells are typically

induced by local antigen stimulation, further underscoring the importance of mucosal-targeted vaccines and treatments in enhancing protection against respiratory viruses (285, 294).

1.6.2.3 Effectiveness of Intranasal Vaccines in Inducing Mucosal Responses

IN vaccines directly stimulate mucosal immune responses, where respiratory pathogens such as SARS-CoV-2 and influenza initiate infection, inducing both sIgA and tissue-resident memory cells at URT. Multiple studies demonstrated superior protection with intranasal IN vaccination relative to IM immunization, particularly in its ability to induce local immunity at the site of viral entry. This approach is proposed as an effective strategy to enhance immunity at the site of SARS-CoV-2 infection, specifically targeting the URT and LRT. In animal models, IN vaccines have been shown to significantly limit viral replication following infection with both ancestral and variant strains of SARS-CoV-2 (268, 275-277, 282, 295, 296). Studies on intranasal vaccines against influenza have demonstrated that mucosal vaccination, compared to the intramuscular route, induces stronger cross-protective immunity against heterosubtypic influenza strains and promotes long-term immune responses (129, 274). By generating mucosal responses at the primary site of infection, IN vaccines are critical not only for preventing the establishment and replication of the virus at an individual level but also for reducing viral transmission at a population level.

Several groups have been evaluating the potential of IN and oral vaccines to block transmission, showing that these vaccines, unlike IM vaccines, significantly reduce SARS-CoV-2 transmission in animal models (233, 267, 268, 275-277, 279, 281, 282, 295-299). Indeed, Langel *et al.*, demonstrate reduced SARS-CoV-2 airborne transmission from intranasally immunized hamsters to naïve hamsters (276). Darling et al. recently demonstrated that IN vaccination reduced infectious virus titers by approximately 100-fold and 100,000-fold in the URT of the primary contact

hamster(299). In addition, Tang *et al.* demonstrate that individuals with prior infection showed increased levels of broadly neutralizing antibodies in BALF relative to vaccinees, despite similar systemic IgG titers (233). While Sheikh *et al.* and Harvel *et al*. highlight the important role that mucosal IgA may have in preventing SARS-CoV-2 infection (229, 235). Both studies show that vaccinated individuals with breakthrough infections from divergent VOCs had lower serum and mucosal IgA titers, despite similar serum IgG levels to those without infections (230, 235). By targeting the respiratory mucosa, IN vaccines induce both systemic and mucosal responses, with the latter having the additional benefit of reducing viral shedding at the site of viral entry and limiting onward transmission.

Over 20 mucosal SARS-CoV-2 vaccine candidates are currently in development, primarily utilizing viral vector platforms, including both replication-competent and replication-deficient designs as overviewed in **Table 1.1** (89, 247, 300, 301). BBV154, an intranasal replication-deficient vaccine developed by Bharat Biotech, was approved in India in 2023 as a booster for adults. It has shown strong immunogenicity in both mice and humans, eliciting potent systemic and mucosal immune responses. Clinical trials demonstrated that while IN vaccination induced neutralizing antibody responses comparable to IM vaccination, salivary IgA levels were significantly higher in those receiving the intranasal vaccine. Ad5-nCoV, a replication-deficient adenovirus-based vaccine developed by CanSino Biologics, was authorized for both primary and booster use in China. It is administered via oral inhalation using a nebulizer, delivering aerosolized vaccine particles to the lungs. Ad5-nCoV has also shown strong immunogenicity in clinical trials, inducing robust neutralizing antibody responses and T-cell activation.

Table 1.1: Current Landscape of Mucosal COVID-19 Vaccines in Clinical Development or Licensed for Use According to WHO COVID-19 Vaccine Tracker (301).

Vaccine Name (Company)	Status	Route of administration	Vaccine Platform, antigen
AD5-nCOV (CanSino)	Licensed in China	Inhaled	Adenovirus type 5 vector (nr), spike
BBV154 (Bharat)	Licensed in India	Intranasal	Chimpanzee adenovirus vector (nr), spike
DelNS1-2019-nCoV-RBD-OPT1 (University of Hong Kong, Beijing Wantai Biological Pharmacy)	Phase III	Intranasal	Influenza virus delNS1 vector (r), RBD
COVI-VAC (Codagenix/Serum Institute of India)	Phase III	Intranasal	Live attenuated virus SARS-CoV-2
CIGB-669 (Center for Genetic Engineering and Biotechnology)	*Phase I/II*	Intranasal	RBD plus hepatitis B virus protein antigen
NDV-HXP-S (CastleVax, Icahn School of Medicine at Mount Sinai	Phase I	Intranasal	Newcastle disease virus vector (r), spike
AdCOVID (Altimmune)	*Phase I,*	Intranasal	Adenovirus vectored (nr), RBD
NDV-HXP-S (CastleVax, Icahn School of Medicine at Mount Sinai	*abandoned*	Intranasal	Newcastle disease virus vector (r), spike
MV-014–212 (Meissa Vaccines)	Phase I	Intranasal	Attenuated RSV vector, spike
CVXGA1 (CyanVac)	Phase I	Intranasal	Parainfluenza 5 vectored (nr), spike
ACM-001 (ACM Biolabs)	Phase I	Intranasal	Recombinant protein, spike
OMV-linked HexaPro spike vaccine (Intra- vacc)	Phase I	Intranasal	Outer membrane vesicles from *Neisseria meningitides* linked to recombinant spike
VXA-CoV2-1 (Vaxart)	Phase II	Oral	Adenovirus vector type 5 vector (nr), spike
bacTRL-Spike oral DNA vaccine (Symvivo)	Phase I	Oral	*Bifidobacterium longum*- DNA based gene transfer into human cells, spike
CoV2-OGEN1 (USSF/Vaxform)	Phase I	Oral	Recombinant protein, spike-NP fusion protein
SARS-COV2 (DreamTec Research)	N.A	Oral	Bacillus subtilis spores, RBD
Ad5-triCoV/Mac or ChAd-triCoV/Ma (McMasters University)	Phase I	Aerosolized	Adenovirus vectored (nr), spike, NP, and polymerase
MVA-SARS-2-ST (Hannover Medical School)	Phase I	Inhaled	MVA vector, spike

*(r) : replication competent viral-vector platform, (nr): replication deficient viral-vector platform

A Canadian-made adenovirus-based vaccine expressing SARS-CoV-2 spike, nucleocapsid, and RNA polymerase proteins, administered via aerosolized inhalation, will enter Phase II clinical trials after completing Phase I by the end of 2024 (302). Following promising preclinical results, the ongoing trial assesses safety, immunogenicity, and correlations between antibodies measured in saliva, BALF, and serum (275, 302). Overall, these mucosal vaccines significantly reduce viral load in the respiratory tract, which is a key factor in decreasing transmission.

Thus, mucosal vaccines represent a promising strategy for simultaneously inducing both systemic and mucosal immunity, offering the potential for more effective protection against recurring infection with respiratory viruses at the site of their entry, thereby reducing onward transmission and the burden of infectious diseases globally.

Rationale, Hypothesis and Objectives

Thesis Rationale

The ongoing impact of circulating and emerging respiratory viruses on health, healthcare systems, and global economies highlights the urgent need for innovative strategies to study viruses and prevent infection. The ongoing mutation and evolution of SARS-CoV-2 have led to the emergence of highly transmissible and immune-evasive variants. Currently available parenteral vaccines, while effective against severe disease, show reduced efficacy in symptomatic infection and transmission against emerging variants. This underscores the need for continuous monitoring SARS-CoV-2 evolution and adaptation of current vaccine strategies.

Understanding the phenotypic characteristics of SARS-CoV-2 can provide critical insights into viral evolution and help identify how these variations impact virus-host interactions and immune evasion. Flow virometry enables rapid and detailed phenotypic analysis of changes in the viral glycoprotein density and that of other surface antigens, which can inform vaccine design and delivery. Additionally, investigating the kinetics of viral infection and the modulation of the host immune response is crucial for elucidating the dynamics of immune evasion and pathogenesis.

The sustained circulation of SARS-CoV-2 and the emergence of new variants highlight the limitations of parenteral vaccines in effectively reducing viral transmission. This inherent limitation of parenteral vaccines necessitates the continual updating and matching of vaccine formulations to the circulating variants, similar to seasonal flu vaccination campaigns. Therefore, next-generation vaccine strategies that elicit mucosal responses at the site of virus infection and replication are critical for preventing the establishment of infection at the individual level and limiting viral spread at the population level.

Thus, new modalities of vaccination that invoke mucosal immunity are crucial to neutralize virus and limit initial infection at point of entry, prevent onward transmission. A key objective of my thesis is to elucidate immunogenic targets for intranasal vaccine design and characterizing the associated mucosal and humoral immune responses in distinct biological compartments will inform optimal vaccine design and delivery, particularly in the context of recurrent infections with continuously evolving SARS-CoV-2. Furthermore, evaluating alternative vaccine production platforms, such as plant-based expression systems for antigen production, may offer rapid, scalable, and effective solutions for vaccine development and deployment, particularly during time sensitive periods such as pandemics.

A comprehensive understanding of a pathogen's phenotypic characteristics, infection dynamics, and associated pathogenesis is essential for designing an effective vaccine (**Figure 1.5)**. This knowledge provides the foundation for targeting key aspects of the pathogen's biology, enabling the development of vaccines that can effectively prevent infection or mitigate disease severity. This thesis explores the development of rapid diagnostic tools for viral detection, characterization of virus-host interactions, the investigation of next-generation vaccine strategies with increased breadth of protection—such as optimal antigen selection, administration routes, and the role of mucosal immunity in reducing viral infection and transmission (**Figure 1.5)**. By integrating these insights, the goal of this thesis is to inform the design of next-generation vaccines to halt the circulation of SARS-CoV-2 and better prepare for future pandemics.

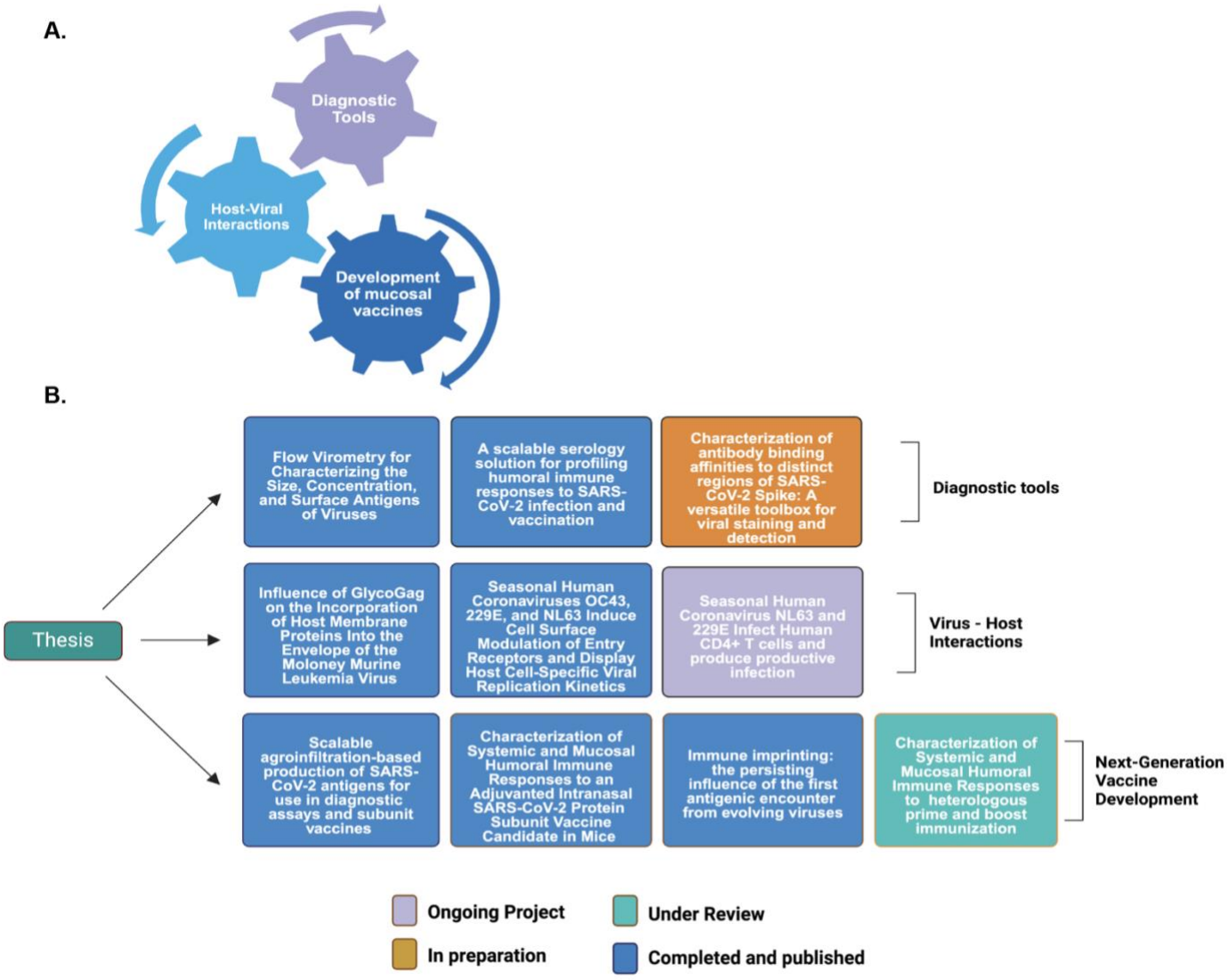

Figure 1.5: Conceptual approach for preclinical research and development in pathogen preparedness.

The development of effective therapeutics and vaccines for novel, emerging, or reemerging pathogens requires both fundamental and applied research**. A)** This process relies on rapid diagnostic tools, a thorough understanding of pathogen biology, and insights into host immune responses. **B)** My PhD dissertation addresses these key areas, including the development of rapid viral diagnostics, the characterization of virus-host interactions, and the exploration of next-generation vaccine strategies. These strategies focus on optimized antigen selection, alternative delivery routes, and the vital role of mucosal immunity in reducing viral infection and transmission.

Objectives:

1. Rapid characterization of known and emerging viruses (chapters 2-3)
   ▪ Development of flow virometry as a tool for the rapid characterization of intact viruses

2. Elucidation of virus-host interactions (chapters 3-4)
   ▪ Investigation of viral kinetics and the modulation of the host's immune response by retroviruses and seasonal coronaviruses following infection.

3. Development of next-generation mucosal vaccines against SARS-CoV-2: Implications for optimal vaccine design and delivery (chapters 5-8).

   - Elucidate immunogenic targets for intranasal vaccine design against SARS-CoV-2.
   - Characterize mucosal and systemic humoral immune responses following heterologous prime and boost vaccination.
   - Evaluate plant produced antigens as potential protein subunit vaccines.

Hypothesis

We hypothesize that characterizing both the structural aspects of viruses and host immune responses to infection and vaccination, particularly humoral responses at distinct biological compartments, will inform the development of improved vaccine designs and delivery methods against continuously evolving respiratory viruses.

2 Chapter 2: Flow Virometry for Characterizing the Size, Concentration, and Surface Antigens of Viruses *(Published)*

Preface: This chapter has been previously published as a research article.

Maltseva M., and Langlois M-A. (2022), Flow Virometry for Characterizing the Size, Concentration, and Surface Antigens of Viruses. ***Current Protocols***, *2*(2), e368.
https://doi.org/10.1002/cpz1.368

2.1 Abstract

Application of flow cytometry principles for the analysis of viruses has been referred to as flow virometry (FVM). FVM is a multiparametric, high-throughput, and sensitive technique that allows viral particles to be detected, quantified, and characterized based on the biophysical properties of the virus and the ex- pression of proteins on their surface. More specifically, by calibrating the flow cytometer with reference materials, it is possible to measure the concentration of intact viral particles in a sample, the abundance of a target antigen on the surface of the virus, and the relative diameter of the virus. Here, we describe a comprehensive overview of procedures used to stain, detect, and quantify viral and host-derived proteins located on the surface of retroviruses. These outlined techniques can be applied for the rapid phenotypic characterization of retroviruses, other enveloped viruses, and generally most viruses at the single- particle level through the direct staining of viruses collected from the super- natant of infected cells, without the need for enrichment or purification.

Basic Protocol 1: Virus production.

Basic Protocol 2: Instrument setup, standardization and quality control for fluorescence quantification.

Basic Protocol 3: Virus detection and quantification.

Basic Protocol 4: Viral surface antigen staining and fluorescence quantification.

Support Protocol 1: Determination of the optimal antibody concentration for virus staining.

Basic Protocol 5: Gain Configuration Optimization

2.2 Introduction

Viral phenotypic analyses are predominantly performed on a virus population using methodologies such as western blot, ELISA, PCR, and mass spectrometry, which are not designed to characterize viruses at the single-particle level and are incapable of assessing inter-particle variabilities. Although electron microscopy can provide extremely useful of target antigen information on single particles, the time-intensive and low through put nature of this technology limits simultaneous virus characterization to only a small portion of the total viral population in a sample. Additionally, these technical approaches are not well suited to characterizing the heterogeneity of viral subpopulations, discern features within these subpopulations, or characterize the antigen composition on the surface of individual viruses on a large scale. However, increasing interest in extracellular vesicles (EVs) has spurred the development of flow cytometry principles for the analysis of submicron particles and renewed the pursuit of analyzing viruses using flow cytometry approaches. In particular, the analysis of viruses by flow cytometry has been referred to as flow virometry (FVM) (Arakelyan, Fitzgerald, Margolis, & Grivel, 2013).

FVM is a rapid, sensitive, and high-throughput technique that can also provide valuable statistical information on the various analyzed features. FVM can measure the concentration of intact viral particles in a sample and characterize some of the physical properties of viruses by the way they scatter light and emit fluorescence when stained with dyes and antibodies (Maltseva & Langlois, 2021; Tang, Renner, Fritzsche, Burger, & Langlois, 2017). When using flow cytometers capable of small-particle analysis, the light scattering properties of the viruses can be used to derive refractive indices (RIs) and viral particle sizes (Brittain et al., 2019; Tang et al., 2019). Additionally, antibodies can be used to stain proteins on the surface of the viruses in a similar manner to cell staining in classical flow cytometry, where fluorescence intensity can provide a measurement of target antigen abundance if adequate calibration is performed on the instrument.

Most enveloped viruses bud at the cell surface or through the endosomal pathway and, in this process, acquire part of the lipid bilayer membrane of the infected cell, which contains cellular and viral proteins (Cantin, Methot & Tremblay,2005; Maltseva & Langlois, 2021). This fragment of the membrane with embedded proteins will then constitute the envelope of the released viruses. Characterizing viral envelope proteins is an appealing research venture due to the insight these antigens can provide on virus cell tropism, the cellular identity of infected cell/tissue reservoirs in

a host, and potential accessible antigenic targets for vaccine development. FVM is rapidly evolving into a more common method in virology as technological advancements are being made on various fronts, including the development of more sensitive analysis hardware, better reagents, and data and methods standardizations (Thery et al., 2018; Tian et al., 2020; Welsh et al., 2020). Although FVM has shown increasing popularity in recent years, it still faces several technical hurdles that hinder the full deployment of its potential. Analysis of viruses by FVM presents several inherent challenges, primarily due to their very small size compared to cells, which places them at the limit of detection of current instruments (Lippe, 2018). A viral particle's surface area can be 1000- to 10,000-fold smaller than that of a cell, and the magnitude of this difference is reflected in surface antigen density and abundance. Therefore, weakly expressed antigens on viruses may fall at or even below the detection limits of an instrument. Careful consideration should be applied to the experimental setup, assay procedures, and data analysis methods to ensure the most robust and reproducible results from these types of experiments.

2.3 Basic Protocol 1: Virus production

Virus production can be achieved through different means depending on the desired experimental goal. These methods will yield viral particles of varying levels of homogeneity and purity. Here we produced viruses by three common methods and analyzed them by light scatter and fluorescence. We produced virus by cell transfection, by harvesting the supernatant of an infected cell population and infected cell clone (Fig. 1). Detailed methods to produce virus and virus expression plasmids used have been described elsewhere (Maltseva & Langlois, 2021, Renner, Tang, Burger, & Langlois, 2020; Tang et al., 2017). The virus used here is replicative murine leukemia virus (MLV) that expresses an envelope-superfolder GFP fusion protein (Env-sfGFP) on its surface (Maltseva & Langlois, 2021, Renner, Tang, Burger, & Langlois, 2020; Tang et al., 2019; Tang et al., 2017). Tagging the envelope glycoprotein with a GFP fluorescent reporter makes these viruses intrinsically fluorescent and easily discernible from background noise. However, these viruses can also be labeled by fluorophore conjugated antibodies directed against host-derived surface proteins or against the Env-sfGFP fusion protein found on the viral envelope, as we have demonstrated in this protocol (Maltseva & Langlois, 2021, Renner et al., 2020; Tang et al., 2019). As shown in Figure 1A, viruses produced by all three methods are resolved with different efficiencies by both light scatter and fluorescence. Although viruses produced by all three methods exhibit a homogenous light scatter and fluorescence intensity distribution, virus produced

from a chronically infected clonal cell line displayed the most monodisperse population in both properties and had a lower background fluorescence compared to the other methods for virus production (Fig. 1B and 1C). Various factors can contribute to the increase in background fluorescence levels, such as the type of media used, the type of transfection reagent, EVs that are concomitantly released by the cells (Tang et al., 2017).

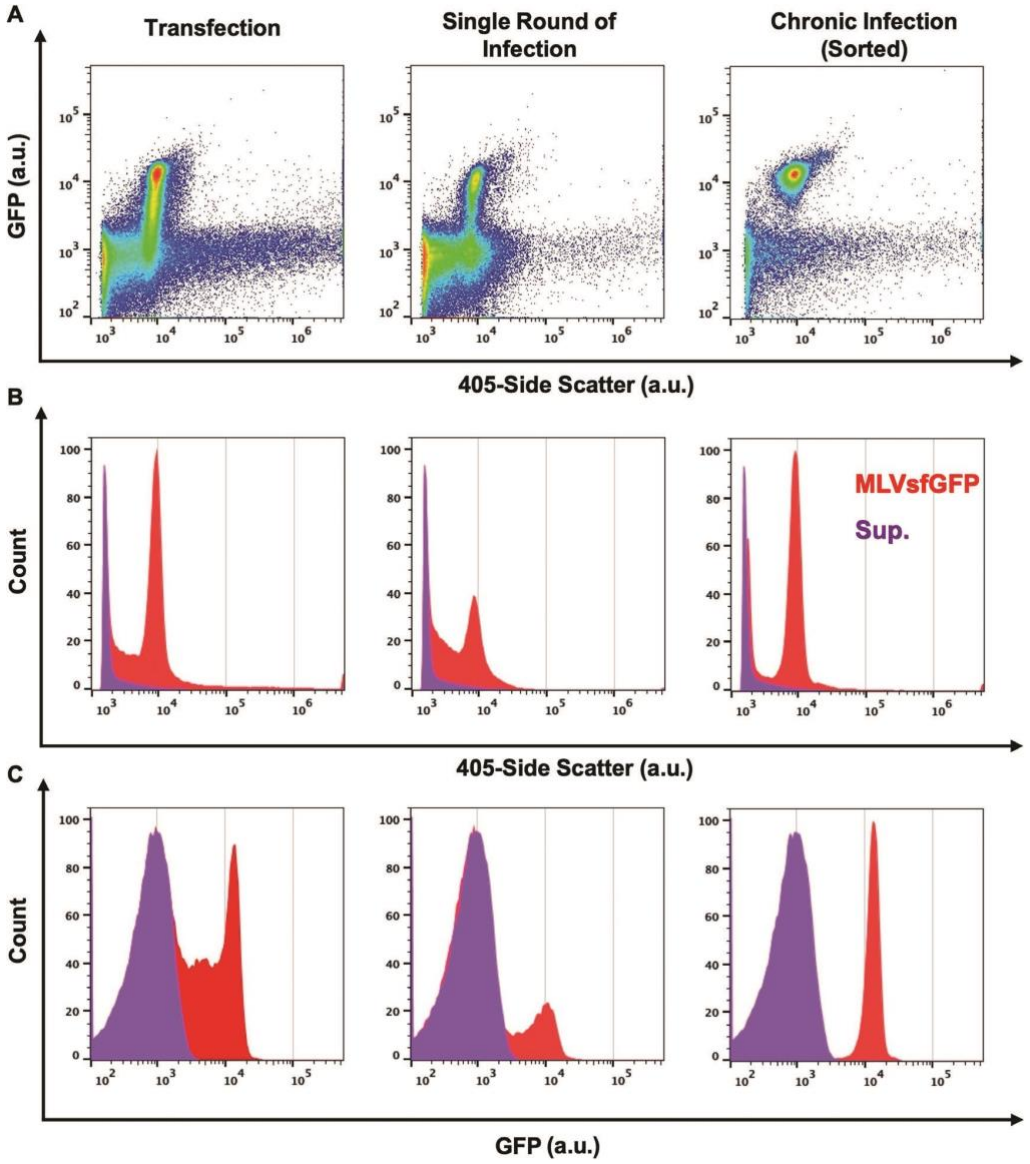

Figure 2.1: Virus production methods.
A) Replicative MLV expressing Env-sfGFP is resolved from background by light scatter and fluorescence when produced through transfection, a single round of infection of a cell population or production of a chronically infected clonal cell line. Produced MLV exhibit a highly homogenous **B)** light scatter and **C)** fluorescence intensity distribution when compared to supernatant (sup.) collected from uninfected cells as visualized with

overlaid histogram plots. Viruses released from chronically infected clonal cells display the most monodisperse population in both light scatter and fluorescence.

Materials

Dulbecco's phosphate-buffered saline (DPBS) (Wisent Bioproducts, catalogue # 311-430-CL)
BD 10 mL Syringe (Catalogue 302995)
100 nm Acrodisc Sterile Syringe Filter (Pall Corporation, catalogue 4611)
200 nm Acrodisc Sterile Syringe Filter (Pall Corporation, catalogue 4602)
450 nm Acrodisc Sterile Syringe Filter (Pall Corporation, catalogue 4615)
12 well plate
6 well plate
96 well plate
75-cm^2 (T-75) tissue culture flasks (Cellstar #658175)
GeneJuice Transfection Reagent (Sigma Aldrich, catalogue 70967)
HEK 293T (ATCC, CRL-3216)
NIH 3T3 mouse fibroblast cells (ATCC, CCL-92)
Chronically infected NIH 3T3 cell clone (#6) (Renner et al., 2020)
DMEM Media high glucose, with L-glutamine, sodium pyruvate and phenol red (Wisent, catalogue number: 319-005-CL)
Fetal bovine serum (Thermo Fisher Scientific, catalogue number: 12483020)
Penicillin-Streptomycin (GE Healthcare, catalogue number: SV30010)
Serum Free DMEM medium (see recipe in Reagents and Solutions)
Complete DMEM medium (see recipe in Reagents and Solutions)
10% EV depleted FBS (see recipe in Reagents and Solutions)
DMEM Phenol Red Free medium (see recipe in Reagents and Solutions)
Tissue Culture incubator (Thermo Fisher Scientific, catalog number: 3110)
Virus expression plasmids (originated from the pMOV-eGFP vector):
    MLV (Tang et al., 2017)
    MLVsfGFP (Renner et al., 2020)
Inverted florescence microscope with a 488 nm LED lamp.
Mo Flo AstriosEQ Fluorescence activated cell sorter cytometer (Beckman Coulter)
Ultracentrifuge 70 Ti Rotor tubes (Polycarbonate tubes and lids) (Beckman Coulter, catalogue number: 3355618)
Ultracentrifuge Rotor Type 70Ti (Beckman Coulter, catalogue number: 337922)
Ultracentrifuge Optima L-XP series (Beckman Coulter, catalogue number: 337922)
Serological pipettes
Eppendorf tubes (1.5 mL)
FACS tubes

Production of virus by transfection

1. Seed 1.0 x 10^5 293T cells in 1 mL per well a 12-well plate with complete DMEM media .
2. Incubate overnight at 37 ℃, 5% CO_2.
3. Prepare the transfection mix by adding 100 μL of serum-free DMEM medium and 3 μL of GeneJuice for each well to be transfected into an Eppendorf tube.
4. Vortex the mixture thoroughly and let sit for 5 mins at room temperature.
5. Add viral plasmid of interest. For this assay, we added 1 μg of plasmid DNA coding for MLV to the sample and mixed by gentle pipetting.

   Here, we produced wild type MLV with no GFP reporter (MLV) and MLV expressing Env-sfGFP (MLVsfGFP). While both viruses are resolved by light scatter by FVM, MLVsfGFP expresses a GFP fluorescent reporter on its surface allowing viral particles to be resolved by both light scatter and fluorescence.Both the MLV and MLVsfGFP plasmids originated from the pMOV-eGFP vector encoding a replicative Moloney-MLV through restriction free cloning as described in (Renner et al., 2020).
6. Incubate the tubes for 10 mins at room temperature.
7. Add the mixture drop wise evenly across entire surface of each well.
8. Gently rock the well plate biaxially on a flat surface for 1 minute.
9. Incubate cells for 8 hours at 37 ℃, 5% CO_2.
10. Wash each well with 1 mL of DPBS for 30 seconds and add 1 mL 100 nm filtered, phenol red-free DMEM medium supplemented with 10% EV depleted FBS.
11. Incubate cells for 64 hours at 37 ℃, 5% CO_2.
12. Harvest the supernatant from the cells and pass through 450 nm Acrodisc syringe filter.

    Virus-containing supernatants can be stored at 4 ℃ *for up to 2 weeks for infection of cells or for FVM analysis.*
13. For FVM analysis, dilute the sample 1:500 in 100 nm filtered DPBS.

Production of virus from an infected cell population (single round infection).

14. Seed 6.0 x 10^5 NIH 3T3 fibroblast cells per well in a 6-well plate in 2 mL complete DMEM media.
15. Incubate overnight at 37 °C, 5% CO_2.
16. Remove existing media from the wells carefully without disturbing the cells and infect the cells using supernatant from 293T cells transfected with the virus expression vector from step 12.

The volume of virus-containing supernatant that is added to cells will depend on whether single or multiple retroviral integrations are desired per cell. Multiple integrations will result in a higher yield of released virus, but the cells may exhibit cytopathic effects and exhibit stunted growth kinetics. To ensure that most infected cells harbor a single retrovirus integration, a multiplicity of infection (MOI) of less than 0.5 should be used. This corresponds to an infection of less than 40% of the total cell population. For cells that are difficult to infect, virus-containing supernatants collected from transfected 293T cells can be concentrated by ultracentrifugation at 100 000 x g for 3 hours at 4 °C, *and the pellet resuspended in a lower volume such as 1 mL of complete DMEM. In this example, we infected the target cells using an MOI of 10 to obtain maximum virus yield.*

17. Incubate for 24 hours and then wash the cells twice with 2 mL of DPBS for 30 seconds to remove input virus.
18. Add 2 mL phenol red-free DMEM media supplemented with 10% EV depleted FBS.
19. Incubate cells for an additional 48 hours at 37 °C, 5% CO_2.
20. Harvest the supernatant from the cells and pass through a 450 nm Acrodisc syringe filter.

Virus-containing supernatants can be stored at 4 °C *for up to 2 weeks for infection of cells or for FVM analysis.*

21. For FVM analysis, dilute the sample 1:500 in 100 nm filtered DPBS.

Production of virus by chronically infected cell clones.

22. Carry out the protocol above (steps 14 to 19 with the modifications that 2.5 x 10^6 NIH 3T3 cells are seeded in a T75 plate and are infected with an MOI of 2 (about 90% infection).

    Complete DMEM media with 10% FBS is used for optimal cell growth.

23. Identify infected cells by GFP fluorescence expression, isolate by fluorescence activated cell sorting (FACS) for a single cell sort and dispense one cell per well into a 96-well plate prefilled with 200 μL complete DMEM media.

    In our assay, infected cells were resuspended in PBS buffer at 1x10^6 cells/mL for a single cell sort of cell expressing high GFP intensity, however each cell sort should be optimized to the FACS instrument and the flow core facility guidelines. Cossarizza et al. highlight helpful considerations for serial cell sorting by flow cytometry (Cossarizza et al., 2019).

24. Incubate cells in 37 $°C$ at 5% CO_2 and allow cells to expand.

    Cell growth should be checked every 2-3 days. Clones should expand within 7-14 days depending on growth rate of the cell.

25. When confluent, transfer 0.5 x 10^5 viable clones that express GFP under a fluorescence microscope to 24-well plates. Incubate cells for 3 days.
26. When confluent, transfer 1 x 10^5 viable clones for further expansion in 12-well plate.
27. Aliquot each cell clone into a FACS tube (0.4 x 10^6 cells per 0.4 mL of PBS) and analyze GFP expression by flow cytometry. Identify and keep clones only with the highest GFP fluorescence intensity for further expansion and downstream analysis.

    In our study, one stably infected clone (#6) was selected for all downstream viral analysis as described in detail in (Renner et al., 2020).

28. Seed 2.5 x 10^6 chronically infected NIH 3T3 cell clone in a 10 cm dish in 10 mL complete DMEM media.
29. Incubate overnight at 37 $°C$, 5% CO_2.
30. Wash cells with DPBS and add 10 mL of 200 nm filtered phenol red-free DMEM medium.
31. Incubate for 48 hours at 37 $°C$, 5% CO_2.

32. Harvest the supernatant from the cells and pass through 450 nm Acrodisc syringe filter.

    Virus-containing supernatants can be stored at 4 °C for up to 2 weeks for infection of cells or for FVM analysis.

33. For FVM analysis, dilute the sample 1:500 in 100 nm filtered DPBS.

2.4 Basic Protocol 2: Instrument setup and quality control for fluorescence quantification standardization and quality control for fluorescence quantification.

Because viral particles used here are very close to the limit of detection for both light scatter and fluorescence of most commercial flow cytometers, an appropriate experimental design and instrument set up are critical to ensure to viral detection and resolution at a single particle level. The methods described in this protocol that outline the necessary steps for fluorescence quantification rely on the principles for light scatter and fluorescence calibration described by Welsh and Jones (Welsh & Jones, 2020). For accurate, reproducible and standardized data reporting, it is crucial to determine the limit of the assay's and instrument's sensitivity for light scatter and fluorescence measurements and to calibrate these values using standardized reference materials. For this purpose, light scatter calibration was performed using National Institute of Standards and Technology (NIST)-certified standard reference beads. Fluorescence calibration and data reporting in quantitative units (or standard units) such as molecules of equivalent soluble fluorophore (MESF) or equivalent reference fluorophore (ERF) is appropriate for fluorescence intensity conversion from arbitrary units (a.u) (Welsh, Van Der Pol, et al., 2020). Reporting of experimental data in standard units can be achieved by using the FCMPASS software, which calibrates light scatter and fluorescence measurements using commercially available reference standards and enables data reporting to conform with the MIFlow-Cyt-EV framework (Welsh, Van Der Pol, et al., 2020). As such, this calibration enables estimation of particle diameter, using known refractive indices of the particles, and relative antigen quantitation which facilitates the comparison of data between experiments and research groups. The protocol below outlines how to prepare fluorescence calibration materials for FCS file calibration, and to evaluate instrument sensitivity and performance. To report data in standard units, calibrated files are generated using the FCMPASS software, which plots the acquired signal intensity in arbitrary units using the manufacturer's predicted values for each bead population and performs a least-squares regression. Figure 2

displays the light scattering and fluorescence features of BD QuantiBrite Phycoerythrin (PE) fluorescence and polystyrene NIST-traceable size reference beads used for calibration. Figure 2C shows that the data points for the beads fall within the 'good fit' range for scatter modeling using the FCM$_{PASS}$ software. Both calibration curves display a high correlation between acquired and predicted values (Fig. 2D). This close correlation is essential to be able to convert fluorescence intensity values into molecule equivalents and report fluorescence measurements in standard units such as PE MESF used in this protocol. To ensure consistent detection the virus population at a single particle level, this protocol additionally outlines how to ensure that viral particles are interrogated one at a time in the flow cytometer. Simultaneous detection of several particles is a phenomenon called "swarm detection or coincidence", where the combined interrogation of multiple particles can lead to a decrease in total events but a concurrent increase in fluorescence intensity (van der Pol, van Gemert, Sturk, Nieuwland, & van Leeuwen, 2012). In order to minimize coincidence of viral particles and determine an optimal sample concentration for acquisition, a range of serially diluted virus-containing samples is analyzed and quantified.

Materials

Dulbecco's phosphate-buffered saline (DPBS) (Wisent Bioproducts, catalogue # 311-430-CL)
BD 10 mL Syringe (Catalogue 302995)
100 nm Acrodisc Sterile Syringe Filter (Pall Corporation, catalogue 4611)
450 nm Acrodisc Sterile Syringe Filter (Pall Corporation, catalogue 4615)
NIST-traceable size calibration reference polystyrene and silica beads
BD PE QuantiBrite Quantitation Kit (Lot 47973, BD Biosciences, catalogue # 340495)
5 mL Polystyrene Round Bottom Tube (Falcon, catalogue 352054)
Chronically infected NIH 3T3 cell clone (#6) (Renner et al., 2020)
DMEM Media high glucose, with L-glutamine, sodium pyruvate and phenol red (Wisent, catalogue number: 319-005-CL)
Fetal bovine serum (Thermo Fisher Scientific, catalogue number: 12483020)
Penicillin-Streptomycin (GE Healthcare, catalogue number: SV30010)
Serum Free DMEM medium (see recipe in Reagents and Solutions)
Complete DMEM medium (see recipe in Reagents and Solutions)
10% EV depleted FBS (see recipe in Reagents and Solutions)
DMEM Phenol Red Free medium (see recipe in Reagents and Solutions)
Tissue Culture incubator (Thermo Fisher Scientific, catalog number: 3110)
16 % Paraformaldehyde (PFA) (Thermo Scientific, catalogue 28906)
FACS tubes
Beckman Coulter CytoFLEX S with 4 Lasers (Mississauga, ON,CA)

FlowJo (CA, USA, version 10.7.1)
FCMPASS software (v3.1, http://nanopass.ccr.cancer.gov) (Welsh & Jones, 2020)

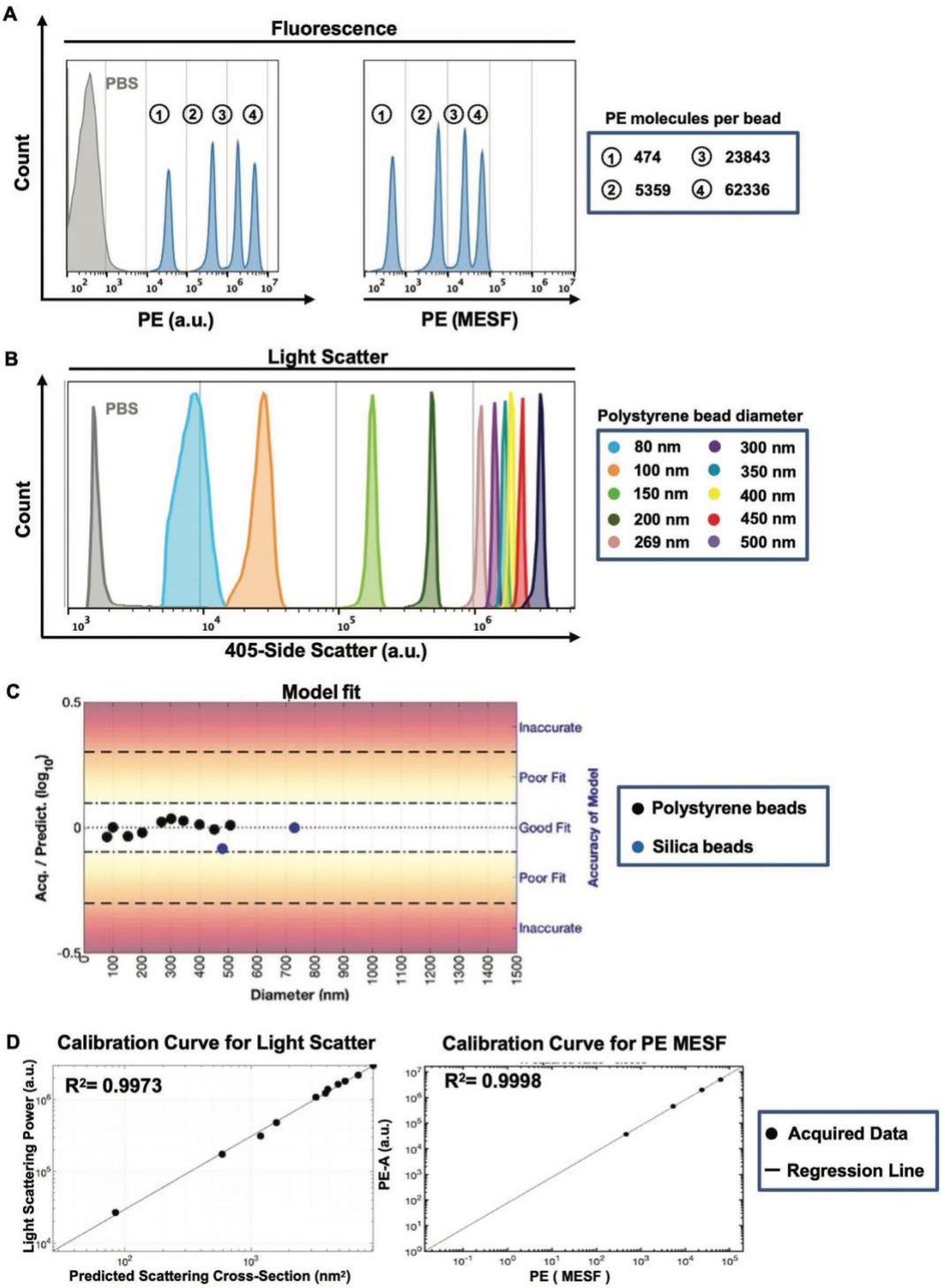

Figure 2.2: Calibration of fluorescence and light scatter using FCMPASS for standardized data reporting and instrument performance evaluation.

A)Detection of QuantiBrite PE beads prior and post fluorescence calibration. **B)** Detection of NIST traceable polystyrene calibration beads prior light scatter calibration. **C)** Quality control plot validating that the light scatter standard points fall within the 'good fit' range with the scatter modeling using FCM_{PASS} software. **D)** Calibration curves of light scatter and fluorescence outputs generated by FCM_{PASS} software showing a high correlation between the acquired and predicted values of the reference beads.

1. Set up the flow cytometer settings according to the manufacturer's recommendation and the assay being calibrated.

   Cytometer utilized for this study was Beckman Coulter CytoFLEX S with 405nm laser for side-scatter light (SSC-H) trigger parameter (1500 a.u threshold) with a 405/10 bandpass filter, 561 nm laser for PE fluorophore with 561-580/30 bandpass filter, 488 nm laser for GFP fluorophore with 488-525/40 bandpass filter, and 640 laser with 640-670/30 bandpass filter. Gain for each detector is as follows 195, 1600, 3000 and 1200 a.u, respectively. All samples were acquired at the lowest sampling rate (10 µL per 60 seconds). Volumetric calibrations were validated by weight using the CytExpert calibration tool. Detailed information of instrument optics, light scatter and fluorescence calibration are summarized in FCM$_{PASS}$ report in Supplementary File 1.

   Selection of the trigger parameter is dependent on the aim of the experiment and the type of flow cytometer. Light scatter or fluorescence can be chosen as the trigger parameter, each one has their own benefits and caveats. In particular, the selection of light scatter enables detection of all particles, including possible contaminants in the sample analyzed, resulting in more events being acquired. Processing a larger number of events may impact the event rate, electronic abort rate and file size (Tang et al., 2017). In contrast, using fluorescence as a trigger parameter will tailor detection of only fluorescently labelled particles, whose signal exceeds the designated threshold, from the sample acquired. It is recommended to set a trigger threshold using the pulse height parameter to allow for the limit of detection to be reported in calibrated units (Welsh & Jones, 2020). As such, light scatter analysis enables evaluation of all particles within a sample. This is especially useful if the goal of the experiment is to characterize a heterogenous viral population, where virions express varying levels of light scattering or cannot be efficiently directly labeled. While fluorescence analysis is suitable when staining is efficient or when viruses express a fluorescent reporter protein. This can allow for the precise enumeration of labeled particles and, in optimal conditions, the quantification of the labeled target antigen. In either scenario, the instrument should be carefully calibrated for the functional range of detection of the parameters being analyzed. This can be achieved by running NIST-

traceable size or fluorescence reference beads to determine the instrument's sensitivity and dynamic range.

2. Filter DPBS through a 100 nm Acrodisc syringe filter.

   100 nm-filtered DPBS is used for all the downstream analysis throughout this protocol in order to reduce possible background noise resulting from small particle contaminants.

3. Run a DPBS-only control.

   This control will assess the instrument opto-electronic noise as well as establish the baseline for background noise. It can be used as the control to determine the threshold of detection. Running this sample periodically throughout the experiment will allow to monitor the cleanliness and stability of the instrument's fluidics following the processing of multiple samples. The 405-SSC parameter plotted against time is helpful to evaluate the consistency of the event rate during sample acquisition.

4. Add 500 μL of filtered DPBS to the BD QuantiBrite PE tube.

   Each tube contains lyophilized beads that are conjugated to four varying levels of PE fluorescence intensity. Many beads that are currently available exhibit much brighter fluorescence intensities compared to enveloped viruses. While it is acknowledged that enveloped viruses have a lower surface area and density of surface proteins available for staining, fluorescent reference beads still provide the necessary standards of fluorescence needed for instrument calibration, quality control and extrapolating surface antigen numbers on viruses.

5. Let sit until the beads at the bottom of tube are fully dissolved, and vortex the tube thoroughly (approximately 3 minutes).

6. Run the sample until the desired number of beads are recorded. The minimum number is 5000 bead events *(Welsh & Jones, 2020)* .

   First plot FSC and SSC area parameters against each other. The beads should be visible on the plot and clustered tightly together. The gain should then be adjusted for each parameter to optimize resolution, similar to adjusting the acquisition settings when running cells. By first gating on the singlet bead population using FSC-A vs. SSC-A plot, the median fluorescence intensity (MFI) in arbitrary units of each bead population can then be determined by plotting the gated population using counts vs. PE-A. The obtained values can be inputted alongside the manufacturer's reference values in the FCM$_{PASS}$ *software which will add the calibration information to the samples run during the same session, enabling reporting of the data in standardized units, and tracking the instrument's longitudinal performance.*

7. Convert raw FCS files into calibrated FCS files that allow reporting of data in standard units.

   Following the steps described in the protocol by Welsh and Jones (Welsh & Jones, 2020) for light scatter calibration and performing fcs file calibration, we displayed our data in units of median diameter (nm) and PE fluorescence intensity (MESF) . This former metric was calibrated based on the conversion of light scatter intensity to estimated diameter using NIST-traceable size calibration reference beads, considering the effective RI of the particle analyzed and the collection angle of the instrument (Welsh & Jones, 2020). While fluorescence intensity is presented in units of median PE MESF using BD PE QuantiBrite beads as explained above. Robust standard deviation (rS.D), instead of standard deviation (SD), was used in order to omit skewing of S.D by outlying events. Additionally, the FCM$_{PASS}$ *software provides an output report with details of cytometer's limit of detection depending on the composition and RI of the particle analyzed (i.e polystyrene versus silica beads) (Supp. File 1). For example, according to this generated output report, the following are the lowest sizes of different composition of partcicles that can be detected by our instrument: 59.1 nm polysterene particle, 80.3 nm silica particle, and viral particles of 82 nm given a RI of 1.45.*

8. Collect 5 mL of virus containing supernatant from chronically infected NIH 3T3 cell clone (#6) cells and filter through a 450 nm Acrodisc syringe filter.

9. Perform serial dilutions of the virus-containing supernatant in 100 nm-filtered DPBS directly in FACS tubes.

   Serial dilutions of the virus samples should be performed. Pipetting volumes larger than 5 µL are recommended to decrease pipetting variations. To achieve 1:125 dilution, 8 µL of viral supernatant was added to 992 µL of 100 nm-filtered DPBS. Begin analyzing the most dilute sample and proceed to the most concentrated sample. This will reduce the risk of contaminating the flow cytometer with viruses and small particles that could affect measurements in the most diluted samples. If the abort rate exceeds the manufacturer's recommendation, in our case 4000 events per second, the sample being run is likely too concentrated which can lead to coincidence. Performing serial dilutions is a commonly used method to favor single particle acquisition and reduce the possibility of swarm detection. Evidence of single particle acquisition can be demonstrated when the measured viral particle count linearly reflects the dilution factor while light scatter intensity or fluorescence signal is maintained constant (Fig. 3) (Kormelink et al., 2016; Tang et al., 2017; Welsh, Van Der Pol, et al., 2020). As shown in Figure 3, particle count per 10 µL of sample volume linearly decreased with the dilution factor while median GFP intensity measurement was maintained linear. This indicates that there was little particle coincidence in our experimental conditions across dilutions tested. For the purposes of our viral analysis, all samples were diluted at a 1:500 dilution factor.

F

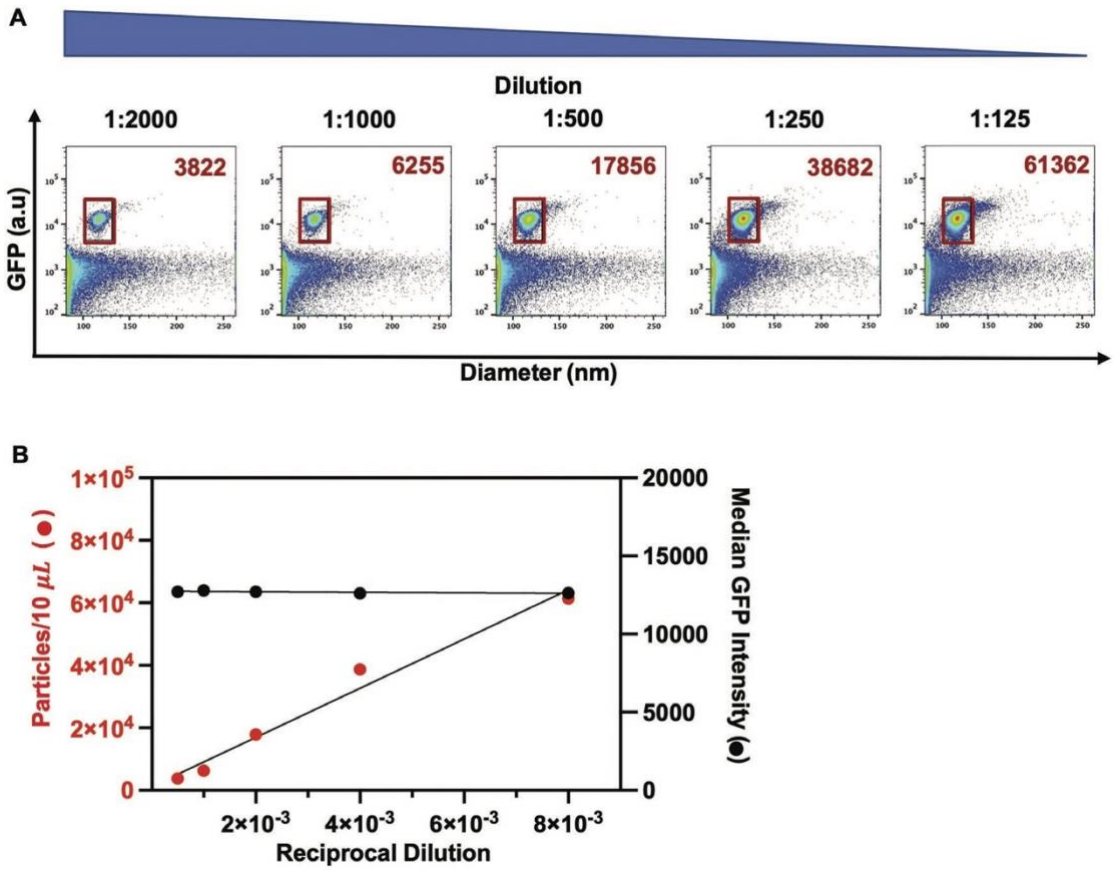

Figure 2.3: Sample dilution and assessment of coincidence.
A) Analysis of serially diluted virus samples to determine the efficiency of single viral particle detection. Plots are listed from left to right in order of decreasing dilution. Indicated in red are the particle counts in each gate. **B)** Serial dilution plot of viral particle concentration (left axis) and FITC median fluorescence (right axis) as a function of the dilution factor. The virus concentration and MFI were calculated from the viral particles count and signal within the red gate (panel A), respectively. All experimental controls were run at the same acquisition settings (flow rate 10 μL per minute, trigger threshold and gain) and during the same data acquisition session as the other samples.

10. Gate on the viral population which should be distinguishable from the background noise.

Virus populations can be resolved or distinguished from background noise by their characteristic light scatter profile. The highly controlled and consistent nature of viral capsid assembly normally results in a homogenous population as illustrated in Figure 1. If the virus is fluorescent or fluorescently stained with dyes or antibodies, it can be additionally resolved from background by using fluorescent channels (Fig. 1C). By gating on the viral population,

the original concentration of a sample can be determined by accounting for the dilution factor and the flow rate.

For example, if the sample was diluted 1:500 as shown in Figure 3A and, acquired at the flow rate of 10 µL for one minute with 17 856 particles detected in the viral gate, the concentration of virus in the supernatant is as follows:

$$\text{Virus conc.} = \frac{particles\ in\ the\ gate}{volume\ acquired\ by\ the\ cytometer} \times\ volume\ of\ sample\ \times dilution\ factor$$

$$\text{Virus concentration} = \frac{17\,856\ particles}{10\ \mu\text{L}}\ \times\ 1\,000\ \mu\text{L}\ \times 500$$

$$\text{Virus concentration} = 8.9\text{x}10^{8}\ \text{particles/mL}$$

11. All instrument parameters used for the data acquisition are presented in Appendix 1: FCMPASS MIFlowCyt-EV Report.

2.5 Basic Protocol 3: Flow virometry analysis

Analyzing virus particles by flow cytometry is challenging due fact that they are often near the limit of detection for both light scatter and fluorescence of most commercial flow cytometers. Consequently, an appropriate experimental design and instrument set up are critical to enable virus detection and resolution from background noise before pursuing downstream analyses. This protocol covers the key issues that should be considered to ensure consistent detection and resolution of the virus population at a single particle level. Similar to the controls outlined in the MIFlowCyt-EV framework for reporting in EV studies, key experimental controls are required for virus detection and quantifications studies (Welsh, Van Der Pol, et al., 2020). These controls include: a buffer only (to evaluate instrument background noise) and supernatant collected from uninfected cells (to evaluate possible presence of EVs). To evaluate changes in light scatter or fluorescence signals, these experimental controls should all be run at the same acquisition settings (flow rate, trigger threshold and gain) and during the same session for all samples. Since several factors influence virus production between experiments, serial dilutions are recommended prior to each experiment in order to determine the optimal particle concentration for acquisition as illustrated in **Basic Protocol 2**.

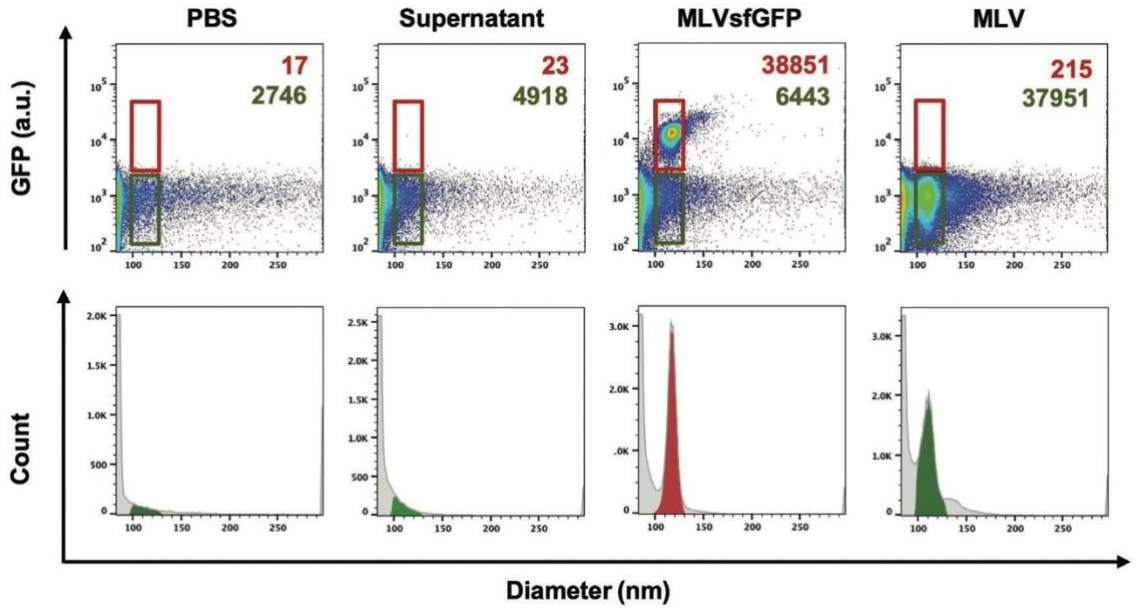

Figure 2.4 Virus quantification and diameter determination.
Gating strategy for virus identification and enumeration of virus from cell supernatants (MLV and MLVsfGFP) compared to buffer (PBS) and supernatant collected from uninfected cells. PBS and supernatant controls allow for the evaluation of instrument background noise and presence of EVs, respectively. MLV sample was used to monitor non-specific antibody staining as it does not express GFP on the viral envelope. Both virus population display a highly monodisperse fluorescence (red gate) and light scatter (green gate) profiles that are not present in the PBS or supernatant controls. Particle counts indicated in red and green are measured from each respective gate in the panel. Particles are reported in units of median diameter (nm). This metric was calibrated based on the conversion of light scatter intensity to estimated diameter using NIST-traceable size calibration reference beads, considering the RI of MLV to be at 1.45.

Table 2.1 Summary of sample concentrations and particle diameters.

Virus*	Concentration (particles/mL)	Median diameter (nm ± SD)
MLV	$1.91x10^9$	109.8 ± 6.8
MLVsfGFP	$1.89\ x10^9$	120.3 ± 4.5

** All samples were passed through a 450nm filter prior to analysis.*

Materials

Dulbecco's phosphate-buffered saline (DPBS) (Wisent Bioproducts, catalogue # 311-430-CL)
BD 10 mL Syringe (Catalogue 302995)
100 nm Acrodisc Sterile Syringe Filter (Pall Corporation, catalogue 4611)
450 nm Acrodisc Sterile Syringe Filter (Pall Corporation, catalogue 4615)
5 mL Polystyrene Round Bottom Tube (i.e. FACS tube) (Falcon, catalogue 352054)
Anti-GFP PE Monoclonal Antibody (BioLegend, clone FM264G)
Beckman Coulter CytoFLEX S with 4 Lasers (Mississauga, ON,CA)
FlowJo (CA, USA, version 10.7.1)

NIST-traceable size calibration reference polystyrene and silica beads
PE BD QuantiBrite Quanitation Kit (Lot 47973, BD Bioscences, catalogue # 340495)
75-cm^2 (T-75) tissue culture flasks (Cellstar #658175)
NIH 3T3 fibroblast cell (ATCC, CCL-92)
Chronically infected NIH 3T3 cell clone (#6) **Basic Protocol 1.**
DMEM Media high glucose, with L-glutamine, sodium pyruvate and phenol red (Wisent, catalogue number: 319-005-CL)
Fetal bovine serum (Thermo Fisher Scientific, catalogue number: 12483020)
Penicillin-Streptomycin (GE Healthcare, catalogue number: SV30010)
Complete DMEM (see recipe in Reagents and Solutions)
DMEM Phenol Red Free medium (see recipe in Reagents and Solutions)
10% EV depleted FBS (see recipe in Reagents and Solutions)
Tissue Culture incubator (Thermo Fisher Scientific, catalog number: 3110)
Serological pipettes
Eppendorf tubes (1.5 mL)
FACS tubes
Refrigerated table-top centrifuge Sorvall ™ ST 40 (Thermo Fisher Scientific, catalog number: 75004524)
FlowJo (CA, USA, version 10.7.1)
FCM$_{PASS}$ software (v3.1, http://nanopass.ccr.cancer.gov) (Welsh & Jones, 2020)

1. Filter 50 mL of the buffer control through 450 nm Acrodisc syringe filter.
2. Dilute all virus samples and controls at chosen dilution factor (from basic protocol 2 step 9) in 100 nm-filtered DPBS FACS tube.

   In our assay, we diluted our samples 1:500, where 4 µL of 450 nm filtered virus containing supernatant was added to 1998 µL of 100 nm-filtered DPBS, vortexed thoroughly and 1 mL of this solution transferred to a FACS tube.
3. Collect 5 mL of supernatant from uninfected control NIH 3T3 cells treated under the same conditions as the chronically infected NIH 3T3 cell clone (#6) cells and filter through 450 nm Acrodisc syringe filter.
4. Dilute the sample 1:500 in 100 nm-filtered DPBS in a FACS tube.
5. Collect 5 mL of virus containing supernatant from chronically infected NIH 3T3 cell clone (#6) cells and filter through a 450 nm Acrodisc syringe filter **(Basic Protocol 1, step 32)**.
6. Dilute the sample 1:500 in 100 nm-filtered DPBS in FACS tube.
7. Acquire assay control and virus containing samples diluted in PBS on the cytometer.
8. Gate on the viral population which should be distinguishable from the background noise.

Virus populations can be resolved from background noise by their characteristic light scatter profile (Fig. 1). If the virus is fluorescent or fluorescently stained with dyes or antibodies, it can be additionally resolved from background using fluorescent channels. As shown in Fig. 4, the virus population expresses a highly monodisperse fluorescence (red gate) and scatter (green gate) profiles that are not present in the buffer only (PBS) or supernatant controls. Here we compared wild type MLV (non-fluorescent) and MLVsfGFP that expresses Env-sfGFP on its surface. Particles in the green gate for PBS are likely salt aggregates and contaminants released from the flow cytometer fluidics, while particles in the green gate of the supernatant control may additionally contain EVs released from the cells. The concentration of intact viral particles in a MLV and MLVsfGFP stock sample was extrapolated from the particle count of the green or red gate, respectively (Table 2). Here we report MLV and MLVsfGFP in units of median diameter (nm) and approximate their size at 109.8 ± 6.8 nm and 120.3 ± 4.5 nm, respectively (Table 2). This parameter was calibrated based on the conversion of light scatter intensity to estimated diameter using NIST-traceable size calibration reference beads, considering the effective RI of MLV (estimated at 1.45) and the collection angle of the instrument (Ma et al., 2016) as shown in ***Basic Protocol 2****.*

2.6 Basic Protocol 4: Viral surface antigen staining and fluorescence quantification.

This protocol outlines the experimental set up for single-colour virus staining. Characterization of the antigenic composition and abundance is predominantly achieved by fluorescence quantification. However, the smaller surface area and number of proteins available for staining on the viral surface necessitates careful consideration of the choice of fluorophore(s) used and the optimal antibody concentration. Determining the optimal staining antibody concentration using a titration is especially crucial to resolve dimly stained virus particles from unstained populations and background noise as illustrated in Figure 5. In this protocol, we optimized the antibody staining conditions using a PE-conjugated antibody that targets the highly expressed Env-sfGFP fusion protein. However, viruses can be labeled by fluorophore conjugated antibodies directed against host-derived surface proteins or viral glycoproteins found on the viral envelope (Maltseva & Langlois, 2021; Renner et al., 2020; Tang et al., 2019). Similarly to cell staining procedures,

attention should be given to the initial virus concentration, antibody incubation time and final antibody concentration (Cossarizza et al., 2019). As previously mentioned, a set of experimental controls stained under the same conditions as the virus samples should be run during the same data acquisition session in order to evaluate changes in light scatter and fluorescence profiles (Fig. 5A).

Materials

Dulbecco's phosphate-buffered saline (DPBS) (Wisent Bioproducts, catalogue # 311-430-CL)
BD 10 mL Syringe (Catalogue 302995)
100 nm Acrodisc Sterile Syringe Filter (Pall Corporation, catalogue 4611)
450 nm Acrodisc Sterile Syringe Filter (Pall Corporation, catalogue 4615)
5 mL Polystyrene Round Bottom Tube (Falcon, catalogue 352054)
Anti-GFP PE Monoclonal Antibody (BioLegend, clone FM264G)
16 % Paraformaldehyde (PFA) (Thermo Scientific, catalogue 28906)
Beckman Coulter CytoFLEX S with 4 Lasers (Mississauga, ON,CA)
FlowJo (CA, USA, version 10.7.1)
NIST-traceable size calibration reference polystyrene and silica beads
BD QuantiBrite phycoerythrin (Davis, Abrams, Iyer, Hoffman, & Bishop) Quanitation Kit (Lot 47973, BD Bioscences, catalogue # 340495)
NIH 3T3 fibroblast cell (ATCC, CCL-92)
Chronically infected NIH 3T3 cell clone (#6) **Basic Protocol 1**
DMEM Media high glucose, with L-glutamine, sodium pyruvate and phenol red (Wisent, catalogue number: 319-005-CL)
Fetal bovine serum (Thermo Fisher Scientific, catalogue number: 12483020)
Penicillin-Streptomycin (GE Healthcare, catalogue number: SV30010)
Complete DMEM (see recipe in Reagents and Solutions)
10% FBS depleted FBS (see recipe in Reagents and Solutions)
DMEM Phenol red Free medium (see recipe in Reagents and Solutions)
Tissue Culture incubator (Thermo Fisher Scientific, catalog number: 3110)
FACS tubes
Refrigerated table-top centrifuge Sorvall ™ ST 40 (Thermo Fisher Scientific, catalog number: 75004524)
FlowJo (CA, USA, version 10.7.1)
FCM$_{PASS}$ software (v3.1, http://nanopass.ccr.cancer.gov) (Welsh & Jones, 2020)

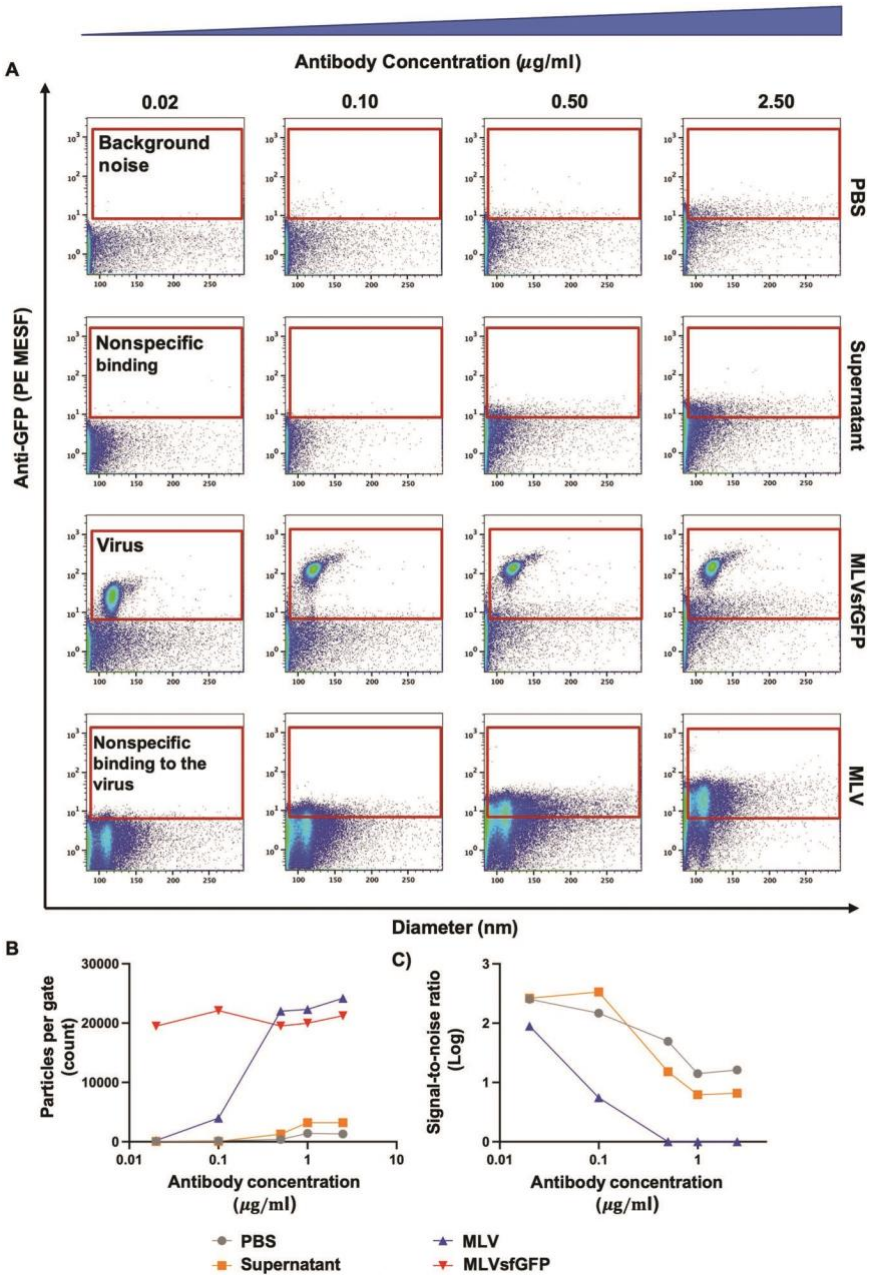

Figure 2.5 Optimization of virus staining and antibody titration for FVM analysis.
A) Five-fold titrations of the anti-GFP PE monoclonal antibody (0.02, 0.10, 0.50, 2.50 μg/mL). Plots are listed from left to right in order of increasing antibody concentration. Background noise, non-specific binding, non-specific binding to the virus and stained virus are designated by the red gate. **B)** Evaluation of particles per gate as a function of the antibody concentration and, **C)** the signal-to-noise ratio for determining the optimal staining concentration that minimizes background. The signal to noise ratio was calculated by using the log difference in particle count in red gate of each assay control and the stained virus.

1. Determine the concentration of virus in the supernatant as shown in **Basic Protocol 2** step 10.
2. Centrifuge antibody tube at 17 000 $x\ g$ for 10 mins in a tabletop centrifuge at 4 $°C$.

In our assay, we used Anti-GFP PE monoclonal antibody. Antibody centrifugation prior to staining reduces antibody aggregates detected during sample acquisition.

3. Prepare the master mixture of antibody diluted in DPBS at twice the pre-determined final concentration.

A master mixture can be made if several virus samples are to be stained with the same antibody. Extra solution should be prepared to account for potential losses during pipetting. Stained experimental controls are crucial to evaluate background fluorescence. In this assay, we used wild type MLV as the control virus, as it is nearly identical to MLVsfGFP but does not express the target antigen for the staining (i.e. GFP. It is used to evaluate non-specific binding with our antibodies as shown in Figure 5. Similarly, an isotype control can be used to evaluate non-specific binding if a suitable control virus is not available. PBS and supernatant collected from uninfected cells were simultaneously labelled as assay controls. In our study, we found that 0.10 µg/mL was the optimal final staining concentration with the anti-GFP PE monoclonal antibody when mixed one to one with virus containing supernatant adjusted to a concentration of $1x10^9$ viral particles/mL. For the staining of one MLVsfGFP sample; PBS, supernatant and MLV assay controls were all labeled under same staining conditions. For each antibody staining, 50 µL of 0.20 µg/mL anti-GFP was mixed with 50 µL of buffer or supernatant. To calculate how much stock antibody sample (200 µg/mL) is added to make a final volume of 0.250 mL of 2x concentrated master mixture (0.20 µg/mL), the following formula was used:

$$Volume\ of\ stock\ antibody = \frac{2X\ of final\ antibody\ concentration\ \ x\ final\ volume}{stock\ antibody\ concentration}$$

$$V_1 = \frac{0.20\ \mu g/mL\ x\ 0.250\ mL}{200\ \mu g/mL}$$

$$V_1 = 2.5\ \mu L$$

As such, $2.5\ \mu L\ \ of\ stock\ antibody\ was\ added\ to\ 247.5\ \mu L\ of$ 100 nm filtered DPBS .

4. Add 50 μL of virus containing supernatant or assay control (PBS or supernatant collected from uninfected cells) to 50 μL of antibody mixture.

   This will result in a two-fold dilution of the antibody and virus concentration. Depending on the optimal particle concentration determined previously for sample acquisition on the cytometer as shown in ***Basic Protocol 2****, the final sample dilution should be modified accordingly.*

5. Pipette the mixture thoroughly.
6. Incubate at 37 $°C$ for 60 minutes protected from light.
7. Fix viral and reagent solution with 16 % PFA to have a final concentration of viral antibody mixture at 2 % PFA and let incubate for 2 hours at 4 $°C$.

   Biosafety Consideration: Viral production and handling should be reviewed by the institution's biosafety officer before beginning experiments. A common practice to safely inactivate viruses is to treat the samples with PFA after the staining process and before running on the flow cytometer.

8. Dilute the sample at the predetermined dilution with 100 nm-filtered DPBS in FACS tube.
9. Run sample on the cytometer.
10. Gate on the viral population and obtain the median fluorescence intensity of the fluorophore during the sample acquisition on the cytometer.
11. Using procedures described in **Basic Protocol 2** step 7, generate calibrated FCS files using reference beads acquired during the same session and the FCM_{PASS} software.
12. Gate on viral population of interest based on light scatter and/or fluorescence profile as described in **Basic Protocol 3**.
13. Quantify light scatter and median fluorescence intensity of the viral population in standard units.

    Here we estimate MLVsfGFP in units of median diameter (nm) and approximate virus particle size at 120.3 ±4.5 nm (Table 2). *Env-GFP surface protein expression is estimated*

at a median PE MESF of 125 ± 26, where the median 25th and 75th percentile MESF are calculated at 107, and 142, respectively (Table 3).

In our study, we observe a highly monodisperse virus population in both fluorescence and light scatter profiles as shown in Figure 1 and 4. Different metrics of reporting such as median fluorescence intensity or a percentile measurement can be applied in cases of non-parametric distribution of protein expression or particle size within the viral population. The detection gate of PE fluorescence was applied between 0 to 1000 PE MESF units. Here we estimate the lower theoretical limit of detection using the 99th percentile measurement of the negative viral population at 13 PE MESF.

Table 2.2 Summary of surface antigen abundance (Env-GFP) measured in PE MESF.

Virus*	Median PE fluorescence (PE MESF ± SD)	25th percentile (PE MESF)	75th percentile (PE MESF)	99th percentile (PE MESF)
MLV	3.1 ± 2.8	1.6	5.3	13.0
MLVsfGFP	124.9 ± 26.3	107.2	141.7	236.6

**All samples were passed through a 450nm filter prior to analysis. Detection gate of PE fluorescence was applied between 0 to 1000 PE MESF units. Samples were stained at the optimal staining concentration of 0.1 µg/mL. Staining of MLV is non-specific given that the antibody targets GFP which is absent in this virus. SD: standard deviation.*

Support Protocol 1 for Basic Protocol 4: Determination of the optimal antibody concentration for virus staining

This protocol outlines the experimental set up and the determination of the optimal antibody concentration for single-colour virus staining. Determining the optimal staining antibody concentration using a titration is crucial to resolve dimly stained virus particles from unstained populations and background noise. An antibody titration is especially important in FVM, as high antibody concentrations can lead to increased background fluorescence and antibody aggregates that can be misinterpreted as positively stained virions.

1. Determine virus particle concentration in the supernatant as described in step 10 of basic protocol 2.
2. Centrifuge antibody at 17 000 *x g* for 10 mins in a tabletop centrifuge.
3. Preform a five-fold titration of the fluorophore conjugated antibody, we first analyzed a in the range of (0.02 – 2.5 μg/mL)

   Refer to the reagent manufacturer's instruction on optimal staining concentration to use as a starting point. Determination of the optimal concentration will also depend on the viral particle concentration, specificity of the antibody, presence of potential non-viral particles that can stain and contribute to an increase in background fluorescence level, etc. The recommended range varies depending on the fluorophore, expected antigen density and fluorophore-to-antigen ratio. We recommend titrating the antibody staining concentration first five-fold to determine the optimal concentration that maximizes the assay's dynamic range, signal to noise ratio and stain index as shown in Figure 5. The optimal antibody concentration calculated is between 0.02 and 0.10 µg/mL. In this concentration range, the particle count for MLVsfGFP is maximal, and background noise and non-specific binding are minimal compared to the higher staining concentrations (Fig. 5B).

4. Mix equal volumes of virus that expresses the target protein of interest with control virus that does not express the protein.

   Alternatively, an isotype antibody stained at the same concentration can be used to evaluate the effect of non-specific binding to background signal.

5. Add 50 μL of virus containing supernatant to 50 μL of antibody mixture.
6. Repeat steps 5-13 of basic protocol 4.
7. Gate on the positively stained and unstained population to obtain the median fluorescence intensity.
8. Determine highest separation between the positively and negatively labelled populations (stain index).

Stain index can be calculated as follows:

$$\textit{Stain index} = \frac{MFI\ of\ postive\ population - MFI\ negative\ population}{SD\ of\ negative\ population}$$

9. Once a five-fold titration is evaluated, repeat steps 4-8 with a more narrow incremental titration in the range of the optimal concentration determined in step 8.

Based on the five-fold antibody titration, a narrower incremental range of staining concentration can be subsequently performed to determine the highest separation (stain index) between the positively and negatively labelled virus populations (Fig. 6). Again, equal numbers of MLV and MLVsfGFP particles are mixed and stained to calculate the stain index. Following the narrower increment titration, we confirm that 0.10 µg/mL of antibody concentration appears to be optimal in our conditions (Fig. 6C). The optimization of these experimental conditions will allow for the most accurate estimation of protein abundance on each virus.

2.7 Basic Protocol 5: Gain configuration optimization

To further increase the resolution of the dimly labelled virus population from background noise, the gain of the parameter being evaluated can be optimized directly on the instrument during acquisition. Similar to the adjustment of acquisition settings in classical flow cytometry for cell analysis, the gain can be optimized to increase the signal and the separation between the positive labelled population and background noise. As shown in Figure 7, we gradually increased the PE gain while keeping the threshold constant and evaluated where the stained viral population or reference beads fell in relation to the gain adjustments. By applying the formula for the calculation of stain index, we determined the optimal separation between our positive and negative populations (Fig. 7B). Furthermore, by acquiring PE QuantiBrite beads at the same gain, we were able to evaluate where the dimmest and brightest bead populations fell in relation to the gain adjustments allowing us to evaluate the dynamic range of detection in respect to our labelled viral population of interest (Fig. 7D). While adjustments in PE gain increased the separation between background noise and the bead population, it can push the brightest bead population off scale consequently affecting the detection range in the PE channel. Once the gain is optimized, the

fluorescence signal of the labelled virus can be compared to that of the reference bead population. In our case, this signal is closest to the dimmest bead population as illustrated in Figure 7D. Once voltage has been optimized during the initial set up, reproducibility can be checked using the reference beads prior to each experiment to maintain optimal resolution.

Materials

Dulbecco's phosphate-buffered saline (DPBS) (Wisent Bioproducts, catalogue # 311-430-CL)
BD 10 mL Syringe (Catalogue 302995)
100 nm Acrodisc Sterile Syringe Filter (Pall Corporation, catalogue 4611)
450 nm Acrodisc Sterile Syringe Filter (Pall Corporation, catalogue 4615)
5 mL Polystyrene Round Bottom Tube (Falcon, catalogue 352054)
Anti-GFP PE Monoclonal Antibody (BioLegend, clone FM264G)
16 % Paraformaldehyde (PFA)
Beckman Coulter CytoFLEX S with 4 Lasers (Mississauga, ON,CA)
FlowJo (CA, USA, version 10.7.1)
NIST-traceable size calibration reference polystyrene and silica beads
BD QuantiBrite phycoerythrin (Davis et al.) Quantitation Kit (Lot 47973, BD Biosciences, catalogue # 340495)
NIH 3T3 fibroblast cell (ATCC, CCL-92)
Chronically infected NIH 3T3 cell clone (#6) **Basic Protocol 1**
DMEM Media high glucose, with L-glutamine, sodium pyruvate and phenol red (Wisent, catalogue number: 319-005-CL)
Fetal bovine serum (Thermo Fisher Scientific, catalogue number: 12483020)
Penicillin-Streptomycin (GE Healthcare, catalogue number: SV30010)
Complete DMEM (see recipe in Reagents and Solutions)
DMEM Phenol Red Free medium (see recipe in Reagents and Solutions)
10% EV depleted FBS (see recipe in Reagents and Solutions)
FACS tubes
Tissue Culture incubator (Thermo Fisher Scientific, catalog number: 3110)
Refrigerated table-top centrifuge Sorvall ™ ST 40 (Thermo Fisher Scientific, catalog number: 75004524)
FlowJo (CA, USA, version 10.7.1)
FCMPASS software (v3.1, http://nanopass.ccr.cancer.gov) (Welsh & Jones, 2020)

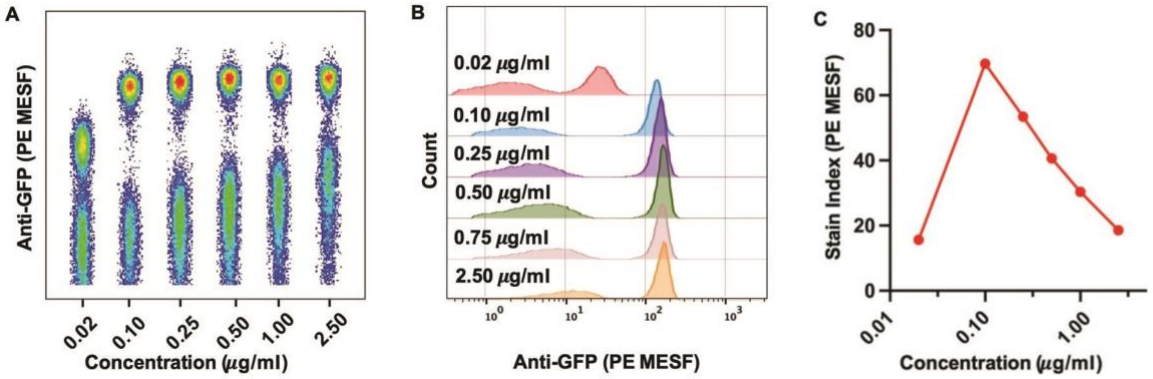

Figure 2.6 Evaluation of target antigen abundance.
A) Dot plot and **B)** histograms of titrated anti-GFP PE monoclonal antibody used to stain equal parts of MLV and MLVsfGFP. **C)** Stain index plot for the determination of the optimal staining concentration that provides minimal nonspecific binding. The stain index was calculated using the median fluorescent intensity in PE MESF of positively and negatively labelled virus populations divided by the standard deviation of the negative population.

1. Repeat steps 1-6 of **Basic Protocol 2**.
2. Run 100 nm filtered DPBS or buffer control.
3. While acquiring buffer control, adjust the instrument's gain configuration in order to increase or decrease the signal value.

   Start sample acquisition with the instrument's recommended settings or setting used during instrument quality control validation.
4. Systematically increase the gain configuration, here we evaluated a range from 500 to 2000.
5. Acquire the buffer control, the stained viral sample of interest and reference beads at each gain increment.

   Fluorescence intensity of labelled virus in MESF units can be compared to background and fluorescence reference beads elucidating the dynamic range of detection in respect to our labelled viral population of interest (Fig. 7D).
6. Gate on the positively stained MLVsfGFP population and the internal negative population (background noise or MLV in case of premixed virus population as used for **Basic Protocol 4** step 4) to obtain the median fluorescence intensity for each.
7. Determine highest separation between the positively and negatively populations using the formulas for the stain index determination.

Calculated as follows:

$$Separation = \frac{MFI\ of\ postive\ population - MFI\ negative\ population}{SD\ of\ negative\ population}$$

Alternatively, the threshold can be modified to enable the inclusion or exclusion of dimmer particles. However, adjusting the threshold could affect particle count and the ability to detect particles that fall within the background noise of the instrument if their signal doesn't exceed the newly adjusted threshold or inversely, detecting more background signals if the threshold is applied too low. For this purpose, the instrument sensitivity and dynamic range of the assay should be carefully evaluated.

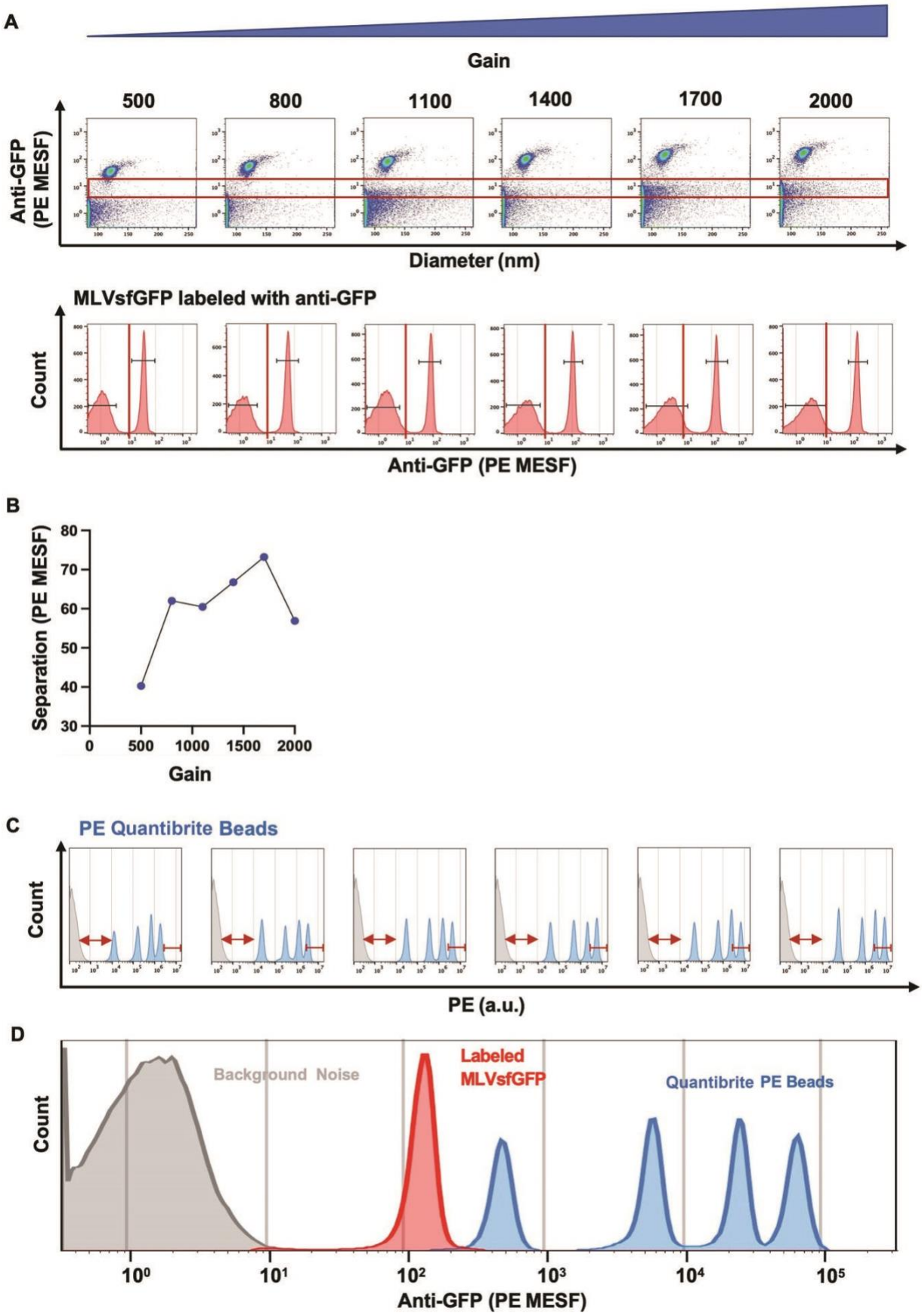
A
Gain
500
800
1100
1400
1700
2000
Anti-GFP (PE MESF)
Diameter (nm)
MLVsfGFP labeled with anti-GFP
Count
Anti-GFP (PE MESF)
B
Separation (PE MESF)
80
70
60
50
40
30
0
500
1000
1500
2000
Gain
C
PE Quantibrite Beads
Count
PE (a.u.)
D
Count
Background Noise
Labeled MLVsfGFP
Quantibrite PE Beads
10⁰
10¹
10²
10³
10⁴
10⁵
Anti-GFP (PE MESF)

Figure 2.7 Optimization of the gain parameter for maximal resolution.
A) Scatter and histogram plots of stained MLVsfGFP acquired by gradually increasing the PE gain on the cytometer. Plots are listed from left to right in order of increasing PE gain. **B)** Separation between the positive viral population and background noise for each gain configuration was calculated using the stain index formula for the determination of optimal separation. **C)** Effect of PE gain increase on the florescence signal of BD QuantiBrite PE bead population. While adjustments in PE gain increased the separation between background noise and the bead population (red arrow), it can skew the brightest bead population off scale (capped line) consequently affecting the detection range in the PE channel. **D)** Overlayed histogram plots of PE MESF quantification of labelled MLVsfGFP and QuantiBrite PE beads compared to labels PBS (background noise).

Reagents and Solutions

Complete DMEM Medium

DMEM with 4.5 g/L glucose, with L-glutamine, sodium pyruvate and phenol red (WISENT, catalogue number:319-005-CL)

10% FBS (Thermo Fisher Scientific, catalogue number: 12483020)

1% Penicillin-Streptomycin (GE Healthcare, catalogue number: SV30010)

Store in fridge (4 °C)

DMEM Phenol Red Free Medium

DMEM with 4.5 g/L glucose, with L-glutamine, sodium pyruvate and no phenol red (WISENT, catalog number:319-051-CL)

10% EV depleted FBS (Thermo Fisher Scientific, catalogue number: 12483020)

1% Penicillin-Streptomycin (GE Healthcare, catalogue number: SV30010)

Store in fridge (4 °C)

10 % EV depleted FBS

FBS (Thermo Fisher Scientific, catalogue number: 12483020) *Store at – 20* °C.

FBS was ultracentrifuged at 73,000xg for 12 hours, and collected carefully to avoid disruption of the EV pellet located on the bottom of the ultracentrifuge tube.

All media used for viral production for FVM analysis was supplemented with this 10% EV depleted FBS to minimize the impact and contamination of bovine EVs in downstream viral analysis by FVM (Kornilov et al., 2018).

Serum Free DMEM Medium

DMEM with 4.5 g/L glucose, with L-glutamine, sodium pyruvate and phenol red (WISENT, catalogue number:319-005-CL)

1% Penicillin-Streptomycin (GE Healthcare, catalogue number: SV30010)

Store in fridge (4 °C)

COMMENTARY

2.8 Background Information

Here, we described detailed FVM method- ology for staining surface proteins on the viral envelope. We used Env-sfGFP as an example, but the procedure would be similar for any desired

target, such as tetraspanins CD9, CD63, and CD81 (Maltseva & Langlois, 2021). These protocols highlight a comprehensive experimental design overview and important considerations and practical aspects for FVM analysis and reproducible data reporting as a result of calibration with reference beads. Given the evolution of the field of small-particle flow cytometry and ongoing developments in instrument optics and reference

particles, the protocols' workflow provides a recommended structure for the experimental design that will evolve concurrently to reflect technological advancements. The technique was initially developed by Hercher et al., who were the first to design a custom cytometer that enabled the detection and analysis of bacteriophages by their light scattering properties; direct analysis, quantification, and characterization of viruses followed suit (Hercher, Mueller, & Shapiro, 1979). The first viral staining targeted the genomes of larger DNA viruses (Brussaard, Marie, & Bratbak, 2000; Chen, Lu, Binder, Liu, & Hodson, 2001). Although initially utilized for the purpose of enumerating viruses, flow cytometry principles were later applied for viral characteri- zation and were instrumental in highlighting the extent of viral heterogeneity within a viral population. This was first illustrated in a study by Arakelyan et al., where differential incorporation of host-derived proteins on HIV-1 virions was observed by FVM, revealing het- erogeneous antigen expression profiles in the viral envelope (Arakelyan et al., 2013). From a therapeutic standpoint, FVM can also be applied as an analytical tool for the evaluation of the quality of virus-like particle (VLP) vaccine preparations (Tang et al., 2016; Vlasak et al., 2016). Here, we show that virus in the supernatants of infected cells can be directly stained and identified by light scatter and fluorescence without the need for additional concentration or manipulations. Importantly, as highlighted by Renner et al., FVM enables detection, enumeration, and characterization of intact viral particles (Renner et al., 2020). As such, one of the advantages of FVM over other high-throughput techniques is the tailored detection of particles whose signal exceeds the designated light scatter threshold, discerning intact virions from ruptured and irregular virus particles and free protein, which may skew the measurements. How- ever, the many overlapping characteristics between EVs and viruses (e.g., egress pathways, size, biophysical properties) make them considerably difficult to discriminate from one another (Nolte-'t Hoen, Cremer, Gallo, & Margolis, 2016). As such, EV contamination is an important confounding factor in most viral analyses. Furthermore, EVs have also been shown to incorporate genomic as well as viral components when released from infected

cells (Nolte-'t Hoen et al., 2016). Currently, there is no consensus on a definitive way to distinguish EVs from non-infectious viral particles, termed VLPs. To address this, we and other groups have fluorescently tagged surface viral glycoproteins or nucleic acid content of viruses to improve viral resolution from EVs (Arakelyan et al., 2013; Brittain et al., 2019; Gaudin & Barteneva, 2015; Landowski, Dabundo, Liu, Nicola, & Aguilar, 2014; Lippe, 2018; Renner et al., 2020; Tang et al., 2017; Maltseva & Langlois, 2021).

Most commercial flow cytometers were designed to analyze cells or particles >500 nm in diameter. Given that viruses are consider-bly smaller in size than cells, these submicron particles often fall at the threshold of instrument detection, which is around 65 to 80 nm in diameter for our instrument (Brittain et al., 2019). As recommended by the MIFlowCyt-EV framework, data reporting in standard units by way of instrument calibration using reference beads is critical for reproducible and accurate measurements. Despite the current paucity of commercial reference particles with fluorescence intensities biologically comparable to those of viruses or EVs, brighter reference beads remain useful tools for fluorescence calibration and extrapolation of target molecule counts (Tang et al., 2019). Thus, care should be taken during the staining optimization stage and cytometer setup to evaluate the dynamic range between the positively stained viral populations and the background fluorescence of a sample, as weakly expressed proteins could be masked by high levels of background noise. Pre-analytical variables such as virus production, collection, storage, and manipulation should also be carefully considered as variables affecting experimental reproducibility. Consequently, all aspects of the experimental design should be carefully monitored given that FVM measurements are obtained near the limit of detection, where small variations in labeling between experiments can lead to confounding results or inaccurate quantification of epitope abundance. The protocols presented here provide an overview of the instrument setup; methods for virus pro- duction; and the staining, detection, and quantification of particle concentration and size and surface antigens on the viral envelope. These protocols should be modified to reflect the goals of the experiment, the flow cytometer used, and the type of virus studied.

2.9 Critical Parameters

Cellular expression of viral and host- derived antigens of interest should be phenotypically characterized prior to their characterization on the surface of viruses. Due to the fundamental process of viral egress, proteins incorporated into cellular membranes will form the viral envelope of nascent viruses released from the cell. Thus, the presence of a protein of interest and the degree to which it is expressed should first be confirmed on the viral producer cells prior to its characterization on the surface of viruses. If the abundance is very low on the cell, it may be undetectable on the virus.

Antibody selection (Basic Protocol 4 and Support Protocol) will depend on the research question. In any case, 1) the density of proteins analyzed; 2) the brightness of the antibody- fluorophore conjugate; 3) spectral overlap with other fluorophores; 4) steric hindrance between the antibody and epitopes, which can prevent proper labeling of all available antigens; and 5) the fluorophore-to-protein ratio should be evaluated, among other factors. In our work, a PE-conjugated fluorophore was used; due its large size, the fluorophore-to- antibody and the antibody-to-epitope ratios are both estimated to be 1:1 (Davis et al., 1998). This ratio should be evaluated in order to accurately estimate epitope abundance.

Selection of the trigger parameter (Basic Protocol 2) is dependent on the aim of the experiment and the type of flow cytometer used. As discussed earlier, either light scatter or fluorescence can be chosen as the trigger parameter. The choice reflects whether the goal of a study is to characterize a heteroge- neous viral population based on virion size, RI, and physical features or to enumerate fluorescently labeled virions and evaluate surface epitope abundance.

Instrument calibration and careful setting optimizations (Basic Protocols 2 to 5) are crit- ical to efficiently resolve particles of interest and report data in a standardized manner. In the case of homogenous or non-parametric viral populations, data can be reported using percentiles (i.e., 25^{th} , 50^{th} , 75^{th} , and 90^{th}) in order to provide an accurate representation of protein incorporation distribution on in- dividual viruses within a viral population. Positively labeled events can be identified based on detection above a certain gate or threshold, such as two SDs or the 99^{th} per-centile above the negative population (Welsh et al., 2020). When reporting measured virus

concentrations, light scattering, or fluores- cence parameters, the range and limit of detection of the cytometer for each parameter should be included as an appendix to ensure the transparency and reproducibility of the data.

2.10 Troubleshooting

Detection of false positive events in buffer and antibody controls

It is critical to evaluate background fluorescence levels in order to assess whether antibody staining (Basic Protocol 4) results in unbound antibody aggregates that are misconstrued as small particles of interest. Thus, the optimal staining concentration (Support Protocol) should be carefully evaluated, as wash steps used for removing unbound antibody in classical cell-based cytometry are primarily omitted in FVM. Furthermore, the optimal signal-to-noise ratio should be identified to ensure maximal separation between positively and negatively stained populations while ensuring minimal levels of nonspecific binding to facilitate resolution of dim signals, as illustrated in Figure 5B.

Detection of false positive events in the supernatant and antibody control

The possible presence and staining of EVs should be carefully evaluated due their concomitant release with viruses from infected cells. As such, supernatant collected from uninfected cells is a critical control for identifying confounding effects related to bystander EV labeling. This control should be compared to a buffer and reagent control and a stained virus control sample to assess differences, if any, in background events and fluorescence signal. Treatment with a detergent (such a Triton X-100) will lyse lipid membrane vesicles, whereas other complexes (e.g., protein complexes, antibody aggregates, buffer salt crystals) will be unaffected. This is therefore an easy way of ensuring that the particles of interest do indeed contain a lipid membrane.

Understanding Results

For accurate, reproducible, and standardized data reporting, it is crucial to determine the instrument's sensitivity for light scatter and fluorescence measurements and to calibrate these values using standardized reference materials. Figure 2 displays the light scattering and fluorescence features of polystyrene NIST-traceable size reference beads and BD Quantibrite PE

fluorescence used for calibration. It is essential to have a high correlation between acquired and theoretical values in order to convert fluorescence intensity values into molecule equivalents and report fluorescence measurements in standard units.

Data analysis can be done in most soft- ware, such as R, FlowJo, or Kaluza, that can process FSC files and generate visual graphs such as dot plots, histograms, and density plots, among others. To ensure single-particle acquisition, the measured viral particle count should linearly reflect the dilution factor while light scatter intensity or fluorescence signal should be maintained constant, as shown in Basic Protocol 2.

Key experimental controls are required for robust virus detection and to set gates as shown in Basic Protocol 3. Once the gates have been defined, light scatter properties of the viruses can be used to derive viral particle sizes, the concentration of intact viral particles in a sample, and the relative abundance of a target antigen on the surface of the virus, as explained in Basic Protocols 3 and 4. Different metrics of reporting other than MFI can be used in cases of non-parametric distribution of protein expression or particle size within the viral population (such as a percentile measurement), as shown in Tables 1 and 2.

Time Considerations

See Table 3 for time considerations associated with the protocols.

Acknowledgments

The authors would like to thank the University of Ottawa Flow Cytometry Core Facility for assistance with some of the flow cytometry analyses. M.M. holds a Queen Elizabeth II Graduate Scholarship in Science and Technology (QEII-GSST). M.-A.L. holds a Canada Research Chair in Molecular Virology and Intrinsic Immunity. This study was supported by a Discovery grant to M.-A.L. by the Natural Sciences and Engineering Research Council (NSERC) of Canada.

Author Contributions: Mariam Maltseva: Performed the experiments; carried out the data analysis; drafted and edited the manuscript; **Marc-André Langlois:** Conceptualization; funding acquisition; methodology; supervision; writing-review and editing.

Conflict of Interest

The authors declare no conflict of interest.

Data Availability Statement

Data files are available from the authors on request.

Time consideration for each protocol

Protocol	Time	Details
Basic Protocol 1: Virus Production		
1. Production of virus by transfection		
2. Production of virus from an infected cell population	4 days	Day 1: 15 mins Day 2: 45 mins Day 4: 5 mins
3. Production of virus by chronically infected cell clones	8 days	Day 1: 15 mins Day 2: 45 mins Day 4: 5 mins Day 5: 15 mins Day 6: 5 mins Day 8: 5 mins
	30 days	Day 1: 15 mins Day 2: 45 mins Day 4: 5 mins Day 5: 15 mins Day 6: 5 mins Day 8: 120 mins Day 12: 10 mins Day 15: 10 mins Day 18: 10 mins Day 21: 10 mins Day 24: 10 mins Day 27: 80 mins Day 28: 10 mins Day 30: 5 mins
Basic Protocol 2: Instrument setup and quality control for fluorescence quantification standardization and quality control for fluorescence quantification	1 day	Day 1: 100 min
Basic Protocol 3: Flow virometry analysis	1 day	Day 1: 30 mins
Basic Protocol 4: Viral surface antigen staining and fluorescence quantification	1 day	Day 1: 210 mins
Support Protocol 1 for Basic Protocol 4: Determination of the optimal antibody concentration for virus staining	2 days	Day 1: 210 mins Day 2: 210 mins

2.11 References

Arakelyan, A., Fitzgerald, W., Margolis, L., & Grivel, J. C. (2013). Nanoparticle-based flow virometry for the analysis of individual virions. *J Clin Invest, 123*(9), 3716-3727. doi:10.1172/JCI67042

Brittain, G. C. t., Chen, Y. Q., Martinez, E., Tang, V. A., Renner, T. M., Langlois, M. A., & Gulnik, S. (2019). A Novel Semiconductor-Based Flow Cytometer with Enhanced Light-Scatter Sensitivity for the Analysis of Biological Nanoparticles. *Sci Rep, 9*(1), 16039. doi:10.1038/s41598-019-52366-4

Brussaard, C. P., Marie, D., & Bratbak, G. (2000). Flow cytometric detection of viruses. *J Virol Methods, 85*(1-2), 175-182. doi:10.1016/s0166-0934(99)00167-6

Cantin, R., Methot, S., & Tremblay, M. J. (2005). Plunder and stowaways: incorporation of cellular proteins by enveloped viruses. *J Virol, 79*(11), 6577-6587. doi:10.1128/JVI.79.11.6577-6587.2005

Chen, F., Lu, J. R., Binder, B. J., Liu, Y. C., & Hodson, R. E. (2001). Application of digital image analysis and flow cytometry to enumerate marine viruses stained with SYBR gold. *Appl Environ Microbiol, 67*(2), 539-545. doi:10.1128/AEM.67.2.539-545.2001

Cossarizza, A., Chang, H. D., Radbruch, A., Acs, A., Adam, D., Adam-Klages, S., . . . Zychlinsky, A. (2019). Guidelines for the use of flow cytometry and cell sorting in immunological studies (second edition). *Eur J Immunol, 49*(10), 1457-1973. doi:10.1002/eji.201970107

Davis, K. A., Abrams, B., Iyer, S. B., Hoffman, R. A., & Bishop, J. E. (1998). Determination of CD4 antigen density on cells: role of antibody valency, avidity, clones, and conjugation. *Cytometry, 33*(2), 197-205. doi:10.1002/(sici)1097-0320(19981001)33:2<197::aid-cyto14>3.0.co;2-p

Gaudin, R., & Barteneva, N. S. (2015). Sorting of small infectious virus particles by flow virometry reveals distinct infectivity profiles. *Nat Commun, 6*, 6022. doi:10.1038/ncomms7022

Gobeil Odai, K., O'Dwyer, C., Steenbergen, R., Shaw, T. A., Renner, T. M., Ghorbani, P., . . . Fullerton, M. D. (2020). In Vitro Hepatitis C Virus Infection and Hepatic Choline Metabolism. *Viruses, 12*(1). doi:10.3390/v12010108

Groot Kormelink, T., Arkesteijn, G. J., Nauwelaers, F. A., van den Engh, G., Nolte-'t Hoen, E. N., & Wauben, M. H. (2016). Prerequisites for the analysis and sorting of extracellular vesicle subpopulations by high-resolution flow cytometry. *Cytometry A, 89*(2), 135-147. doi:10.1002/cyto.a.22644

Hercher, M., Mueller, W., & Shapiro, H. M. (1979). Detection and discrimination of individual viruses by flow cytometry. *J Histochem Cytochem, 27*(1), 350-352. doi:10.1177/27.1.374599

Kornilov, R., Puhka, M., Mannerstrom, B., Hiidenmaa, H., Peltoniemi, H., Siljander, P., . . . Kaur, S. (2018). Efficient ultrafiltration-based protocol to deplete extracellular vesicles from fetal bovine serum. *J Extracell Vesicles, 7*(1), 1422674. doi:10.1080/20013078.2017.1422674

Landowski, M., Dabundo, J., Liu, Q., Nicola, A. V., & Aguilar, H. C. (2014). Nipah virion entry kinetics, composition, and conformational changes determined by enzymatic virus-like particles and new flow virometry tools. *J Virol, 88*(24), 14197-14206. doi:10.1128/JVI.01632-14

Lippe, R. (2018). Flow Virometry: a Powerful Tool To Functionally Characterize Viruses. *J Virol, 92*(3). doi:10.1128/JVI.01765-17

Ma, L., Zhu, S., Tian, Y., Zhang, W., Wang, S., Chen, C., . . . Yan, X. (2016). Label-Free Analysis of Single Viruses with a Resolution Comparable to That of Electron Microscopy and the Throughput of Flow Cytometry. *Angew Chem Int Ed Engl, 55*(35), 10239-10243. doi:10.1002/anie.201603007

Maltseva, M & Langlois, M.-A. (2021). Influence of GlycoGag on the Incorporation of Host Membrane Proteins Into the Envelope of the Moloney Murine Leukemia Virus. *Frontiers in Virology,* 1*:747253.* doi: 10.3389/fviro.2021.747253

Nolte-'t Hoen, E., Cremer, T., Gallo, R. C., & Margolis, L. B. (2016). Extracellular vesicles and viruses: Are they close relatives? *Proc Natl Acad Sci U S A, 113*(33), 9155-9161. doi:10.1073/pnas.1605146113

Pizzato, M. (2010). MLV glycosylated-Gag is an infectivity factor that rescues Nef-deficient HIV-1. *Proc Natl Acad Sci U S A, 107*(20), 9364-9369. doi:10.1073/pnas.1001554107

Renner, T. M., Tang, V. A., Burger, D., & Langlois, M. A. (2020). Intact Viral Particle Counts Measured by Flow Virometry Provide Insight into the Infectivity and Genome Packaging Efficiency of Moloney Murine Leukemia Virus. *J Virol, 94*(2). doi:10.1128/JVI.01600-19

Tang, V. A., Fritzsche, A. K., Renner, T. M., Burger, D., Lannigan, J. A., Brittain, G. C., . . . Langlois, M.-A. (2019). Engineered Retroviruses as Fluorescent Biological Reference Particles for Nanoscale Flow Cytometry. *bioRxiv*, 614461. doi:10.1101/614461

Tang, V. A., Renner, T. M., Fritzsche, A. K., Burger, D., & Langlois, M. A. (2017). Single-Particle Discrimination of Retroviruses from Extracellular Vesicles by Nanoscale Flow Cytometry. *Sci Rep, 7*(1), 17769. doi:10.1038/s41598-017-18227-8

Tang, V. A., Renner, T. M., Varette, O., Le Boeuf, F., Wang, J., Diallo, J. S., . . . Langlois, M. A. (2016). Single-particle characterization of oncolytic vaccinia virus by flow virometry. *Vaccine, 34*(42), 5082-5089. doi:10.1016/j.vaccine.2016.08.074

Thery, C., Witwer, K. W., Aikawa, E., Alcaraz, M. J., Anderson, J. D., Andriantsitohaina, R., . . . Zuba-Surma, E. K. (2018). Minimal information for studies of extracellular vesicles 2018 (MISEV2018): a position statement of the International Society for Extracellular Vesicles and update of the MISEV2014 guidelines. *J Extracell Vesicles, 7*(1), 1535750. doi:10.1080/20013078.2018.1535750

Tian, Y., Gong, M., Hu, Y., Liu, H., Zhang, W., Zhang, M., . . . Yan, X. (2020). Quality and efficiency assessment of six extracellular vesicle isolation methods by nano-flow cytometry. *J Extracell Vesicles, 9*(1), 1697028. doi:10.1080/20013078.2019.1697028

van der Pol, E., van Gemert, M. J., Sturk, A., Nieuwland, R., & van Leeuwen, T. G. (2012). Single vs. swarm detection of microparticles and exosomes by flow cytometry. *J Thromb Haemost, 10*(5), 919-930. doi:10.1111/j.1538-7836.2012.04683.x

Vlasak, J., Hoang, V. M., Christanti, S., Peluso, R., Li, F., & Culp, T. D. (2016). Use of flow cytometry for characterization of human cytomegalovirus vaccine particles. *Vaccine, 34*(20), 2321-2328. doi:10.1016/j.vaccine.2016.03.067

Welsh, J. A., & Jones, J. C. (2020). Small Particle Fluorescence and Light Scatter Calibration Using FCMPASS Software. *Curr Protoc Cytom, 94*(1), e79. doi:10.1002/cpcy.79

Welsh, J. A., Van Der Pol, E., Arkesteijn, G. J. A., Bremer, M., Brisson, A., Coumans, F., . . . Jones, J. C. (2020). MIFlowCyt-EV: a framework for standardized reporting of extracellular vesicle flow cytometry experiments. *J Extracell Vesicles, 9*(1), 1713526. doi:10.1080/20013078.2020.1713526

3 Chapter 3: Influence of GlycoGag on the Incorporation of Host Membrane Proteins into the Envelope of the Moloney Murine Leukemia Virus. *(Published)*

Chapter 3: Influence of GlycoGag on the Incorporation of Host Membrane Proteins into the Envelope of the Moloney Murine Leukemia Virus

Preface: This chapter has been previously published as a research article.

Maltseva M., and Langlois M-A. (2021), *Influence of GlycoGag on the Incorporation of Host Membrane Proteins into the Envelope of the Moloney Murine Leukemia Virus*.
Frontiers in Virology, *1,* 747253. 10.3389/fviro.2021.747253

3.1 Abstract

Analysis of viral particle heterogeneity produced from infected cells has been limited by the inefficiency of traditional analytical methods to characterize large populations of viruses at an individual particle level. Flow virometry (FVM) is an emerging technique based on flow cytometry principles that enables a high throughput, multiparametric, and phenotypic characterization of viruses at a single particle resolution. Here, we performed FVM to analyze surface markers found on Murine Leukemia Virus (MLV) and glycosylated Gag-deficient (glycoGag) MLV. The glycoGag viral accessory protein has several roles in the MLV viral infection cycle including directing retroviral assembly and particle release at lipid rafts. Based on previous studies, we hypothesize that glycoGag modulates host protein incorporation into the viral envelope during viral assembly and budding. Here, by using FVM, we reveal that glycoGag is associated with an increased incorporation of the host-derived tetraspanins CD81 and CD63 along with the lipid raft marker and immune antigen Thy1.2 during the assembly and release of viral particles from infected NIH 3T3, EL4, and primary CD4+ T cells. Moreover, we show differences in the uptake of host proteins by viruses that are released from the two cell lines and primary T lymphocytes. Additionally, at the individual viral particle level, we observed a degree of expression heterogeneity of host-derived antigens within the viral population. Finally, certain cellular antigens can show either enrichment or exclusion from the viral envelope depending on whether glycoGag

is expressed by the virus. This suggests that glycoGag is involved in a mechanism of selective host protein incorporation into the viral envelope.

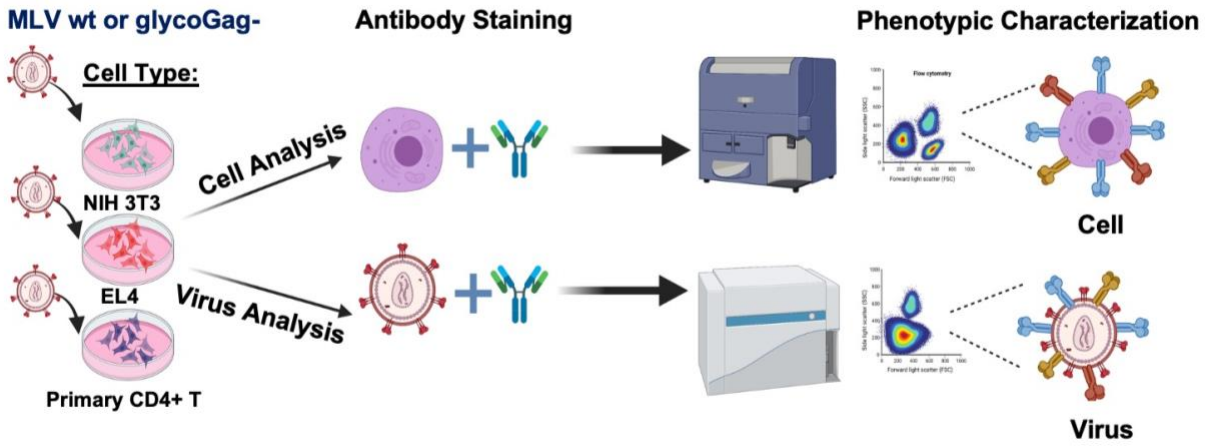

Highlights

When retroviruses egress from an infected cell, they capture some of the cell membrane which becomes part of its viral envelope. Host proteins are not randomly inserted into the envelope of budding retroviral particles. Certain cellular and viral factors influence the type and abundance of host proteins incorporated into the viral envelope at the site of viral egress. These proteins can have functional roles in immune escape, infectivity and even pathogenesis. Here we explore how the retroviral accessory protein glycoGag can modulate host protein incorporation into the viral envelope.

3.2 Introduction

Retroviruses are a diverse group of enveloped, single-stranded, RNA viruses that infect a wide variety of vertebrates. Murine Leukemia Virus (MLV) is often used as the prototypical model to study more complex retroviruses such as the Human Immunodeficiency Virus type 1 (HIV-1) and Human T-cell Lymphotropic Virus (HTLV). MLV is a simple enveloped retrovirus, initially presumed to code for three essential genes that are required for the retroviral replication cycle: Group Specific Antigen (Gag), envelope glycoprotein (Env), and viral RNA-dependent DNA polymerase and integrase (Pol). However, it has been shown that the MLV genome can also code for an additional glycosylated variant of Gag known as glycoGag which harbors an additional 88 amino acids in its N-terminus (**Figure 1A**) (1–3). Recognition of an alternative CUG start codon

upstream and in frame of the *gag* gene codes for a new leader sequence that directs the glycoGag protein to the endoplasmic reticulum for N-glycosylation. Upon posttranslational modification, glycoGag is cleaved into two subunits with the amino-terminal cleavage product of the protein becoming membrane-associated and subsequently inserted into the viral envelope of budding progeny virions in the $N_{exo}C_{cyto}$ orientation of a type I integral membrane protein (1, 4–6).

GlycoGag has been postulated to be an accessory protein of MLV since it is not required for viral replication *in vitro* but enhances the replication and pathogenesis of MLV *in vivo* (7– 14). GlycoGag has also been shown to influence viral budding in the producer cell by directing virion assembly and release to lipid raft microdomains, which are lipid-rich environments in the cell membrane that are highly saturated in cholesterol (10, 11). Finally, glycoGag provides stability to the viral core and aids MLV in circumventing the antagonistic functions of host restriction factors including the APOBEC3 cytidine deaminase and serine incorporated proteins (Serinc) (3, 6, 15–17).

The majority of newly assembled retroviral particles bud at the cell surface (18). In doing so, they capture a portion of the lipid bilayer from the cell, viral glycoproteins, and host-associated surface markers. This process ensures a highly controlled and precisely executed colocalization, incorporation, and assembly of all the virus' structural components. In the case of MLV, particles released are structurally extremely homogenous and monodisperse (6, 19–21). However, the underlying mechanism that governs host cellular antigen uptake by retroviruses and budding viruses is not clearly understood. Several different models have been proposed, including both passive and active models of host-derived antigen incorporation (22–24). The former suggests that the producer cell type predominantly determines the viral antigenic profile (22). In contrast, several studies have shown that cellular surface antigen uptake is not only a passive outcome of viral egress, and that viral components can directly influence their specific uptake. This active uptake model involves a selective mechanism of antigen incorporation that can be observed by the extent of viral phenotypic variability of surface markers and their effect on infection, adhesion, neutralization, and pathogenesis (22–29).

Many of these studies note that antigen expression levels on the surface of a host cell do not necessarily correlate by stoichiometry to the abundance of a given protein on the viral envelope (25, 28–30). Although the cell type from which the viral particles are released from is an important

determinant of viral envelope composition, viral factors may also play an active role in influencing the envelope's antigenic composition. For example, myristylation sites detected in the viral matrix protein are essential for targeting Gag assembly to detergent-resistant microdomains and lipid rafts, areas in which MLV and HIV-1 preferentially egress from (28, 31–33). In conjunction, Fan and colleagues have shown that glycoGag of wild-type MLV facilitates viral release through lipid rafts (10, 11). Intriguingly, Jalaguier et al. (26) have demonstrated that certain viral matrix mutations significantly impact host-derived ICAM1 incorporation in the HIV-1 viral envelope thereby elucidating the matrix protein's contribution to host protein incorporation. Furthermore, HIV-1 accessory proteins Nef and viral protein u (Vpu) downregulate host surface antigens such as CD4, MHC class I, and tetherin (6, 15–17, 30, 34–36). Functionally similar to Nef in some aspects, glycoGag first delocalizes the host restriction factors Serinc 3 and Serinc 5 from the plasma membrane by clathrin-dependent endocytosis and subsequently induces their processing through lysosomal degradation (6, 16, 17, 37). Despite extensive investigation into the role of HIV-1's accessory proteins and the various observations of down-modulation of select antigens on the surface of the infected cells, the impact of viral factors on the viral envelope composition has been understudied.

Viral surface antigens have been mostly characterized indirectly through bulk methodologies (e.g., Western Blot, ELISA, mass spectrometry) due to the relative scarcity of technologies capable of characterizing large numbers of viruses in a population at a single particle level. Bulk analyses generally lack the ability to provide critical information on: i) the surface protein composition of individual enveloped viruses, ii) the heterogeneity of viral populations, and iii) the presence of viral subpopulations (38, 39). While electron microscopy is extremely effective at investigating antigens on individual viruses, it is restricted in the number of particles analyzed simultaneously, labor intensive and only provides a relatively small snapshot of the heterogenous viral population. Recently, flow cytometry principles have been adapted to analyze submicron particles such as viruses and extracellular vesicles (EVs) (19, 20, 38– 40). Analysis of viruses by flow cytometry is a technique called flow virometry (FVM) which provides information regarding the relative size of viruses in a population, their light-scattering features indicative of population homogeneity, the abundance of total intact particles in a sample, and the relative expression level of proteins on their surface (20).

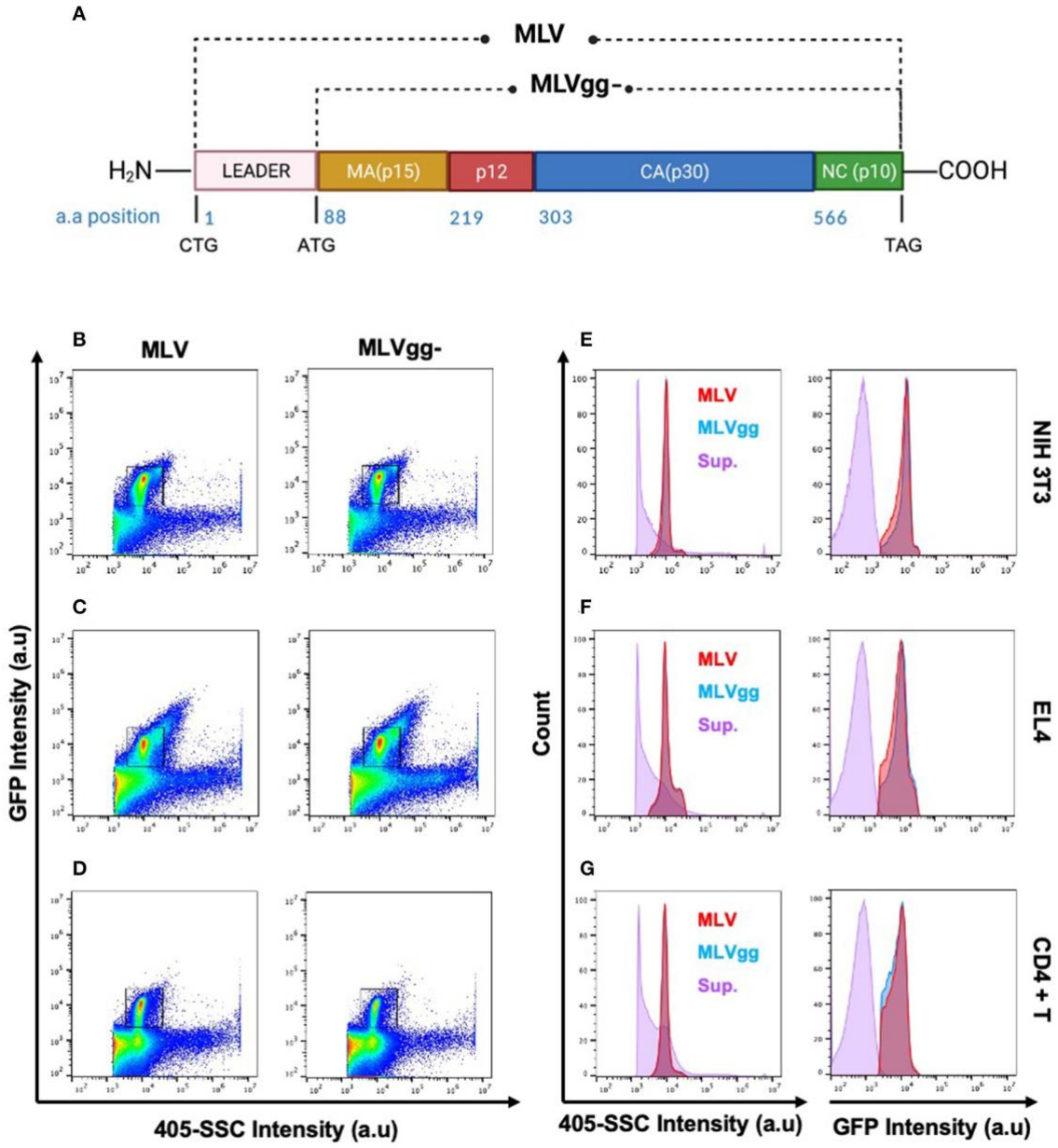

Figure 3.1 Identification of the viral population by side scatter and GFP fluorescence.

A) Schematic representation of wild-type MLV (MLV) and glycogag-deficient (MLVgg-) Gag proteins of MLV. MLV virions present a similar scatter plot profile to MLVgg- virions when released from B,E) NIH 3T3 fibroblast, C,F) EL4 T lymphocytes and D,G) primary CD4+ T cells. The viral population of interest is resolved from background by sfGFP fluorescence and side scatter (405-SCC) intensity (B-D). Gated particles express a similar monodisperse 405-SSC and sfGFP profile and are resolved from supernatant (sup.) collected from uninfected cells visualized as a histogram (E-G).

Here, we investigated by FVM the impact of glycoGag on the incorporation of host-derived proteins into the viral envelope of Moloney MLV. For this purpose, we compared the uptake of host surface antigens between wild-type MLV (MLV) and glycoGag-deficient (MLVgg-) particles released from three different murine cell types. Both viruses are replicationcompetent and express an Env-sfGFP fusion protein on their surface (19). We performed a direct comparison of

populations of these two MLV variants released from infected NIH 3T3 fibroblasts, EL4 T lymphocytes, and primary CD4+ T cells. Our study revealed a broad range in expression of host-derived proteins in the envelope of populations of the two viruses. We also show that the glycoGag accessory protein is associated with a selective increase or decrease in the incorporation of certain host-derived proteins into the viral envelope. Thus, our findings further support a role for glycoGag in governing host cellular protein incorporation into the MLV envelope during viral release.

3.3 Materials and Method

Mice

All breeding and experiments performed on animals were conducted in accordance with the Ontario Animals for Research Act and were approved by the University of Ottawa Animal Ethics Committee (protocol number ME-133). As previously described by our lab, Apobec3-deficient ($mA3^{-/-}$) mice (mA3-knockout mice) were backcrossed 12 times to a C57BL/6 mouse background (41). C57BL/6 (mA3 wild-type [WT]) and mA3-KO mice were maintained in the barrier unit of the University of Ottawa Animal Care Facility.

Cell Culture

Mouse embryonic fibroblasts (NIH 3T3) were cultured in DMEM (Wisent), and mouse T lymphocytes (EL4) and primary CD4+ T lymphocytes were cultured in RPMI 1640 (Wisent) and propagated in an incubator at 37°C with 5% CO_2. Media was supplemented with 10% FBS (Corning), 100U/mL penicillin, and 100µg/mL streptomycin (Wisent). Mouse splenocytes were isolated from mA3-knockout 6-week old C57BL/6 mice. Briefly, spleens were homogenized by enforcing passage through a 70 µm nylon cell strainer as previously described (3). Primary CD4+ T cells were isolated with total CD4 T cell isolation kit (Miltenyi Biotec) using MACS separator following the manufacturer's instructions. Following isolation, cells were activated with anti-CD3 (1μg/mL) (clone 172A, Biolegend) and anti-CD28 (1 µg/mL) (clone E18, Biolegend) antibodies and resuspended in RPMI 1640 media substituted with human IL-2 50 units/mL (Peprotech) and 0.01 M Betamercaptoethanol (BME) (Sigma) for 48 hours.

Expression plasmids and virus production

Plasmids encoding WT and glycogag-deficient Moloney MLV-sfGFP (MLVgg-) were described previously by our group (19, 21). Briefly, both plasmids were generated using restriction-free cloning to replace eGFP in the proline-rich region of Env in Moloney MLV vector with a sfGFP as previously reported (6, 42). Forward primer 5'-TTCAGTCACCAAACCACCCAGTGGGAGCAAGGGCGAGGAACTGTTCACC-3', and reverse primer 5'-CGGTACGTACGCACCGGTGGACTTGT ACAGCTTGTACAGCTCGTCCATGCCGTGGG-3' were used. Thus, both WT and MLVgg-express sfGFP as a fusion protein with Env, where sfGFP is exposed on the outer side of the viral

envelope. Consequently, wild-type MLV has an additional 88 amino acid leader sequence compared to the MLVgg- due the recognition of an alternative CUG start codon upstream and in frame of the *gag* gene (Fig. 1A). MLV and MLVgg- were produced from chronically infected NIH 3T3 cells as previously described (6, 15, 19, 20). Virus harvested from stably infected NIH 3T3 cells was used to infect EL4 cells. Briefly, chronically infected NIH 3T3 cells were seeded at $2.5x10^6$ in a 10 cm dish and cultured for 72 hours. Collected viral supernatant was filtered through a 0.45μm filter and ultra-centrifuged at 100,000g for 3.5 hours in a 70Ti rotor at 4°C. Lastly, the viral pellet was resuspended in RPMI 1640 and used to infect EL4 cells seeded in a 6 well plate at $5x10^5$ cells per well. Infected EL4 cells were identified by sfGFP expression and were subsequently sorted by flow cytometry. These cells were expanded and used for this study. For viral production, chronically infected NIH 3T3 and EL4 cells were seeded at $5x10^6$ cells in a 10 cm dish in 10 mL of DMEM media (Wisent) or RPMI 1640 media (Wisent) that did not contain phenol red, supplemented with 10% (v/v) EV-depleted FBS, and cultured for 72 hours. Viral supernatants were collected, centrifuged at 900g for 5 mins, and filtered with a 0.45μm filter. Lastly, the supernatant was diluted in 0.1μm filtered 1X PBS (Wisent) and analyzed by FVM analysis without additional enrichment.

Ex vivo infections of primary CD4+ T cells.

Activated primary CD4+ T cells were infected with either MLV or MLVgg-. As previously described, viral supernatant harvested from chronically infected NIH 3T3 producer cells was collected, filtered through a 0.45μm filter, and ultra-centrifuged at 100,000g for 3.5 hours in a 70Ti rotor at 4°C. The viral pellet was resuspended in RPMI 1640 medium (IL-2 50 units/mL, 0.01 M BME) and used to spin infect activated primary CD4 T cells. At 24 hours post-infection, cells were washed thoroughly with PBS and resuspended in RPMI 1640 media supplemented with (IL-2 50 units/mL, 0.01M BME, and 1 ng/mL IL-7 (Miltenyi Biotec)). After 48 hours of incubation, viral supernatants were collected and used for FVM analysis as described. Cells were analyzed by flow cytometry for sfGFP expression and screened for select antigen expression (Table 1).

Flow Virometry Analysis and Staining

A detailed methodology is available online describing antibody staining of the viruses and instrument settings (19, 21). Briefly, FVM analysis was conducted on a CytoFLEX S (Beckman Coulter) using the 405nm SSC-H as the threshold parameter (threshold of 1500 a.u). All viral supernatants were filtered and centrifuged prior to dilution in 0.1 μm 1X PBS. Prior to viral staining, the antibody was centrifuged at 17 000g for 10 min in order to decrease the presence of antibody aggregates. Briefly, all viral antibody labeling was performed with 1:1 ratio viral supernatant to PE-conjugated antibody aliquot at final concertation of 0.2 to 1.6 μg/mL for $1x10^9$ viral particles for 60 mins at 37°C. Stained viral supernatant was diluted in 0.1 μm filtered PBS and acquired for 60 seconds at a low setting at a sampling rate of 10 μL/min. Table 1 includes a detailed description of all PE-fluorophore conjugated antibodies used in this study. Figure 1 illustrates the gating strategy utilized for antigen detection in the viral population of interest. Table

3 and 4 include a detailed description of labelled Moloney MLV particles for select antigens that were significantly higher than media labelled with antibody control.

Flow Cytometry

For flow cytometry analysis of uninfected and infected cells, cells were stained with the same antibodies as used in flow virometry analysis (Table 1) for 20 minutes at 4°C. Excess antibody was removed by washing with 0.2% BSA-PBS.

Table 3.1 List of Antibodies used for cell and viral staining.

Antibody Name	Clone	Company
PE–Conjugated monoclonal anti-CD81	Eat2	BioLegend
PE–Conjugated monoclonal anti-CD63	NVG-2	BioLegend
PE–Conjugated monoclonal anti-CD9	KMC8	BD Biosciences
PE–Conjugated monoclonal anti-CD3	17A2	BioLegend
PE–Conjugated monoclonal anti-LFA-1	H155-78	BioLegend
PE–Conjugated monoclonal anti-CD45	30-F11	BioLegend
PE–Conjugated monoclonal anti-CXCR4	2B11	BD Biosciences
PE–Conjugated monoclonal anti-CD29	HMB1-1	BioLegend
PE–Conjugated monoclonal anti-CD69	H12F3	BioLegend
PE–Conjugated monoclonal anti-CD4	RM4-5	BioLegend
PE–Conjugated monoclonal anti-Thy1.2	53-2.1	BioLegend
PE–Conjugated monoclonal anti-CD55	RIKO-3	BioLegend
PE–Conjugated monoclonal anti-CD59	mCD59.3	BioLegend
PE–Conjugated monoclonal anti-CD317	129c1	BioLegend
PE–Conjugated monoclonal anti-GFP	FM264G	BioLegend
PE–Conjugated polyclonal anti-V5	Ab72480	Abcam

Data and Statistical Analysis

Flow cytometry and FVM data was analyzed with FlowJo v.10.7.1 (FlowJo, Ashland, OR). For cell analysis, FSC-height versus FSC-area and SSC-area versus FSC-area were used to exclude cell aggregates and debris. Statistical analysis to test for normal distribution, multiple unpaired t test and unpaired Mann-Whitney test was performed using GraphPad Prism (GraphPad Software, San Diego, CA). To analyze the presence and distribution of host-derived antigens on the surface of individual MLV particles, the viral supernatants were stained against the previously described antibodies chosen for cell phenotypic analysis. We set out to assess the two separate null hypotheses stipulated as follows:

H_0: MLV viral particles do not uptake cell-derived antigens on their viral envelope during budding, thus the signal intensity between stained MLV virus and negative control does not differ.

H_1: MLV viral particles do uptake cell-derived antigens on their viral envelope during budding, thus the signal intensity between stained MLV virus and negative control is different.

H_0': The glycoGag protein of MLV virus does not increase the incorporation of the cell-derived antigens compared to the MLVgg-.

H_1': The glycoGag protein of MLV does increase the incorporation of the cell-derived antigens compared to the MLVgg-.

The distribution normality of the samples' data was tested using D'Agostino-Pearson and Kolomogorov-Smirnov statistical criteria. Data distribution of all the samples analyzed was confirmed not to be of Gaussian distribution (K2>191, KS>0.06, n>10000, p<0.0001) on a high significance level. Therefore, to assess whether the null hypothesis is rejected and whether there is indeed a statistically significant difference in signal between the two MLV viruses, the Mann-Whitney test was applied. The standard error of mean (SEM) of each sample was calculated as $SEM = \frac{SD}{\sqrt{N}}$.

3.4 Results

Generation of chronically and transiently infected virus producer cells

To analyze the effect of the glycoGag accessory protein on the uptake of host proteins between cell types, we chronically infected the NIH 3T3 fibroblast and EL4 T lymphocyte cell lines with wild-type MLV and glycogag deficient MLV. Infected cells were identified by sfGFP expression and sorted by flow cytometry. Viral supernatants collected from NIH 3T3 cells were used to transiently infect primary CD4+ T cells *ex vivo*. Activated primary total CD4+ T cells isolated from APOBEC3-deficient ($mA3^{-/-}$) mice were infected with either MLV or MLVgg- as described in the methods section. Supernatants from chronically and transiently infected cells were collected for viral staining and FVM analysis throughout the study without further enrichment or purification.

Viruses produced by all three infected cell types were resolved from the background by both 405-side scatter intensity (405-SSC) and sfGFP fluorescence (Fig. 1). Analysis of MLV virions showed a highly monodisperse GFP+ population above non-fluorescent population composed of EVs and background noise that is most visible compared to overlaid signal of supernatant collected from uninfected cells (Fig. 1E-1G). These GFP^+ particles display heterogeneity in 405-SSC intensity that is slightly different for each cell type analyzed. Diversity in particle size, refractive index (RI),

protein or nucleic acid composition, or lipid content of the cell membrane that constitutes the viral envelope can all be factors influencing this heterogeneity (20, 43-45). The gating strategy used for stained particles is depicted in Figure 2 using CD81 as an example. The GFP+ virus population can be clearly resolved from the instrument background (Fig. 1 and Fig. 2). We have shown previously that Env-sfGFP expressed on EVs account for less than 0.3% of total GFP+ particles released from infected or transfected cells, and are thereby negligible in the overall virus particle count (19, 20).

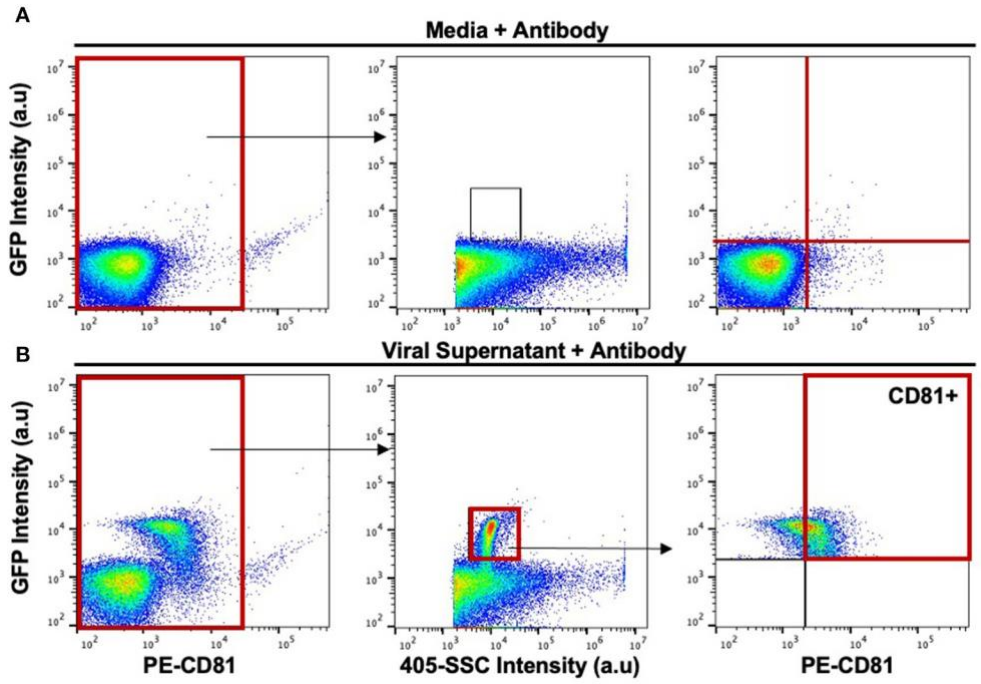

Figure 3.2 Gating strategy for the phenotypic analysis of host-derived proteins on the surface of the viral envelope of MLV virions.

A) Stained media-only control was used to assess background fluorescence and antibody aggregates. The background noise within this gate was used to set upper and lower gates to identify labelled virions (top rightmost panel). A) Stained MLVsfGFP virus with anti-CD81 was identified based on GFP and side scatter expression. CD81+ particles were located based on gates applied in B).

Determining the dynamic range of signal-to-noise for virus stainings.

Small particle flow cytometry and FVM face a significant challenge in analyzing surface antigen abundance on viruses due to the substantially smaller particle sizes, surface area, and antigen abundance compared to cells. For cell labeling, quantification of highly expressed proteins resulted in a dynamic range of $\sim 2-2.5$ logs in separation between the positive and the negative signals for CD81, Thy 1.2 and GFP (Fig.3A and 3D). In contrast, we observed a very limited dynamic

range in our viral stainings (Fig. 3B-3E). However, the contour plots clearly indicate that all of these antigens tested can be clearly resolved from the isotype control (Fig. 3C). The Env-sfGFP fusion protein trimer is estimated at ~300 molecules in the MLV viral envelope (21). Yet, the analysis of stained MLVsfGFP and nonspecific labelling with anti-GFP-PE revealed a separation of ~1.5 log between the two populations on our instrument (Fig. 3B and 3D-E). For the phenotypic characterization of surface antigens in this study, we used PE-conjugated antibodies as the PE fluorophore produced the highest stain index from the three fluorophores tested in our previous study (21).

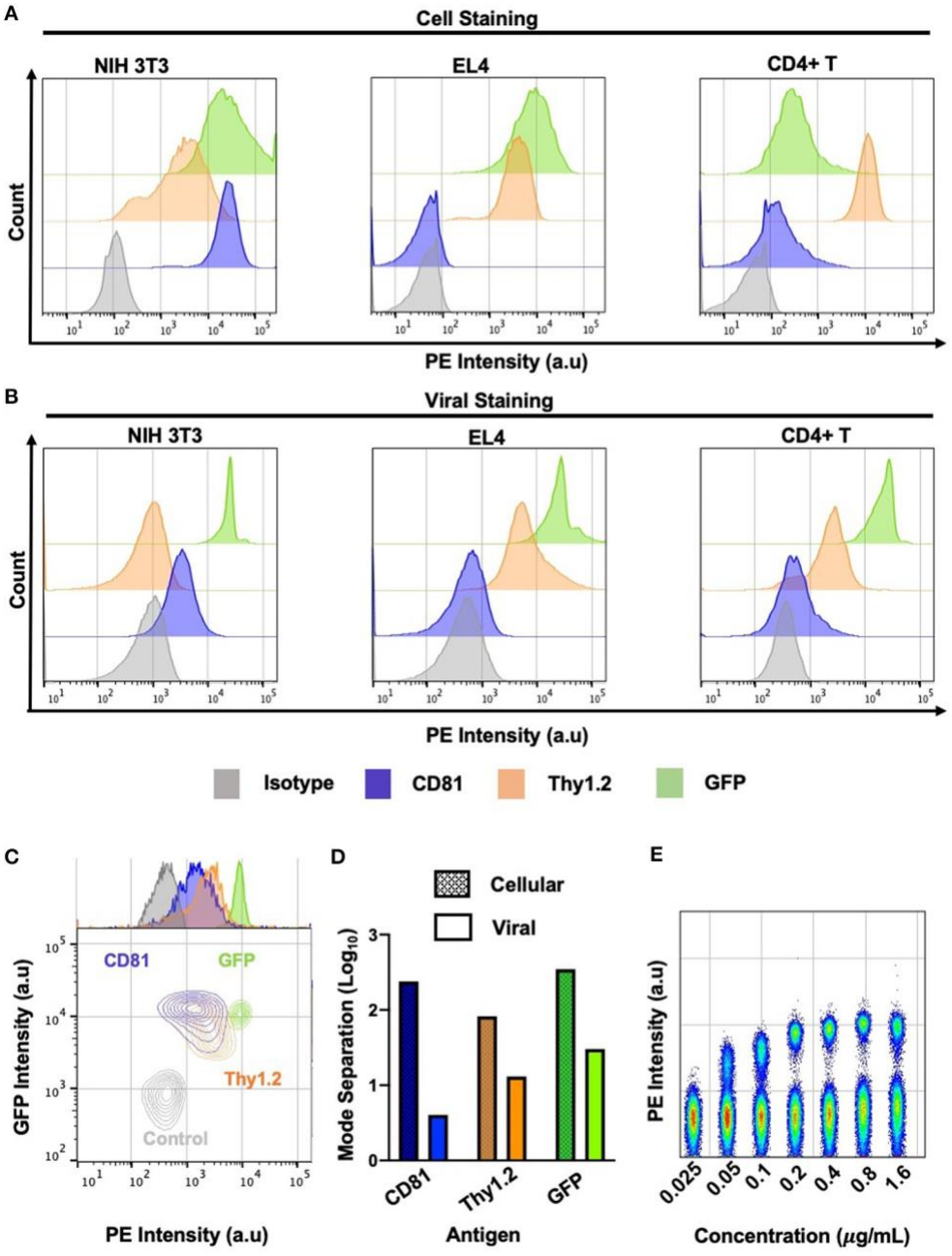

Figure 3.3 Dynamic range of cellular and viral staining.
A) Phenotypic analysis of labelled infected murine NIH 3T3, EL4, and primary CD4+ T cells by flow cytometry against select cellular antigens of low and high abundance. B) Phenotypic analysis of labelled MLV virions released from three murine cell types by flow virometry. C) Overlaid contour plots of labelled virus from B) where CD81+ is MLV released from NIH 3T3 cells, Thy1.2+ MLV was released from primary CD4+ T cells and GFP+ is MLV released from NIH 3T3 cell. Control MLVnoGFP virus released from NIH 3T3 was labelled with an GFP-PE antibody. D) Mode separation between positive and negative labelled cells (dotted) and virions (solid color) from C). E) Titration of anti-GFP PE antibody from 0.025 μg/ml to 1.6 μg/ml. Staining performed on a mixture of equal proportions of MLVnoGFP and MLVsfGFP virus particles.

To determine the optimal antibody concentration for viral staining, we titrated the anti-GFP-PE antibody on a mix of equal proportions of MLVsfGFP and MLV particles with no GFP reporter (MLVnoGFP), where the latter acted as a control to assess for non-specific binding (Fig.3E). As such, the dynamic range is closely affected by antigen expression levels in the viral envelope and the background fluorescence of the sample, which hinders the resolution of viral particles with low levels of antigen expression.

Detection and Quantification of Surface Proteins on Cells and Progeny Virions.

Next, we performed a phenotypic screen of surface antigens with a panel of 15 antibodies on three uninfected or infected cell types, and also on the produced virions (Fig. 4). Targets for these antibodies were selected based on their previously described incorporation into HIV-1's and EV's envelope, their abundance as tissue specific markers and as proteins that preferentially partition to lipid rafts (11,22, 25,29,40,46). We present the data as a heatmap of median fluorescence intensity. Our assessment of surface antigens on non-infected and chronically infected NIH 3T3 fibroblast cells with MLV and MLVgg- demonstrate similar phenotypic profiles (Fig. 4A). NIH 3T3 cells expressed tetraspanin-enriched microdomains (TEMs) antigens CD81, CD63, and CD9, the CD29 integrin marker, and lipid raft markers CD55, and Thy1.2. Of note, CD81 and CD63 were the most abundantly expressed cell-derived markers while sfGFP was the most abundant antigen on the surface of the chronically infected NIH 3T3 cells. Uninfected and chronically infected EL4 T lymphocytes expressed similar phenotypic profiles, with CD45, Thy1.2, and LFA-1 being the most abundantly detected antigens, followed by CD3 and CXCR4 (Fig. 4A). There was generally low expression of other lipid raft marker (CD55, CD59 and CD317) on EL4 cells. Lastly, primary CD4+ T cells displayed a similar phenotypic profile to the EL4 T cells, with the expression of CD45, Thy1.2, and LFA-1 being the highest, followed by CD3, CD29, and CD9. There was

minimal expression of CD81, CD63, and CD55 on the primary CD4+ T cells. We noted similar phenotypic profiles between MLV and MLVgg-infected cells (Table 2).

Table 3.2 Median fluorescence intensity of infected cells stained for select antigens*.

Cell Type	Antigen	MLV	MLVgg-
NIH 3T3	**CD81**	20086 ± 679	21885 ± 237
	CD63	9274 ± 120	13479 ± 190
	GFP	23915 ± 489	21105 ± 1056
EL4	**CD81**	44 ± 25	45 ± 20
	CD63	73 ± 20	77 ± 1
	CD45	6733 ± 29	5600 ± 68
	Thy1.2	3620 ± 19	2929 ± 19
	GFP	7936 ± 72	8468 ± 81
CD4+ T	**CD81**	148 ± 17	155 ± 13
	CD63	129 ± 24	133 ± 31
	CD9	1163 ± 13	1188 ± 17
	CD45	32061 ± 69	29189 ± 62
	Thy1.2	10311 ± 30	7785 ± 34
	GFP	232 ± 15	325 ± 19

*As determined by flow cytometry. Results are displayed as median fluorescence intensity of infected GFP positive cells $\pm$ standard error of the mean. Values represent the combined average of 3 experiments.

To measure host-derived antigens on the surface of individual MLV particles, the viral supernatant collected from these infected cells was stained using the same panel of antibodies used for the phenotyping of the infected cells (Fig. 4B). From the 15 viral stainings that were performed on MLV and MLVgg- virions, we noted that Env-sfGFP was the most abundantly expressed protein on the viral envelope (Fig. 4B). Intriguingly, while Env-sfGFP was the highest expressed cellular antigen on chronically infected NIH 3T3 cells, its abundance was lower on infected primary CD4+ T cells. Nevertheless, despite its varied expression between cell types, sfGFP-Env is expressed at similar levels on the virions released from these cells. (Fig. 3B). Analysis of virions released from NIH 3T3 show presence of the highly abundant cellular tetraspanin markers CD81 and CD63 on

the viral envelope of both variants (Fig. 4B). These differences can be visualized more clearly when the data is presented as contour plots (Fig. 5A). Other cellular markers present on the cell

surface were not detected in the viral envelope of MLV. The characterization of virus released from EL4 cells revealed the presence of the highly abundant mouse T cell and lipid raft marker Thy1.2 (Figs. 4B). Intriguingly, low levels of the T cell CD45 marker were detected on MLV virions (Figs. 4B and Table 3-4). Lastly, we detected an overall low abundance of the tetraspanin marker CD63 (Fig. 4B), suggestive of possible viral egress through the endosomal pathway as this antigen was not present on the cell surface (Fig. 4A and Fig. 6) (47, 48). For this purpose, we calculated the virus-to-cell surface antigen expression ratio between MLV and MLVgg- to that of their respective producer cells (Fig. 6). Next, we evaluated whether retroviral phenotypic analysis using FVM could be performed directly on virions released from primary cells infected *ex vivo*. Similar to the results with virus released from EL4 cells, Thy1.2 was the most concentrated host-derived protein on the viral envelope, followed by CD45, and CD9 (Fig. 4B). Despite CD45 being

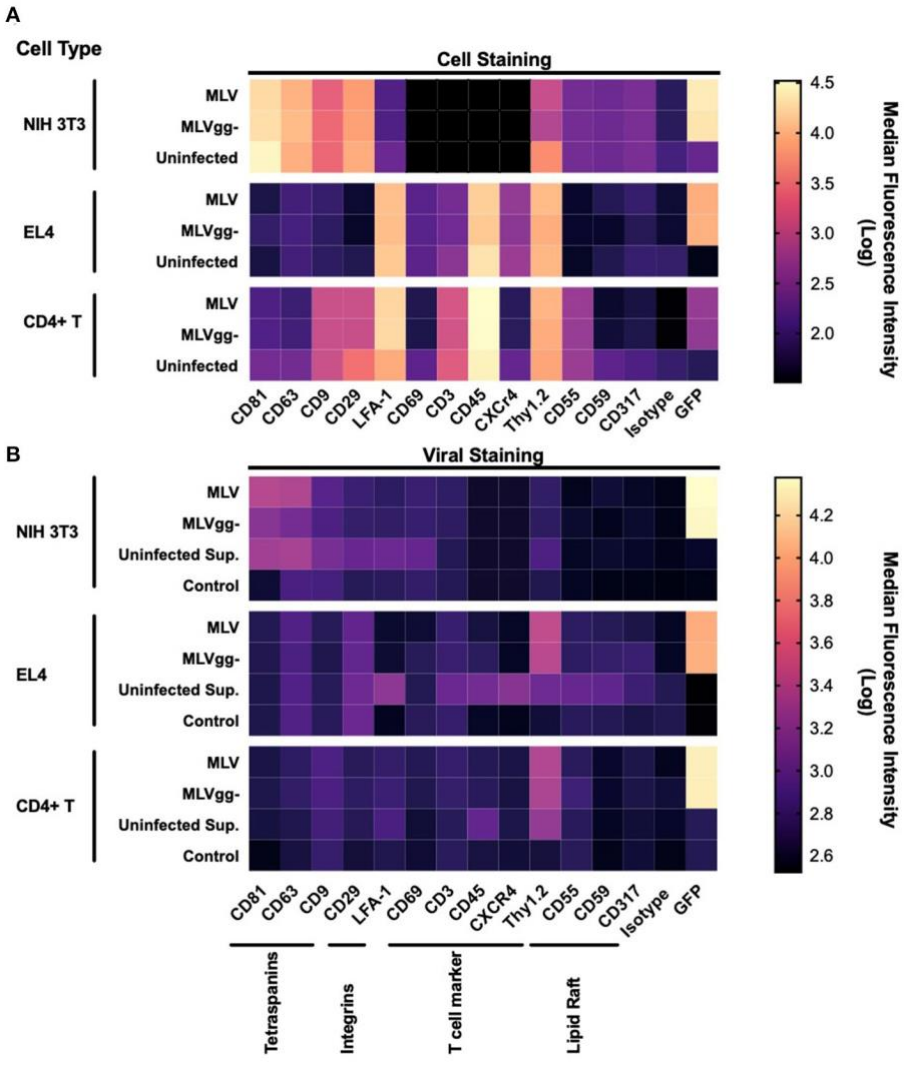

Figure 3.4 Phenotypic analysis of surface antigens on murine cells and on MLV and MLVgg- particles.

A) Heat map of surface antigens analyzed on uninfected and infected NIH 3T3, EL4, and primary CD4+ T cells with a panel of 15 PE-conjugated antibodies. B) Heat map of surface antigen expression intensity on MLV and MLVgg- virions released from infected NIH 3T3, EL4, and primary CD4+ T cells. Supernatants from uninfected cells were also analysed (Uninfected Sup.). Media-only with antibody was used to assess background fluorescence and non-specific binding. Tile intensity is the median fluorescence intensity transformed into log. Presented data was compiled from 3 to 4 experiments.

among the most abundantly expressed antigens on lymphocytes (Fig. 4A), CD45 is observed at low abundance on virions released from both EL4 and CD4+ T cells (Fig. 6 and Table 3-4). Interestingly, although only a portion of the cells staining positive for tetraspanin markers CD81 and CD63, we observe a preferential uptake or enrichment of these TEM markers on the surface of the virus (Fig. 6).

Table 3.3 MLV particles positively stained for select antigens*.

Cell Type	Antigen	MLV		MLVgg-	
		Stained Particles (%)	Particles Analyzed	Stained Particles (%)	Particles Analyzed
NIH 3T3	**CD81**	74.7±0.20	236049	47.4±0.30	207446
	CD63	34.4±0.30	237026	23.7±0.20	209624
EL4	**CD81**	0.62±0.07	77088	0.59±0.07	76076
	CD63	1.20±0.10	70682	0.98±0.09	73136
	CD45	5.89±0.29	44345	5.65±0.28	46130
	Thy1.2	79.7±0.49	44092	80.2±0.46	50192
CD4+ T	**CD81**	8.03±0.43	26231	9.58±0.51	22443
	CD63	1.53±0.19	28377	1.43±0.26	13595
	CD45	2.55±0.25	26382	3.30±0.31	21727
	Thy1.2	60.1±0.77	26796	58.4 ± 0.87	21080

*As determined by FVM using the gating strategy described in Figure 2. Results are displayed as percentage of positively labelled viral particles ± margin of error with a 99% confidence interval determined using the statistical z-score approach. The value demonstrated represent a combined average of 3-4 experiments.

GlycoGag Modulates Host-Derived Antigens on the surface of MLV

We next compared host-derived antigen expression between MLV and MLVgg- released from the three cell types. FVM analysis revealed that CD81 and CD63 on the surface of virus released from NIH 3T3 cells were present on 74.7%, and 34.4% of MLV virions, and on 47.6% and 23.6% of MLVgg- virions, respectively (Table 3, Fig. 5A). Furthermore, we measured a 66% increase of CD81 antigen abundance on MLV particles compared to MLVgg- virions released from NIH 3T3 cells. CD63 was also increased by 23% on the viral envelope of MLV virions (Fig. 7A).

Similarly, we reported an approximate 20% increase of CD81 protein expression on MLV over MLVgg- virions released from primary CD4+ T cells, while CD63 abundance was comparable between the two viruses (Fig. 7C). The antigenic distribution of CD81 and CD63 on MLV virions released from CD4+ T cells showed one dominant monodisperse population and a separate discrete subpopulation expressing an increased PE signal (Fig. 5B). Additionally, we detected an approximate 2% increase of CD9 protein expression on MLV compared to MLVgg- particles released from CD4+ T cells (Fig. 7C). Interestingly, CD45 protein expression was significantly increased on MLVgg- particles released from both EL4 and primary CD4+ T infected cells. In particular, we observed a 31% antigen increase on MLVgg- virions produced by EL4 cells, while this increase was less pronounced (∼5 %) when released from CD4+ T cells (Fig. 7B and 7C). To elucidate glycoGag's role on viral budding at lipid rafts microdomains, we labeled MLV particles with antibodies against lipid raft markers CD55, CD59, CD317, and Thy1.2. However, only Thy1.2 was expressed on all cell types tested, while CD55 was only weakly expressed on NIH 3T3 and primary CD4+ T cells (Fig. 4A). Thy1.2 was the only lipid raft marker detected on 79.7% and 80.2%, and 60.1% and 58.4% of MLV and MLVgg- particles released from EL4 and CD4+ T cells, respectively (Table 3). In support of the findings observed by Fan *et al.*, we revealed a significantly increased expression of Thy1.2 on MLV virions released from EL4 cells (∼14 %) while this increase was less pronounced with virus released from primary CD4+ T cells (∼2%) (Fig. 7B-C) (11). We consistently measured a slightly elevated fluorescent intensity on wild-type MLV, however whether this small difference is biologically relevant is unknown. Analysis of Thy1.2 expression revealed a highly heterogeneous distribution of this cellular antigen between the two MLV variants released from EL4 and primary CD4+ T infected cells (Fig. 5B).

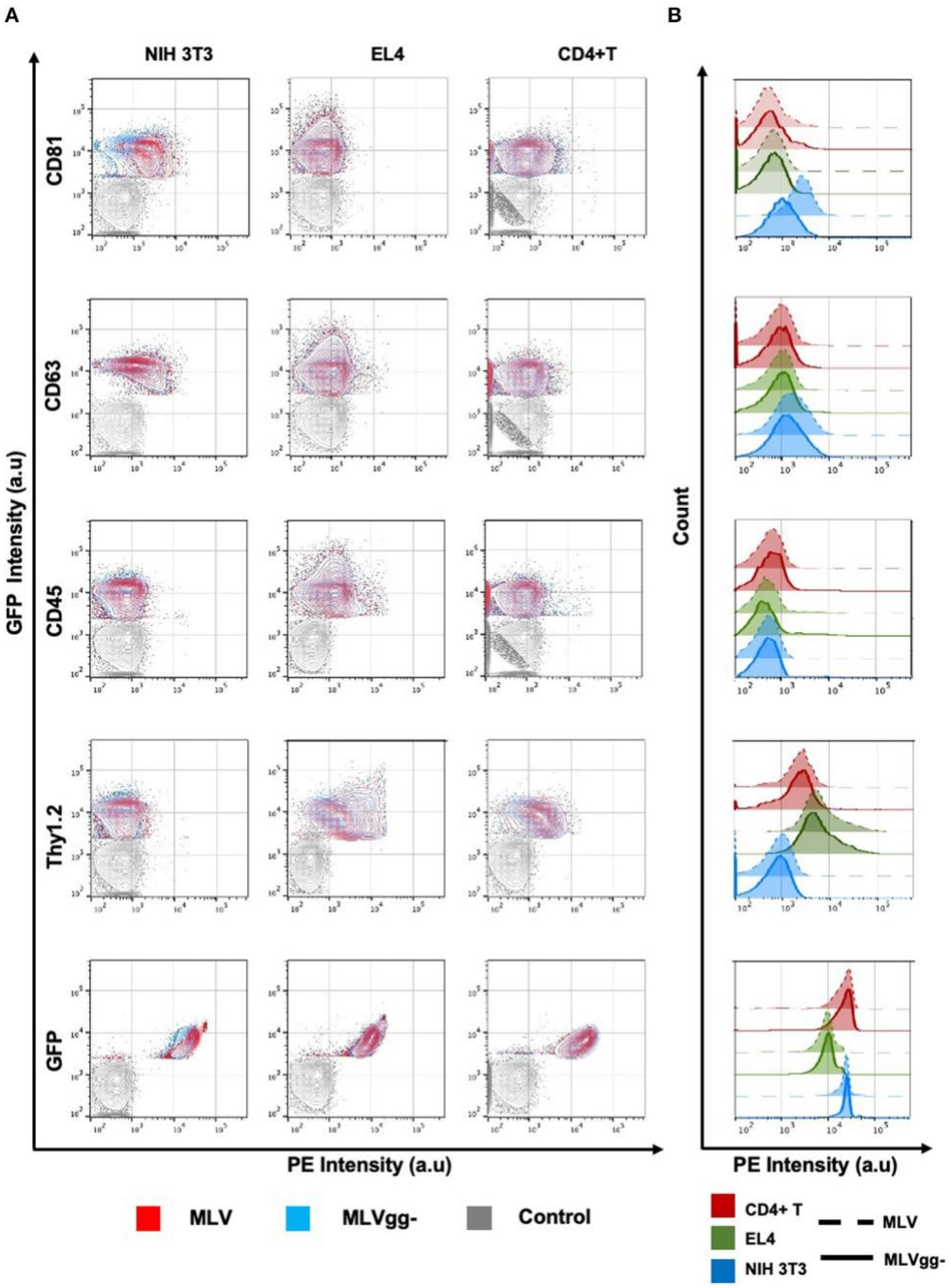

Figure 3.5 Analysis of antigenic heterogeneity between MLV and MLVgg- virions released from murine cells.

A) Contour plots of superimposed labelled MLV, MLVgg- and media-only with antibody control (Control). Antigenic heterogeneity varies between the two variants and the cell types that virions were released from. B) Histogram plot of labelled MLV and MLVgg- against selected antigens from A) released from three different murine cell types: NIH 3T3, EL4 and primary CD4+ T cells.

approximate 2% increase of CD9 protein expression on MLV compared to MLVgg- particles released from CD4+ T cells (Fig. 7C). Interestingly, CD45 protein expression was significantly increased on MLVgg- particles released from both EL4 and primary CD4+ T infected cells. In

particular, we observed a 31% antigen increase on MLVgg- virions produced by EL4 cells, while Taken together, our results reveal a selective increase in TEM and Thy1.2 antigen incorporation within the viral envelope of MLV virions produced by NIH 3T3, EL4, and primary CD4+ T cells. Our findings provide support that glycoGag can direct the incorporation of specific host-derived proteins during viral assembly and egress.

Table 3.4 Median fluorescence intensity of MLV particles stained for select antigens*

Cell Type	Antigen	MLV	MLVgg-	Control (Media + Antibody)	Isotype Control	
					MLV	MLVgg-
NIH 3T3	**CD81**	2290 ± 5	1377 ± 4	353 ± 1	891 ± 3	854 ± 3
	CD63	2026 ± 5	1644 ± 6	396 ± 1	781 ± 2	704 ± 2
	GFP	23796 ± 26	23150 ± 27	379 ± 1	781 ± 2	704 ± 2
EL4	**CD81**	566 ± 16	539 ± 4	516 ± 1	545 ± 1	552 ± 1
	CD63	863 ± 6	884 ± 5	772 ± 1	813 ± 3	661 ± 2
	CD45	794 ± 10	1148 ± 9	689 ± 2	729 ± 4	838 ± 4
	Thy1.2	5583 ± 51	4916 ± 40	1047 ± 3	709 ± 2	899 ± 2
	GFP	20310 ± 53	19476 ± 107	603 ± 1	709 ± 2	899 ± 2
CD4+ T	**CD81**	802 ± 9	673 ± 10	353 ± 1	596 ± 4	589 ± 6
	CD63	652 ± 6	653 ± 6	397 ± 1	598 ± 4	572 ± 5
	CD45	663 ± 10	697 ± 13	420 ± 1	740 ± 4	731 ± 6
	Thy1.2	2318 ± 14	2275 ± 18	663 ± 10	598 ± 4	572 ± 5
	GFP	19869 ± 66	20711 ± 54	440 ± 1	598 ± 4	572 ± 5

*As determined by FVM using the gating strategy described in Figure 2. Results are displayed as median fluorescence intensity of gated viral or aggregate free (control media and antibody) population ± standard error of mean. The value demonstrated represent a combined average of 3-4 experiments.

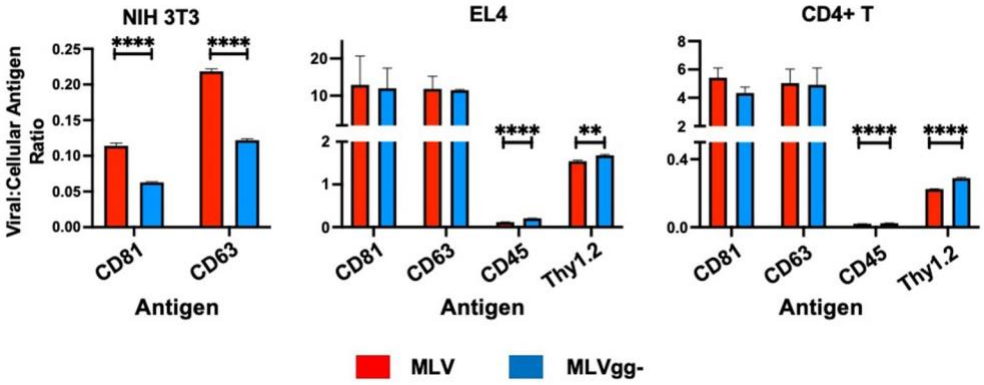

Figure 3.6 Surface antigen expression levels in the viral envelope relative to that of their infected cell of origin

Bar graphs of virus-to-cell surface antigen expression ratios and antigen expression differences between MLV and MLVgg- released from NIH 3T3, EL4 and primary CD4+ T cells. The median fluorescent intensity of antigens expressed on MLV and MLVgg- was divided by the median fluorescence intensity of cognate antigens expressed on their respective producer cell. Presented data was compiled from 3 experiments. Statistical analysis was performed with the multiple unpaired t test with Welch's correction. Significant antigen expression enrichment observed on the MLV relative to MLVgg- for NIH 3T3 cells for CD81 ($p<0.00001$) and CD63 ($p<0.00001$). In contrast, virus-to-cell surface antigen expression levels were found to be significantly enriched on the MLVgg- for: EL4 cells: CD45 ($p<0.00001$), Thy1.2 ($p<0.0001$); and primary CD4+ T cell cells: CD45 ($p<0.00001$) and Thy1.2 ($p<0.00001$).

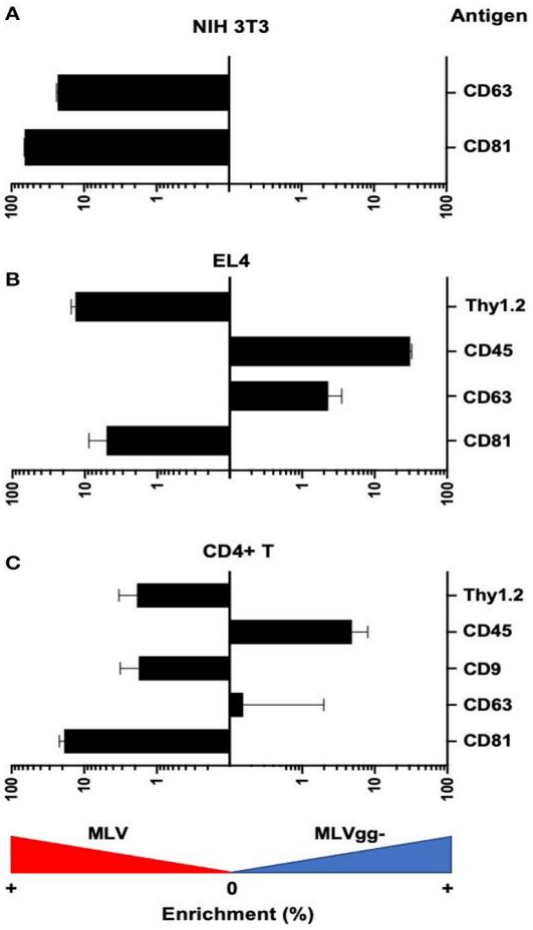

***Figure 3.7* Differences in antigen expression between MLV and MLVgg- virions released from different murine cells.**

Bar graph of the enrichment in surface antigen expression between MLV and MLVgg- released from A) NIH 3T3, B) EL4 and C) primary CD4+ T cells. Pooled median fluorescence intensity of antigens expressed on MLV was divided by the pooled median fluorescence intensity of antigens expressed on MLVgg-. Statistical analysis was performed with the Mann-Whitney test. Significant antigen enrichment observed on the MLV viral envelope relative to MLVgg- for virions released from NIH 3T3 cells: CD81 ($p<0.0001$), CD63 ($p<0.0001$); EL4 cells: CD81 ($p<0.0001$), CD63 ($p<0.0001$), Thy1.2 ($p<0.0001$); primary CD4+ T cells: CD81 ($p<0.0001$) and Thy1.2 ($p<0.001$). In contrast, CD45 was found to be significantly enriched in the MLVgg- viral envelope relative to MLV for virions released from EL4 cells ($p<0.0001$) and primary CD4+ T cell cells ($p<0.0001$). Results are displayed as median fluorescence intensity of gated viral population $\pm$ standard error margin. Presented data was compiled from 3-4 experiments.

3.5 Discussion

The aim of our study was to better understand host antigen uptake by retroviruses and the effect of glycoGag accessory protein on this process. We revealed that the abundance of antigen expression on the surface of a cell does not necessarily result in proportional expression on the surface of a retrovirus. An important challenge in this study was that the dynamic range for the detection of labelled antigens on a virus is limited by a much smaller surface area compared to that of a cell, thus resulting in poor sensitivity to detect antigens with very low levels of expression. This challenge is highlighted when a comparison between cellular and viral stainings is performed. For cells, we observed a ~ 2.5 log separation between the negative and positive populations for the most abundant antigens we tested. In contrast, for viral staining this was reduced to a ~1.5 log separation at most. For highly expressed cellular markers such as CD81 and Thy1.2, where the majority of the viral population was positively labeled, we report an even greater decrease in the ratio of separation between positive and negative signals relative to their cellular expression (Fig. 3).

In some cases, we detected highly expressed cell-derived markers on the virus surface in a proportion to antigen density on the cell. Interestingly, we also observed instances where there was either a relative enrichment of antigens on the surface of the virus compared to the cognate infected cell, or the opposite (Fig. 6). In particular, despite high expression on cells, we did not detect CD29 or LFA-1 in the viral envelope of virions released from NIH 3T3 or EL4 and primary CD4+ T cells (Fig. 4). Intriguingly, we revealed low levels of CD45 on MLV released from infected lymphocytes. This is in contrast to its absence from the HIV-1 envelope (25, 28, 29, 49, 50). CD45 is abundantly expressed on the surface of lymphocytes, covering as much as 10-25% of the total surface area (51). As such, if the viral egress mechanism was passive, a higher relative amount of virion incorporated CD45 antigen would be expected in the viral envelope. This was not the case in our findings. Taken together, these data indicate a selective process of host protein acquisition that can enrich or decrease the incorporation specific host-derived proteins found in the virus envelope. Prior studies have demonstrated that the site of retroviral egress on the cell surface, but also alternative egress pathways such as through the endosomal pathway, can influence the type and abundance of host antigens captured in the viral envelope (12, 18, 48, 52-54).

Next, we investigated the influence of glycoGag on host antigen incorporation in the viral envelope, specifically the uptake of lipid raft markers. However, due to low or absent expression of these markers on the cells analyzed in our study, we only measured a significant reduction of the lipid raft marker Thy1.2 on MLVgg- particles released from EL4 T lymphocytes and primary CD4+ T cells. We observed a similar amount of positive labelled Thy1.2 MLV and MLVgg- virions released from infected EL4 and primary CD4+ T cells. However, the increased antigen abundance observed on MLV compared to MLVgg- suggests that glycoGag promotes increased incorporation of Thy1.2, but it must also be considered that the site of egress for MLV virions could have higher Thy1.2 density. Yet, Thy1.2 expression on MLVgg- virions suggests that they egress at sites which Thy1.2 also partitions to and potentially highlights a role for Thy1.2 in viral replication (25, 28, 29, 49, 50). In contrast, we observed a significant enrichment of CD45 protein on MLVgg- particles compared to MLV virions (Fig. 7B-C and Table 4). This further supports previous findings, which showed that glycoGag directs viral egress at lipid raft rich microdomains that are generally very poor in CD45 (25, 28, 55).

Furthermore, the HIV-1 gag protein has been shown to induce lipid raft and TEM domain merging at the site of its viral assembly, while in the absence of viral infection these two domains are distinct (46). In addition, Gaudin et al. suggest that some types of retroviruses may induce a similar mechanism of coalescence as they showed labeled virions that were positive for both host-derived CD9 and the lipid raft marker cholera toxin B (40). As such, glycoGag could also induce a similar reorganization of cellular microdomains. We observed an enrichment of the tetraspanin markers on MLV compared to MLVgg- virions produced from 3T3 NIH cells. Similarly, we noted an increase of CD81 on MLV released from primary CD4+ T cells compared to MLVgg-. These observations highlight how expression of glycoGag influences the uptake of host proteins by viruses that are released from different cell types. Several studies show an effect by glycoGag on viral assembly and the modulation of host proteins to enhance viral pathogenicity (7, 8, 10-12, 15, 16, 37, 56, 57). GlycoGag's evident beneficial function *in vivo* is further supported by the reversion from a glycoGag-deficient phenotype back to wild-type (7, 14). Thus, this raises the intriguing possibility that the glycoGag protein has evolved functions to positively impact the incorporation of biologically significant cellular proteins to aid in its pathogenicity. Two important questions arise from our observations: 1) whether glycoGag reorganizes cellular microdomains at viral

assembly sites, and 2) what are the downstream pathways that govern glycoGag-induced cellular microdomain reorganization. These findings will provide the necessary information for elucidating the pathway by which glycoGag can selectively modulate the uptake of host protein incorporation.

3.6 Conclusion

We set out to detect and quantify host-derived antigens on the surface of Moloney MLV and investigate how the virus-encoded accessory protein glycoGag influences this uptake. Here, we revealed a high degree of viral diversity in antigen abundance on the viral envelope when comparing MLV wild-type and glycogag-deficient variants released from the three murine cell types tested in our study. As such, our analysis at the individual viral particle level shows the extent of viral phenotypic heterogeneity of cell-derived antigens, which this is further accentuated by the infected cell type. We uncovered the intriguing possibility that glycoGag protein plays a role in increasing the incorporation of select host-derived antigens during viral assembly and release. How this heterogeneity in host-derived antigen uptake influences infectivity, pathogenicity and immune escape still remains to be fully assessed.

Acknowledgements

M.M. holds a Queen Elizabeth II Graduate Scholarship in Science and Technology (QEII-GSST). M.-A.L. holds a Canada Research Chair in Molecular Virology and Intrinsic Immunity. This study was supported by a Discovery grant to M-A Langlois by the Natural Sciences and Engineering Research Council (NSERC) of Canada.

Conflicts of interest

The authors declare no competing interests.

Author contributions

M.M. performed the experiments, carried out the data analysis and drafted the manuscript. M.-A.L. designed the study, provided guidance, supervised the data analysis, and drafted the manuscript. All authors approved the submitted version.

3.7 References

1. Edwards SA, Fan H. gag-Related polyproteins of Moloney murine leukemia virus: evidence for independent synthesis of glycosylated and unglycosylated forms. J Virol. 1979;30(2):551-63.
2. Prats AC, De Billy G, Wang P, Darlix JL. CUG initiation codon used for the synthesis of a cell surface antigen coded by the murine leukemia virus. J Mol Biol. 1989;205(2):363-72.
3. Rosales Gerpe MC, Renner TM, Belanger K, Lam C, Aydin H, Langlois MA. N-linked glycosylation protects gammaretroviruses against deamination by APOBEC3 proteins. J Virol. 2015;89(4):2342-57.
4. Fujisawa R, McAtee FJ, Zirbel JH, Portis JL. Characterization of glycosylated Gag expressed by a neurovirulent murine leukemia virus: identification of differences in processing in vitro and in vivo. J Virol. 1997;71(7):5355-60.
5. Pillemer EA, Kooistra DA, Witte ON, Weissman IL. Monoclonal antibody to the amino-terminal L sequence of murine leukemia virus glycosylated gag polyproteins demonstrates their unusual orientation in the cell membrane. J Virol. 1986;57(2):413-21.
6. Renner TM, Belanger K, Lam C, Gerpe MCR, McBane JE, Langlois MA. Full-Length Glycosylated Gag of Murine Leukemia Virus Can Associate with the Viral Envelope as a Type I Integral Membrane Protein. J Virol. 2018;92(6).
7. Chun R, Fan H. Recovery of Glycosylated gag Virus from Mice Infected with a Glycosylated gag-Negative Mutant of Moloney Murine Leukemia Virus. J Biomed Sci. 1994;1(4):218-23.
8. Corbin A, Prats AC, Darlix JL, Sitbon M. A nonstructural gag-encoded glycoprotein precursor is necessary for efficient spreading and pathogenesis of murine leukemia viruses. J Virol. 1994;68(6):3857-67.
9. Fan H, Chute H, Chao E, Feuerman M. Construction and characterization of Moloney murine leukemia virus mutants unable to synthesize glycosylated gag polyprotein. Proc Natl Acad Sci U S A. 1983;80(19):5965-9.
10. Low A, Datta S, Kuznetsov Y, Jahid S, Kothari N, McPherson A, et al. Mutation in the glycosylated gag protein of murine leukemia virus results in reduced in vivo infectivity and a novel defect in viral budding or release. J Virol. 2007;81(8):3685-92.
11. Nitta T, Kuznetsov Y, McPherson A, Fan H. Murine leukemia virus glycosylated Gag (gPr80gag) facilitates interferon-sensitive virus release through lipid rafts. Proc Natl Acad Sci U S A. 2010;107(3):1190-5.
12. Nitta T, Tam R, Kim JW, Fan H. The cellular protein La functions in enhancement of virus release through lipid rafts facilitated by murine leukemia virus glycosylated Gag. mBio. 2011;2(1):e00341-10.
13. Schwartzberg P, Colicelli J, Goff SP. Deletion mutants of Moloney murine leukemia virus which lack glycosylated gag protein are replication competent. J Virol. 1983;46(2):538-46.
14. Stavrou S, Nitta T, Kotla S, Ha D, Nagashima K, Rein AR, et al. Murine leukemia virus glycosylated Gag blocks apolipoprotein B editing complex 3 and cytosolic sensor access to the reverse transcription complex. Proc Natl Acad Sci U S A. 2013;110(22):9078-83.
15. Ahi YS, Zhang S, Thappeta Y, Denman A, Feizpour A, Gummuluru S, et al. Functional Interplay Between Murine Leukemia Virus Glycogag, Serinc5, and Surface Glycoprotein Governs

Virus Entry, with Opposite Effects on Gammaretroviral and Ebolavirus Glycoproteins. mBio. 2016;7(6).
16. Li S, Ahmad I, Shi J, Wang B, Yu C, Zhang L, et al. Murine Leukemia Virus Glycosylated Gag Reduces Murine SERINC5 Protein Expression at Steady-State Levels via the Endosome/Lysosome Pathway to Counteract SERINC5 Antiretroviral Activity. J Virol. 2019;93(2).
17. Shi J, Xiong R, Zhou T, Su P, Zhang X, Qiu X, et al. HIV-1 Nef Antagonizes SERINC5 Restriction by Downregulation of SERINC5 via the Endosome/Lysosome System. J Virol. 2018;92(11).
18. Freed EO. HIV-1 assembly, release and maturation. Nat Rev Microbiol. 2015;13(8):484-96.
19. Renner TM, Tang VA, Burger D, Langlois MA. Intact Viral Particle Counts Measured by Flow Virometry Provide Insight into the Infectivity and Genome Packaging Efficiency of Moloney Murine Leukemia Virus. J Virol. 2020;94(2).
20. Tang VA, Renner TM, Fritzsche AK, Burger D, Langlois MA. Single-Particle Discrimination of Retroviruses from Extracellular Vesicles by Nanoscale Flow Cytometry. Sci Rep. 2017;7(1):17769.
21. Tang VA, Fritzsche AK, Renner TM, Burger D, Lannigan JA, Brittain GC, et al. Engineered Retroviruses as Fluorescent Biological Reference Particles for Nanoscale Flow Cytometry. bioRxiv. 2019:614461.
22. Tremblay MJ, Fortin JF, Cantin R. The acquisition of host-encoded proteins by nascent HIV-1. Immunol Today. 1998;19(8):346-51.
23. Burnie J, Guzzo C. The Incorporation of Host Proteins into the External HIV-1 Envelope. Viruses. 2019;11(1).
24. Cantin R, Methot S, Tremblay MJ. Plunder and stowaways: incorporation of cellular proteins by enveloped viruses. J Virol. 2005;79(11):6577-87.
25. Esser MT, Graham DR, Coren LV, Trubey CM, Bess JW, Jr., Arthur LO, et al. Differential incorporation of CD45, CD80 (B7-1), CD86 (B7-2), and major histocompatibility complex class I and II molecules into human immunodeficiency virus type 1 virions and microvesicles: implications for viral pathogenesis and immune regulation. J Virol. 2001;75(13):6173-82.
26. Jalaguier P, Cantin R, Maaroufi H, Tremblay MJ. Selective acquisition of host-derived ICAM-1 by HIV-1 is a matrix-dependent process. J Virol. 2015;89(1):323-36.
27. Lawn SD, Roberts BD, Griffin GE, Folks TM, Butera ST. Cellular compartments of human immunodeficiency virus type 1 replication in vivo: determination by presence of virion-associated host proteins and impact of opportunistic infection. J Virol. 2000;74(1):139-45.
28. Nguyen DH, Hildreth JE. Evidence for budding of human immunodeficiency virus type 1 selectively from glycolipid-enriched membrane lipid rafts. J Virol. 2000;74(7):3264-72.
29. Orentas RJ, Hildreth JE. Association of host cell surface adhesion receptors and other membrane proteins with HIV and SIV. AIDS Res Hum Retroviruses. 1993;9(11):1157-65.
30. Abdel-Mohsen M, Kuri-Cervantes L, Grau-Exposito J, Spivak AM, Nell RA, Tomescu C, et al. CD32 is expressed on cells with transcriptionally active HIV but does not enrich for HIV DNA in resting T cells. Science Translational Medicine. 2018;10(437).
31. Ding L, Derdowski A, Wang JJ, Spearman P. Independent segregation of human immunodeficiency virus type 1 Gag protein complexes and lipid rafts. J Virol. 2003;77(3):1916-26.

32. Graham DR, Chertova E, Hilburn JM, Arthur LO, Hildreth JE. Cholesterol depletion of human immunodeficiency virus type 1 and simian immunodeficiency virus with beta-cyclodextrin inactivates and permeabilizes the virions: evidence for virion-associated lipid rafts. J Virol. 2003;77(15):8237-48.
33. Waheed AA, Freed EO. The Role of Lipids in Retrovirus Replication. Viruses. 2010;2(5):1146-80.
34. Chaudhuri R, Lindwasser OW, Smith WJ, Hurley JH, Bonifacino JS. Downregulation of CD4 by human immunodeficiency virus type 1 Nef is dependent on clathrin and involves direct interaction of Nef with the AP2 clathrin adaptor. J Virol. 2007;81(8):3877-90.
35. Garcia JV, Miller AD. Serine phosphorylation-independent downregulation of cell-surface CD4 by nef. Nature. 1991;350(6318):508-11.
36. Haller C, Muller B, Fritz JV, Lamas-Murua M, Stolp B, Pujol FM, et al. HIV-1 Nef and Vpu are functionally redundant broad-spectrum modulators of cell surface receptors, including tetraspanins. J Virol. 2014;88(24):14241-57.
37. Ahi YS, Yimer D, Shi G, Majdoul S, Rahman K, Rein A, et al. IFITM3 Reduces Retroviral Envelope Abundance and Function and Is Counteracted by glycoGag. mBio. 2020;11(1).
38. Lippe R. Flow Virometry: a Powerful Tool To Functionally Characterize Viruses. J Virol. 2018;92(3).
39. Morales-Kastresana A, Telford B, Musich TA, McKinnon K, Clayborne C, Braig Z, et al. Labeling Extracellular Vesicles for Nanoscale Flow Cytometry. Sci Rep. 2017;7(1):1878.
40. Gaudin R, Barteneva NS. Sorting of small infectious virus particles by flow virometry reveals distinct infectivity profiles. Nat Commun. 2015;6:6022.
41. Langlois MA, Kemmerich K, Rada C, Neuberger MS. The AKV murine leukemia virus is restricted and hypermutated by mouse APOBEC3. J Virol. 2009;83(22):11550-9.
42. Tsuruyama T, Liu W, Yoshikawa K. In vitro murine leukemia retroviral integration and structure fluctuation of target DNA. PLoS One. 2012;7(2):e31533.
43. Brittain GCt, Chen YQ, Martinez E, Tang VA, Renner TM, Langlois MA, et al. A Novel Semiconductor-Based Flow Cytometer with Enhanced Light-Scatter Sensitivity for the Analysis of Biological Nanoparticles. Sci Rep. 2019;9(1):16039.
44. Forster F, Medalia O, Zauberman N, Baumeister W, Fass D. Retrovirus envelope protein complex structure in situ studied by cryo-electron tomography. Proc Natl Acad Sci U S A. 2005;102(13):4729-34.
45. Yeager M, Wilson-Kubalek EM, Weiner SG, Brown PO, Rein A. Supramolecular organization of immature and mature murine leukemia virus revealed by electron cryo-microscopy: implications for retroviral assembly mechanisms. Proc Natl Acad Sci U S A. 1998;95(13):7299-304.
46. Hogue IB, Grover JR, Soheilian F, Nagashima K, Ono A. Gag induces the coalescence of clustered lipid rafts and tetraspanin-enriched microdomains at HIV-1 assembly sites on the plasma membrane. J Virol. 2011;85(19):9749-66.
47. Molle D, Segura-Morales C, Camus G, Berlioz-Torrent C, Kjems J, Basyuk E, et al. Endosomal trafficking of HIV-1 gag and genomic RNAs regulates viral egress. J Biol Chem. 2009;284(29):19727-43.
48. Morita E, Sundquist WI. Retrovirus budding. Annu Rev Cell Dev Biol. 2004;20:395-425.

49. Arakelyan A, Fitzgerald W, Margolis L, Grivel JC. Nanoparticle-based flow virometry for the analysis of individual virions. J Clin Invest. 2013;123(9):3716-27.
50. Trubey CM, Chertova E, Coren LV, Hilburn JM, Hixson CV, Nagashima K, et al. Quantitation of HLA class II protein incorporated into human immunodeficiency type 1 virions purified by anti-CD45 immunoaffinity depletion of microvesicles. J Virol. 2003;77(23):12699-709.
51. Hořejší V. The leucocyte Antigen FactsBook. Immunol Today. 1998;2nd Edition.
52. Dowlatshahi DP, Sandrin V, Vivona S, Shaler TA, Kaiser SE, Melandri F, et al. ALIX is a Lys63-specific polyubiquitin binding protein that functions in retrovirus budding. Dev Cell. 2012;23(6):1247-54.
53. Leung K, Kim JO, Ganesh L, Kabat J, Schwartz O, Nabel GJ. HIV-1 assembly: viral glycoproteins segregate quantally to lipid rafts that associate individually with HIV-1 capsids and virions. Cell Host Microbe. 2008;3(5):285-92.
54. Ashok A, Hegde RS. Prions and retroviruses: an endosomal rendezvous? EMBO Rep. 2006;7(7):685-7.
55. Liao Z, Cimakasky LM, Hampton R, Nguyen DH, Hildreth JE. Lipid rafts and HIV pathogenesis: host membrane cholesterol is required for infection by HIV type 1. AIDS Res Hum Retroviruses. 2001;17(11):1009-19.
56. Pizzato M. MLV glycosylated-Gag is an infectivity factor that rescues Nef-deficient HIV-1. Proc Natl Acad Sci U S A. 2010;107(20):9364-9.
57. Wu Y, Olety B, Weiss ER, Popova E, Yamanaka H, Gottlinger H. Potent Enhancement of HIV-1 Replication by Nef in the Absence of SERINC3 and SERINC5. mBio. 2019;10(3).

4 Chapter 4: Seasonal human coronaviruses OC43, 229E, and NL63 induce cell surface modulation of entry receptors and display host cell-specific viral replication kinetics. (Published)

Preface: This chapter has been previously published as a research article.

*Siragam V., *Maltseva M., Castonguay N., Galipeau Y., Srinivasan M., Soto J., Dankar S., Langlois M-A. (2024), **Seasonal human coronaviruses OC43, 229E, and NL63 induce cell surface modulation of entry receptors and display host cell-specific viral replication kinetics.** ***Microbiology Spectrum***, 12:e04220-23.https://doi.org/10.1128/spectrum.04220-23

4.1 Abstract

The emergence of the COVID-19 pandemic prompted an increased interest in seasonal human coronaviruses. OC43, 229E, NL63, and HKU1 are endemic seasonal coronaviruses that cause the common cold and are associated with generally mild respiratory symptoms. In this study, we identified cell lines that exhibited cytopathic effects (CPE) upon infection by three of these coronaviruses and characterized their viral replication kinetics and the effect of infection on host surface receptor expression. We found that NL63 produced CPE in LLC-MK2 cells, while OC43 produced CPE in MRC-5, HCT-8, and WI-38 cell lines, while 229E produced CPE in MRC-5 and WI-38 by day 3 post-infection. We observed a sharp increase in nucleocapsid and spike viral RNA (vRNA) from day 3 to day 5 post-infection for all viruses; however, the abundance and the proportion of vRNA copies measured in the supernatants and cell lysates of infected cells varied considerably depending on the virus-host cell pair. Importantly, we observed modulation of coronavirus entry and attachment receptors upon infection. Infection with 229E and OC43 led to a downregulation of CD13 and GD3, respectively. In contrast, infection with NL63 and OC43 leads to an increase in ACE2 expression. Attempts to block entry of NL63 using either soluble ACE2 or anti-ACE2 monoclonal antibodies demonstrated the potential of these strategies to greatly reduce infection. Overall, our results enable a better understanding of seasonal coronaviruses infection kinetics in permissive cell lines and reveal entry receptor modulation that may have implications in facilitating co-infections with multiple coronaviruses in humans.

Importance: Seasonal human coronavirus is an important cause of the common cold associated with generally mild upper respiratory tract infections that can result in respiratory complications for some individuals. There are no vaccines available for these viruses, with only limited antiviral therapeutic options to treat the most severe cases. A better understanding of how these viruses interact with host cells is essential to identify new strategies to prevent infection-related complications. By analyzing viral replication kinetics in different permissive cell lines, we find that cell-dependent host factors influence how viral genes are expressed and virus particles released. We also analyzed entry receptor expression on infected cells and found that these can be up- or down-modulated depending on the infecting coronavirus. Our findings raise concerns over the possibility of infection enhancement upon co-infection by some coronaviruses, which may facilitate genetic recombination and the emergence of new variants and strains.

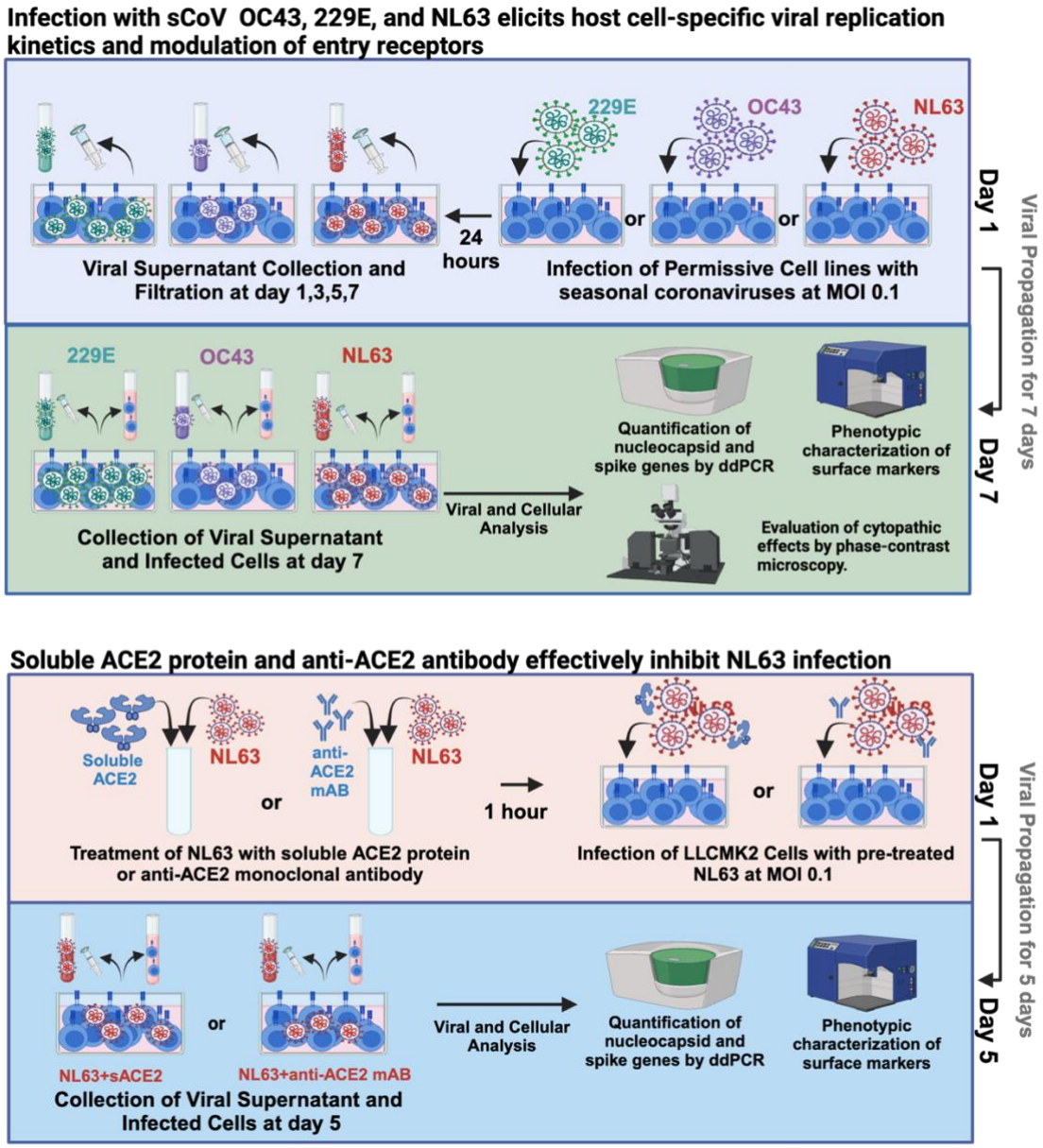

4.2 Introduction:

Human coronaviruses (HCoVs) OC43, 229E, NL63, and HKU1 are seasonal endemic viruses circulating worldwide that cause mostly non-severe upper tract respiratory infections (1–5). It is estimated that they account for 15%–30% of all the common cold cases (6). Epidemiological studies on respiratory infections have reported that OC43 is the most prevalent strain in humans followed by NL63, 229E, and HKU1 (7–9). While HCoVs generally cause mild symptoms in healthy individuals, some reports have shown that NL63 and 229E can cause life-threating respiratory problems, such as pneumonia, leading to respiratory distress syndrome in immunocompromised individuals (10, 11).

Phylogenetically, OC43 and HKU1 belong to the betacoronavirus genus that includes highly pathogenic coronaviruses such as MERS-CoV, SARS-CoV, and SARS-CoV-2. Coronaviruses 229E and NL63, both belong to the alphacoronavirus genus (12). OC43, 229E, and NL63 use different viral attachment and entry receptors including peptidases, cell adhesion molecules, and sugars. In the case of 229E, the cellular receptor is CD13 (aminopeptidase N), while OC43 and HKU1 both bind sialic acid (9-O-acetylated ganglioside; GD3) for cell attachment, and HKU1 uses the protease TMPRSS2 as its protein receptor (12–15). NL63 makes use of heparin sulfate for cell attachment and angiotensin-converting enzyme 2 (ACE2) for cell entry, while the protein receptor for OC43 has still not been identified (16, 17). Of interest, previous studies have reported the inhibitory role of soluble ACE2 (sACE2) to prevent SARS-CoV-2 infection, which also shares ACE2 as an entry receptor with NL63 (18). However, the blocking effect of sACE2 or monoclonal ACE2 antibody therapy for NL63 infections has not been reported. Alternatively, interferons as potential antiviral regulators against OC43 and 229E infections have been recently studied (19). Although some antiviral drugs such as the RNA-dependent RNA polymerase inhibitor remdesivir and the protease inhibitor nirmatrelvir can inhibit OC43, 229E, and NL63 in laboratory assays (20–22), these are not commonly prescribed to infected patients. In fact, there are very few antiviral drugs and no vaccines for common cold coronaviruses (23).

Although seasonal coronaviruses have been studied using animal models (24), most of our knowledge of these viruses has been acquired using cell line models (4, 25– 27). Cell lines of various types and animal origins have been used to understand the mechanism of virus entry into cells (15, 17, 28), viral replication (4, 29), cytopathic effects (CPE) (26, 30), and to test the neutralizing ability of antibodies (31). While viral replication and pathogenesis have been

extensively characterized for highly pathogenic coronaviruses like SARS-CoV-2, there is a gap in knowledge of HCoV viral replication kinetics in permissive cell lines and their effects on the host cells. In this study, we identified permissive cell lines susceptible to cytopathic effects upon OC43, 229E, and NL63 infection and then characterized replication kinetics in these cells by tracking vRNA transcripts coding for the nucleocapsid (N) and spike (S) proteins. We also investigated the modulation of key cell receptors and attachment markers following infection. Finally, we tested the effects of soluble ACE2 and anti-ACE2 monoclonal antibodies at blocking NL63 infection. This detailed study of HCoV infection provides a better understanding of the replication and infection of these viruses in cell culture models which can help prompt the development of treatments, antivirals, and cures for the common cold.

4.3 Materials and Methods

Cell culture

HCT-8 cells (human ileocecal adenocarcinoma; ATCC/CCL-244), HEK 293T cells (human embryonic kidney; CRL-3216/ATCC), HEK293/ACE2-stable cell line (HEK293 cells stably expressing angiotensin-converting enzyme 2; BEI Resources/NR-52511) were grown in RPMI-1640 medium supplemented with 100 units/mL penicillin (P), 100 µg/mL streptomycin, and 10% FBS. MRC-5 cells (human lung fibroblasts; CCL-17/ATCC), WI-38 cells (human fetal lung; CCL-75/ATCC), Vero E6 cells (African green monkey kidney cells; CRL-1586/ATCC), and Calu-3 cells (human non-small-cell lung adenocarcinoma; HTB-55/ATCC) were grown in DMEM (MUTICELL#319-005-CL) medium supplemented with 100 units/mL penicillin, 100 µg/mL streptomycin, and 10% FBS. BEAS-2B cells (human bronchial epithelial; CRL-9609ATCC) were grown in bronchial epithelial cell growth basal media (Lonza/CC-3170). LLC-MK-2 cells (rhesus monkey kidney; CCL-7/ ATCC) were cultured in MEM (GIBCO #11095-080) supplemented with 100 units/mL penicillin and 100 µg/mL streptomycin (P/S), 2 mM L-glutamine, 1× non-essential amino acids (NEAA), and 3% FBS. All cell lines were cultured in a ventilate T-75 flask at 37°C in a 5% CO_2 humidified incubator. All cell lines were tested for mycoplasma contamination and remained negative.

Seasonal virus strains and stock propagation

Virus strains were obtained from ATCC and were used to infect their recommended permissive cell line. 229E (stock, VR-740/ATCC) was propagated on MRC-5 cells, OC43 (CR-1558/ATCC) on HCT-8 cells, and NL63 (BEI Resources/NR-470) on LLC-MK2 cells. The permissive host cells (MRC-5, or HCT and LLC MK2) were maintained at a confluency of 80%–90% 24–48 hours prior to infection. The cells were infected with a multiplicity of infection (MOI) of 0.1 or 0.01 at 35°C for 229E, 33°C for OC43, and 34°C for NL63 for 1 hour for virus adsorption with rocking every 10–20 minutes. The virus culture media for 229E (DMEM + 3% FBS + 1% P/S), OC43 (RPMI + 3% FBS + 1% P/S), and NL63 (MEM + 3% FBS + 1% P/S) were added to the dish (e.g., 1 mL per 25 cm^2) to stop the virus adsorption. Viruses were harvested by scrapping the infected cells with a

cell scrapper followed by centrifugation at 500 × *g* for 10 minutes. The supernatant was collected in aliquots and quickly frozen at −80°C.

TCID50 and CPE assays

Virus titers of 229E, or OC43 and NL63 were determined by tissue culture infection dose 50 ($TCID_{50}$) assay on their ATCC-recommended cell lines. MRC-5 (20,000 cells), HCT-8 cells (100,000 cells), and LLC-MK2 cells (300,000 cells) were seeded at their respective densities in 48-well plate (Fig. 1). The cells were checked for confluency (70%–80%), and the virus dilutions (10-fold serial dilution) were performed. Cell culture media (360 µL) were added to each well, and 40 µL of the virus dilution (10-fold) was added to each well. Mock represents the negative control having media only. The plates were incubated at their respective temperatures (229E at 35°C; OC43 at 33°C; NL63 at 34°C/5% CO_2). The plates were shaken every 20 minutes. After 1–2 hours of incubation, media were removed, and 400 µL of the culture media supplemented with 1× DMEM-high glucose + 10% BSA + 100× NEAA + 100× (100 mM) sodium pyruvate + 100× (200 mM) L-glutamine, 100× penicillin (10,000 units/mL)-streptomycin (10,000 µg/mL), and TPCK-treated trypsin (0.5 µg/mL) was added. $TCID_{50}$ of the viruses was calculated according to Reed-Muench method (32). Based on virus titers ($TCID_{50}$) and cell number, multiplicities of infection were determined for the infection experiments.

All cell lines detailed in **Table 1** were tested for cytopathic effects following infection at an MOI of 0.1 by all three HCoVs studied here. The cells were observed daily for CPE following infection under a ZOE Cell Imager (BIO-RAD/1450031) using its phase-contrast setting to monitor cell rounding, clumping, and detachment 3 days post-infection (dpi). CPE was rated empirically by operator-perceived intensity of cellular deformation and detachment: +, less than 20% cell detachment and mild morphological changes start to appear; ++, 20%–60% cell detachment and clear morphological changes in most cells; +++, 60%–100% cell detachment and severe morphological changes.

HCoV infection and RNA extraction

MRC-5, HCT-8, and LLC-MK2 cell lines were cultured to reach 60%–80% confluence in 6-well plates. The following day, cell lines were inoculated with their respective virus strains at MOI 0.01 and 0.1. Virus adsorption was done for 1 hour at 35°C (229E virus), 33°C (OC43 virus), or 34°C (NL63) followed by the addition of the respective virus culture media. Cells were infected with their respective virus strains and further incubated for the following days to monitor the infection

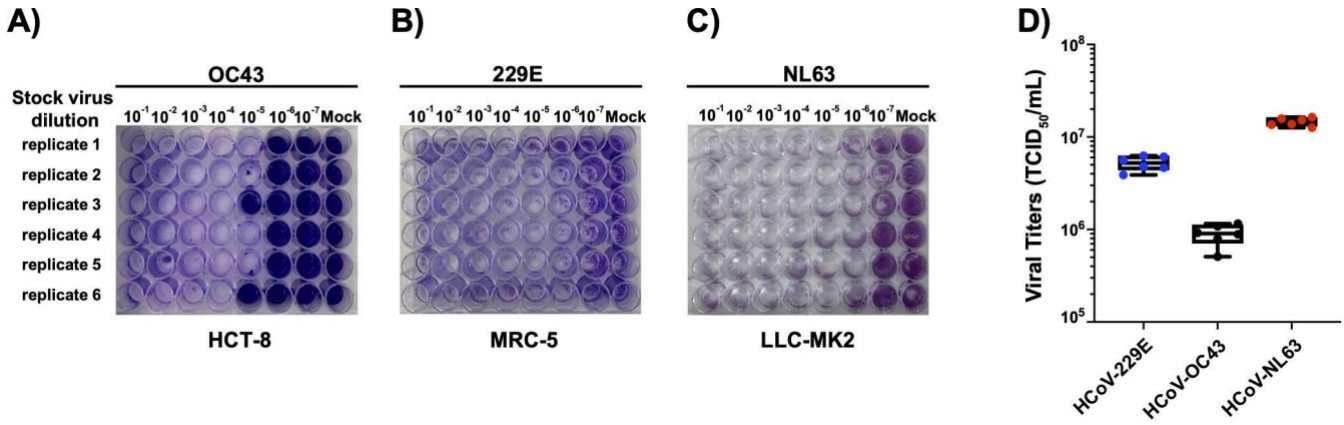

Figure 4.1 OC43, 229E, and NL63 titration by $TCID_{50}$.

(A) HCT-8 cells, **(B)** MRC-5 cells, and **(C)** LLC-MK2 were grown in 48-well tissue culture plates under standard conditions. When the cells **(A–C)** were confluent (75%), the media were removed, and the cells were infected with seven different 10-fold dilutions (10^{-1}–10^{-7}) of OC43 virus (HCT-8), 229E virus (MRC-5), or NL63 virus (LLC-MK2). The cytopathic effect in the wells was monitored for 7 days under a ZOE Cell Imager. A significant CPE is noted as cell death and disturbed cell morphology. The number of wells with CPE (empty wells) and without CPE (filled with crystal violet stain) was counted according to Reed and Muench method (31). **(D)** Shows the calculation of viral $TCID_{50}$ titers. Each individual data point in D represents a viral $TCID_{50}$ titer calculation from one of six biological replicates for each virus (229E, OC43, and NL63). The $TCID_{50}$ titer is the average of the six biological replicates.

Table 4.1 Susceptibility of various cell lines to CPE following infection by HCoVs

Cell line tested	Cell type	Human coronavirus tested	Intensity of CPE at day 3 pi[a]
BEAS-2B	Human bronchial	OC43	−
		229E	−
		NL63	−
Calu-3	Human lung cancer	OC43	−
		229E	−
		NL63	−
HCT-8	Human colon cancer	OC43	+
		229E	−
		NL63	−
LLC-MK2	Rhesus monkey kidney cells	OC43	−
		229E	−
		NL63	++
MRC-5	Human fetal lung	OC43	+++
		229E	+
		NL63	−
Vero E6	ıfrican green monkey kidney	OC43 229E	±** −
		NL63	−
WI-38	Human fetal lung	OC43	+++
		229E	++
		NL63	−
293T and 293T ACE2	Human embryonic kidney	OC43 229E	− −
		NL63	−

[a]Infection was confirmed by detection of both S and N by droplet digital PCR. Infection was performed at an MOI of 0.01. CPE was assessed by phase-contrast light microscopy. +, less than 20% cell detachment and mild morphological changes start to appear; ++, 20%–60% cell detachment and clear morphological changes in most cells; +++, 60%–100% cell detachment and severe morphological changes; **, very mild CPE at 3 dpi was inconsistent across biological replicates (n = 3).

and CPE (Table 1): 7 days for OC43, 5–7 days for 229E, and 7–10 days for NL63. HCoV-infected cells were examined under ZOE Cell Imager for the CPE formation followed by total vRNA extraction (QIAamp vRNA Mini Kit [Qiagen # 52904]) from culture supernatants and cell lysates along with uninfected cells (control mock) on different dpi (1–5). Absolute quantification of vRNA

copies of N and S for OC43, 229E, or NL63 viruses was determined by Bio-Rad one-step reverse transcription droplet digital PCR (RT-ddPCR).

RT-ddPCR on vRNA

Duplex, probe-based, one-step RT-ddPCR (1-Step RT-ddPCR Advanced Kit for Probes, Bio-Rad, Hercules, CA) was used to determine the absolute quantification of N and S vRNA copy numbers in culture supernatants and cell lysates using the OC43, 229E, or NL63 primer-probe sets, and 18S was used as reference gene control to normalize the levels of intracellular vRNA. Primers and probes used in this study were synthesized by Integrated DNA Technologies, Inc (IDT, Kanata, Canada) (Table 2). For all the experimental samples, a master mix for each virus (e.g., OC43, or 229E, or NL63) was prepared having 5.5 µL One-Step RT-ddPCR advanced supermix, 2.2 µL RT, 1.1 µL DTT, 1.1 µL (250 nM) 20× primer/probe, 5.5 µL RNA template, and 6.6 µL RNase-free water to make a total reaction volume of 22 µL. The blank for the RNA extraction control is nuclease-free water. Mock-uninfected and -infected samples were included with three biological replicates. The reactions were then emulsified by using a QX200 droplet generator (Bio-Rad, Hercules, CA). Droplets that are generated were transferred to a new microplate, and PCR was performed in a thermocycler C1000 (Bio-Rad, Hercules, CA). The reaction conditions for target gene N and S were as follows: reverse transcription step was performed at 50°C, for 60 minutes, followed by polymerase activation at 95°C/10 minutes, and 39 cycles of denaturation at 95°C/30 s, annealing/extension at 55°C/60 s (target gene N), or 60°C/60 s (target gene S), respectively. Deactivation of polymerase was done at 98°C for 10 minutes, and droplets were stabilized at 4°C for 30 minutes. Droplets were then read by a Bio-Rad two-channel automated QX200 droplet reader. The results were then analyzed by QuantaSoft Analysis Pro v.1.0 (Bio-Rad, Hercules, CA). VRNA levels of target genes N or S were normalized to 18S. In this article, the data from the ddPCR experiments are presented as vRNA genome copies per microliter (VRG) of reaction mix calculated from the number of positive and negative droplets in the samples based on the following equation (33).

Table 4.2 Primers and probes used for ddPCR

Target gene	Forward primer	Reverse primer	Probe
N OC43	5′-GGCGCAATTAGGTTTGACAG-3′	5′-TCCTCTGCAGTCAACTCTCT-3′	′−6 FAM/TG CCC AAA A/ZEN/G CCG CGT GCA G/3′IABkFQ
N 229E	5′-ACTTTGGAAGTGCAGGTGTT-3′	5′-AAGGTGATGGTCTTTGGG-3′	′−6 FAM/TG AGC TTG T/ZEN/G CCG TCA ACA GCT GC/3′IABkFQ
N NL63	5′-ATAAGCCTCTTTCTCAACCCAG-3′	5′-ATCACGAGGACCAAAGCAC-3′	′−6 FAM/AA ACC TCG T/ZEN/T GGA AGC GTG TTC CT/3′IABkFQ
RBD OC43	5′-TCTTTAGTTGGCATAGGTGAGC-3′	5′-GGTCGGCAAGTACAAGAATTG-3′	′−6 FAM/AC TGT TCG G/ZEN/G TCT TGC TGT TAA AAG TGA/3′IABkFQ
RBD 229E	5′-CCTGTTGAGGGTGTTAGTTCC-3′	5′-GTTACCTGAAGTTGATGTGTACG-3′	′−6 FAM-TC TGG TGT G/ZEN/G GTG TTA TTC GCG T/3′IABkFQ
RBD NL63	5′-CTTGGTTTTAAAAATGTTTCCACTGG-3′	5′-TGTAGTAAGTTTTGCAAGCCATATC-3′	′−6 FAM/TG GTG CCA T/ZEN/G ACC GCT GTT AAT GA/3′IABkFQ
18S	5′-CGCCGCTAGAGGTGAAATTCT-3′	5′-CATTCTTGGCAAATGCTTTCG-3′	′-HEX/AA GTG GAC T/ZEN/C ATT CCA ATT ACA GGG CCT/3′IABkFQ

Detection of surface markers and receptors by flow cytometry following coronavirus infection

Permissive cells (MRC-5, HCT-8, and NL63) were cultured in 6-well plate to attain 75% confluency. Cells were infected at an MOI of 0.1. Five days post-infection, cells were harvested to prepare single-cell suspension by lifting the cells with 5 mM EDTA followed by centrifugation at 500 × *g* for 5 minutes, and 0.5 × 10^6 cells were aliquoted per FACS tube. The following antibodies and isotypes were used to quantify the surface marker expression and receptor modulation in the uninfected (control) and infected cells: PE anti-human CD13, anti-human CD147 (isotype-control antibody mouse IgG1 κ, BioLegend); and anti-human CD326 (isotype-control antibody mouse IgG2a κ; BioLegend); human anti-ACE2 antibody (isotype-control antibody Goat IgG; R&D Systems) and anti-GD3, 9-O-acetyl (clone UM4D4; isotype-control antibody mouse IgM κ; Millipore Sigma). Cells were stained with CD13, CD147, CD326, ACE2, and GD3 antibodies, and their corresponding isotypes were incubated for 30 minutes on ice followed by washing with 0.2% BSA-PBS two times. Cells stained with anti-ACE2 and anti-GD3 were further incubated with secondary antibodies Alexa Fluor 488-labeled sheep anti-goat and goat anti-mouse (Invitrogen) for 30 minutes. After incubation, cells were washed twice with 0.2% BSA-PBS, resuspended in 2% BSB-PFA, and analyzed by Flow Cytometry on BD Celesta instrument (Beckman Coulter) using FlowJo software. Flow cytometry data were further analyzed using FlowJo Software v.10.7.1 (FlowJo, Ashland, OR). For cell analysis, SSC-area vs FSC-area followed by FSC-height vs FSC-area and SSC-area vs FSC-area were used to exclude cell aggregates and debris. Live/dead stain BV421 dye was used to exclude dead cells from analysis.

Blocking of NL63 infection by soluble ACE2 and monoclonal anti-ACE2 antibody

LLC MK2 cells were seeded in 48-well plates (5 × 10^5 cells per well) in MEM medium containing 3% FBS. Prior to incubation of soluble ACE2 (National Research Council Canada) with NL63 virus on LLC MK2 cells, the following dilution of sACE2 and NL63 virus was prepared. sACE2 (5 or 15 mg) or control protein OVA albumin (Sigma/A5503) was mixed with NL63 virus at MOI 0.1 (1:1) in a final volume of 100 µL in a separate 48-well plate in MEM medium (3% FBS) at 37°C for 30 minutes. After incubation, the sACE2 + NL63 virus mixture was added to the host cells LLC MK2 (24 hours post-seeding) and incubated at 34°C for a second incubation for 24 hours. The following day, the treated LLC MK2 cells were washed with PBS and replaced with infection media (MEM 3% FBS), and cells were monitored to check the blocking effect on NL63 infection until 7 dpi. At the end point day 7, the culture supernatants and cell lysates are harvested to measure the vRNA copies of N and S by ddPCR following vRNA extraction. In a similar approach to monitor the blocking effect on NL63 infection using anti-ACE2 (human), monoclonal blocking antibody that recognizes ACE2 (AdipoGen Life Sciences#AC384), host LLC MK2 cells (48-well plate, 5 × 10^5 cells/well) were incubated with human ACE2 monoclonal blocking antibody (10, 40, and 120 µg/mL) or unrelated control antibody (40 µg/mL; anti-DC-SIGN) for 1–2 hours with intermittent shaking followed by the addition of NL63 virus (MOI #0.1) in a final volume of 100 µL per well at 34°C. After 24 hours post-infection, cells were washed with PBS and replaced with infection media (3%).

Statistical analysis

Statistical analyses were performed with multiple unpaired *t*-test with Welch's correction, and unpaired Mann-Whitney test was performed using GraphPad Prism (GraphPad Software, San Diego, CA version 9.5.1)

4.4 Results

Characterization of cell lines and evaluation of cytopathic effects

We selected a number of cell lines that were previously reported in the literature to be permissive to infection and viral replication of HCoVs (Table 1) (4, 25, 27, 29, 34). Our first objective was to identify the cell lines most susceptible to infection by HCoV and that also display cytopathic effects within a short 3-day time frame. We infected these cells with the three most prevalent HCoVs, OC43, 229E, and NL63, and assessed which ones displayed CPE that resulted in morphological changes and dysmorphic appearances in the cell monolayer with disturbed cell-to-cell aggregates or clumps after 3 days. The intensity of CPE, ranging from − to +++, was determined empirically by phase-contrast microscopy. Cells exhibiting CPE were tested by ddPCR to confirm the expression of S and N vRNAs. We used a $TCID_{50}$ assay (Fig. 1) to determine the viral titers for the infections by taking into consideration the number of wells with and without CPE based on the methodology of Reed and Muench (32). Permissive cell lines identified in this study are HCT-8 (human colon cancer), MRC-5 (human fetal lung), LLC-MK2 (Rhesus monkey kidney), and WI-38 (human fetal lung). Infection of HCT-8, WI-38, and MRC-5 with OC43 virus showed apparent CPE at day 3 pi with complete disturbance (+++) of the cell monolayer at day 5 pi (Fig. 2A, D, and G). MRC-5 and WI-38 cells infected with 229E showed increasing CPE from day 3 pi (Fig. 3A and D). Similarly, LLC-MK2 cells also started to display CPE upon NL63 infection from day 3 pi (Fig. 4A). At day 5 pi, the infected LLC-MK2 cells showed aggregation. We also assessed infection of MRC-5, WI-38, and HCT-8 cells infected with NL63; however, no CPE or viral replication was measured in these cells, in agreement with the previous reports (25).

Characterization of OC43, 229E, and NL63 viral replication kinetics

The culture supernatants and the cell lysates of permissive cells were infected with OC43, 229E, and NL63 at an MOI of 0.01 and were harvested at days 1, 3, and 5 post-infection. For OC43 with MRC-5 and WI-38 (Fig. 2B, C, E, F, H, and I), 229E (Fig. 3B, C, E, and F), and NL63 (Fig. 4B and C), cell lysates show similar or higher vRNA copies of N and S in comparison to supernatants. However, for OC43 propagation in HCT-8 cells, we observe higher vRNA copies of N and S in the culture supernatant than in the cell lysate (Fig. 2B and C). We also see in these cells an increase in OC43 N and S vRNA copies starting from day 3 to day 5 post-infection and a drop in S vRNA levels in the lysates for HCT-8 at day 5 pi (Fig. 2B and C), possibly due to advanced cell death.

Considering data from previous reports of NL63 infection in LLC-MK2 cells, the lower NL63 N and S vRNA levels detected in the supernatants compared to the lysates may be due to inefficient release of virions in the supernatants (17, 29, 35). Also, total vRNA copies detected varied depending on the cell types tested. For OC43 and 229E, WI-38 appeared the most favorable cell line for vRNA N expression, with ranges above 10^6 copies/mL for OC43 and above 10^5 copies/mL for 229E in the lysates at day 7 (Fig. 2E and 3E). Additionally, for all conditions tested, except infection of MRC-5 by 229E (Fig. 3B and C) and LLC-MK2 infection by NL63 (Fig. 4B and C), N vRNA levels are consistently several logs higher than S levels. For these combinations of virus and cells, it was the opposite where S transcripts were more abundant than N. Overall, the results show that HCoV displays variable replication kinetics depending on the specific virus and permissive host cell combination.

Cell surface marker expression on HCT-8 cells following OC43 infection

Here, we characterized surface expression of GD3, CD13, CD147, CD326, and ACE2 protein on HCT-8 prior and after infection with OC43. We measured receptor expression as the percentage of total cells expressing a given receptor, and we also measured the mean fluorescence intensity (MFI) emitted from all positive cells. CD13 (aminopeptidase N; APN) is the main surface protein receptor for 229E infection and is highly expressed on respiratory epithelial cells (12, 36). ACE2 is the primary receptor for NL63, and SARS-CoV and SARS-CoV-2 (16, 37, 38). CD147 is a transmembrane glycoprotein expressed on epithelial and immune cells that is proposed to be an alternative receptor for SARS-CoV and SARS-CoV-2 infection (39, 40). It is unknown if CD147 plays a role in NL63 entry. CD326 is a marker of colon carcinoma cells; it is known to be highly expressed on HCT-8 cells and is used in our study as a control that is unlikely to be affected by infection. OC43 binds to 9-*O*-acetylated sialic acid attached to oligosaccharide molecules located on glycoproteins on the surface of cells (14, 41). As such, this virus does not have a known specific protein surface receptor. However, ganglioside GD3 (9-*O*-acetyl-GD3) can be used by OC43 as a cellular entry receptor and is highly expressed in human leukemia cells (42).

Our assays detected low expression (8%) of GD3 in uninfected HCT-8 cells (Fig. 5A and D). We present the data as a scatter plot of a single representative assay (Fig. 5A and B) and the compiled data summary of two-three biological repeats (Fig. 5D and E). Histogram plots of stained

uninfected and infected cells relative to the corresponding isotype controls: IgG1 (CD13 and CD147) and IgG2b (CD326) and goat IgG (ACE2) are presented in Fig. 5C. After infection of HCT-8, significantly fewer cells expressed the OC43 attachment receptor GD3 (2% of total), and those that did expressed less of it as shown by a reduction of about twofold in MFI (Fig. 5D and E). We also detected expression of CD147 (100%) and CD326 (100%) surface antigens in all cells, and lower levels of CD13 (12%) and ACE-2 (17%) expression (Fig. 5A and D). Expression profiles detected for these antigens are in-line with previous observations made on colon tissues (43–47). Interestingly, infection with OC43 leads to a significant upregulation of ACE2 expression (30%) when compared to uninfected cells (Fig. 5D and E). In contrast, we observed significant downregulation of CD326 MFI following infection (Fig. 5E), while there were no differences in overall cell expression for CD326, CD13, and CD147 (Fig. 5D). We did not present surface marker expression on WI-38 cells infected with 229E or OC43, or MRC-5 infected with OC43, given the intense and rapid CPE and cell death that compromised flow cytometry analysis.

Cell surface marker expression on MRC-5 cells following 229E infection

Next, we characterized surface expression of CD13, CD147, CD326, and ACE2 proteins in uninfected and infected MRC-5 cells with 229E. No detectable expression of GD3 was measured on MRC-5 or LLC-MK2 cells (data not shown). Nearly all MRC-5 cells expressed high levels of CD13 (91%) and CD147 (100%) surface antigens and much lower levels of CD326 (0.8%) and ACE2 (13%) markers (Fig. 6A and C). High expression of CD147 was in-line with previously reported studies characterizing lung epithelial cells (46, 48). Infection of MRC-5 cells with 229E virus leads to an important decrease in cells expressing 229E cellular receptor CD13, from 99% to 55% (Fig. 6A and B). MFI and the percentage of cells expressing each marker prior and following infection with OC43 are summarized in Fig. 6D and E. Although CD326 and ACE2 expression were slightly reduced following 229E infection, these did not attain statistical significance.

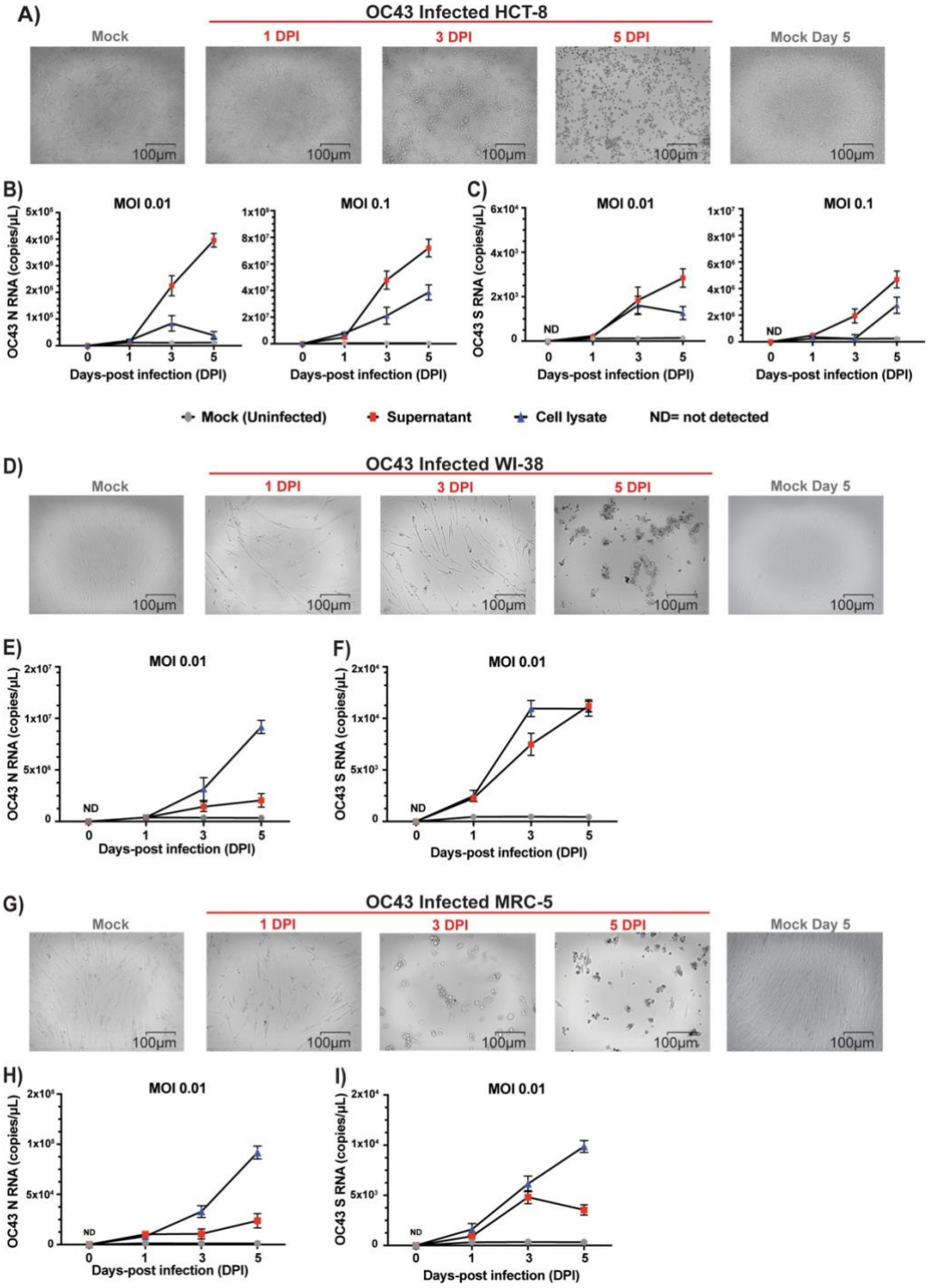

Figure 4.2 CPE evaluation and replication kinetics of OC43 infection.

(A) HCT-8, (D) WI-38, or (G) MRC-5 cells were infected with OC43 (virus titer: 8.89×10^5 TCID50/mL) at an MOI of 0.01. CPE of the infected cells along with mock (uninfected cells) were monitored for morphological changes in the cell monolayer. Images of the cells were captured at different days post-infection (day 0 to day 5 dpi) along with uninfected mock by ZOE Cell Imager. The reference bar is 100 microns. HCT-8 cells (B and C), WI-38 cells (E and F), or MRC-5 cells (H and I) infected with OC43 virus (MOI = 0.01 and/or 0.1) and cell lysates and supernatants were harvested at 0, 1, 3, and 5 days post-infection. Viral RNA copies of nucleocapsid (N), panels B, E, and H, and spike (S), panels C, F, and I, were then quantified by ddPCR. ND, not detected. Data represent the average MOI and standard deviation of three biological replicates with each three technical replicates per time point (n = 9).

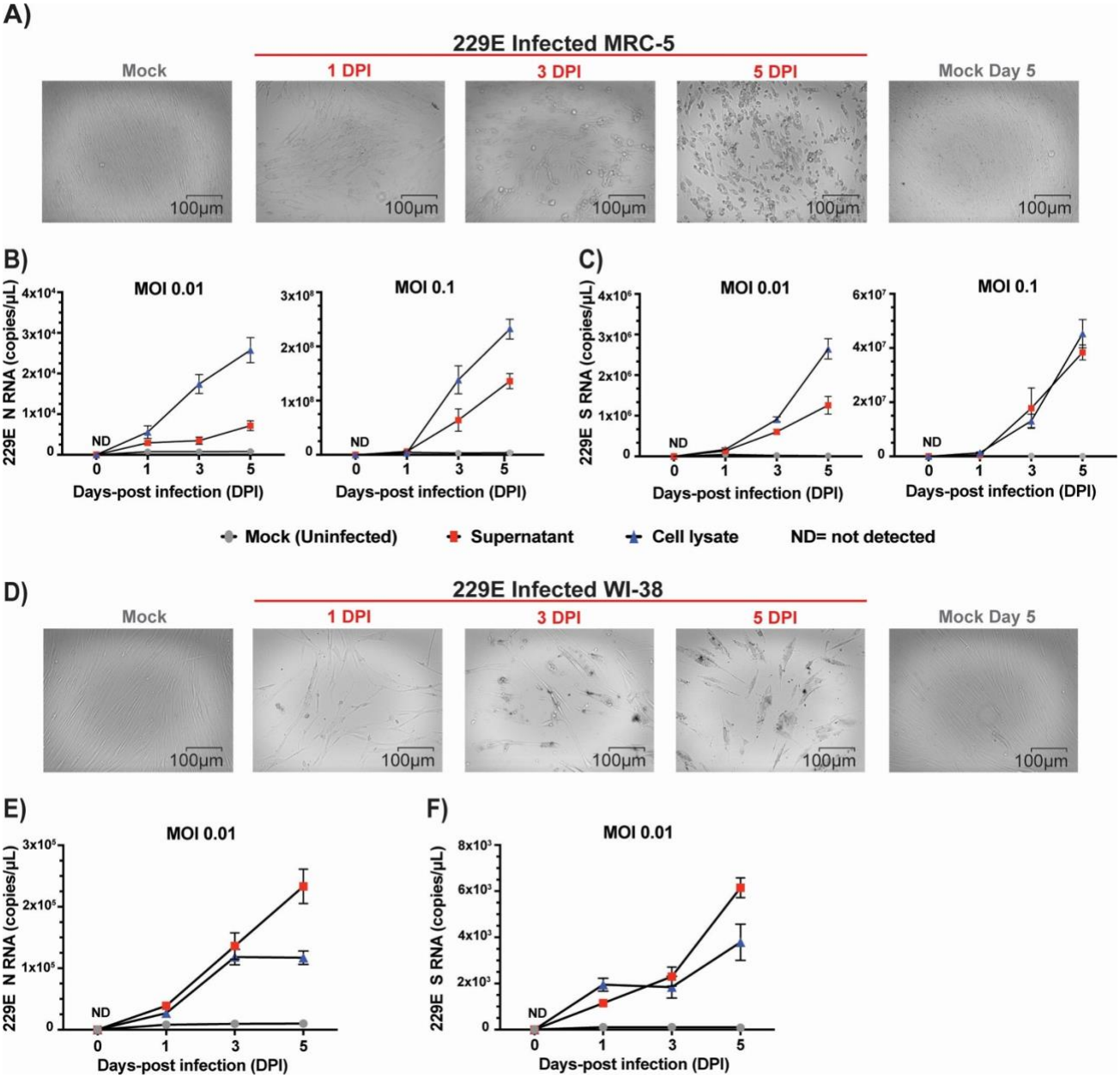

Figure 4.3 CPE evaluation and replication kinetics of 229E infection.

(A) MRC-5 cells or WI-38 cells (D) were infected with HCoV-229E (virus titer: 5.64×10^6 $TCID_{50}$/mL) at an MOI of 0.01. CPE of the infected cells along with mock (uninfected cells) were monitored for morphological changes in the cell monolayer. Images of the cells were captured at different days post-infection (day 0 to day 5 dpi) along with uninfected mock by ZOE Cell Imager. The reference bar is 100 microns. MRC-5 cells (B and C) or WI-38 cells (E and F) were infected with 229E virus (MOI = 0.01 and/or 0.1), and cell lysates and supernatants were harvested at 0, 1, 3, and 5 days post-infection. Viral RNA copies of nucleocapsid (N), panels B and E, and spike (S), panels C and F, were then quantified by ddPCR. ND, not detected. Data represent the average MOI and standard deviation of three biological replicates with each three technical replicates per time point (n = 9).

Cell surface marker expression on LLC-MK2 cells following NL63 infection

Lastly, we characterized surface expression of CD13, CD147, CD326, and ACE2 proteins in uninfected and infected LLC-MK2 cells with NL63 virus. We detected high expression of CD13 (81%), as previously reported (47, 49), and CD147 (99%), and lower expression of ACE2 (27%) surface receptor in uninfected LLC-MK2 cells (Fig. 7A). Infection with NL63 leads to a 2.3-fold increase in cells expressing NL63 cellular receptor ACE2 (Fig. 7B through D). Although we did observe a small upregulation of CD13 and CD326 expression in infected cells, these did not reach statistical significance (Fig. 7D). Previous studies have shown the involvement of CD147 in SARS-CoV-2 infections (40, 50). However, CD147 expression remained unaffected by NL63 infection as shown here (Fig. 7D and and E).

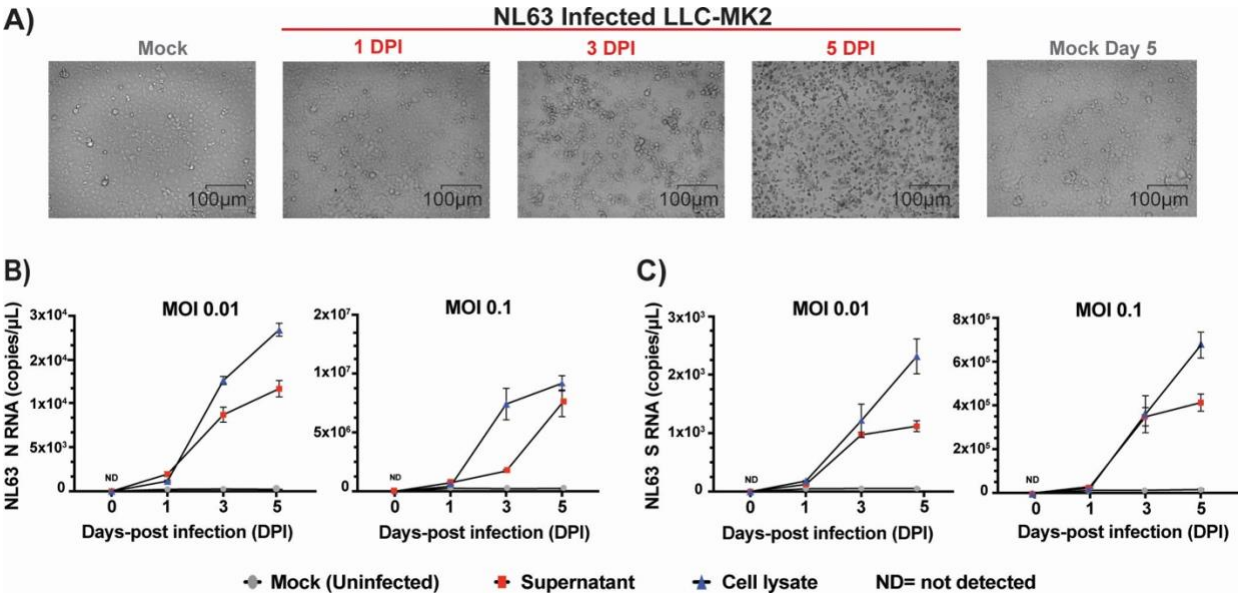

Figure 4.4 CPE evaluation and replication kinetics of NL63 infection.

(A) LLC-MK2 cells infected with NL63 (virus titer: 1.58 × 10^6 TCID50/mL) at an MOI of 0.01. CPE of the infected cells along with mock (uninfected cells) were monitored for morphological changes in the cell monolayer. Images of the cells were captured at different days post-infection (day 0 to day 5 dpi) along with uninfected mock by ZOE Cell Imager. The reference bar is 100 microns. LLC-MK2 cells were infected with NL63 virus (MOI = 0.01 and/or 0.1), and cell lysates and supernatants were harvested at 0, 1, 3, and 5 days post-infection. Viral RNA copies of nucleocapsid (N), panel B, and spike (S), panel C, were then quantified by ddPCR. ND, not detected. Data represent the average MOI and standard deviation of three biological replicates with each three technical replicates per time point (n = 9).

Soluble ACE2 protein and anti-ACE2 antibody effectively inhibit NL63 infection

Given that ACE2 is the major receptor for NL63 infection and having now established viral infection assays to measure vRNA expression, we wanted to investigate the efficiency of blocking antibodies and soluble ACE2 as infection prevention strategies. While therapeutic approaches that target ACE2 have been developed for SARS-CoV-2, it is not known if these can also inhibit NL63 infection (51–56).

LLC-MK2 cells were infected with NL63 (MOI of 0.1), and supernatants were harvested 5 days later. Supernatants (MOI equivalent of 0.1) were pre-treated with sACE2 or control protein (soluble ovalbumin) for 30 minutes prior to infection of LLC-MK2 cells (Fig. 8A and C). Similarly, LLC-MK2 cells were pre-treated with a blocking anti-ACE2 mAb or an unrelated control antibody (anti-DC-SIGN) for 30 minutes prior to infection (Fig. 8B and D). Five days after infection, we measured S and N vRNAs in the supernatants and lysates of infected cells. Both the culture supernatants and cell lysates of virus-infected LLC-MK2 cells with prior treatment of the virus with sACE2 led to a significantly attenuated production of N and S vRNA copies, of about 83% and 89% in supernatants and 96% and 88 % in lysates at the highest dose of 10 μg/mL, respectively (Fig. 8C). Similarly, treatment of LLC-MK2 cells with the human monoclonal ACE2 (anti-ACE2 mAb) blocking antibody shown to be capable of SARS-CoV-2 inhibition (56) also inhibited NL63 infection in a dose-dependent manner (Fig. 8B and D). Both the NL63 N and S vRNA levels were significantly reduced by 76% and 68% in supernatants and 89% and 86% in lysates at the highest dose of 120 mg/mL, respectively (Fig. 8D). However, neither soluble ACE2 nor anti-ACE2 was capable of completely blocking the infection in these conditions.

4.5 Discussion

An in-depth understanding of common cold seasonal coronavirus transmission, infection, pathogenicity, and the impact of reoccurring infections on human health is incomplete (2, 57, 58). In fact, only very recently was the functional receptor for HKU1 identified (15). Moreover, given that these viruses have zoonotic and co-infection potential to create new recombinant strains, they are of particular interest in light of the current SARS-CoV-2 pandemic (59, 60). This work studied the characteristics of HCoVshost cell interactions, CPE, and replication kinetics in commonly used human and animal cell lines. We used cell culture models of human lung, colon cancer, and rhesus monkey kidney cell lines that are fibroblastic and epithelial in origin as platforms to study the impact of infection on the host cell and attachment receptors.

Viral replication and CPE analysis demonstrated that of all the cell lines tested (Table 1), MRC-5, HCT-8, and LLC MK2 are the most suitable in our conditions to study OC43, 229E, and NL63 *in vitro*. While WI-38 did get infected by OC43 and 229E, the cells exhibited severe CPE that compromised our ability to perform flow cytometry analysis. We also considered to perform plaque assays for our study; however, we were unsuccessful to obtain sufficiently defined plaques that were amenable to quantification following OC43, 229E, and NL63 infection (data not shown). Cells that are permissive to infection do not necessarily demonstrate CPE or support plaque formation using standard methods (26, 30). However, some other groups have reported, albeit with varying success, plaques following HCoV infection using specialized protocols (4, 61).

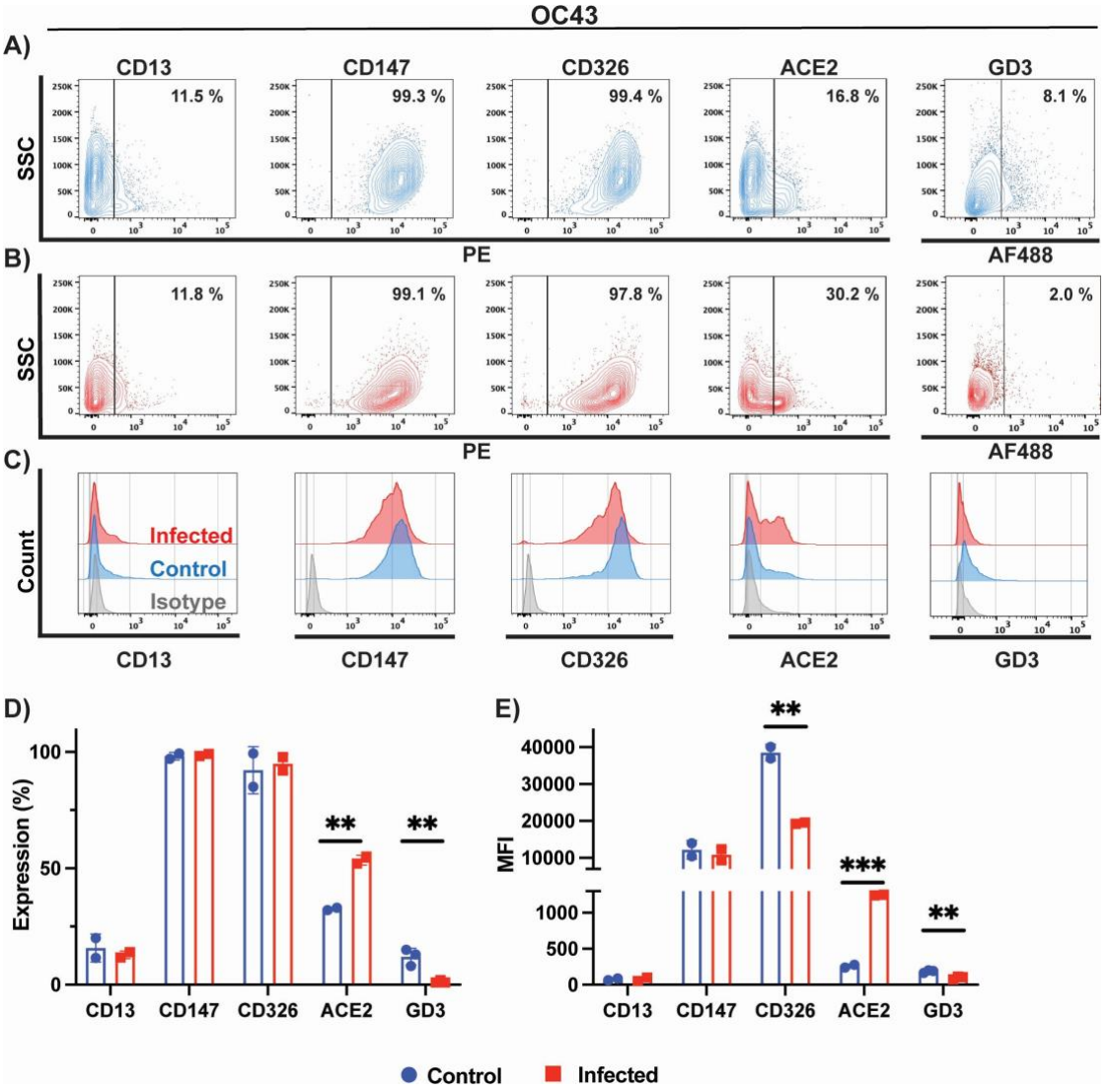

Figure 4.5 Phenotypic characterization of cell surface markers of OC43-infected cells.

Phenotypic characterization of (A) uninfected (blue) and (B) OC43-infected HCT-8 cells (red). CD13, CD147, CD326, ACE2, and GD3 expression were probed by flow cytometry. (C) Histogram plots of control and infected HCT-8 cells relative to isotype control (gray). Histograms plots showing (D) percentage of cells expressing a given marker and (E) mean fluorescence intensity. Data in panels D and E represent the mean of two biological replicates for all antigens except GD3, where three biological replicates were carried out. Statistical analysis was performed with the multiple unpaired *t*-test with Welch's correction. Only results that reached statistical significance were identified: * $P \leq 0.033$, ** $P \leq 0.002$, *** $P \leq 0.0001$, **** $P \leq 0.0001$.

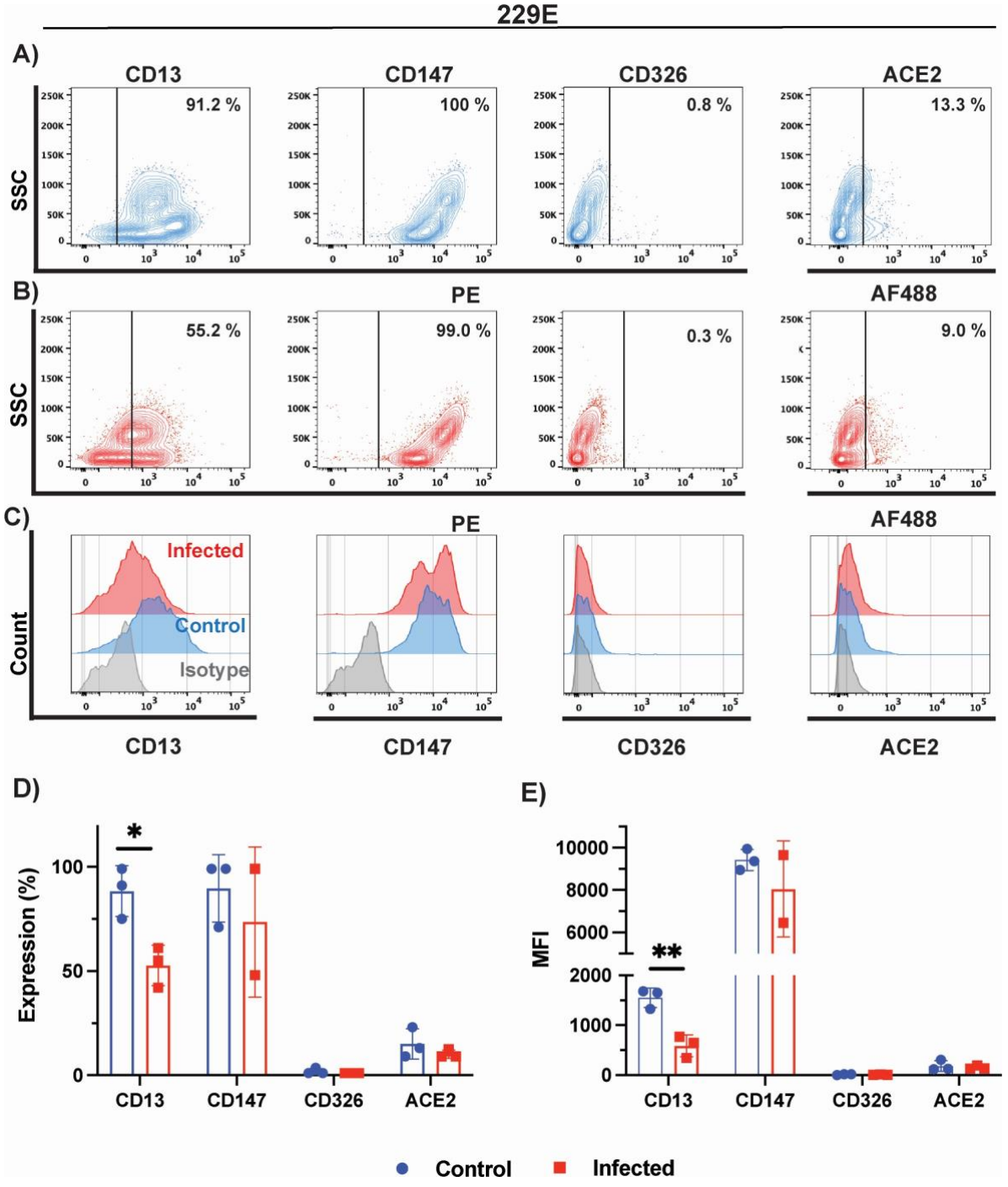

Figure 4.6 Phenotypic characterization of cell surface markers of 229E-infected cells.
Phenotypic characterization of (A) uninfected (blue) and (B) 229E-infected MRC-5 cells (red). CD13, CD147, CD326, and ACE2 expression were probed by flow cytometry. (C) Histogram plots of control and infected MRC-5 cells relative to isotype control (gray). Histograms plots showing (D) percentage of cells expressing a given marker and (E) mean fluorescence intensity. Data in panels D and E represent the mean of three biological replicates, except for CD147 where two biological replicates were carried out. Statistical analysis was

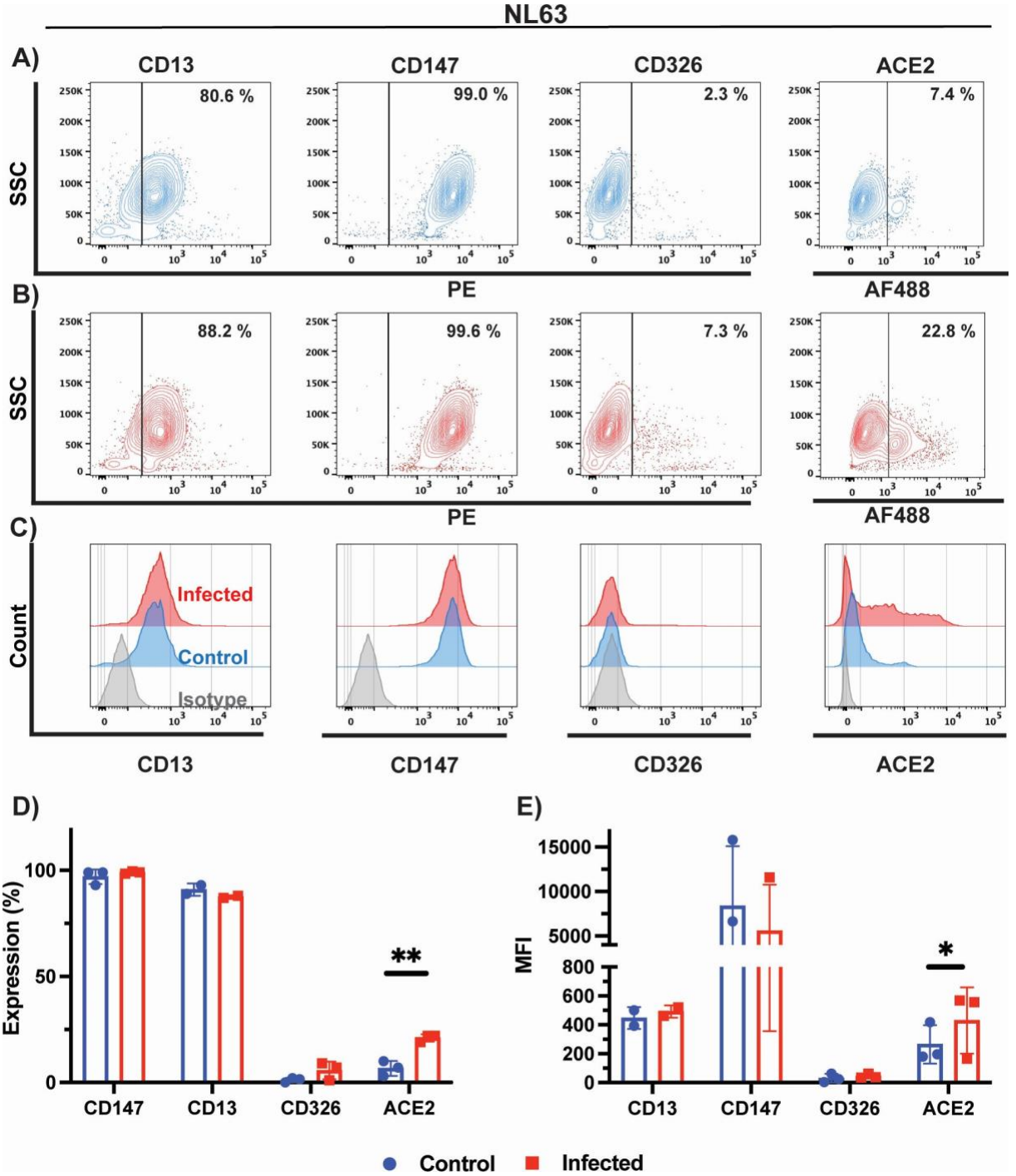

performed with the multiple unpaired *t*-test with Welch's correction. Only results that reached statistical significance were identified: * $P \leq 0.033$, ** $P \leq 0.002$, *** $P \leq 0.0001$, **** $P \leq 0.0001$.

Figure 4.7 Phenotypic characterization of cell surface markers of NL63-infected cells. Phenotypic characterization of (A) uninfected (blue) and (B) NL63-infected LLC-MK2 cells (red). CD13, CD147, CD326, and ACE2 expression were probed by flow cytometry. (C) Histogram plots of control and

infected LLC-MK2 cells relative to isotype control (gray). Histograms plots showing (D) percentage of cells expressing a given marker and (E) mean fluorescence intensity. Data in panels D and E represent the mean of three biological replicates, except for CD13 where two biological replicates were carried out. Statistical analysis was performed with the multiple unpaired *t*-test with Welch's correction. Only results that reached statistical significance were identified: * $P \leq 0.033$, ** $P \leq 0.002$, *** $P \leq 0.0001$, **** $P \leq 0.0001$.

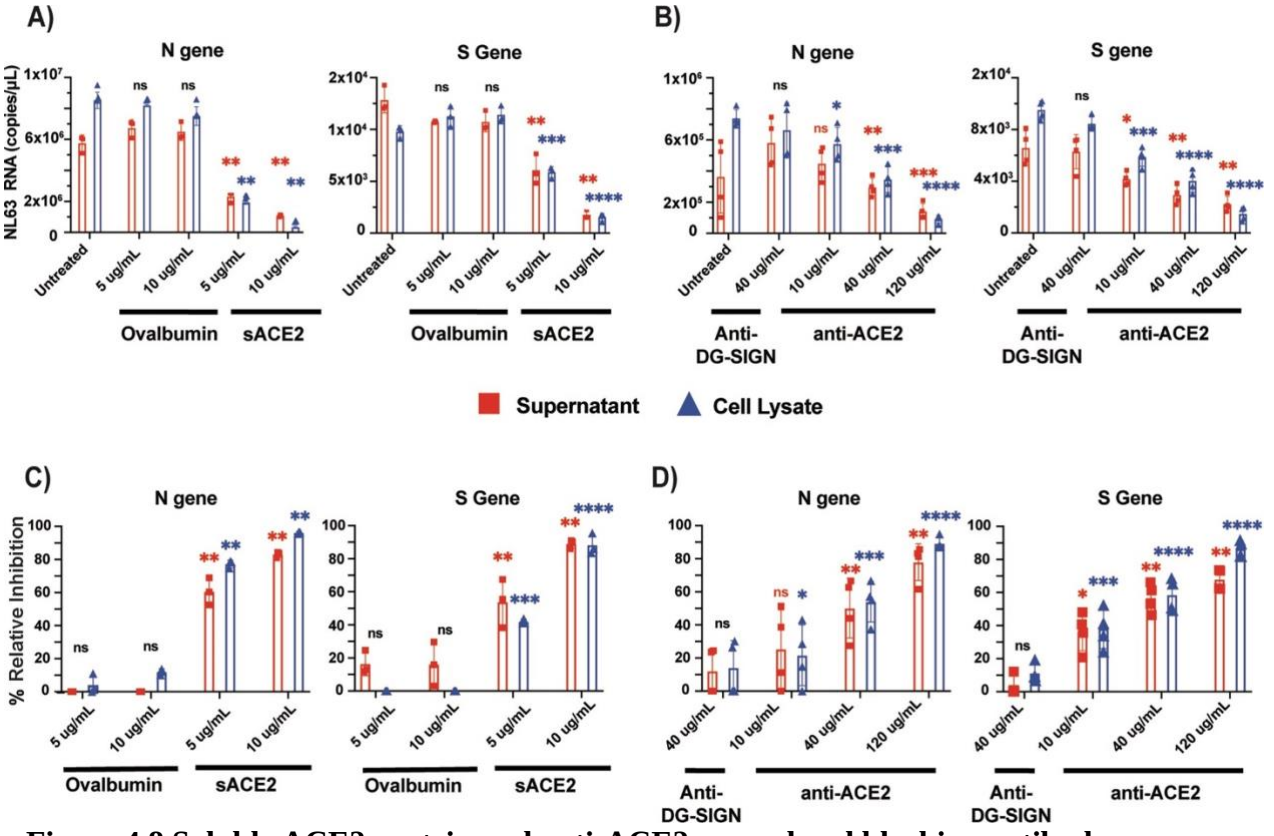

Figure 4.8 Soluble ACE2 protein and anti-ACE2 monoclonal blocking antibody inhibit NL63 infection in LLC-MK2 cells.

(A) Treatment with soluble ACE2 or control protein ovalbumin at 5 and 10 mg/mL was pre-incubated with NL63 virus at MOI 0.1 (virus titer: 8.89×10^5 TCID50/mL) for 1 hour, and the protein and virus mixture complex was added to the LLC-MK2 cells. (B) Similarly, cells were incubated for 1 hour with human anti-ACE2 monoclonal blocking antibody (10, 40, and 120 µg/mL) or unrelated control antibody (anti-DC-SIGN; 40 µg/mL) followed by addition of NL63 virus (MOI 0.1). Five days post-infection, both culture supernatants and cell lysates were harvested for quantification of nucleocapsid (N) and spike (S) vRNA copies by ddPCR. Percent relative viral inhibition following treatment with (C) sACE2 or (D) anti-ACE2 monoclonal antibody compared to their respective untreated control. Data represent three biological replicates for sACE2 or four (anti-ACE2) with three technical replicates per experiment. Statistical analysis was performed using an unpaired *t*-test with Welch's correction ($P < 0.05$) relative to untreated control. n.s. denoted as no statistical difference; * $P \leq 0.033$, ** $P \leq 0.002$, *** $P \leq 0.0001$, **** $P \leq 0.0001$.

Viral RNA analyses revealed that OC43, 229E, and NL63 replication in host cells steadily increased by day 3 pi, followed by CPE and dysmorphic cell appearances (Fig. 1 to 4). This is supported by previous reports of HCT-8 and MRC-5 infections with OC43, where the cells displayed obvious CPE at day 2 or 3 pi (26). However, the expression profiles and abundance of vRNAs in both supernatants and cell lysates for each virus-host cell pair varied significantly over the 5-day analysis period. Accumulation of vRNA was consistently higher in cell lysates than in supernatants, except for OC43 infecting HCT-8 cells where it was the opposite (Fig. 2B and C). Also, there was a general trend whereby more N than S vRNA was measured in both lysates and supernatants for all virus-host cell pairs, except for MRC-5 cells infected by 229E that displayed 100-fold higher levels of S than N (10^4 vs 10^6 copies per mL) (Fig. 3B and C). The overall canvas that emerges is one where cell-intrinsic factors influence the outcome of viral replication and release. These can include restriction factors that inhibit viral, for instance, budding and egress, or hinder viral genome replication and stability such as RNA-editing enzymes (62–65). Interferon and antiviral responses may also play an important role in viral spread and CPE in cell cultures (19).

Some viruses modulate surface receptors and co-receptors on the surface of the cell. For example, in the case of HIV, the virus downregulates CD4 expression on lymphocytes via the viral nef protein to avoid co-infections and superinfections that could lead to host cell genome instability (66). In this study, we analyzed the surface expression of CD13, CD147, CD326, GD3, and ACE2 on infected and uninfected MRC-5, HCT-8, and LLC-MK2 cells by flow cytometry. We tracked both the proportion of cells expressing the receptor and the receptor expression intensity, MFI. While we observed a fourfold decrease in GD3 on HCT-8 cells following OC43 infection, as well as a 1.7-fold decrease in CD13 expression following 229E infection, we were surprised to observe a significant increase in ACE2 receptor expression and MFI following NL63 infection of LLC-MK2 cells (2.3-fold) but also following OC43 infection (1.8-fold). Induction of ACE2 expression following infection with NL63 and the highly prevalent OC43 may be a source of concern for coronavirus co-infections. Although cytokine and interferon responses induced during the primary infection by OC43 and NL63 will likely have an inhibitory effect on co-infection by another

coronavirus utilizing ACE2 for entry (67), a strong induction in receptor expression could tilt the balance in favor of the incoming virus. There is currently very little information in the published literature about the frequency of such co-infections and their possible role in creating recombination events with SARS-CoV-2 (68).

Currently, there are no approved or licensed antiviral compounds for the treatment of the common cold caused by seasonal HCoV infections. Previous studies have shown that sACE2 or engineered variants of sACE2 may be beneficial for the treatment of COVID-19 infection (18, 69). LLC-MK2 cells treated with the highest dose of sACE2 (120 µg/mL) reduced the expression of N and S vRNA of NL63 by 90% in viral lysates (Fig. 8B and D). Similarly, human anti-ACE2 monoclonal blocking antibody inhibited in a dose-dependent manner (10, 40, and 120 µg) NL63 infection (Fig. 8B and D). These data indicate that targeting the entry receptor appears to be very effective at inhibiting this virus. However, we also attempted to use a polyclonal anti-ACE2 antibody to block NL63 without success (data not shown), suggesting that there may be few critical neutralizing epitopes in the spike-ACE2 interface for NL63 entry and that these should be prioritized to develop a therapy. Soluble ACE2 also proved to a capable inhibitor of NL63 but to somewhat a lesser degree.

In summary, our study showed that HCoVs OC43, 229E, and NL63 display differential replication kinetics and CPE in permissive host cells, highlighting the underlying involvement of cell-intrinsic factors that influence the expression of viral genes and virus egress. We also demonstrate that HCoV OC43 and NL63 infection upregulate the expression of the entry receptor ACE2 on host cells, raising opportunities for possible co-infection and recombination with other HCoVs (68, 70, 71). How HCoVs recombine and evolve in a given host remains an important topic to better understand the emergence of new viral strains of coronaviruses.

ACKNOWLEDGMENTS

This study was supported by a COVID-19 Rapid Response grant by the Canadian Institutes of Health Research (CIHR; #VR2-172722) to M.-A.L. M.M. holds an Ontario Graduate Scholarship. Y.G. holds a Canadian Institute of Health Research (CIHR) Frederick Banting and Charles Best graduate scholarship (CGS-Doctoral, 476885). N.C. holds a CIHR Frederick Banting and Charles Best graduate scholarship (CGS-M). M.-A.L. holds a Faculty of Medicine Chair of Excellence in Pandemic Viruses and Preparedness Research.

V.S., M.M., and M.-A.L. designed the study. V.S., M.M., N.C., M.M.S., J.H.S., and S.D. performed the experiments. V.S., M.M., Y.G., and M.-A.L. analyzed the data. V.S., M.M., Y.G., and M.A.L. wrote the manuscript. All authors edited the final version of the manuscript.

AUTHOR AFFILIATIONS

[1]Department of Biochemistry, Microbiology and Immunology, Faculty of Medicine, University of Ottawa, Ottawa, Canada
[2]The Center for Infection, Immunity, and Inflammation (CI3), University of Ottawa, Ottawa, Canada

AUTHOR CONTRIBUTIONS

Vinayakumar Siragam, Conceptualization, Formal analysis, Methodology, Writing – original draft | Mariam Maltseva, Conceptualization, Data curation, Formal analysis, Investigation, Methodology, Writing – original draft | Nicolas Castonguay, Formal analysis, Investigation, Methodology | Yannick Galipeau, Formal analysis, Methodology, Writing – review and editing | Mrudhula Madapuji Srinivasan, Methodology | Justino Hernandez Soto, Methodology | Samar Dankar, Methodology | Marc-André Langlois, Conceptualization, Formal analysis, Funding acquisition, Investigation, Project administration, Resources, Supervision, Writing – review and editing

DATA AVAILABILITY

The data used in this study can be obtained by request from the corresponding author.

4.6 References

1. Channappanavar R, Perlman S. 2020. Age-related susceptibility to coronavirus infections: role of impaired and dysregulated host immunity. J Clin Invest 130:6204–6213. https://doi.org/10.1172/ JCI144115
2. Pyrc K, Berkhout B, van der Hoek L. 2007. Antiviral strategies against human coronaviruses. Infect Disord Drug Targets 7:59–66. https://doi.org/10.2174/187152607780090757
3. Gorse GJ, Patel GB, Vitale JN, O'Connor TZ. 2010. Prevalence of antibodies to four human coronaviruses is lower in nasal secretions than in serum. Clin Vaccine Immunol 17:1875–1880. https://doi.org/10.1128/ CVI.00278-10
4. Bracci N, Pan HC, Lehman C, Kehn-Hall K, Lin SC. 2020. Improved plaque assay for human coronaviruses 229E and OC43. PeerJ 8:e10639. https://doi.org/10.7717/peerj.10639
5. Jin M, Shi N, Wang M, Shi C, Lu S, Chang Q, Sha S, Lin Y, Chen Y, Zhou H, Liang K, Huang X, Shi Y, Huang G. 2020. CD45: a critical regulator in immune cells to predict severe and non-severe COVID-19 patients. Aging12:19867–19879. https://doi.org/10.18632/aging.103941
6. Corman VM, Muth D, Niemeyer D, Drosten C. 2018. Hosts and sources of endemic human coronaviruses. Adv Virus Res 100:163–188. https://doi.org/10.1016/bs.aivir.2018.01.001
7. Masse S, Capai L, Villechenaud N, Blanchon T, Charrel R, Falchi A. 2020. Epidemiology and clinical symptoms related to seasonal coronavirus identified in patients with acute respiratory infections consulting in primary care over six influenza seasons (2014-2020) in France. Viruses 12:630. https://doi.org/10.3390/v12060630
8. Nickbakhsh S, Ho A, Marques DFP, McMenamin J, Gunson RN, Murcia PR. 2020. Epidemiology of seasonal coronaviruses: establishing the context for the emergence of coronavirus disease 2019. J Infect Dis 222:17–25. https://doi.org/10.1093/infdis/jiaa185
9. Jean A, Quach C, Yung A, Semret M. 2013. Severity and outcome associated with human coronavirus OC43 infections among children. Pediatr Infect Dis J 32:325–329. https://doi.org/10.1097/INF.-0b013e3182812787
10. Vassilara F, Spyridaki A, Pothitos G, Deliveliotou A, Papadopoulos A. 2018. A rare case of human coronavirus 229E associated with acute respiratory distress syndrome in a healthy adult. Case Rep Infect Dis 2018:6796839. https://doi.org/10.1155/2018/6796839
11. Wang Y, Li X, Liu W, Gan M, Zhang L, Wang J, Zhang Z, Zhu A, Li F, Sun J, Zhang G, Zhuang Z, Luo J, Chen D, Qiu S, Zhang L, Xu D, Mok CKP, Zhang F, Zhao J, Zhou R, Zhao J. 2020. Discovery of a subgenotype of human coronavirus Nl63 associated with severe lower respiratory tract infection in China, 2018. Emerg Microbes Infect 9:246–255. https://doi.org/10.1080/22221751.2020.1717999
12. Lachance C, Arbour N, Cashman NR, Talbot PJ. 1998. Involvement of aminopeptidase N (CD13) in infection of human neural cells by human coronavirus 229E. J Virol 72:6511–6519. https://doi.org/10.1128/JVI.72.8.6511-6519.1998
13. Szczepanski A, Owczarek K, Bzowska M, Gula K, Drebot I, Ochman M, Maksym B, Rajfur Z, Mitchell JA, Pyrc K. 2019. Canine respiratory coronavirus, bovine coronavirus, and human coronavirus OC43: receptors and attachment factors. Viruses 11:328. https://doi.org/10.3390/v11040328
14. Hulswit RJG, Lang Y, Bakkers MJG, Li W, Li Z, Schouten A, Ophorst B, van Kuppeveld FJM, Boons G-J, Bosch B-J, Huizinga EG, de Groot RJ. 2019. Human coronaviruses OC43 and HKU1 bind to 9-O-acetylated sialic acids via a conserved receptor-binding site in spike protein domain A. Proc Natl Acad Sci U S A 116:2681–2690. https://doi.org/10.1073/pnas.1809667116
15. Saunders N, Fernandez I, Planchais C, Michel V, Rajah MM, Baquero Salazar E, Postal J, Porrot F, Guivel-Benhassine F, Blanc C, et al. 2023. TMPRSS2 is a functional receptor for human coronavirus HKU1. Nature 624:207–214. https://doi.org/10.1038/s41586-023-06761-7
16. Hofmann H, Pyrc K, van der Hoek L, Geier M, Berkhout B, Pöhlmann S. 2005. Human coronavirus Nl63 employs the severe acute respiratory syndrome coronavirus receptor for cellular entry. Proc Natl Acad Sci U S A 102:7988–7993. https://doi.org/10.1073/pnas.0409465102
17. Milewska A, Nowak P, Owczarek K, Szczepanski A, Zarebski M, Hoang A, Berniak K, Wojarski J, Zeglen S, Baster Z, Rajfur Z, Pyrc K. 2018. Entry of human coronavirus NL63 into the cell. J Virol 92:e01933-17. https://doi. org/10.1128/JVI.01933-17
18. Monteil V, Kwon H, Prado P, Hagelkrüys A, Wimmer RA, Stahl M, Leopoldi A, Garreta E, Hurtado Del Pozo C, Prosper F, Romero JP, Wirnsberger G, Zhang H, Slutsky AS, Conder R, Montserrat N, Mirazimi A, Penninger JM. 2020. Inhibition of SARS-CoV-2 infections in engineered human tissues using clinical-grade soluble human ACE2. Cell 181:905–913. https://doi. org/10.1016/j.cell.2020.04.004
19. Duncan JKS, Xu D, Licursi M, Joyce MA, Saffran HA, Liu K, Gohda J, Tyrrell DL, Kawaguchi Y, Hirasawa K. 2023. Interferon regulatory factor 3 mediates effective antiviral responses to human coronavirus 229E and OC43 infection. Front Immunol 14:930086. https://doi.org/10.3389/fimmu.2023.930086
20. Brown AJ, Won JJ, Graham RL, Dinnon KH, Sims AC, Feng JY, Cihlar T, Denison MR, Baric RS, Sheahan TP. 2019. Broad spectrum antiviral remdesivir inhibits human endemic and zoonotic deltacoronaviruses with a highly divergent RNA dependent RNA polymerase. Antiviral Res 169:104541. https://doi.org/10.1016/j.antiviral.2019.104541
21. Wang Y, Li P, Rajpoot S, Saqib U, Yu P, Li Y, Li Y, Ma Z, Baig MS, Pan Q. 2021. Comparative assessment of favipiravir and remdesivir against human coronavirus Nl63 in molecular docking and cell culture models. Sci Rep 11:23465. https://doi.org/10.1038/s41598-021-02972-y 22. Li J, Wang Y, Solanki K, Atre R, Lavrijsen M, Pan Q, Baig MS, Li P. 2023. Nirmatrelvir exerts distinct antiviral potency against different human coronaviruses. Antiviral Res 211:105555. https://doi.org/10.1016/j.antiviral.2023.105555
23. Zumla A, Chan JFW, Azhar EI, Hui DSC, Yuen K-Y. 2016. Coronaviruses - drug discovery and therapeutic options. Nat Rev Drug Discov 15:327–347. https://doi.org/10.1038/nrd.2015.37
24. Liu D, Chen C, Chen D, Zhu A, Li F, Zhuang Z, Mok CKP, Dai J, Li X, Jin Y, et al. 2023. Mouse models susceptible to HCoV-229E and HCoV-NL63 and cross protection from challenge with SARS-CoV-2. Proc Natl Acad Sci U S A 120:e2202820120. https://doi.org/10.1073/pnas.2202820120
25. Schildgen O, Jebbink MF, de Vries M, Pyrc K, Dijkman R, Simon A, Müller A, Kupfer B, van der Hoek L. 2006. Identification of cell lines permissive for human coronavirus Nl63. J Virol Methods 138:207–210. https://doi. org/10.1016/j.jviromet.2006.07.023
26. Schirtzinger EE, Kim Y, Davis AS. 2022. Improving human coronavirus OC43 (HCoV-OC43) research comparability in studies using HCoV-OC43 as a surrogate for SARS-CoV-2. J Virol Methods 299:114317. https://doi. org/10.1016/j.jviromet.2021.114317
27. Weil T, Lawrenz J, Seidel A, Münch J, Müller JA. 2022. Immunodetection assays for the quantification of seasonal common cold coronaviruses OC43, Nl63, or 229E infection confirm nirmatrelvir as broad coronavirus inhibitor. Antiviral Res 203:105343. https://doi.org/10.1016/j.antiviral.2022.105343

28. Owczarek K, Szczepanski A, Milewska A, Baster Z, Rajfur Z, Sarna M, Pyrc K. 2018. Early events during human coronavirus OC43 entry to the cell. Sci Rep 8:7124. https://doi.org/10.1038/s41598-018-25640-0
29. Dijkman R, Jebbink MF, Deijs M, Milewska A, Pyrc K, Buelow E, van der Bijl A, van der Hoek L. 2012. Replication-dependent downregulation of cellular angiotensin-converting enzyme 2 protein expression by human coronavirus Nl63. J Gen Virol 93:1924–1929. https://doi.org/10.1099/vir.0.043919-0
30. Hirose R, Watanabe N, Bandou R, Yoshida T, Daidoji T, Naito Y, Itoh Y, Nakaya T. 2021. A cytopathic effect-based tissue culture method for HCoV-OC43 titration using TMPRSS2-expressing VeroE6 cells. mSphere 6:e00159-21 https://doi.org/10.1128/mSphere.00159-21
31. Mukherjee S, Dowd KA, Manhart CJ, Ledgerwood JE, Durbin AP, Whitehead SS, Pierson TC. 2014. Mechanism and significance of cell type-dependent neutralization of flaviviruses. J Virol 88:7210–7220. https://doi.org/10.1128/JVI.03690-13
32. Reed LJ, Muench H. 1938. A simple method of estimating fifty per cent endpoints12. Am J Epidemiol. 27:493–497. https://doi.org/10.1093/oxfordjournals.aje.a118408
33. Enlow W, Piret J, Boivin G. 2020. Droplet digital PCR and immunohistochemistry techniques to detect Zika virus in the central nervous system of mice, p 41–57. In Kobinger GRacine T (ed), Zika virus: methods and protocols. Springer US, New York.
34. Friedman HM, Koropchak C. 1978. Comparison of WI-38, MRC-5, and IMR-90 cell strains for isolation of viruses from clinical specimens. J Clin Microbiol 7:368–371. https://doi.org/10.1128/jcm.7.4.368-371.1978 35. Milewska A, Zarebski M, Nowak P, Stozek K, Potempa J, Pyrc K. 2014. Human coronavirus Nl63 utilizes heparan sulfate proteoglycans for attachment to target cells. J Virol 88:13221–13230. https://doi.org/10.1128/JVI.02078-14
36. Wang G, Deering C, Macke M, Shao J, Burns R, Blau DM, Holmes KV, Davidson BL, Perlman S, McCray PB. 2000. Human coronavirus 229E infects polarized airway epithelia from the apical surface. J Virol 74:9234–9239. https://doi.org/10.1128/jvi.74.19.9234-9239.2000 37. Walls AC, Park YJ, Tortorici MA, Wall A, McGuire AT, Veesler D. 2020. Structure, function, and antigenicity of the SARS-CoV-2 spike glycoprotein. Cell 181:281–292. https://doi.org/10.1016/j.cell.2020.02.058
38. Shang J, Ye G, Shi K, Wan Y, Luo C, Aihara H, Geng Q, Auerbach A, Li F. 2020. Structural basis of receptor recognition by SARS-CoV-2. Nature 581:221–224. https://doi.org/10.1038/s41586-020-2179-y
39. Chen Z, Mi L, Xu J, Yu J, Wang X, Jiang J, Xing J, Shang P, Qian A, Li Y, Shaw PX, Wang J, Duan S, Ding J, Fan C, Zhang Y, Yang Y, Yu X, Feng Q, Li B, Yao X, Zhang Z, Li L, Xue X, Zhu P. 2005. Function of HAb18G/CD147 in invasion of host cells by severe acute respiratory syndrome coronavirus. J Infect Dis 191:755–760. https://doi.org/10.1086/427811
40. Wang K, Chen W, Zhang Z, Deng Y, Lian J-Q, Du P, Wei D, Zhang Y, Sun XX, Gong L, et al. 2020. CD147-spike protein is a novel route for SARSCoV-2 infection to host cells. Sig Transduct Target Ther 5:283. https://doi. org/10.1038/s41392-020-00426-x
41. Tortorici MA, Walls AC, Lang Y, Wang C, Li Z, Koerhuis D, Boons G-J, Bosch B-J, Rey FA, de Groot RJ, Veesler D. 2019. Structural basis for human coronavirus attachment to sialic acid receptors. Nat Struct Mol Biol 26:481–489. https://doi.org/10.1038/s41594-019-0233-y
42. Li Z, Lang Y, Liu L, Bunyatov MI, Sarmiento AI, de Groot RJ, Boons G-J. 2021. Synthetic O-acetylated sialosides facilitate functional receptor identification for human respiratory viruses. Nat Chem 13:496–503. https://doi.org/10.1038/s41557-021-00655-9
43. Jahangiri L, Ishola T, Pucci P, Trigg RM, Pereira J, Williams JA, Cavanagh ML, Gkoutos GV, Tsaprouni L, Turner SD. 2021. The role of autophagy and lncRNAs in the maintenance of cancer stem cells. Cancers (Basel) 13:1239. https://doi.org/10.3390/cancers13061239
44. Vázquez-Iglesias L, Barcia-Castro L, Rodríguez-Quiroga M, Páez de la Cadena M, Rodríguez-Berrocal J, Cordero OJ. 2019. Surface expression marker profile in colon cancer cell lines and sphere-derived cells suggests complexity in CD26(+) cancer stem cells subsets. Biol Open 8:bio041673. https://doi.org/10.1242/bio.041673
45. Belov L, Zhou J, Christopherson RI. 2010. Cell surface markers in colorectal cancer prognosis. Int J Mol Sci 12:78–113. https://doi.org/10.3390/ijms12010078
46. Iacono KT, Brown AL, Greene MI, Saouaf SJ. 2007. CD147 immunoglobulin superfamily receptor function and role in pathology. Exp Mol Pathol 83:283–295. https://doi.org/10.1016/j.yexmp.2007.08.014
47. Dixon J, Kaklamanis L, Turley H, Hickson ID, Leek RD, Harris AL, Gatter KC. 1994. Expression of aminopeptidase-N (CD 13) in normal tissues and malignant neoplasms of epithelial and lymphoid origin. J Clin Pathol 47:43–47. https://doi.org/10.1136/jcp.47.1.43
48. Landras A, Reger de Moura C, Jouenne F, Lebbe C, Menashi S, Mourah S. 2019. CD147 is a promising target of tumor progression and a prognostic biomarker. Cancers (Basel) 11:1803. https://doi.org/10.3390/cancers11111803
49. Van der Hauwaert C, Savary G, Gnemmi V, Glowacki F, Pottier N, Bouillez A, Maboudou P, Zini L, Leroy X, Cauffiez C, Perrais M, Aubert S. 2013. Isolation and characterization of a primary proximal tubular epithelial cell model from human kidney by CD10/CD13 double labeling. PLoS One 8:e66750. https://doi.org/10.1371/journal.pone.0066750
50. Fenizia C, Galbiati S, Vanetti C, Vago R, Clerici M, Tacchetti C, Daniele T. 2021. SARS-CoV-2 entry: at the crossroads of CD147 and ACE2. Cells 10:1434. https://doi.org/10.3390/cells10061434
51. Du W, Hurdiss DL, Drabek D, Mykytyn AZ, Kaiser FK, GonzálezHernández M, Muñoz-Santos D, Lamers MM, van Haperen R, Li W, et al. 2022. An ACE2-blocking antibody confers broad neutralization and protection against omicron and other SARS-CoV-2 variants of concern. Sci Immunol 7:eabp9312. https://doi.org/10.1126/sciimmunol.abp9312 52. Zhang H, Lv P, Jiang J, Liu Y, Yan R, Shu S, Hu B, Xiao H, Cai K, Yuan S, Li Y. 2023. Advances in developing ACE2 derivatives against SARS-CoV-2. Lancet Microbe 4:e369–e378. https://doi.org/10.1016/S2666-5247(23)00011-3
53. Krishnamurthy S, Lockey RF, Kolliputi N. 2021. Soluble ACE2 as a potential therapy for COVID-19. Am J Physiol Cell Physiol 320:C279– C281. https://doi.org/10.1152/ajpcell.00478.2020
54. Abd El-Aziz TM, Al-Sabi A, Stockand JD. 2020. Human recombinant soluble ACE2 (hrsACE2) shows promise for treating severe COVID-19. Signal Transduct Target Ther 5:258. https://doi.org/10.1038/s41392-020-00374-6
55. Monteil V, Dyczynski M, Lauschke VM, Kwon H, Wirnsberger G, Youhanna S, Zhang H, Slutsky AS, Hurtado Del Pozo C, Horn M, Montserrat N, Penninger JM, Mirazimi A. 2021. Human soluble ACE2 improves the effect of remdesivir in SARS-CoV-2 infection. EMBO Mol Med 13:e13426. https://doi.org/10.15252/emmm.202013426
56. Wang C, Li W, Drabek D, Okba NMA, van Haperen R, Osterhaus ADME, van Kuppeveld FJM, Haagmans BL, Grosveld F, Bosch B-J. 2020. A human monoclonal antibody blocking SARS-CoV-2 infection. Nat Commun 11:2251. https://doi.org/10.1038/s41467-020-16256-y
57. Fischer N, Dauby N, Bossuyt N, Reynders M, Gérard M, Lacor P,

Daelemans S, Lissoir B, Holemans X, Magerman K, Jouck D, Bourgeois M, Delaere B, Quoilin S, Van Gucht S, Thomas I, Barbezange C, Subissi L. 2021. Monitoring of human coronaviruses in Belgian primary care and hospitals, 2015-20: a surveillance study. Lancet Microbe 2:e105–e114. https://doi.org/10.1016/S2666-5247(20)30221-4

58. Edridge AWD, Kaczorowska J, Hoste ACR, Bakker M, Klein M, Loens K, Jebbink MF, Matser A, Kinsella CM, Rueda P, Ieven M, Goossens H, Prins M, Sastre P, Deijs M, van der Hoek L. 2020. Seasonal coronavirus protective immunity is short-lasting. Nat Med 26:1691–1693. https://doi.org/10.1038/s41591-020-1083-1
59. Li Q, Shah T, Wang B, Qu L, Wang R, Hou Y, Baloch Z, Xia X. 2022. Crossspecies transmission, evolution and zoonotic potential of coronaviruses. Front Cell Infect Microbiol 12:1081370.
60. Kane Y, Wong G, Gao GF. 2023. Animal models, zoonotic reservoirs, and cross-species transmission of emerging human-infecting coronaviruses. Annu Rev Anim Biosci 11:1–31. https://doi.org/10.1146/annurev-animal-020420-025011
61. Fausto A, Otter CJ, Bracci N, Weiss SR. 2023. Improved culture methods for human coronaviruses HCoV-OC43, HCoV-229E, and HCoV-NL63. Curr Protoc 3:e914. https://doi.org/10.1002/cpz1.914
62. Dudley JP. 2023. APOBECs: our fickle friends? PLoS Pathog 19:e1011364. https://doi.org/10.1371/journal.ppat.1011364
63. Chemudupati M, Kenney AD, Bonifati S, Zani A, McMichael TM, Wu L, Yount JS. 2019. From APOBEC to ZAP: diverse mechanisms used by cellular restriction factors to inhibit virus infections. Biochim Biophys Acta Mol Cell Res 1866:382–394. https://doi.org/10.1016/j.bbamcr.2018. 09.012
64. Song Y, He X, Yang W, Wu Y, Cui J, Tang T, Zhang R. 2022. Virus-specific editing identification approach reveals the landscape of A-to-I editing and its impacts on SARS-CoV-2 characteristics and evolution. Nucleic Acids Res 50:2509–2521. https://doi.org/10.1093/nar/gkac120
65. Ringlander J, Fingal J, Kann H, Prakash K, Rydell G, Andersson M, Martner A, Lindh M, Horal P, Hellstrand K, Kann M. 2022. Impact of ADAR-induced editing of minor viral RNA populations on replication and transmission of SARS-CoV-2. Proc Natl Acad Sci U S A 119:e2112663119. https://doi. org/10.1073/pnas.2112663119
66. Lama J. 2003. The physiological relevance of CD4 receptor downmodulation during HIV infection. Curr HIV Res 1:167–184. https://doi.org/10.2174/1570162033485276
67. Karki R, Kanneganti TD. 2022. Innate immunity, cytokine storm, and inflammatory cell death in COVID-19. J Transl Med 20:542. https://doi.org/10.1186/s12967-022-03767-z
68. Pollett S, Conte MA, Sanborn M, Jarman RG, Lidl GM, Modjarrad K, Maljkovic Berry I. 2021. A comparative recombination analysis of human coronaviruses and implications for the SARS-CoV-2 pandemic. Sci Rep 11:17365. https://doi.org/10.1038/s41598-021-96626-8
69. Chan KK, Dorosky D, Sharma P, Abbasi SA, Dye JM, Kranz DM, Herbert AS, Procko E. 2020. Engineering human ACE2 to optimize binding to the spike protein of SARS coronavirus 2. Science 369:1261–1265. https://doi. org/10.1126/science.abc0870
70. Shao N, Zhang C, Dong J, Sun L, Chen X, Xie Z, Xu B, An S, Zhang T, Yang F. 2022. Molecular evolution of human coronavirus-NL63, -229E, -HKU1 and -OC43 in hospitalized children in China. Front Microbiol 13:1023847. https://doi.org/10.3389/fmicb.2022.1023847
71. Müller NF, Kistler KE, Bedford T. 2022. A bayesian approach to infer recombination patterns in coronaviruses. Nat Commun 13:4186. https://doi.org/10.1038/s41467-022-31749-8

5 Chapter 5: Characterization of systemic and mucosal humoral immune responses to an adjuvanted intranasal SARS-CoV-2 protein subunit vaccine candidate in mice. *(Published)*

Preface: This chapter has been previously published as a research article.

Maltseva M., Galipeau Y., Renner T.M., Deschatelets L., Durocher Y., Akache B.. and Langlois M-A. (2022). Characterization of systemic and mucosal humoral immune responses to an adjuvanted intranasal SARS-CoV-2 protein subunit vaccine candidate in mice.
Vaccines, *11*(1), p.30. https://doi.org/10.3390/vaccines11010030

Abstract:

Continuous viral evolution of SARS-CoV-2 has resulted in variants capable of immune evasion, vaccine breakthrough infections and increased transmissibility. New vaccines that invoke mucosal immunity may provide a solution to reducing virus transmission. Here, we evaluated the immunogenicity of intranasally administered subunit protein vaccines composed of a stabilized SARS-CoV-2 spike trimer or the receptor binding domain (RBD) adjuvanted with either cholera toxin (CT) or an archaeal lipid mucosal adjuvant (AMVAD). We show robust induction of immunoglobulin (Ig) G and IgA responses in plasma, nasal wash and bronchoalveolar lavage in mice only when adjuvant is used in the vaccine formulation. While the AMVAD adjuvant was more effective at inducing systemic antibodies against the RBD antigen than CT, CT was generally more effective at inducing overall higher IgA and IgG titers against the spike antigen in both systemic and mucosal compartments. Furthermore, vaccination with adjuvanted spike led to superior mucosal IgA responses than with the RBD antigen and produced broadly targeting neutralizing plasma antibodies against ancestral, Delta and Omicron variants in vitro; whereas adjuvanted RBD elicited a narrower antibody response with neutralizing activity only against ancestral and Delta variants. Our study demonstrates that intranasal administration of an adjuvanted protein subunit vaccine in immunologically naïve mice induced both systemic and

mucosal neutralizing antibody responses that were most effective at neutralizing SARS-CoV-2 variants when the trimeric spike was used as an antigen compared to RBD.

5.1 Introduction

The ongoing emergence of highly transmissible SARS-CoV-2 variants of concern (VOCs) have significantly hampered vaccine effectiveness against infection, COVID-19 disease and transmission [1–3]. Reduced vaccine effectiveness can also be attributed to immune evasion by VOCs, waning immunity following prolonged periods post vaccination or natural infection and poor induction of mucosal immunity [4,5]. Currently, approved intramuscular (IM) vaccines induce robust systemic immunity which protects against severe disease yet leaves the individual vulnerable to infection and reinfection at the primary point of viral entry at the upper respiratory tract (URT) [6,7]. Indeed, breakthrough infections with viral shedding, with both Delta and Omicron variants, have been reported in fully vaccinated individuals, highlighting the possibility of onward viral transmission despite vaccination [8–10]. While vaccine boosting has significantly increased vaccine effectiveness against severe disease and hospitalization, continued viral evolution and emergence of highly transmissible VOCs highlight the need for revaluating our vaccine strategy, due to the shortcomings of currently available vaccines in reducing transmission [4]. In the effort to curtail the COVID-19 pandemic, next generation vaccines must address immune evasion and provide improved cross-protection against rapidly emerging SARS-CoV-2 variants at the point of entry in order to reduce viral transmission.

Several groups have been evaluating transmission blocking strategies that target SARS-CoV-2 entry. The spike protein of SARS-CoV-2 is the primary antigenic target of currently approved vaccines due to its high immunogenicity, abundant viral surface expression and ability to elicit both humoral and cell-mediated responses [11–18]. The spike protein also demonstrates effective mucosal and systemic induction of humoral and cell-mediated immunity through oral and intranasal vaccination in various animal models [19–30]. Notably, a majority of these vaccine candidates are based on an adenoviral platform which expresses the spike trimer protein of the parental strain of SARS-CoV-2. Indeed, these groups demonstrated superior protection with intranasal vaccination relative to intramuscular immunization upon subsequent viral challenge, in

both the upper and lower respiratory tract, against the ancestral strain and VOCs [19,21,23,24,28]. These strategies targeting the respiratory mucosa reveal effective protection against disease and reduced viral shedding in mice, hamsters and non-human primates [19–21,23–25,30,31]. While spike trimer formulations are more commonplace, vaccines targeting the receptor binding domain (RBD) of the spike have been proposed, given its direct interaction with the cognate entry receptor, angiotensin-converting enzyme 2 (ACE2) [32]. Additionally, many potent RBD-specific neutralizing antibodies have been characterized from convalescent and vaccinated individuals [13,16,17,33–36]. While the immunogenicity of these antigens has been extensively characterized following intramuscular immunization in pre-clinical animal models, their relative immunogenicity as intranasal vaccine targets against emerging VOC remain unclear. To our knowledge, this is the first study directly comparing the systemic and mucosal humoral responses following the intranasal administration of SARS-CoV-2 spike and RBD antigens in mice.

Adjuvants are often essential for directing antigen-specific immune responses and overcoming weak immunogenicity of protein subunit vaccines. Due to adjuvants' intrinsic immunomodulatory properties, their combined administration with an antigen elicits superior and long-lasting immune responses while overcoming natural tolerances of mucosal compartments to antigens administered alone [7,37,38]. Indeed, mucosal adjuvants need to overcome the harsh conditions of mucosal tissues (e.g., low pH, continuous mucociliary clearance and local enzymes) and rapidly permeate mucus layers in order to induce efficacious responses and establish immune memory [39,40]. Cholera toxin (CT) is produced by *Vibrio cholerae* and its combined intranasal administration with an antigen has been shown to elicit potent antigen-specific IgA responses in the URT and T cell-mediated responses in animal models [41–45]. Although CT is among the most effective mucosal adjuvants in animal models, due to safety concerns linked to toxin-mediated neuroinflammation that correlate with Bell's palsy, its use as an adjuvant has been precluded from the clinic [43,46,47]. In contrast, the archaeal polar lipid mucosal vaccine adjuvant and delivery (AMVAD) system used in this study is a self-adjuvating mucosal vaccine delivery system with an established preclinical safety profile that does not require any additional immunostimulants and can withstand a broad range of pH [48–51]. AMVAD is characterized by its polar lipid and large spherical structure which aggregates in a grape-like formation, thereby encapsulating the antigen [48,52]. Various antigens and formulations of lipid archaeosome-based adjuvants administered intramuscularly

have been evaluated in vivo and were shown to elicit robust cell-mediated and humoral responses through recruitment and activation of macrophages and dendritic cells [53–56]. In turn, while intranasal immunization using these specific adjuvants is less explored, Patel et al. demonstrate that intranasally administered ovalbumin adjuvanted with AMVAD induced robust mucosal and systemic ovalbumin IgA responses in mice [48].

In this study, we investigated the immunogenicity of an intranasally administered protein subunit vaccine expressing the stabilized SARS-CoV-2 full spike trimer ectodomain or RBD adjuvanted with either CT or AMVAD. We show robust induction of IgG and IgA responses in plasma, nasal wash and bronchoalveolar lavage fluid (BALF) in mice. We observed induction of mucosal and systemic neutralizing IgA and IgG responses. The observed systemic responses were of superior or similar neutralization capacity compared to serum antibodies elicited in humans by SARS-CoV-2 infection or two doses of mRNA vaccine, respectively. Mucosal IgA and systemic IgG antibody titers correlated with neutralizing antibody levels in BALF and plasma, respectively. Given the need for the development of next generation vaccines that target SARS-CoV-2 at the primary site of infection, our findings highlight the immunogenicity of an adjuvanted subunit vaccine platform in stimulating both mucosal and systemic humoral responses in mice and eliciting neutralizing antibodies against emerging SARS-CoV-2 variants.

5.2 Materials and Methods

Protein Production

RBD protein was produced in HEK 293F cells and purified. Briefly, a plasmid generously provided by Florian Krammer (Mount Sinai, New York, NY, USA) encoding the Wuhan-Hu-1 RBD (MN908947) sequence coding for the amino acid 319–541 and fused with the N-terminal SARS-CoV-2 spike secretory signal and a C-terminal hexa-histidine tag was transfected into 293F cells cultivated in Freestyle 293 expression media (Thermo Fisher, #12338018) at 37 ◦C, 7% CO_2, while shaking (125 rpm). A total of 600 million cells resuspended in 200 mL were transfected with 200 µg of plasmid using ExpiFectamine (Thermo Fisher, 14525, Waltham, MA, USA). Three days post-transfection, cell supernatant was harvested by centrifugation (4000× *g* for 20 min at 4 ◦C) and filtered through a low binding 0.22 µm Stericup vacuum filter (Millipore Sigma, S2GPU10RE, Burlington, MA, USA). The filtered supernatant was incubated for 2 h at room temperature with 6 mL of Ni-NTA resin (Qiagen, 30210, Hilden, Germany). The column containing the mix of supernatant and resin was washed four times with a washing buffer containing 20 mM imidazole, 300 mM NaCl and 57.5 mM of $NaH_2PO_4 \cdot H_2O$. The RBD protein was then eluted with three column volumes of the elution buffer containing 234 mM of imidazole, 300 mM NaCl and 57.5 mM of $NaH_2PO_4 \cdot H_2O$. The eluted solution was concentrated, and the buffer was replaced with PBS using a 10 kDa Amicon filter (Millipore Sigma, UFC901008). RBD protein integrity was

verified by SDS-PAGE, aliquoted to minimize freeze–thaw cycles and stored at −80 °C. Prefusion trimer spike production details are published elsewhere [57].

Mice Immunization and Sample Collection

All experiments performed on mice were conducted in accordance with Ontario Animals for Research Act and were approved by the University of Ottawa Animal Ethics Committee (protocol BMI-3649). Female BALB/C mice (6–12 weeks) were obtained from Charles River Laboratories (Saint-Constant, Canada). Prior to each immunization, mice were anesthetized with isoflurane and vaccinated intranasally (25 µL per nare) with 20 µg RBD or spike protein admixed with cholera toxin (CT) (1 µg per dose) used here as a positive control (Sigma, Oakville, ON, Canada) or AMVAD mucosal adjuvant (400 µg per dose) on days 0 and 21. The AMVAD formulation was prepared with total polar lipids from *Methanobrevibacter smithii* and combined with antigen in a saline-based solution containing a final concentration of 15 mM $CaCl_2$, as previously described [48,51]. Control groups include mice vaccinated with phosphate-buffered saline (PBS), protein alone (spike) and adjuvant alone (CT or AMVAD). Plasma was collected periodically throughout the study via submandibular vein and heart puncture at end point. Seven days post boost, bronchoalveolar lavage fluids (BALF) and nasal wash were collected to assess for mucosal humoral responses. Nasal wash and BALF samples were concentrated through 50 kDa Pierce Protein Concentrators column (Thermo Fisher Scientific, Waltham, MA, USA) according to the manufacturer's instructions, with volumes normalized prior to concentration.

Indirect ELISA to Evaluate Anti-SARS-CoV-2 Immunoreactivity in Serum Samples (Serology)

The same SARS-CoV-2 trimer spike or RBD antigens that were administered for immunizations for used as coating antigens for serological assays. SARS-CoV-2 trimer spike or RBD were diluted in sterile 1X PBS (Wisent Bioproducts, 311-010-CL, St-Bruno, QC, Canada) to 4 µg/mL and coated onto 384-well Immuno plates (Thermo Fisher, #60372, Waltham, MA, USA) (10 µL/well) overnight at 4 °C. Plates were washed three times with 100 µL of PBS-T and blocked for 1 h with a blocking buffer (PBS-T + 3% non-fat milk powder, *w*/*v*) on a shaker at room temperature. Serum samples were diluted 1:100 (following first immunization) and (1:2000 following second immunization), BALF was diluted 4- to 30-fold and nasal wash was diluted 4-fold in dilution buffer (PBS-T + 1% non-fat milk powder, *w*/*v*). After blocking, plates were washed thrice with PBS-T, and followed by addition of 10 µL of the respective diluted samples. The plates were incubated for 2 h on a shaker at room temperature, washed thrice with PBS-T followed by the addition of 10 µL of the respective secondary-HRP antibody at specified dilutions: 1:4000 secondary IgG Anti-Mouse, Human ads-HRP (Southern Biotech, 1030-05, Birmingham, AL, USA) and 1:1000 secondary Anti-Mouse IgA-HRP (Southern Biotech, 1040-05, Birmingham, AL, USA). Plates were incubated for 1 h on a shaker, washed thrice with PBS-T followed by the addition with 10 µL of the SuperSignal ELISA Pico Chemiluminescent Substrate (Thermo Scientific, 37069, Waltham, MA, USA). Luminescence intensity was measured with BIOTEK Synergy Neo2 plate reader for 20 ms/well at a read height of 1.0 mm. Wells filled with dilution

buffer in place of sample accounted for background luminescence and were subtracted from the sample values.

Surrogate Neutralization ELISA (snELISA) Assay to Evaluate Neutralization Activity in Serum Samples

The described methodology was adapted from the surrogate neutralization ELISA assay, as shown in Colwill et al. and Demone et al., for the evaluation of the relative inhibition of neutralizing antibodies to spike or RBD protein from binding to soluble ACE2 [57,58]. Briefly, SARS-CoV-2 spike or RBD protein were diluted in sterile 1X PBS to 8 µg/mL and coated onto 384-well Immuno plates (12.5 µL/well) overnight at 4 °C. Plates were washed 3 times with PBS-T and blocked for 1 h while shaking. Plasma samples were 1:6 serially diluted in a dilution buffer while BALF was left undiluted, applied to wells (20 µL/well) and incubated for 2 h while shaking at room temperature. Plates were washed thrice, followed by the addition of biotinylated ACE2, as shown in
Abe et al. [59], diluted to 0.35 ng/µL in a dilution buffer (20 µL/well). Plates were washed thrice with PBS-T followed by the addition of 20 µL per well of Streptavidin–Peroxidase polymer (Sigma, S2438, Oakville, ON, Canada) diluted in dilution buffer to 1.25 ng/µL. Following 1 h incubation, plates were washed thrice with PBS-T and freshly diluted SuperSignal ELISA Pico Chemiluminescent Substrate (mixed 1:1 ratio and diluted in equal volume with dH_2O, (*V*:*V*)) was applied (20 µL/well). Following 5 min of incubation while shaking, luminescence intensity was measured with BIO-TEK Synergy Neo2 plate reader for 20 ms/well at a read height of 1.0 mm. To assess the maximum binding signal, control wells were filled with a dilution buffer in place of serum followed by the addition of ACE2,
as previously. Relative percent inhibition was calculated as follows:

$$\% \, Inhibition = \left(1 - \frac{average\ mean\ of\ serum}{average\ mean\ of\ maximum}\right) \times 100$$

Serum dilution resulting in a 50% inhibition (half-maximal inhibitory dilution (ID_{50})) of spike or RBD protein from binding ACE2 receptor was determined using 4-parameter fitting with GraphPad Prism 9.1.2 software. When no neutralization activity was observed, the ID_{50} of the sample was arbitrarily set as half of the lowest dilution.

Patient Samples, Collection and Ethics Approval

Use of human samples for this study was approved by the University of Ottawa Ethics Review Board: Certificates H-04-20-5727, H-04-21-6643 and H-07-20-6009. The negative sample was taken from an individual with no history of SARS-CoV-2 infection and tested with PCR. Pooled negative samples were obtained from individuals negative for SARS-CoV-2 as tested by PCR and serology assay. Pooled serum samples were obtained from convalescent (2–16 weeks post-infection) or vaccinated patients (2–4 weeks post-vaccination) enrolled in surveillance studies

from different research studies post-2019. Samples were collected using standard phlebotomy procedures. Samples were de-identified and held at 4 ˚C for short-term handling and testing at University of Ottawa CL2+ biocontainment facility. All research was performed in accordance with current guidelines and regulations.

5.3 Results

Intranasal Administration of Adjuvanted RBD and Spike Antigens Induces Robust Humoral Systemic Responses in Mice

To assess immunogenicity of the intranasal subunit protein vaccine platform, we compared the ability of a stabilized prefusion trimeric spike or the RBD in eliciting mucosal and systemic antibody responses. Given that intranasally administered protein subunit vaccines have been shown to be poorly immunogenic on their own, we additionally assessed two different adjuvants: AMVAD and CT. Balb/c mice (n = 3/group) were immunized with controls (phosphate-buffered saline (PBS), soluble full spike trimer ectodomain, RBD, AMVAD or CT alone) or protein adjuvanted vaccine combinations (AMVAD + RBD, CT + RBD, AMVAD + spike, CT + spike) on day 0 and 21 (Figure 1A). Due to the limited amount of sample volumes obtained during the study and the numerous analyses we wanted to conduct, samples from immunized mice in each group were pooled together after confirming that the antibody responses in individual mice were similar. Figure 1B shows RBD or spike-specific IgG titers at various dilutions of three individual mice relative to pooled plasma samples, highlighting highly consistent seroconversion and antibody levels between mice within each group. Systemic antigen-specific IgG and IgA responses in plasma were measured after prime (day 20) (Figure 1C) or boost (day 35) (Figure 1D) immunization by enzyme-linked immunosorbent assay (ELISA) against RBD or spike. Following a single immunization, we show that there was poor induction of IgA antibodies with controls, including unadjuvanted antigens, as expected. In contrast, adjuvanted spike protein with AMVAD or CT elicited robust IgG titers in plasma (Figure 1C) that were significantly greater than with the adjuvanted RBD vaccine formulation after a single dose. As expected, we observed similar levels of RBD- and spike-directed IgG antibodies in mice immunized with the AMVAD + RBD vaccine formulation, highlighting that antibodies generated against RBD can access their epitopes on the trimeric spike. Following boosting, we observed a significant increase in both IgA and IgG antibody titers in plasma of mice immunized with either RBD- or spike-adjuvanted formulations, while controls showed no responses (Figure 1D). Consistent with previous results, we observed

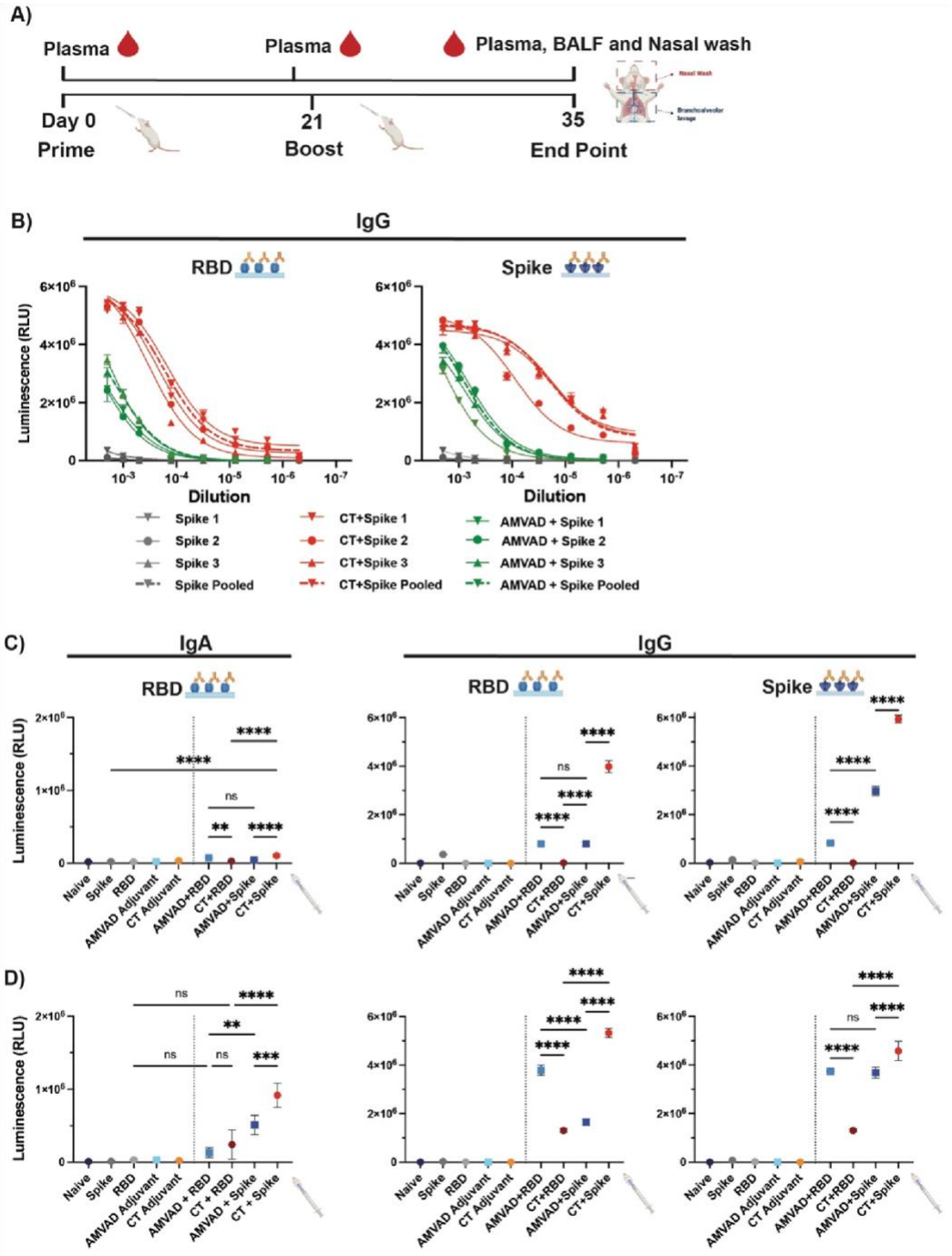

Figure 5.1 Humoral systemic responses from intranasal administration with adjuvanted RBD or spike antigens.

(**A**) Experimental design: Balb/c mice were intranasally immunized with RBD or spike protein adjuvanted with CT or AMVAD mucosal adjuvant on days 0 and 21. Control groups include mice vaccinated with phosphate-buffered saline (PBS), protein alone (RBD or spike) and adjuvant alone (CT or AMVAD). Seven days post-boost, plasma, bronchoalveolar lavage fluids (BALF) and nasal wash were collected to assess humoral responses. (**B**) Evaluation of RBD- and spike-specific IgG titers in plasma of individual mice vs. pooled plasma collected at end point. (**C**) Measurement of RBDand spike-specific IgA and IgG responses in plasma collected after first dose (day 20) (1/100 dilution) and (**D**) after second dose (day 35) (1/2000 dilution), analyzed by an indirect

ELISA. Statistical significance was calculated by one-way ANOVA followed by Tukey correction; n.s.: no statistical difference; ** $p \leq 0.01$, *** $p \leq 0.001$, **** $p \leq 0.0001$. Individual mice samples were pooled and analyzed in triplicate.

comparable levels of RBD- and spike-directed IgG titers in mice immunized with adjuvanted RBD. While there was a greater titer of spike- compared to RBD-directed IgG responses in the AMVAD + spike formulation; boosting induced a greater proportion of RBD-specific antibodies in this group. In contrast, vaccination with CT + spike induced the greatest humoral responses of all vaccine combinations tested, consistent with previously reported results [41,43,48,60], with endpoint IgG titers near assay saturation (~5×10^6) (Figure 1D).

Induction of robust systemic humoral immunity, in particular neutralizing responses, has been shown to be a strong correlate of protection against severe disease [11,33,61,62]. Next, we functionally assessed the neutralizing responses of antibodies in plasma following the second immunization using a surrogate ELISA neutralization (snELISA) assay shown to quantitatively correlate with pseudotyped or infectious virus neutralization assay [57]. We evaluated the relative inhibition of ACE2–spike and ACE2–RBD ligand interactions and showed that neutralization responses followed the trends of systemic IgG titers (Figure 2A). Consistent with previous observations with antibody responses, we saw similar ID_{50} values of ACE2–RBD and ACE2–spike interactions with plasma of mice immunized with AMVAD + RBD (Figure 2B). In alignment with the ELISA results (Figure 1D), mice immunized with AMVAD + RBD showed significantly greater inhibition of ACE2–RBD than that observed with AMVAD + spike, thus suggesting that RBD immunogen focused antibody responses upon protective neutralizing epitopes localized within the RBD, preventing ACE2–RBD ligand interaction. In contrast, the ID_{50} of ACE2–spike interactions was comparable following immunizations with either AMVAD + RBD or AMVAD + spike, highlighting that neutralizing activity is not exclusively RBD directed. This is in line with other studies that suggest the influence of alternative neutralizing epitopes on the spike protein beyond the RBD, such as those in the N-terminal domain (Figure 2B) [18,33,63–65].

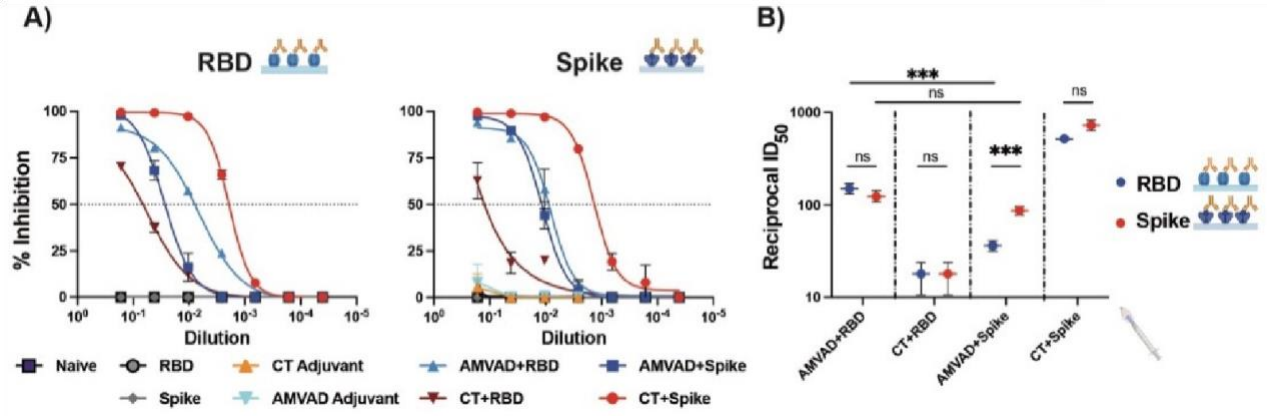

Figure 5.2 Systemic neutralizing antibodies induced by the intranasal administration with adjuvanted RBD or spike antigens.

(A) Measurement of relative inhibition of soluble ACE2 and immobilized RBD or spike interaction by neutralizing antibodies in plasma collected at endpoint by surrogate neutralization ELISA (snELISA). (**B**) Reciprocal ID_{50} neutralizing titer of adjuvanted vaccine formulations in blocking RBD (blue) or spike (red) and ACE2 ligand interaction. This assay is representative of technical triplicates and presented as mean ± standard deviation. Statistical significance was calculated by one-way ANOVA followed by Tukey correction; n.s.: no statistical difference; *** $p \leq 0.001$. Individual mice samples were pooled and analyzed in triplicate.

Adjuvanted Spike Antigen Immunization Induces Robust and Neutralizing Mucosal Responses in Mice

Given the limited ability of currently available vaccines in inducing mucosal immunity, we set out to investigate mucosal humoral responses at the point of viral entry, the respiratory mucosa. To this end, we characterized IgA and IgG responses in BALF and nasal wash collected at the end point. We show that adjuvants are required for the induction of robust IgG and IgA responses (Figure 3). In particular, we observed significantly greater IgA and IgG titers in mice immunized with spike-adjuvanted formulations. Consistent with systemic antibody levels, AMVAD + spike-immunized mice showed robust spike- and RBDspecific IgA titers in BALF; however, AMVAD + RBD antibody levels were very low against both antigens at the experimental endpoint and did not reach statistical significance relative to RBD control (Figure 3A). While both of the RBD-adjuvanted formulations induced IgG responses against spike and RBD in BALF, only CT + RBD-vaccinated mice showed measurable IgA titers. Interestingly, the AMVAD + RBD formulation induced measurable IgA titers in the nasal wash that are comparable to AMVAD + spike (Figure 3B), and these are overall higher than IgG levels. This highlights the ability of intranasal adjuvated-

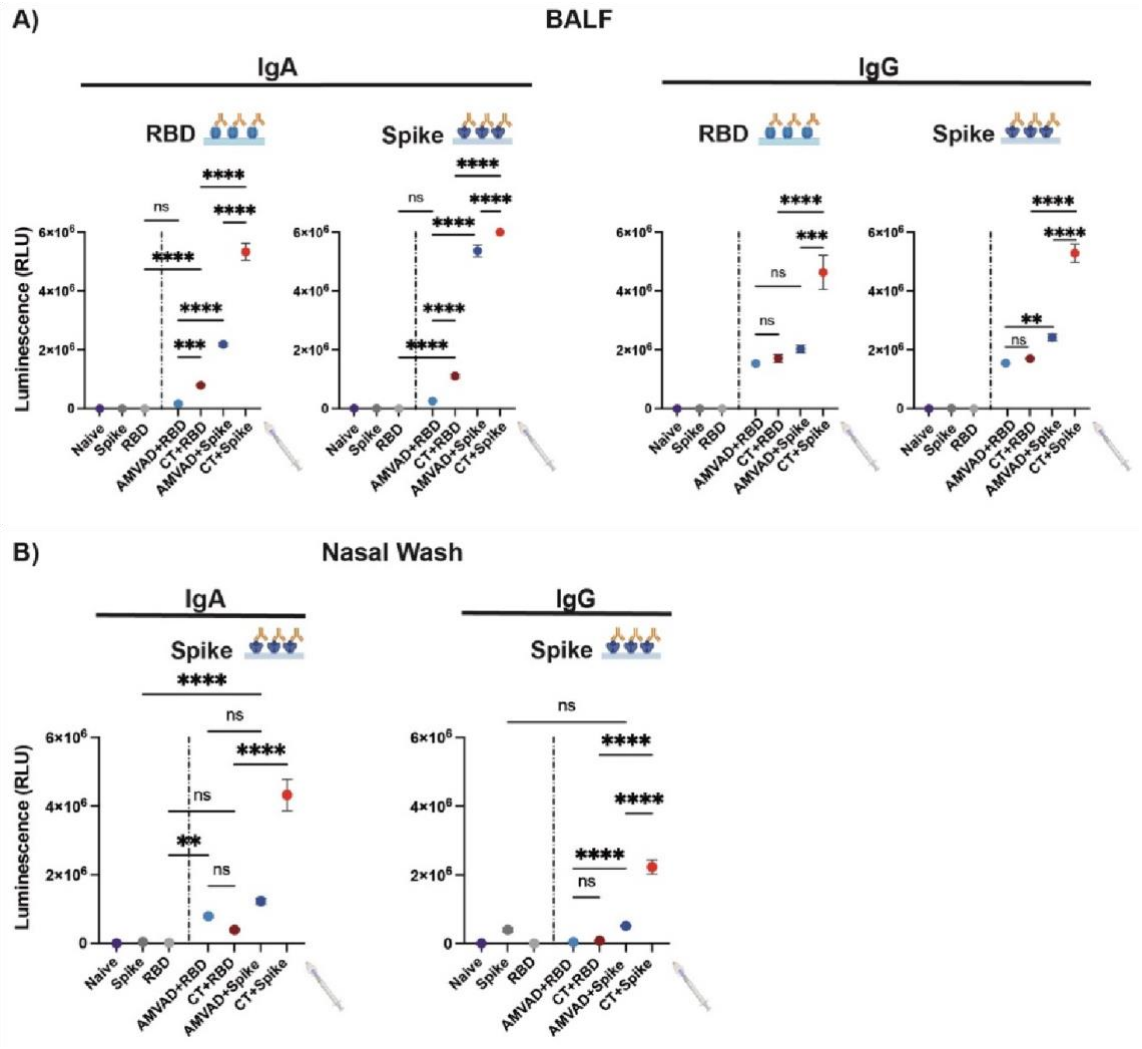

Figure 5.3 Antibody responses in BALF and the nasal cavity from intranasal administration with adjuvanted RBD or spike antigens.

Measurement of RBD- and spike-specific IgA and IgG responses in (**A**) BALF and (**B**) nasal wash collected at end point. BALF was diluted 4- and 30-fold for measurement of IgA and IgG specific titers, respectively. Nasal wash was diluted four-fold. Statistical significance was calculated by one-way ANOVA followed by Tukey correction; n.s.: no statistical difference; ** $p \leq 0.01$, *** $p \leq 0.001$, **** $p \leq 0.0001$. Individual mice samples were pooled and analyzed in triplicate.

antigen administration to more specifically induce IgA responses depending on the anatomical location within the mucosal compartment. Of note, the relative mucosal antibody titers measured in our study could be skewed given the high collection volume of buffer used during BALF and nasal wash sample acquisition relative to plasma collection.

Production of Neutralization Responses in Plasma of Immunized Mice against Ancestral and Variants of SARS-CoV-2

Next, we compared the relative inhibition of ACE2–spike interactions by neutralizing antibodies in plasma and BALF for the ancestral, Delta and Omicron variants (Figure 4). We show that both adjuvanted RBD and spike formulations induced neutralizing antibodies in plasma against the spike proteins of Delta, but only CT–spike and, to a lesser extent, AMVAD + spike, induced the production of neutralizing antibodies against the spike of the Omicron variant (B.1.1.529) (Figure 4A,B). In particular, vaccination of mice with AMVAD-adjuvanted RBD or spike elicited superior inhibition of ACE2–spike interactions for Wuhan and Delta variants compared to natural SARS-CoV-2 infection in humans (i.e., pooled convalescent (pooled conv.); Alpha variant) and similar inhibition as pooled plasma from individuals vaccinated with two doses of the Pfizer mRNA vaccine (Figure 4A,B). Despite overall lower neutralization titers in BALF relative to levels observed in plasma, we showed that neutralization responses significantly correlated to IgA titers. Indeed, only spike-adjuvanted immunized mice showed weak but detectable neutralizing titers against SARS-CoV-2, with only CT + spike showing neutralizing activity against all the variants tested, while there was poor induction of mucosal neutralization with the adjuvanted RBD formulations (Figure 4C).

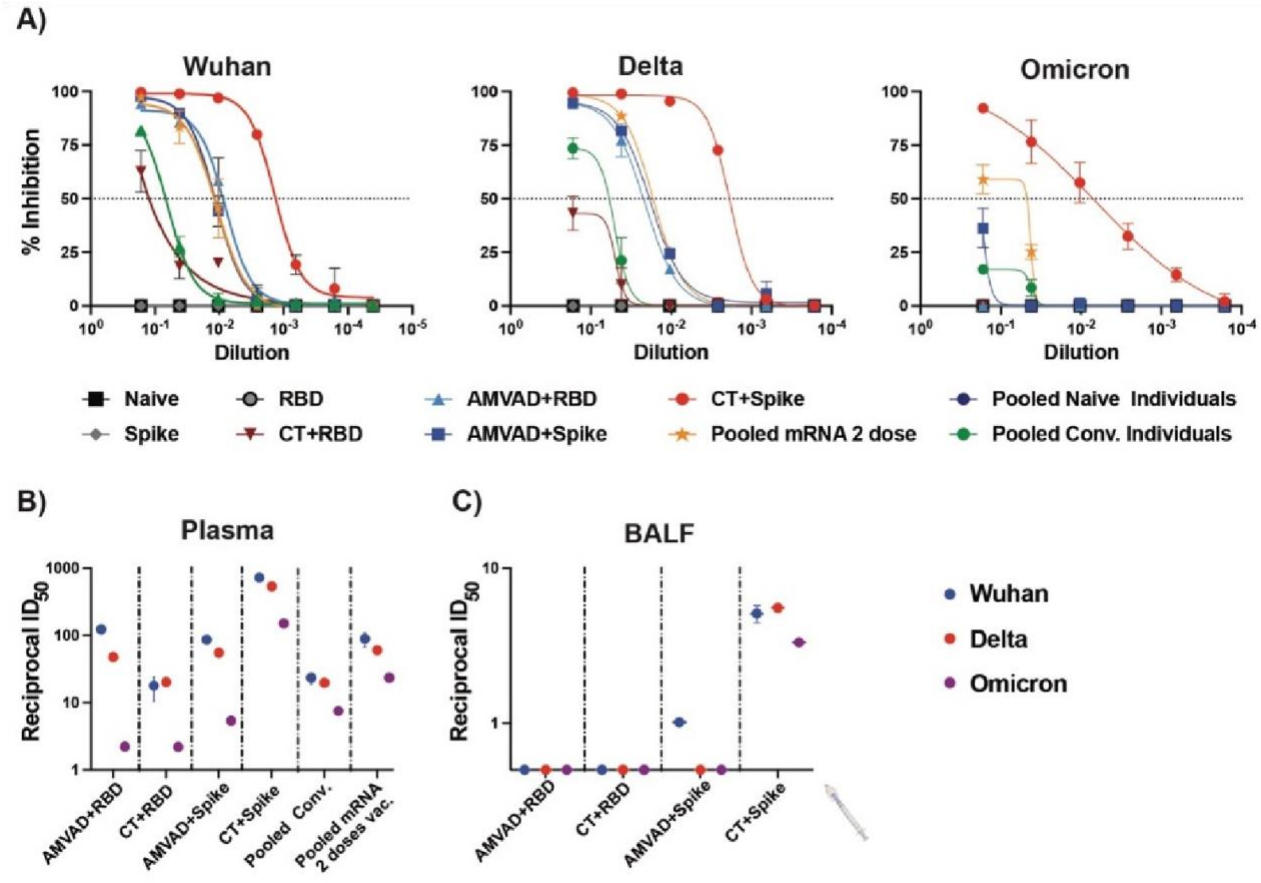

Figure 5.4 Neutralizing antibodies produced in plasma and BALF against SARS-CoV-2 variants.

(A) Measurement of relative inhibition of ligand interaction between soluble ACE2 and Wuhan ancestral reference strain, Delta variant and Omicron variant spike protein by neutralizing antibodies in plasma at endpoint analyzed by snELISA. Reciprocal ID_{50} neutralizing titer of adjuvanted vaccine formulations in (**B**) plasma and (**C**) BALF blocking Wuhan reference strain (blue), Delta variant (red) and Omicron variant (purple) spike and ACE2 ligand interaction. This assay is representative of technical triplicates and presented as mean ± standard deviation.

5.4 Discussion

Currently approved vaccines for SARS-CoV-2 induce robust humoral and cell-mediated immunity, which protect against severe disease, yet leave individuals vulnerable to infection at the URT where entry and replication first arise. Continued persistence of SARS-CoV-2, emergence of VOCs and poor induction of mucosal immunity contribute to decreased vaccine effectiveness against COVID-19 infection and onward transmission. Mucosal immunity is a critical component in the prevention and reduction of respiratory pathogen transmission [6,7]. Indeed, humoral responses in the mucosal compartment eliminate pathogens through various mechanisms,

including blocking viral attachment to the cognate receptor via neutralizing antibodies, complement fixation and antibody-dependent cellular cytotoxicity [66,67]. As such, a growing body of work in the literature highlights the important role of mucosal secretory IgA in protecting against respiratory bacterial and viral pathogens that infect through the oral or nasal routes [7,19–21,23,26–30,66–75]. Stimulation of these humoral- and tissue-specific cell-mediated responses could be indispensable to blunt viral infection at the site of SARS-CoV-2 replication and limit viral transmission.

Since potent humoral responses have been shown to be a strong correlate of vaccine effectiveness and protection against COVID-19, we first analyzed mucosal and systemic IgG and IgA responses in mice vaccinated with spike and RBD adjuvanted with either CT or AMVAD. We show robust induction of IgG and IgA in plasma, nasal wash and BALF in mice vaccinated with two doses of adjuvanted protein vaccines, but not with protein or adjuvant alone. In line with previous reports, our data suggests that the combined administration of antigen with AMVAD likely led to its direct delivery to antigen-presenting cells for effective protein processing and presentation. Although the mechanism of action of AMVAD remains to be elucidated, its grape-like structure encompasses the antigen and acts as a delivery vehicle to elicit both humoral and cellular response [48,52]. Of note, we observed that vaccination with the RBD-adjuvanted vaccine favored RBD directed antibodies in both systemic and mucosal compartments, while immunization with adjuvanted spike induced broadly targeting antibodies that encompassed epitopes within and beyond the RBD domain. These findings were recapitulated when we evaluated relative inhibition of ACE2–spike and ACE2–RBD ligand interaction, where there was significantly lower inhibition of ACE2–RBD interaction in mice immunized with AMVAD + spike relative to AMVAD + RBD, yet comparable inhibition of ACE2–spike interaction between these two groups. Although immunization with RBD led to robust induction of systemic neutralizing antibodies blocking ACE2–RBD interactions for both ancestral and Delta variants, these neutralizing antibodies were poorly cross-reactive against the Omicron variant, which harbors more than 15 mutations within the RBD alone, suggesting that these antibodies likely targeted epitopes on the RBD prone to antigenic drift and escape by emerging VOCs [29,76–79]. In line with other comparative protein subunit antigen immunogenicity studies via intramuscular vaccination [1,53,80,81], our findings suggest that intranasal immunization with adjuvanted spike formulation induced greater breadth of neutralizing antibodies that target both conserved and

variable epitopes of the spike. In addition, trimeric spike has been shown to be more immunogenic given the larger T cell epitope repertoire leading to a greater recruitment of T helper follicular cells and, thereby, an enhanced humoral response relative to the RBD antigen, as shown by Tan et al. [80]. Indeed, non-RBD directed antibodies have been shown to be important for both mucosal and systemic humoral immunity in preventing severe disease from both SARS-CoV-1 and SARS-CoV-2 infection [64,82,83].

In plasma, we observed that high levels of IgG correlated with increased neutralization titers, while in BALF, potent IgA levels correlated with neutralizing responses as observed in previous influenza and SARS-CoV-2 vaccination studies [29,66,75,84]. Notably, AMVAD + spike formulation induced significantly greater IgA levels in both plasma and BALF relative to AMVAD + RBD immunization. Given that RBD + AMVAD-immunized mice showed low levels of IgA and undetectable neutralizing activity in BALF, we speculate that mucosal IgA antibodies largely contributed to ACE2–spike inhibition observed in spike-adjuvanted groups. Thus, the spike's superior immunogenicity could also be attributed to its larger and stabilized trimeric structure compared to RBD's monomer, where the spike protein's repetitive trimeric antigen presentation could increase cross-linking to B cell receptors, inducing greater B cell activation and IgA response [85,86].

Induction of protective humoral immunity has been a major focus in COVID-19 vaccine development. Nevertheless, robust induction of secretory IgA antibodies is crucial given their potent and broadly neutralizing capabilities [20,29,66–69,71,87,88]. Studies of intranasal vaccines against influenza have highlighted that mucosal vaccination, compared to the intramuscular route, elicited potent cross-protection against heterosubtypic challenge of influenza and showed long-term immunity [66,89]. Additionally, in a proof-of-concept study, Xiao et al. demonstrated that intranasal immunization with defective viral particles provides powerful prophylactic, broad-spectrum protection from infection by SARS-CoV-2 and influenza virus by blocking viral replication and preventing reinfection [90]. This is further reiterated by several groups that showed superior protection with intranasal relative to intramuscular immunization in mice against challenge with ancestral SARS-CoV-2 strain and VOCs [19–21,23,24,30]. Indeed, Langel et al., demonstrated reduced SARS-CoV-2 airborne transmission in intranasally immunized hamsters [21]. In addition, Tang et al. demonstrated that convalescent individuals show increased levels of broadly neutralizing antibodies in BALF relative to vaccinated individuals, despite similar

systemic IgG titers [29]. Epidemiological surveillance studies highlight the important role that mucosal IgA may have in preventing SARS-CoV-2 infection. In fact, Sheikh et al. and Havervall et al. demonstrated that vaccinated participants who experienced breakthrough infections with divergent VOCs had lower titers of serum and mucosal IgA relative to those who did not experience an infection despite having comparable serum IgG titers [72,73]. Here, we showed an adjuvanted subunit vaccine platform that induced robust mucosal and systemic total and neutralizing antibody responses against rapidly emerging SARS-CoV-2 variants. In our direct comparison of the immunogenic profiles of SARS-CoV-2 spike and RBD antigens, we highlight the relative merit of additional epitopes of the larger spike protein that improve protein immunogenicity at the respiratory mucosa and neutralizing activity against VOCs. Continued SARS-CoV-2 transmission and replication, and selection pressure induced by vaccination or prior infection has led to the emergence of highly transmissible VOCs. Given the persistence of the SARS-CoV-2 pandemic and the shortcomings of currently available vaccines in effectively blocking transmission, our study may offer insights for selecting immunogenic targets for intranasal vaccine design against current and future VOCs. Thus, new modalities of vaccination that invoke mucosal immunity are crucial to neutralize the virus, limit the initial infection at the point of entry, prevent onward transmission and curtail the COVID-19 pandemic.

Author Contributions: Conceptualization, M.-A.L., B.A. and M.M.; methodology, M.-A.L., B.A., Y.G. and M.M.; formal analysis, M.-A.L., T.M.R., B.A. and M.M.; investigation, M.-A.L., T.M.R., L.D., Y.D., B.A. and M.M.; data curation, M.-A.L., T.M.R., B.A. and M.M.; writing—original draft preparation, M.-A.L., and M.M.; writing—review and editing, M.-A.L., T.M.R., L.D., Y.D., B.A., Y.G. and M.M.; supervision, M.-A.L.; project administration, M.-A.L.; funding acquisition, M.-A.L. All authors have read and agreed to the published version of the manuscript.

Funding: This study was supported in part by a COVID-19 Rapid Response grant by the Canadian Institutes of Health Research (CIHR; #VR2-172722) and by a grant supplement by the COVID-19 Immunity Task Force (CITF) to M-A Langlois. Production of COVID-19 reagents was financially supported by the NRC's Pandemic Response Challenge Program. M.M. holds an Ontario Graduate Scholarship. Y.G. holds a CIHR Frederick Banting and Charles Best graduate scholarship (CGS-Doctoral).

Institutional Review Board Statement: Use of human samples for this study was approved by the University of Ottawa Ethics Review Board: Certificates H-04-20-5727, H-04-21-6643 and H-07-20-6009.
All experiments performed on mice were conducted in accordance with Ontario Animals for Research
Act and were approved by the University of Ottawa Animal Ethics Committee (protocol BMI-3649).

Informed Consent Statement: Informed consent was obtained from all subjects involved in the study.

Data Availability Statement: The data presented in this study are available on request from the corresponding author. The data are not publicly available due to confidentiality issues with interviewees.

Acknowledgments: We sincerely thank Anthony Carter and the uOttawa surgical ACVS core for their technical support with sample set up and acquisition.

Conflicts of Interest: The authors declare no conflict of interest.

5.5 References

1. Cele, S.; Jackson, L.; Khoury, D.S.; Khan, K.; Moyo-Gwete, T.; Tegally, H.; San, J.E.; Cromer, D.; Scheepers, C.; Amoako, D.; et al. SARS-CoV-2 Omicron has extensive but incomplete escape of Pfizer BNT162b2 elicited neutralization and requires ACE2 for infection. *medRxiv* **2021**. [CrossRef]
2. Chemaitelly, H.; Tang, P.; Hasan, M.R.; AlMukdad, S.; Yassine, H.M.; Benslimane, F.M.; Al Khatib, H.A.; Coyle, P.; Ayoub, H.H.; Al Kanaani, Z.; et al. Waning of BNT162b2 Vaccine Protection against SARS-CoV-2 Infection in Qatar. *N. Engl. J. Med.* **2021**, *385*, e83. [CrossRef] [PubMed]
3. Greaney, A.J.; Starr, T.N.; Gilchuk, P.; Zost, S.J.; Binshtein, E.; Loes, A.N.; Hilton, S.K.; Huddleston, J.; Eguia, R.; Crawford, K.H.D.; et al. Complete Mapping of Mutations to the SARS-CoV-2 Spike Receptor-Binding Domain that Escape Antibody Recognition. *Cell Host Microbe* **2021**, *29*, 44–57.e9. [CrossRef] [PubMed]
4. Menni, C.; May, A.; Polidori, L.; Louca, P.; Wolf, J.; Capdevila, J.; Hu, C.; Ourselin, S.; Steves, C.J.; Valdes, A.M.; et al. COVID-19 vaccine waning and effectiveness and side-effects of boosters: A prospective community study from the ZOE COVID Study. *Lancet Infect. Dis.* **2022**, *22*, 1002–1010. [CrossRef] [PubMed]
5. Singanayagam, A.; Hakki, S.; Dunning, J.; Madon, K.J.; Crone, M.A.; Koycheva, A.; Derqui-Fernandez, N.; Barnett, J.L.; Whitfield, M.G.; Varro, R.; et al. Community transmission and viral load kinetics of the SARS-CoV-2 delta (B.1.617.2) variant in vaccinated and unvaccinated individuals in the UK: A prospective, longitudinal, cohort study. *Lancet Infect. Dis.* **2022**, *22*, 183–195. [CrossRef]
6. Krammer, F. SARS-CoV-2 vaccines in development. *Nature* **2020**, *586*, 516–527. [CrossRef] [PubMed]
7. Lavelle, E.C.; Ward, R.W. Mucosal vaccines—Fortifying the frontiers. *Nat. Rev. Immunol.* **2022**, *22*, 236–250. [CrossRef]
8. Kemp, S.A.; Cheng, M.T.K.; Hamilton, W.L.; Kamelian, K.; Indian, S.-C.-G.C.; Singh, S.; Rakshit, P.; Agrawal, A.; Illingworth, C.J.R.; Gupta, R.K. Transmission of B.1.617.2 Delta variant between vaccinated healthcare workers. *Sci. Rep.* **2022**, *12*, 10492. [CrossRef]
9. Chia, P.Y.; Ong, S.W.X.; Chiew, C.J.; Ang, L.W.; Chavatte, J.M.; Mak, T.M.; Cui, L.; Kalimuddin, S.; Chia, W.N.; Tan, C.W.; et al. Virological and serological kinetics of SARS-CoV-2 Delta variant vaccine breakthrough infections: A multicentre cohort study. *Clin. Microbiol. Infect.* **2022**, *28*, 612.e1–612.e7. [CrossRef]
10. Lange, B.; Gerigk, M.; Tenenbaum, T. Breakthrough Infections in BNT162b2-Vaccinated Health Care Workers. *N. Engl. J. Med.* **2021**, *385*, 1145–1146. [CrossRef]
11. Bartsch, Y.C.; Fischinger, S.; Siddiqui, S.M.; Chen, Z.; Yu, J.; Gebre, M.; Atyeo, C.; Gorman, M.J.; Zhu, A.L.; Kang, J.; et al. Discrete SARS-CoV-2 antibody titers track with functional humoral stability. *Nat. Commun.* **2021**, *12*, 1018. [CrossRef] [PubMed]
12. Bartsch, Y.C.; Wang, C.; Zohar, T.; Fischinger, S.; Atyeo, C.; Burke, J.S.; Kang, J.; Edlow, A.G.; Fasano, A.; Baden, L.R.; et al. Humoral signatures of protective and pathological SARS-CoV-2 infection in children. *Nat. Med.* **2021**, *27*, 454–462. [CrossRef] [PubMed]
13. Brouwer, P.J.M.; Caniels, T.G.; van der Straten, K.; Snitselaar, J.L.; Aldon, Y.; Bangaru, S.; Torres, J.L.; Okba, N.M.A.; Claireaux, M.; Kerster, G.; et al. Potent neutralizing antibodies from COVID-19 patients define multiple targets of vulnerability. *Science* **2020**, *369*, 643–650. [CrossRef]
14. Cao, Y.; Su, B.; Guo, X.; Sun, W.; Deng, Y.; Bao, L.; Zhu, Q.; Zhang, X.; Zheng, Y.; Geng, C.; et al. Potent Neutralizing Antibodies against SARS-CoV-2 Identified by High-Throughput Single-Cell Sequencing of Convalescent Patients' B Cells. *Cell* **2020**, *182*, 73–84.e16. [CrossRef] [PubMed]

15. Kreer, C.; Zehner, M.; Weber, T.; Ercanoglu, M.S.; Gieselmann, L.; Rohde, C.; Halwe, S.; Korenkov, M.; Schommers, P.; Vanshylla, K.; et al. Longitudinal Isolation of Potent Near-Germline SARS-CoV-2-Neutralizing Antibodies from COVID-19 Patients. *Cell* **2020**, *182*, 843–854.e12. [CrossRef] [PubMed]
16. Rogers, T.F.; Zhao, F.; Huang, D.; Beutler, N.; Burns, A.; He, W.T.; Limbo, O.; Smith, C.; Song, G.; Woehl, J.; et al. Isolation of potent

SARS-CoV-2 neutralizing antibodies and protection from disease in a small animal model. *Science* **2020**, *369*, 956–963. [CrossRef] 17. Zost, S.J.; Gilchuk, P.; Case, J.B.; Binshtein, E.; Chen, R.E.; Nkolola, J.P.; Schafer, A.; Reidy, J.X.; Trivette, A.; Nargi, R.S.; et al. Potently neutralizing and protective human antibodies against SARS-CoV-2. *Nature* **2020**, *584*, 443–449. [CrossRef]
18. Liu, L.; Wang, P.; Nair, M.S.; Yu, J.; Rapp, M.; Wang, Q.; Luo, Y.; Chan, J.F.; Sahi, V.; Figueroa, A.; et al. Potent neutralizing antibodies against multiple epitopes on SARS-CoV-2 spike. *Nature* **2020**, *584*, 450–456. [CrossRef]
19. Afkhami, S.; D'Agostino, M.R.; Zhang, A.; Stacey, H.D.; Marzok, A.; Kang, A.; Singh, R.; Bavananthasivam, J.; Ye, G.; Luo, X.; et al. Respiratory mucosal delivery of next-generation COVID-19 vaccine provides robust protection against both ancestral and variant strains of SARS-CoV-2. *Cell* **2022**, *185*, 896–915.e19. [CrossRef]
20. Mao, T.; Israelow, B.; Suberi, A.; Zhou, L.; Reschke, M.; Pena-Hernandez, M.A.; Dong, H.; Homer, R.J.; Saltzman, W.M.; Iwasaki, A. Unadjuvanted intranasal spike vaccine booster elicits robust protective mucosal immunity against sarbecoviruses. *Science* **2022**, *378*, eabo2523. [CrossRef]
21. Langel, S.N.; Johnson, S.; Martinez, C.I.; Tedjakusuma, S.N.; Peinovich, N.; Dora, E.G.; Kuehl, P.J.; Irshad, H.; Barrett, E.G.; Werts, A.; et al. Adenovirus type 5 SARS-CoV-2 vaccines delivered orally or intranasally reduced disease severity and transmission in a hamster model. *Sci. Transl. Med.* **2022**, *14*, eabn6868. [CrossRef] [PubMed]
22. Diaz, M.F.; Calderon, K.; Rojas-Neyra, A.; Vakharia, V.N.; Choque-Guevara, R.; Montalvan-Avalos, A.; Poma-Acevedo, A.; Rios-Matos, D.; Agurto-Arteaga, A.; Cauti-Mendoza, M.G.; et al. Intranasal vaccination of hamsters with a Newcastle disease virus vector expressing the S1 subunit protects animals against SARS-CoV-2 disease. *Sci. Rep.* **2022**, *12*, 10359. [CrossRef] [PubMed]
23. Hassan, A.O.; Feldmann, F.; Zhao, H.; Curiel, D.T.; Okumura, A.; Tang-Huau, T.L.; Case, J.B.; Meade-White, K.; Callison, J.; Lovaglio, J.; et al. A single intranasal dose of chimpanzee adenovirus-vectored vaccine protects against SARS-CoV-2 infection in rhesus macaques. *bioRxiv* **2021**. [CrossRef] [PubMed]
24. Bricker, T.L.; Darling, T.L.; Hassan, A.O.; Harastani, H.H.; Soung, A.; Jiang, X.; Dai, Y.N.; Zhao, H.; Adams, L.J.; Holtzman, M.J.; et al. A single intranasal or intramuscular immunization with chimpanzee adenovirus-vectored SARS-CoV-2 vaccine protects against pneumonia in hamsters. *Cell Rep.* **2021**, *36*, 109400. [CrossRef] [PubMed]
25. van Doremalen, N.; Purushotham, J.N.; Schulz, J.E.; Holbrook, M.G.; Bushmaker, T.; Carmody, A.; Port, J.R.; Yinda, C.K.; Okumura, A.; Saturday, G.; et al. Intranasal ChAdOx1 nCoV-19/AZD1222 vaccination reduces viral shedding after SARS-CoV-2

D614G challenge in preclinical models. *Sci. Transl. Med.* **2021**, *13*, eabh0755. [CrossRef] [PubMed]
26. King, R.G.; Silva-Sanchez, A.; Peel, J.N.; Botta, D.; Dickson, A.M.; Pinto, A.K.; Meza-Perez, S.; Allie, S.R.; Schultz, M.D.; Liu, M.; et al. Single-Dose Intranasal Administration of AdCOVID Elicits Systemic and Mucosal Immunity against SARS-CoV-2 and Fully Protects Mice from Lethal Challenge. *Vaccines* **2021**, *9*, 881. [CrossRef]
27. An, X.; Martinez-Paniagua, M.; Rezvan, A.; Sefat, S.R.; Fathi, M.; Singh, S.; Biswas, S.; Pourpak, M.; Yee, C.; Liu, X.; et al. Singledose intranasal vaccination elicits systemic and mucosal immunity against SARS-CoV-2. *iScience* **2021**, *24*, 103037. [CrossRef]

28. Du, Y.; Xu, Y.; Feng, J.; Hu, L.; Zhang, Y.; Zhang, B.; Guo, W.; Mai, R.; Chen, L.; Fang, J.; et al. Intranasal administration of a recombinant RBD vaccine induced protective immunity against SARS-CoV-2 in mouse. *Vaccine* **2021**, *39*, 2280–2287. [CrossRef]
29. Tang, J.; Zeng, C.; Cox, T.M.; Li, C.; Son, Y.M.; Cheon, I.S.; Wu, Y.; Behl, S.; Taylor, J.J.; Chakraborty, R.; et al. Respiratory mucosal immunity against SARS-CoV-2 following mRNA vaccination. *Sci. Immunol.* **2022**, *7*, eadd4853. [CrossRef]
30. Stark, F.C.; Akache, B.; Deschatelets, L.; Tran, A.; Stuible, M.; Durocher, Y.; McCluskie, M.J.; Agbayani, G.; Dudani, R.; Harrison, B.A.; et al. Intranasal immunization with a proteosome-adjuvanted SARS-CoV-2 spike protein-based vaccine is immunogenic and efficacious in mice and hamsters. *Sci. Rep.* **2022**, *12*, 9772. [CrossRef]
31. Hassan, A.O.; Kafai, N.M.; Dmitriev, I.P.; Fox, J.M.; Smith, B.K.; Harvey, I.B.; Chen, R.E.; Winkler, E.S.; Wessel, A.W.; Case, J.B.; et al. A Single-Dose Intranasal ChAd Vaccine Protects Upper and Lower Respiratory Tracts against SARS-CoV-2. *Cell* **2020**, *183*, 169–184.e13. [CrossRef] [PubMed]
32. Kleanthous, H.; Silverman, J.M.; Makar, K.W.; Yoon, I.K.; Jackson, N.; Vaughn, D.W. Scientific rationale for developing potent RBD-based vaccines targeting COVID-19. *npj Vaccines* **2021**, *6*, 128. [CrossRef] [PubMed]
33. Garcia-Beltran, W.F.; Lam, E.C.; Astudillo, M.G.; Yang, D.; Miller, T.E.; Feldman, J.; Hauser, B.M.; Caradonna, T.M.; Clayton, K.L.; Nitido, A.D.; et al. COVID-19-neutralizing antibodies predict disease severity and survival. *Cell* **2021**, *184*, 476–488 e411. [CrossRef] [PubMed]
34. Pinto, D.; Park, Y.J.; Beltramello, M.; Walls, A.C.; Tortorici, M.A.; Bianchi, S.; Jaconi, S.; Culap, K.; Zatta, F.; De Marco, A.; et al. Cross-neutralization of SARS-CoV-2 by a human monoclonal SARS-CoV antibody. *Nature* **2020**, *583*, 290–295. [CrossRef]
35. Barnes, C.O.; Jette, C.A.; Abernathy, M.E.; Dam, K.A.; Esswein, S.R.; Gristick, H.B.; Malyutin, A.G.; Sharaf, N.G.; Huey-Tubman, K.E.; Lee, Y.E.; et al. SARS-CoV-2 neutralizing antibody structures inform therapeutic strategies. *Nature* **2020**, *588*, 682–687. [CrossRef]
36. Piccoli, L.; Park, Y.J.; Tortorici, M.A.; Czudnochowski, N.; Walls, A.C.; Beltramello, M.; Silacci-Fregni, C.; Pinto, D.; Rosen, L.E.; Bowen, J.E.; et al. Mapping Neutralizing and Immunodominant Sites on the SARS-CoV-2 Spike Receptor-Binding Domain by Structure-Guided High-Resolution Serology. *Cell* **2020**, *183*, 1024–1042. [CrossRef]
37. Liang, Z.; Zhu, H.; Wang, X.; Jing, B.; Li, Z.; Xia, X.; Sun, H.; Yang, Y.; Zhang, W.; Shi, L.; et al. Adjuvants for Coronavirus Vaccines. *Front. Immunol.* **2020**, *11*, 589833. [CrossRef]
38. Fujkuyama, Y.; Tokuhara, D.; Kataoka, K.; Gilbert, R.S.; McGhee, J.R.; Yuki, Y.; Kiyono, H.; Fujihashi, K. Novel vaccine development strategies for inducing mucosal immunity. *Expert Rev. Vaccines* **2012**, *11*, 367–379. [CrossRef]
39. Chugh, Y.; Kapoor, P.; Kapoor, A.K. Intranasal drug delivery: A novel approach. *Indian J. Otolaryngol. Head Neck Surg.* **2009**, *61*, 90–94. [CrossRef]
40. Wang, Y.Y.; Lai, S.K.; So, C.; Schneider, C.; Cone, R.; Hanes, J. Mucoadhesive nanoparticles may disrupt the protective human mucus barrier by altering its microstructure. *PLoS ONE* **2011**, *6*, e21547. [CrossRef]
41. McGee, D.W.; Elson, C.O.; McGhee, J.R. Enhancing effect of cholera toxin on interleukin-6 secretion by IEC-6 intestinal epithelial cells: Mode of action and augmenting effect of inflammatory cytokines. *Infect. Immun.* **1993**, *61*, 4637–4644. [CrossRef] [PubMed]

42. Lucas, C.; Vogels, C.B.F.; Yildirim, I.; Rothman, J.E.; Lu, P.; Monteiro, V.; Gehlhausen, J.R.; Campbell, M.; Silva, J.; Tabachnikova, A.; et al. Impact of circulating SARS-CoV-2 variants on mRNA vaccine-induced immunity. *Nature* **2021**, *600*, 523–529. [CrossRef] [PubMed]
43. Lycke, N.; Bemark, M. Mucosal adjuvants and long-term memory development with special focus on CTA1-DD and other ADP-ribosylating toxins. *Mucosal Immunol.* **2010**, *3*, 556–566. [CrossRef] [PubMed]
44. Kim, Y.G. Microbiota Influences Vaccine and Mucosal Adjuvant Efficacy. *Immune Netw.* **2017**, *17*, 20–24. [CrossRef]
45. Clements, J.D.; Norton, E.B. The Mucosal Vaccine Adjuvant LT(R192G/L211A) or dmLT. *mSphere* **2018**, *3*, e00215-18. [CrossRef]
46. Lewis, D.J.; Huo, Z.; Barnett, S.; Kromann, I.; Giemza, R.; Galiza, E.; Woodrow, M.; Thierry-Carstensen, B.; Andersen, P.; Novicki, D.; et al. Transient facial nerve paralysis (Bell's palsy) following intranasal delivery of a genetically detoxified mutant of *Escherichia coli* heat labile toxin. *PLoS ONE* **2009**, *4*, e6999. [CrossRef]
47. Mutsch, M.; Zhou, W.; Rhodes, P.; Bopp, M.; Chen, R.T.; Linder, T.; Spyr, C.; Steffen, R. Use of the inactivated intranasal influenza vaccine and the risk of Bell's palsy in Switzerland. *N. Engl. J. Med.* **2004**, *350*, 896–903. [CrossRef]
48. Patel, G.B.; Zhou, H.; Ponce, A.; Chen, W. Mucosal and systemic immune responses by intranasal immunization using archaeal lipid-adjuvanted vaccines. *Vaccine* **2007**, *25*, 8622–8636. [CrossRef]
49. Patel, G.B.; Zhou, H.; Ponce, A.; Harris, G.; Chen, W. Intranasal immunization with an archaeal lipid mucosal vaccine adjuvant and delivery formulation protects against a respiratory pathogen challenge. *PLoS ONE* **2010**, *5*, e15574. [CrossRef]
50. Patel, G.B.; Chen, W. Archaeal lipid mucosal vaccine adjuvant and delivery system. *Expert Rev. Vaccines* **2010**, *9*, 431–440. [CrossRef]
51. Patel, G.B.; Ponce, A.; Zhou, H.; Chen, W. Safety of intranasally administered archaeal lipid mucosal vaccine adjuvant and delivery (AMVAD) vaccine in mice. *Int. J. Toxicol.* **2008**, *27*, 329–339. [CrossRef]
52. Patel, G.B.; Ponce, A.; Zhou, H.; Chen, W. Structural characterization of archaeal lipid mucosal vaccine adjuvant and delivery (AMVAD) formulations prepared by different protocols and their efficacy upon intranasal immunization of mice. *J. Liposome Res.* **2008**, *18*, 127–143. [CrossRef] [PubMed]
53. Akache, B.; Renner, T.M.; Tran, A.; Deschatelets, L.; Dudani, R.; Harrison, B.A.; Duque, D.; Haukenfrers, J.; Rossotti, M.A.; Gaudreault, F.; et al. Immunogenic and efficacious SARS-CoV-2 vaccine based on resistin-trimerized spike antigen SmT1 and SLA archaeosome adjuvant. *Sci. Rep.* **2021**, *11*, 21849. [CrossRef] [PubMed]
54. Akache, B.; Deschatelets, L.; Harrison, B.A.; Dudani, R.; Stark, F.C.; Jia, Y.; Landi, A.; Law, J.L.M.; Logan, M.; Hockman, D.; et al.
Effect of Different Adjuvants on the Longevity and Strength of Humoral and Cellular Immune Responses to the HCV Envelope Glycoproteins. *Vaccines* **2019**, *7*, 204. [CrossRef] [PubMed]
55. Krishnan, L.; Sad, S.; Patel, G.B.; Sprott, G.D. The potent adjuvant activity of archaeosomes correlates to the recruitment and activation of macrophages and dendritic cells In Vivo. *J. Immunol.* **2001**, *166*, 1885–1893. [CrossRef] [PubMed]
56. Krishnan, L.; Dicaire, C.J.; Patel, G.B.; Sprott, G.D. Archaeosome vaccine adjuvants induce strong humoral, cell-mediated, and memory responses: Comparison to conventional liposomes and alum. *Infect. Immun.* **2000**, *68*, 54–63. [CrossRef]

57. Colwill, K.; Galipeau, Y.; Stuible, M.; Gervais, C.; Arnold, C.; Rathod, B.; Abe, K.T.; Wang, J.H.; Pasculescu, A.; Maltseva, M.; et al. A scalable serology solution for profiling humoral immune responses to SARS-CoV-2 infection and vaccination. *Clin. Transl. Immunol.* **2022**, *11*, e1380. [CrossRef]
58. Demone, J.; Maltseva, M.; Nourimand, M.; Nasr-Sharif, M.; Galipeau, Y.; Alarcon, E.I.; Langlois, M.A.; MacLean, A.M. Scalable agroinfiltration-based production of SARS-CoV-2 antigens for use in diagnostic assays and subunit vaccines. *PLoS ONE* **2022**, *17*, e0277668. [CrossRef]
59. Abe, K.T.; Li, Z.; Samson, R.; Samavarchi-Tehrani, P.; Valcourt, E.J.; Wood, H.; Budylowski, P.; Dupuis, A.P., II; Girardin, R.C.; Rathod, B.; et al. A simple protein-based surrogate neutralization assay for SARS-CoV-2. *JCI Insight* **2020**, *5*, e142362. [CrossRef]
60. Mattsson, J.; Schon, K.; Ekman, L.; Fahlen-Yrlid, L.; Yrlid, U.; Lycke, N.Y. Cholera toxin adjuvant promotes a balanced Th1/Th2/Th17 response independently of IL-12 and IL-17 by acting on Gsalpha in $CD11b^{+}$ DCs. *Mucosal Immunol.* **2015**, *8*, 815–827. [CrossRef]
61. Cromer, D.; Steain, M.; Reynaldi, A.; Schlub, T.E.; Wheatley, A.K.; Juno, J.A.; Kent, S.J.; Triccas, J.A.; Khoury, D.S.; Davenport, M.P. Neutralising antibody titres as predictors of protection against SARS-CoV-2 variants and the impact of boosting: A meta-analysis. *Lancet Microbe* **2022**, *3*, e52–e61. [CrossRef] [PubMed]
62. Khoury, D.S.; Cromer, D.; Reynaldi, A.; Schlub, T.E.; Wheatley, A.K.; Juno, J.A.; Subbarao, K.; Kent, S.J.; Triccas, J.A.; Davenport, M.P. Neutralizing antibody levels are highly predictive of immune protection from symptomatic SARS-CoV-2 infection. *Nat. Med.* **2021**, *27*, 1205–1211. [CrossRef] [PubMed]
63. Li, T.; Han, X.; Gu, C.; Guo, H.; Zhang, H.; Wang, Y.; Hu, C.; Wang, K.; Liu, F.; Luo, F.; et al. Potent SARS-CoV-2 neutralizing antibodies with protective efficacy against newly emerged mutational variants. *Nat. Commun.* **2021**, *12*, 6304. [CrossRef] [PubMed]
64. Ng, K.W.; Faulkner, N.; Finsterbusch, K.; Wu, M.; Harvey, R.; Hussain, S.; Greco, M.; Liu, Y.; Kjaer, S.; Swanton, C.; et al. SARS-CoV-2 S2-targeted vaccination elicits broadly neutralizing antibodies. *Sci. Transl. Med.* **2022**, *14*, eabn3715. [CrossRef] [PubMed]
65. Chi, X.; Yan, R.; Zhang, J.; Zhang, G.; Zhang, Y.; Hao, M.; Zhang, Z.; Fan, P.; Dong, Y.; Yang, Y.; et al. A neutralizing human antibody binds to the N-terminal domain of the Spike protein of SARS-CoV-2. *Science* **2020**, *369*, 650–655. [CrossRef] [PubMed]
66. Oh, J.E.; Song, E.; Moriyama, M.; Wong, P.; Zhang, S.; Jiang, R.; Strohmeier, S.; Kleinstein, S.H.; Krammer, F.; Iwasaki, A. Intranasal priming induces local lung-resident B cell populations that secrete protective mucosal antiviral IgA. *Sci. Immunol.* **2021**, *6*, eabj5129. [CrossRef] [PubMed]
67. Iwasaki, A. Exploiting Mucosal Immunity for Antiviral Vaccines. *Annu. Rev. Immunol.* **2016**, *34*, 575–608. [CrossRef] [PubMed]
68. Lindley, R.A.; Steele, E.J. Analysis of SARS-CoV-2 haplotypes and genomic sequences during 2020 in Victoria, Australia, in the context of putative deficits in innate immune deaminase anti-viral responses. *Scand. J. Immunol.* **2021**, *94*, e13100. [CrossRef]
69. Gorczynski, R.M.; Lindley, R.A.; Steele, E.J.; Wickramasinghe, N.C. Nature of Acquired Immune Responses, Epitope Specificity and Resultant Protection from SARS-CoV-2. *J. Pers. Med.* **2021**, *11*, 1253. [CrossRef]
70. Wilkie, B.N. Respiratory tract immune response to microbial pathogens. *J. Am. Vet. Med. Assoc.* **1982**, *181*, 1074–1079.

71. Sheikh-Mohamed, S.; Sanders, E.C.; Gommerman, J.L.; Tal, M.C. Guardians of the oral and nasopharyngeal galaxy: IgA and protection against SARS-CoV-2 infection. *Immunol. Rev.* **2022**, *309*, 75–85. [CrossRef] [PubMed]
72. Sheikh-Mohamed, S.; Isho, B.; Chao, G.Y.C.; Zuo, M.; Cohen, C.; Lustig, Y.; Nahass, G.R.; Salomon-Shulman, R.E.; Blacker, G.; Fazel-Zarandi, M.; et al. Systemic and mucosal IgA responses are variably induced in response to SARS-CoV-2 mRNA vaccination and are associated with protection against subsequent infection. *Mucosal Immunol.* **2022**, *15*, 799–808. [CrossRef] [PubMed]
73. Havervall, S.; Marking, U.; Svensson, J.; Greilert-Norin, N.; Bacchus, P.; Nilsson, P.; Hober, S.; Gordon, M.; Blom, K.; Klingstrom, J.; et al. Anti-Spike Mucosal IgA Protection against SARS-CoV-2 Omicron Infection. *N. Engl. J. Med.* **2022**, *387*, 1333–1336. [CrossRef] [PubMed]
74. Cervia, C.; Nilsson, J.; Zurbuchen, Y.; Valaperti, A.; Schreiner, J.; Wolfensberger, A.; Raeber, M.E.; Adamo, S.; Weigang, S.; Emmenegger, M.; et al. Systemic and mucosal antibody responses specific to SARS-CoV-2 during mild versus severe COVID-19.
J. Allergy Clin. Immunol. **2021**, *147*, 545–557.e9. [CrossRef]
75. Sterlin, D.; Mathian, A.; Miyara, M.; Mohr, A.; Anna, F.; Claer, L.; Quentric, P.; Fadlallah, J.; Devilliers, H.; Ghillani, P.; et al. IgA dominates the early neutralizing antibody response to SARS-CoV-2. *Sci. Transl. Med.* **2021**, *13*, eabd2223. [CrossRef]
76. Schmidt, F.; Muecksch, F.; Weisblum, Y.; Da Silva, J.; Bednarski, E.; Cho, A.; Wang, Z.; Gaebler, C.; Caskey, M.; Nussenzweig, M.C.; et al. Plasma Neutralization of the SARS-CoV-2 Omicron Variant. *N. Engl. J. Med.* **2022**, *386*, 599–601. [CrossRef]
77. Burki, T.K. Omicron variant and booster COVID-19 vaccines. *Lancet Respir. Med.* **2022**, *10*, e17. [CrossRef]
78. Liu, L.; Iketani, S.; Guo, Y.; Chan, J.F.; Wang, M.; Liu, L.; Luo, Y.; Chu, H.; Huang, Y.; Nair, M.S.; et al. Striking antibody evasion manifested by the Omicron variant of SARS-CoV-2. *Nature* **2022**, *602*, 676–681. [CrossRef]
79. Yamasoba, D.; Kimura, I.; Nasser, H.; Morioka, Y.; Nao, N.; Ito, J.; Uriu, K.; Tsuda, M.; Zahradnik, J.; Shirakawa, K.; et al. Virological characteristics of the SARS-CoV-2 Omicron BA.2 spike. *Cell* **2022**, *185*, 2103–2115.e19. [CrossRef]
80. Tan, H.X.; Juno, J.A.; Lee, W.S.; Barber-Axthelm, I.; Kelly, H.G.; Wragg, K.M.; Esterbauer, R.; Amarasena, T.; Mordant, F.L.; Subbarao, K.; et al. Immunogenicity of prime-boost protein subunit vaccine strategies against SARS-CoV-2 in mice and macaques. *Nat. Commun.* **2021**, *12*, 1403. [CrossRef]
81. Mandolesi, M.; Sheward, D.J.; Hanke, L.; Ma, J.; Pushparaj, P.; Perez Vidakovics, L.; Kim, C.; Adori, M.; Lenart, K.; Lore, K.; et al. SARS-CoV-2 protein subunit vaccination of mice and rhesus macaques elicits potent and durable neutralizing antibody responses. *Cell Rep. Med.* **2021**, *2*, 100252. [CrossRef] [PubMed]
82. Zhong, X.; Yang, H.; Guo, Z.F.; Sin, W.Y.; Chen, W.; Xu, J.; Fu, L.; Wu, J.; Mak, C.K.; Cheng, C.S.; et al. B-cell responses in patients who have recovered from severe acute respiratory syndrome target a dominant site in the S2 domain of the surface spike glycoprotein. *J. Virol.* **2005**, *79*, 3401–3408. [CrossRef] [PubMed]
83. Zohar, T.; Loos, C.; Fischinger, S.; Atyeo, C.; Wang, C.; Slein, M.D.; Burke, J.; Yu, J.; Feldman, J.; Hauser, B.M.; et al. Compromised Humoral Functional Evolution Tracks with SARS-CoV-2 Mortality. *Cell* **2020**, *183*, 1508–1519.e12. [CrossRef] [PubMed]
84. Butler, S.E.; Crowley, A.R.; Natarajan, H.; Xu, S.; Weiner, J.A.; Bobak, C.A.; Mattox, D.E.; Lee, J.; Wieland-Alter, W.; Connor,

R.I.; et al. Distinct Features and Functions of Systemic and Mucosal Humoral Immunity Among SARS-CoV-2 Convalescent Individuals. *Front. Immunol.* **2020**, *11*, 618685. [CrossRef] [PubMed]

85. Bachmann, M.F.; Zinkernagel, R.M. Neutralizing antiviral B cell responses. *Annu. Rev. Immunol.* **1997**, *15*, 235–270. [CrossRef] 86. Bachmann, M.F.; Jennings, G.T. Vaccine delivery: A matter of size, geometry, kinetics and molecular patterns. *Nat. Rev. Immunol.* **2010**, *10*, 787–796. [CrossRef]
87. Suzuki, T.; Kawaguchi, A.; Ainai, A.; Tamura, S.; Ito, R.; Multihartina, P.; Setiawaty, V.; Pangesti, K.N.; Odagiri, T.; Tashiro, M.; et al. Relationship of the quaternary structure of human secretory IgA to neutralization of influenza virus. *Proc. Natl. Acad. Sci. USA* **2015**, *112*, 7809–7814. [CrossRef]
88. Zeng, W.; Ma, H.; Ding, C.; Yang, Y.; Sun, Y.; Huang, X.; He, W.; Xiang, Y.; Gao, Y.; Jin, T. Characterization of SARS-CoV-2-specific antibodies in COVID-19 patients reveals highly potent neutralizing IgA. *Signal Transduct. Target. Ther.* **2021**, *6*, 35. [CrossRef]
89. Zens, K.D.; Chen, J.K.; Farber, D.L. Vaccine-generated lung tissue-resident memory T cells provide heterosubtypic protection to influenza infection. *JCI Insight* **2016**, *1*, e85832. [CrossRef]
90. Xiao, Y.; Lidsky, P.V.; Shirogane, Y.; Aviner, R.; Wu, C.T.; Li, W.; Zheng, W.; Talbot, D.; Catching, A.; Doitsh, G.; et al. A defective viral genome strategy elicits broad protective immunity against respiratory viruses. *Cell* **2021**, *184*, 6037–6051.e14. [CrossRef]

6 Chapter 6: Systemic and Mucosal Antibody Responses to SARS-CoV-2 Variant-Specific Prime-and-Boost and Prime-and-Spike Vaccination: A Comparison of Intramuscular and Intranasal Bivalent Vaccine Administration in a Murine Model

Maltseva M., Galipeau, Y., McClauskie P., Castonguay N., Cooper C., and Langlois M-A. (2024). (Submitted to npj Vaccines)

6.1 Abstract

The rapid genetic evolution of SARS-CoV-2 has led to the emergence of immune-evading, highly transmissible variants of concern (VOCs). This prompts the need for next-generation vaccines that elicit robust mucosal immunity in the airways to directly curb viral infection. Here, we investigate the impact of heterologous variant prime-boost regimens on humoral responses, focusing on intramuscular (IM) and intranasal (IN) routes of administration. Using a murine model, we assessed the immunogenicity of unadjuvanted protein boosts with Wu-1, Omicron BA.4/5, or Wu-1 + BA.4/5 spike antigens following monovalent or bivalent IM priming with mRNA-LNP vaccines. IM priming induced strong systemic total and neutralizing antibody responses that were further enhanced by IN boosts with BA.4/5. IN boosting achieved the broadest serum neutralization across all VOCs tested. Notably, bivalent mRNA-LNP IM priming induced robust, cross-variant serum neutralizing antibody production, independent of subsequent IN boost combinations. IgA production correlated more strongly with neutralization in bronchoalveolar lavage than IgG, with compartmentalized mucosal responses observed exclusively in IN-boosted mice. Our findings highlight the benefit of including distinct antigenic variants in the prime vaccination followed by a variant-tailored IN boost to elicit both systemic and mucosal variant-specific responses that are potentially capable of reducing SARS-CoV-2 transmission.

HIGHLIGHTS

- Intranasal (IN) prime and spike vaccination is more effective than intramuscular (IM) prime and boost at producing IgA response across diverse mucosal compartments.
- Monovalent RNA-LNP IM priming establishes the reference for variant-specific imprinting
- Bivalent mRNA-LNP IM priming expands neutralizing antibody breadth in serum against new variants.
- Bivalent mRNA-LMP IM priming enables the IN booter vaccination to neutralize specific variants more efficiently.
- Variant-specific IN boosting significantly broadens serum neutralization, outperforming monovalent mRNA-LNP IM boosting.
- Variant-specific IN boosting induces distinct antigen-specific IgA responses in nasal wash and BALF.

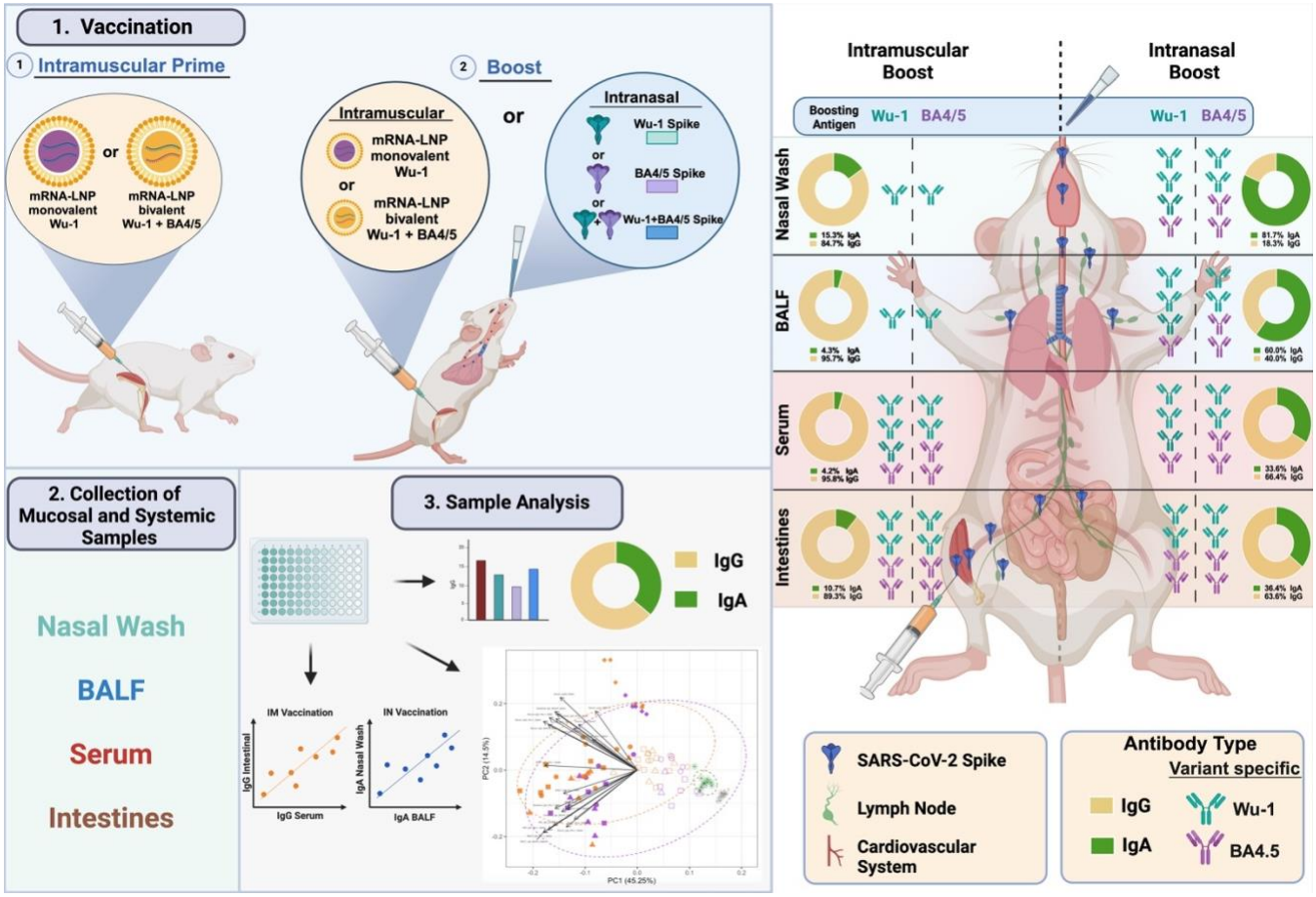

6.2 Introduction

The ongoing genetic evolution of severe acute respiratory syndrome coronavirus-2 (SARS-CoV-2) and the emergence of highly transmissible VOCs have significantly hampered vaccine effectiveness against transmission and symptomatic infection [1-17]. Although booster doses offer protection against severe disease and hospitalization, challenges such as waning immunity, continuous exposure to immune-evasive VOC, and insufficient induction of mucosal immunity have notably decreased vaccine effectiveness, contributing to the sustained circulation of SARS-CoV-2 [5-11,17-23]. The spike protein of SARS-CoV-2 serves as the primary antigenic target of currently approved vaccines, owing to its high immunogenicity, which elicits robust cellular and humoral responses [24-29]. The substantial antigenic distance between the recently emerged VOCs and the ancestral (Wu-1) SARS-CoV-2 strain, on which the initial COVID-19 vaccines were based, prompts the need to update and tailor vaccines to match the spike proteins of predicted circulating variants, akin to the strategy used in seasonal influenza vaccination.

Following the emergence of Omicron and its sub-variants, vaccine effectiveness and the induction of *de novo* variant-specific responses has varied after boosting with updated, variant-tailored vaccines[30-39]. While boosting with these updated vaccines led to a marked increase in neutralizing antibody titers, the highest responses were directed against the ancestral strain, with varying levels of neutralization of recently emerged VOCs, such as Omicron sub-variants XBB.1.5, EG.5.1, and JN.1[4,20,31,40-44 37 45]. These sub-variants possess mutations in key antigenic sites, enabling them to still evade neutralizing antibodies boosted by updated, variant tailored vaccines[43,44,46]. This diminished neutralization of current VOCs emphasizes the immune system's propensity to favor cross-reactive recall responses with greater affinity to the original strain over the generation of *de novo* antibodies specific to latest exposure, an immunological phenomenon known as immune imprinting [4,20,37,40,41,47-50 51-53]. Thus, boosting strategies that address immune evasion and enhance cross-protection at the site of viral entry are crucial to counter the challenges posed by the continuous emergence of antigenically mismatched variants.

Although intramuscular (IM) vaccination elicits potent systemic cellular and humoral immune responses against respiratory viruses, it leaves vaccine recipients susceptible to infection and viral replication at the primary entry point for SARS-CoV-2, the upper respiratory tract (URT). Mucosal

humoral and cellular responses have been shown to correlate with protection against breakthrough infections caused by recently emerged VOCs [22,23,42,54-58]. Several studies have demonstrated superior protection *in vivo* with oral and intranasal (IN) vaccinations compared to IM vaccination, due to the induction of local immunity in the URT, which limits viral replication and significantly reduces onward transmission of SARS-CoV-2 [22,59-78]. Recent studies have explored several prime-boost approaches, including different vaccine platforms and IN boosting strategies, in the context of pre-existing systemic immunity [22,69,71-74,78,79]. Notably, Mao et al. showed that an IM prime with an mRNA-LNP vaccine followed by an IN boost with an unadjuvanted SARS-CoV-2 spike protein—a strategy referred to as "Prime and Spike"—leverages systemic immunity to elicit robust mucosal immune responses [72]. Collectively, these studies indicate IN boosting, rather than relying on repeated IM vaccinations, may be a more effective strategy for achieving sustained and potent protection against SARS-CoV-2 reinfection. However, a gap remains in understanding how intranasal boosting strategies tailored to circulating variants affect humoral responses with pre-existing immunity induced by an antigenically distant strain.

In this study, we adapted the "Prime and Spike" approach by Mao *et al.* to examine the effects of heterologous prime-boost regimens on humoral responses, focusing on different administration routes and variant-tailored vaccine formulations[72]. Understanding the impact of different vaccination strategies on immune responses across different anatomical compartments may aid in inducing protective mucosal responses against SARS-CoV-2 variants. Our findings indicate that the IM prime predominantly shapes the systemic humoral responses, driven primarily by neutralizing antibodies, while the IN boost further amplifies and focuses them. In contrast, the IN boost, rather than IM prime, had a greater influence on the outcome of variant-specific mucosal responses. Notably, we highlight that bivalent priming with two distinct variants significantly broadened the repertoire of overall neutralizing antibody responses against circulating VOCs at the start, which was further enhanced and focused by variant-specific IN boosting.

6.3 Results

We set out to assess the effect of a heterologous prime and boost vaccine regimens based on different administration routes (IM prime – IM boost vs. IM prime – IN boost) and vaccine formulations (homologous or heterologous prime – boost) on humoral responses in bulb/c mice

(Table 1). Mice were initially IM primed with either 1 μg monovalent mRNA-LNP encoding for SARS-CoV-2 Wu-1 antigen (n=5 per group) or a bivalent mRNA-LNP encoding for SARS-CoV-2 Wu-1 and BA4/5 antigens (n=7 per group). After 21 days, mice were boosted with either a second dose of a matching IM mRNA-LNP vaccine or an IN administration of an unadjuvanted Wu-1, BA.4/5, or admixed Wu-1+BA4/5 formulation of stabilized SARS-CoV-2 spike protein at 1 or 10 μg doses (Fig. 1A and Supp. Fig. 3). Control groups received PBS, one dose of IM mRNA-LNP, two doses of unadjuvanted protein via IN only or 1 dose of IM mRNA followed by IN boost with unadjuvanted NL63 seasonal coronavirus spike protein (Table 1). To evaluate the immunogenicity of the different immunization routes and heterologous prime-boost vaccine formulations, we focused on characterizing IgG and IgA antibody responses in distinct immunological and anatomical compartments. Thus, two weeks post-boost, we collected plasma, bronchoalveolar lavage (BAL), nasal and intestinal biofluids for a direct comparison of induced antibody profiles following different vaccine regimens (Fig. 1A).

Table 6.1 Prime-boost vaccination regimens administered to mice.

Type of administration (Prime – Boost)	**Type of vaccine formulation (Prime – Boost)**	**Prime** (day 1)	**Boost** (day 21)
IM – IN (control)	-	PBS	PBS
IM (control)	-	Monovalent mRNA-LNP	PBS
IM (control)	-	Bivalent mRNA-LNP	PBS
IN – IN (control)	Homologous	Wu-1 protein	Wu-1 protein
IM – IM (control)	Homologous	Monovalent mRNA-LNP	Monovalent mRNA-LNP
IM – IN	Homologous	Monovalent mRNA-LNP	Wu-1 protein
IM – IN	Heterologous	Monovalent mRNA-LNP	BA4/5 protein
IM – IN	Heterologous	Monovalent mRNA-LNP	Wu-1 + BA4/5 protein
IM – IM (control)	Homologous	Bivalent mRNA-LNP	Bivalent mRNA-LNP
IM – IN	Homologous	Bivalent mRNA-LNP	Wu-1 protein
IM – IN	Homologous	Bivalent mRNA-LNP	BA4/5 protein
IM – IN	Homologous	Bivalent mRNA-LNP	Wu-1 + BA4/5 protein
IM – IN	Heterologous	Bivalent mRNA-LNP	NL63 protein

*__IM__: intramuscular LMP-mRNA Monovalent: Pfizer-Comirnaty monovalent Wuhan (Wu-1) or bivalent (Wu-1 + BA.4/5) (1µg dose of total vaccine); **IN**: intranasal unadjuvanted spike protein as indicated (1µg or 10µg doses of total antigen).

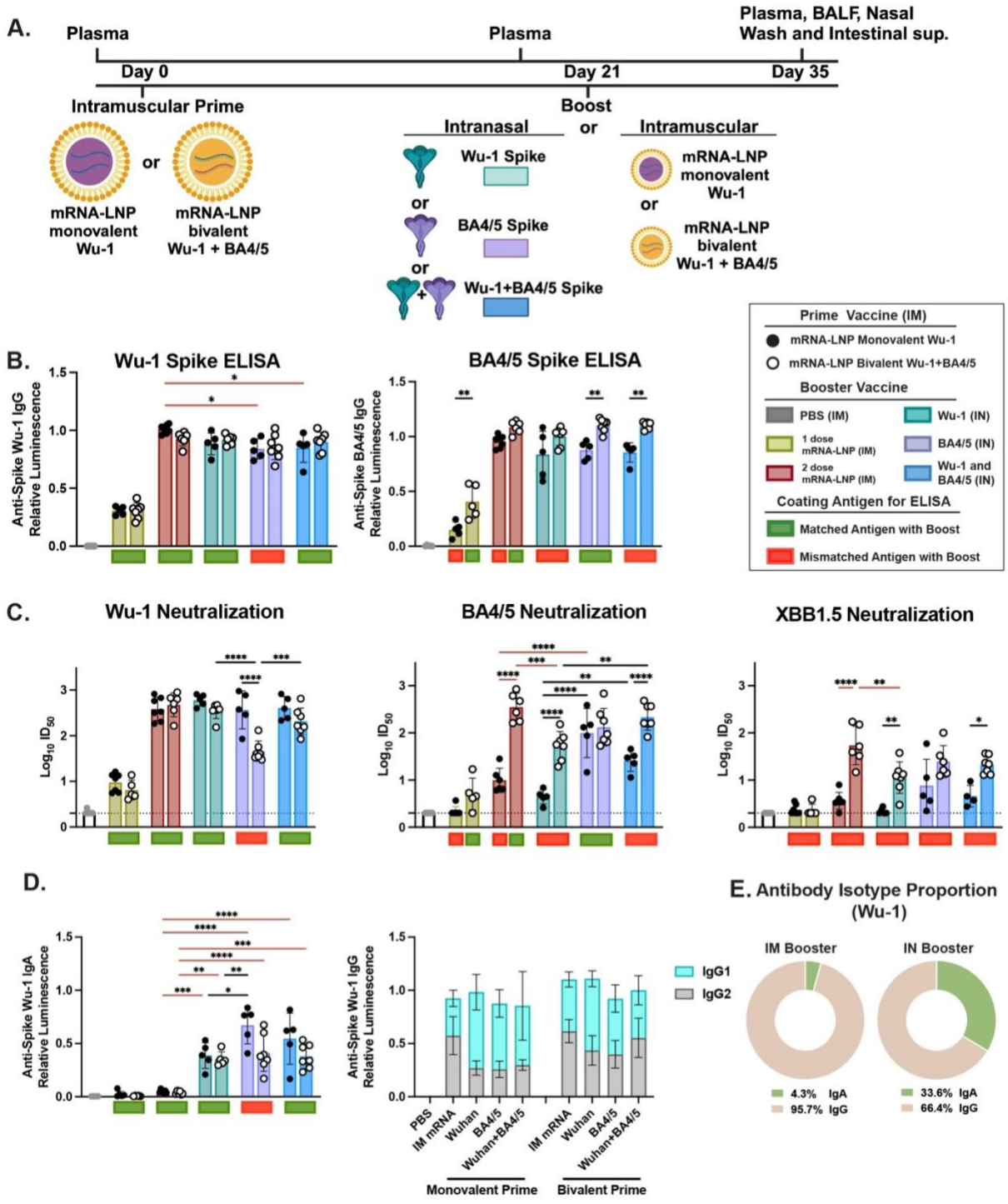

Figure 6.1 Characterization of systemic immune responses following a heterologous systemic prime and mucosal IN boost vaccination.

A) Experimental design and heterologous vaccine formulation. Balb/c mice were intramuscularly (IM) primed with a monovalent (Wu-1) or bivalent (Wu-1 + BA4/5) mRNA vaccine and intranasally boosted with unadjuvanted Wu-1 spike, BA4/5 spike or Wu-1+BA4/5 spike on days 0 and 21, respectively. Control groups received PBS, 1 or 2 doses of IM mRNA and 2 dose of protein only via IN. Two weeks post-boost, plasma, bronchoalveolar lavage fluid (BALF), nasal wash and intestines were collected to assess humoral responses. **B)** Measurement of Wu-1 spike and BA4/5 spike specific IgG relative titers in serum collected at end point. **C)** Recipracal ID_{50} neutralization titers relative to inhibition of soluble ACE2 and immobilized Wu-1 spike, BA4/5 spike and XBB1.5 spike interaction. **D)** Measurement of Wu-1 spike specific IgA titers and superimposed IgG1

and IgG2 titers in serum. **E)** Relative proportion of Wu-1 specific IgG and IgA isotypes in serum. Serum was diluted 1:500 for the measure of IgG specific titers. Data reflect results obtained from one biological replicate and is representative as average of 3 technical replicates. For statistical analysis, antibody titers were log-transformed and analyzed by a one-way ANOVA with Tukey's multiple comparisons test. Unless otherwise stated, groups were significantly greater than PBS and 1 dose controls. Pairwise comparison was conduceted between different booster vaccine formulations within a monovalent or bivalent prime cohort or to assess difference between two differently primed counterparts. ****p < 0.0001, **p < 0.01, *p < 0.05, n.s. no significant difference

Following a single dose of either the monovalent or bivalent mRNA-LNP IM vaccination, all mice exhibited detectable levels of IgG antibodies in serum (Supp. Fig. 1A). IN administration of a 1 μg or 10 μg dose of unadjuvanted protein boosted both IgG and IgA levels in serum, whereas IM administration of the mRNA-LNP vaccine only boosted IgG responses (Fig. 1 and Supp. Fig. 3). An IM prime followed IN boost induced systemic Wu-1-specific IgG levels comparable to those observed after two IM mRNA-LNP doses, with significantly higher IgA levels detected in IN boosted mice (Fig. 1B, 1D, and 1E), consistent with previous findings by *Mao. et al.* Indeed, Wu-1-specific IgG levels were comparable among mice receiving either a homologous or heterologous IN boost (Fig. 1B). Notably, we detected significantly higher BA4/5-specific IgG titers in mice primed bivalently and boosted IN with BA4.5 or BA4.5+Wu-1 antigens compared to their monovalently primed counterparts. A strong correlation ($r= 0.84$, $P<0.001$) was observed between of BA4/5- and Wu-1- specific IgG antibodies in monovalently primed mice, indicating high antibody cross-reactivity between these antigens. In contrast, no correlation ($r=0.39$) was detected in bivalently primed mice, potentially suggesting presence of BA4/5-specific antibody responses (Supp. Fig.1D). Additionally, although T follicular helper cells were not evaluated in this study, we detected lower ratio of IgG1 over IgG2 in bivalent primed mice (Fig. 1D), suggesting a potential skewing towards a Th1 response[80].

Mao *et al*, have previously reported that unadjuvanted IN boosting with SARS-CoV-1 spike protein, which shares 76% amino acid identity to Wu-1 SARS-CoV-2 spike, leveraged systemic immunity induced by prior vaccination with monovalent Wu-1 mRNA-LNP, and elicited cross-reactive humoral responses. We next sought to determine whether IN boosting with an unadjuvanted NL63 spike, a divergent seasonal coronavirus that also utilizes the ACE2 receptor for cell entry and shares 26 % amino acid identity to Wu-1 SARS-CoV-2 spike, could boost and induce cross-reactive humoral responses. However, we found that IgG levels were comparable to

those observed in mice after a single dose of IM mRNA-LNP, with no detectable NL63-specific IgG responses (Supp. Fig.1B). This finding highlights the specificity of memory responses and the importance of using a more closely matched boosting antigen to leverage systemic immunity induced by prior vaccination. This experiment clearly shows that the IM mRNA-LNP prime response did not produce antibodies, or cross-reactive antibodies that could be boosted by a genetically divergent unadjuvanted boost.

IM prime shapes systemic humoral responses, primarily driven by variant-specific neutralizing responses.

Although some statistically significant differences were observed, overall, total antibody responses showed minimal variation among the different vaccination groups (Fig. 1B). We next assessed neutralizing activity using a surrogate neutralization ELISA assay (snELISA) to evaluate the breadth of antibody responses from heterologous prime-boost formulations and administration routes (Fig. 1C; Supp. Fig. 3B), as systemic neutralizing responses are a well-established correlate of vaccine efficacy [81,82]. The snELISA assay we used measures the relative inhibition of spike to ACE2 receptor binding, as previously described by our group, and shown to quantitatively correlate with pseudotyped or infectious virus neutralization assays [83].

Spike binding inhibition for a specific variant was generally superior in mice boosted with the corresponding matched antigen, regardless of whether the boost was administered IN or IM (Fig.1C; Suppl. Fig. 3B). In line with the serological data, we observed comparable Wu-1 spike inhibition in mice that were boosted via IM or IN, except those primed with the bivalent mRNA-LNP vaccine and boosted with BA4/5 antigen (mismatched), likely due to significantly lower levels of Wu-1 RBD-specific IgG antibody (Supp. Fig. 1A). In contrast, a significant reduction in BA4/5 spike neutralization was observed in monovalently primed and Wu-1 (mismatched) boosted mice compared to those boosted with BA4/5 antigen (matched) or their bivalently primed counterparts (Fig.1C; Suppl. Fig. 3B). Furthermore, boosting with Wu-1 antigen failed to elicit any neutralizing activity against XBB1.5 spike, while boosting with the more closely related BA4/5 antigen enhanced neutralization.

Notably, IN boost with BA4/5 antigen (matched) induced significantly superior BA4/5 spike neutralization and, although not statistically significant, enhanced neutralization against XBB1.5 compared to mice receiving monovalent mRNA-LNP vaccine IM boost. However, boosting with either Wu-1 or BA4/5 antigens resulted in skewed neutralizing response specific to the boosting

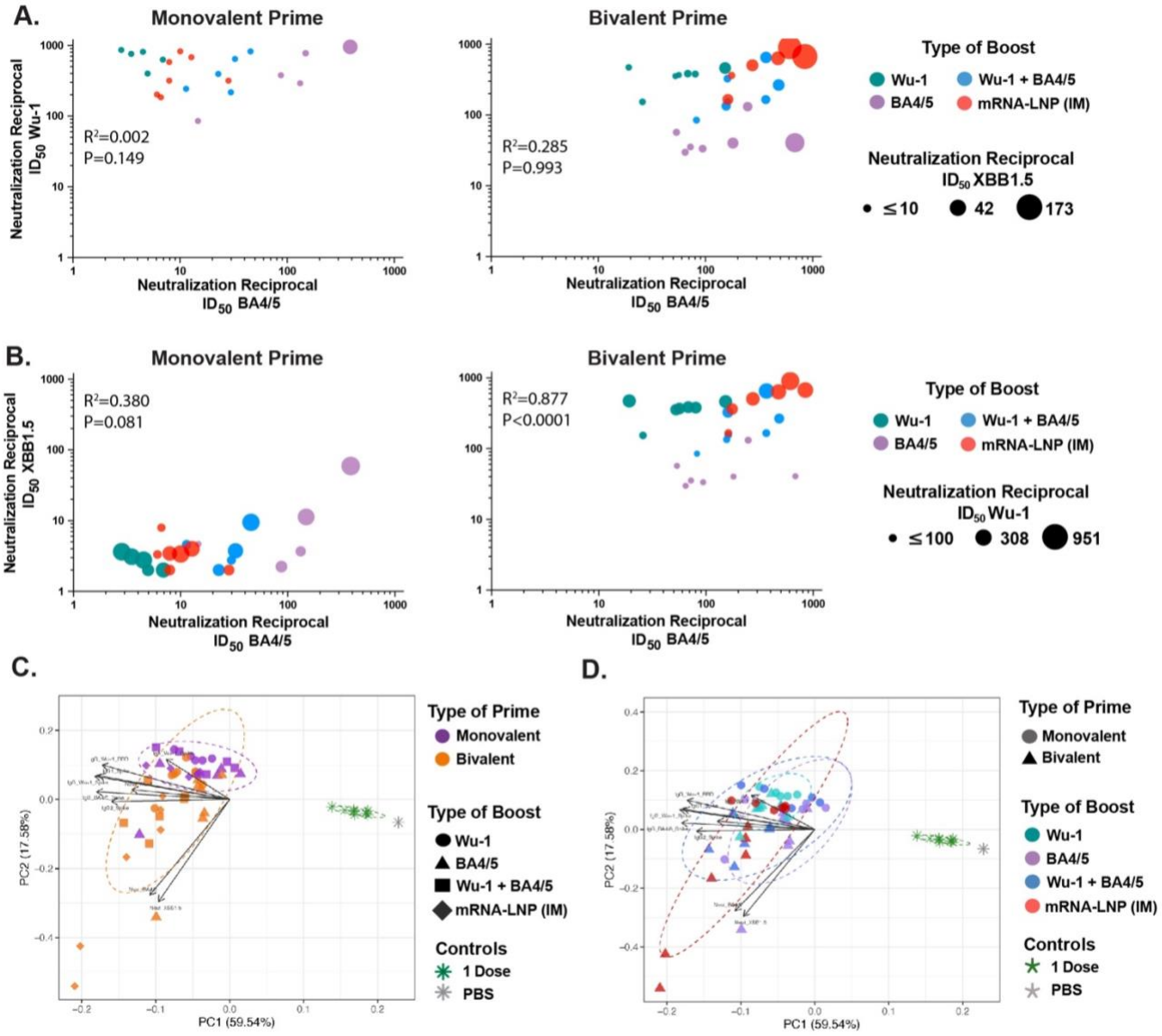

Figure 6.2 Prime vaccination drives differential humoral (total and neutralizing) responses in serum, while booster vaccination further refines these responses.

A) Correlation between BA4/5 and Wu-1 neutralization (ID_{50}) reciprocal titers, colored on the basis of type of boost and where the size of each appoint additionally reflects neutralization potency against XBB1.5 variant. **B)** Correlation between BA4/5 and XBB1.5 ID_{50} reciprocal titers, colored on the basis of type of boost and where the size of each appoint additionally reflects neutralization potency against Wu-1 variant. Principal component analysis (PCA) of differentially expressed antibody responses in serum, PCA was applied to individual mice, where one point reflects all antibody response tested for an individual mouse in serum as summarized in figure 1. The PCA was colored on the basis of **A)** type of prime and **B)** type of boost to depict to differential trends of antibody clustering elicited by different vaccination regiments.

antigen (Fig. 1C and 2A). Indeed, Wu-1 homologous prime-boost vaccination resulted in significant decrease in neutralization activity against antigenically distant SARS-CoV-2 variants (Fig. 1C, 2A and 2B). This effect was mitigated by heterologous boosting with the BA4/5 antigen, which likely elicited cross-reactive or *de novo* BA4/5 specific responses given the maintained inhibition of Wu-1 spike but markedly improved neutralization against BA4/5 spike (Fig. 1C, 2A, and 2B). Interestingly, we found that BA4/5+Wuhan boost elicited comparable or superior spike neutralization across all three variants evaluated in bivalent primed mice, relative to matched or mismatched variant-specific boosts (Fig. 1C, 2A, and 2B). In contrast, mice that were primed with the monovalent Wu-1 mRNA-LNP vaccine and boosted with the BA4/5+Wuhan vaccine exhibited diminished neutralization of BA4/5 and XBB1.5. This suggests that the BA4/5+Wuhan boost led to the induction of cross-reactive recall responses to epitopes shared between the primary (Wu-1) and secondary (Wu-1 and BA4/5) exposures, rather than generating BA4/5-specific *de novo* antibodies, indicating an immune imprinting response.

Bivalent mRNA-LNP IM prime broadens neutralizing responses in serum

Overall, we found a positive correlation between spike neutralization activity and Wu-1 or BA4/5 specific IgG antibody titers when the boosting antigen matched with the variant used in the snELISA (Supp. Fig. 1C). Importantly, significantly superior BA4/5 and XBB1.5 spike neutralization was noted in bivalent primed mice. Indeed, we observed a strong positive correlation (Spearman $r=0.877$, $P<0.0001$) between BA4/5 and XBB1.5 spike neutralization in bivalently primed mice compared to monovalently primed groups (Spearman $r=0.380$, $P=0.081$) (Fig. 2B). Next, we performed a principal components analysis (PCA) which included paired total and neutralizing responses across the various prime and boost groups (Fig. 2C and 2D). The first two principal components explained 77% of the variation in the data. By coloring the data points according to the type of prime or boost vaccine formulation, we were able to visualize the relative influence of each vaccine formulation on the overall humoral response outcome. Notably, we observed differential clustering based on the type of prime rather than the boost, which was primarily driven by variant specific neutralizing responses (Fig. 2C and 2D).

Following an IN boost with a 1 μg dose of unadjuvanted protein, similar patterns in variant-specific systemic responses emerged where groups boosted with the corresponding (matched) antigen generally developed the greatest reactivity and variant-specific neutralizing responses (Supp. Fig 3A and 3B). Notably, Wu-1 homologous prime-boost regimen led to Wu-1-skewed total and neutralizing responses while bivalently primed mice exhibited significantly greater total and neutralizing responses (Supp. Fig 3E). Indeed, although 1 μg IN boosted mice grouped separately in the PCA, the bivalently primed mice clustered more closely with the 10 μg boosted groups (Supp. Fig 4A and 4B). Taken together, these results suggest that bivalent priming expands the breath of neutralizing responses beyond what can be elicited with variant-specific boosting. Therefore, our data suggests that the prime vaccine shapes the outcome of total and neutralizing responses in serum, while the booster further refines these responses.

Variant-specific IN vaccines induce distinct antigen-specific IgA responses in nasal and BAL biofluids.

IM administration typically favours Ig class switching to IgG over IgA. However, stimulating the respiratory mucosa through vaccination or infection has been shown to induce robust production of IgA locally or in other distinct mucosal compartments. Indeed, the IN boost, but not the IM boost, induced robust mucosal Ig responses as detected in BAL and nasal biofluids, which predominantly favoured IgA. We observed that the antigen dose administered via IN route was important, as total Ig and neutralizing responses were significantly lower following a 1 μg dose of unadjuvanted protein IN boost relative to the 10 μg dose, which effectively boosted both IgG and IgA levels (Fig. 3 and Supp. Fig. 5). We found that an IN boost induced comparable Wu-1-specific IgA levels across the differentially (matched or mismatched) boosted mice, which was significantly higher than those observed after two doses of mRNA-LNP administered IM (Fig. 3A). However, we detected significantly greater BA4/5-specific IgA levels in mice IN boosted with the BA4/5 (matched) and, although not statistically significant, with Wu-1+BA4/5 antigen (matched), than with the Wu-1 antigen (mismatched) boost. While we observed an overall positive correlation between BA.4/5- and Wu-1-specific IgA antibodies when all IN boosted mice were analyzed together ($r=0.837$, $P<0.0001$) (Supp. Fig. 2A), this correlation was only positive in groups boosted with BA.4/5 ($r = 0.87$, $P=0.001$) and Wu-1 + BA.4/5 ($r = 0.87$, $P=0.003$) antigens. No correlation was observed in the Wu-1 boosted group ($r = 0.20$, $P= 0.543$). In general, in contrast

to differences in BA4/5-specific IgG levels between monovalent and bivalently primed mice observed in serum, differences in BA4/5-specific IgA levels were influenced by the vaccine formulation of the boost rather than the prime.

Next, we evaluated spike neutralizing activity in BAL biofluid, and found detectable but weak neutralization activity in mice that were IN boosted with the 10 μg dose of unadjuvanted protein (Fig. 3B). Consistent with systemic neutralizing responses, spike-ACE2 binding inhibition for specific variants was superior in mice boosted with the corresponding (matched) or closely related antigen. In line with the serological data, we observed comparable Wu-1 inhibition in mice across differentially IN boosted mice and was notably higher than that observed following two doses of mRNA-LNP via IM vaccination. However, similar to the findings in serum, mice primed with the bivalent mRNA-LNP vaccine and boosted with BA4/5 antigen (mismatched) exhibited significantly lower Wu-1 spike inhibition. Generally, an IN boost with BA4/5 with BA4/5+Wu-1 antigen (matched) elicited enhanced BA4/5 and XBB1.5 spike neutralization, which was significantly higher than that observed in mice IM boosted with the monovalent mRNA-LNP. Given that mucosal IgA has been shown to effectively inhibit viral infection in vitro across both animal models and human studies[23,65,72,75,79,84], we sought to determine the contribution of IgA relative to IgG in mucosal neutralization activity *in vitro*. We found that IgA antibody titers positively correlated with spike neutralizing activity against Wu-1 ($r=0.615$, $P<0.0001$) and BA4/5 ($r=0.678$, $P<0.0001$) compared to IgG (Fig. 3E and 3F). Furthermore, no correlation was observed between Wu-1 and BA4/5 or BA4/5 and XBB1.5 neutralization (Supp. Fig. 2B and 2C). Indeed, we observed distinct clustering based on the route of administration in the PCA and dose of the IN booster, where 1 μg IN and IM boosted mice grouped independently from the 10 ug boosted mice (Fig. 3G and Supp. Fig. 5E). Taken together, these findings suggest that in contrast to serum, where the prime vaccination overwhelmingly dictated the humoral response outcome, humoral responses in the BALF were predominantly influenced by the booster formulation, with antigen-specific IgA response as the primary driver.

Next, we assessed mucosal IgG and IgA levels in the nasal biofluid (Fig. 4A and Supp. Fig. 6). Only mice that received the 10 μg IN boost developed high levels of IgA, which were significantly greater than in those that received two doses of mRNA-LNP via IM. Notably, as in BALF, similar

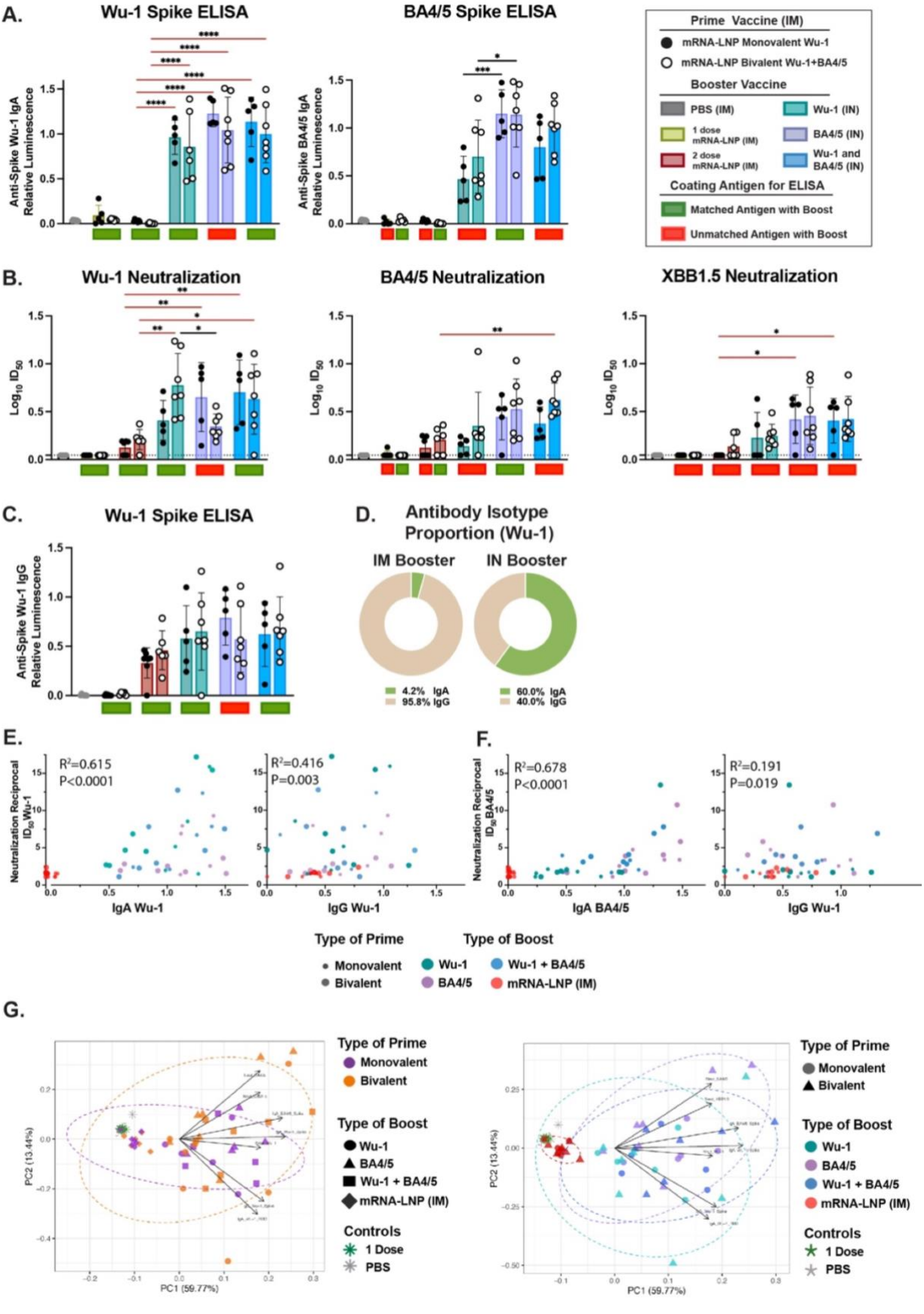
A.
Wu-1 Spike ELISA
BA4/5 Spike ELISA
Anti-Spike Wu-1 IgA Relative Luminescence
Anti-Spike BA4/5 IgA Relative Luminescence
Prime Vaccine (IM)
mRNA-LNP Monovalent Wu-1
mRNA-LNP Bivalent Wu-1+BA4/5
Booster Vaccine
PBS (IM)
1 dose mRNA-LNP (IM)
2 dose mRNA-LNP (IM)
Wu-1 (IN)
BA4/5 (IN)
Wu-1 and BA4/5 (IN)
Coating Antigen for ELISA
Matched Antigen with Boost
Unmatched Antigen with Boost
B.
Wu-1 Neutralization
BA4/5 Neutralization
XBB1.5 Neutralization
Log10 ID50
C.
Wu-1 Spike ELISA
Anti-Spike Wu-1 IgG Relative Luminescence
D.
Antibody Isotype Proportion (Wu-1)
IM Booster
IN Booster
4.2% IgA
95.8% IgG
60.0% IgA
40.0% IgG
E.
R²=0.615
P<0.0001
R²=0.416
P=0.003
Neutralization Reciprocal ID50 Wu-1
IgA Wu-1
IgG Wu-1
F.
R²=0.678
P<0.0001
R²=0.191
P=0.019
Neutralization Reciprocal ID50 BA4/5
IgA BA4/5
IgG Wu-1
Type of Prime
Monovalent
Bivalent
Type of Boost
Wu-1
BA4/5
Wu-1 + BA4/5
mRNA-LNP (IM)
G.
PC1 (59.77%)
PC2 (13.44%)
Type of Prime
Monovalent
Bivalent
Type of Boost
Wu-1
BA4/5
Wu-1 + BA4/5
mRNA-LNP (IM)
Controls
1 Dose
PBS

Figure 6.3 Characterization of BALF mucosal immune responses following a heterologous systemic prime and mucosal boost vaccination.

A) Measurement of Wu-1 spike and BA4/5 spike specific IgA in branchoalveolar lavage fluid (BALF) collected at end point. **B)** Recipracal ID_{50} neutralization titers relative to inhibition of soluble ACE2 and immobilized Wu-1 spike, BA4/5 spike and XBB1.5 spike interaction. **C)** Measurement of Wu-1 spike specific IgG titers and **D)** relative proportion of Wu-1 specific IgG and IgA isotypes in BALF. Correlation between **E)** Wu-1 and **F)** BA4/5 neutralization (ID_{50}) reciprocal titers and IgG and IgA isotypes, colored on the basis of type of boost. **G)** Principal component analysis (PCA) of differentially expressed antibody responses in BALF, PCA was applied to individual mice, where one point reflects all antibody response tested for an individual mouse in BALF. The PCA was colored on the basis of type of prime and type of boost to depict to differential trends of antibody clustering elicited by different vaccination regiments. Data reflect results obtained from one biological replicate and is representative as average of 3 technical replicates. BALF was diluted 1:30 for the measure of IgA specific titers. For statistical analysis, antibody titers were log- transformed and then analyzed by a one-way ANOVA with Tukey's multiple comparisons test. ****$p < 0.0001$, **$p < 0.01$, *$p < 0.05$, n.s. no significant difference.

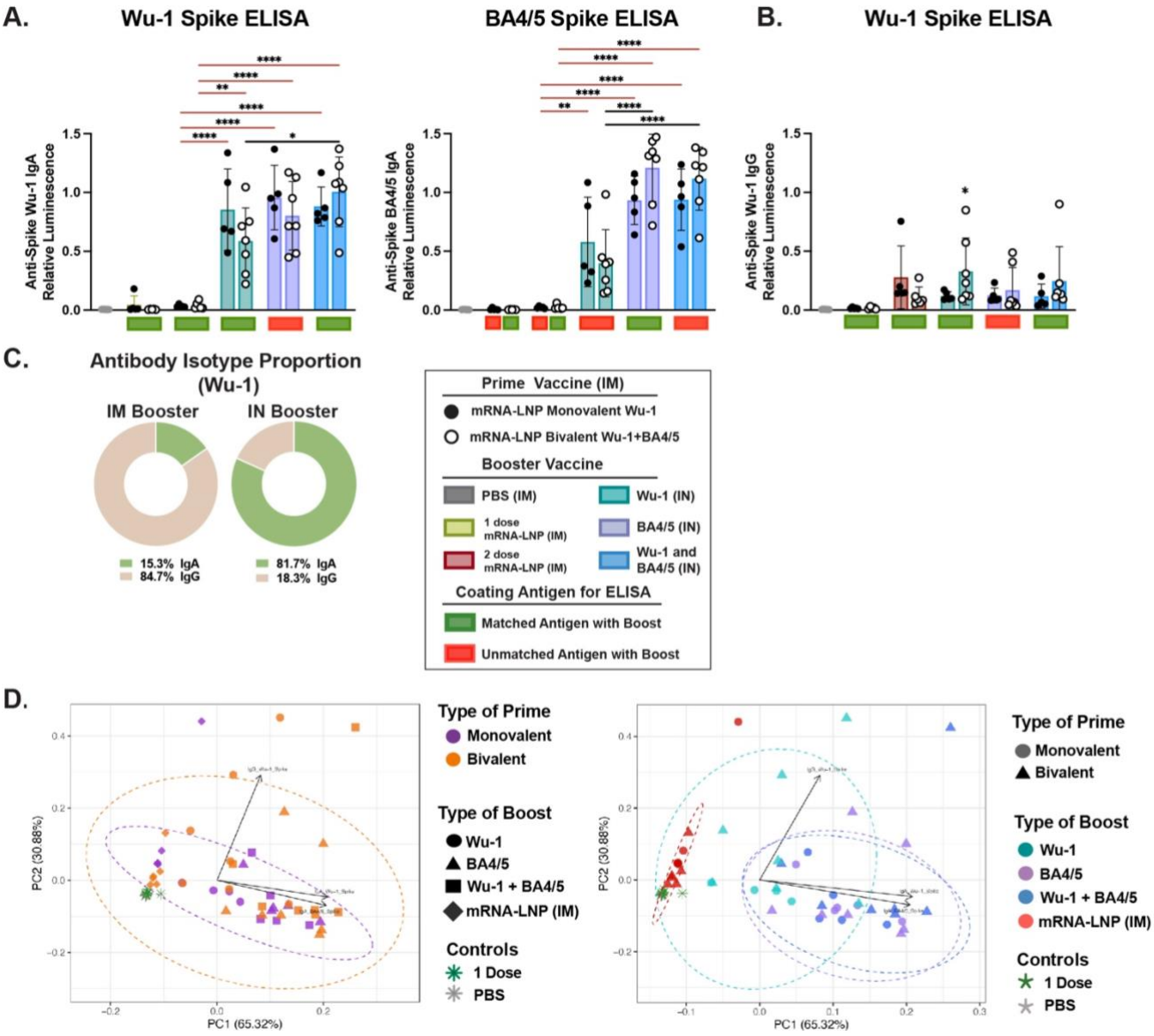

Figure 6.4 Characterization of mucosal immune responses in nasal wash following a heterologous systemic prime and mucosal boost vaccination.

A) Measurement of Wu-1 spike and BA4/5 spike specif IgA in nasal wash collected at end point. **B)** Measurement of Wu-1 spike specific IgG titers and **C)** relative proportion of Wu-1 specific IgG and IgA isotypes in nasal wash. **E)** PCA of differentially expressed antibody responses in nasal wash, PCA was applied to individual mice, where one point reflects all antibody response tested for an individual mouse as summarized in panels A-B. The PCA was colored on the basis of type of prime and type of boost to depict to differential trends of antibody clustering elicited by different vaccination regiments. Data reflects results obtained from one biological replicate and is representative as average of 2-3 technical replicates. Nasal wash was diluted 1:5 for the measure of IgA specific titers. For statistical analysis, antibody titers were log- transformed and then analyzed by a one-way ANOVA with Tukey's multiple comparisons.

pattern emerged in variant-specific IgA responses, with groups boosted with the BA4/5 or BA4.5+Wu-1 exhibiting significantly higher BA4/5-specific IgA titers. We found a strong correlation (r= 0.81, P<) between BA4/5- and Wu-1- specific IgA antibodies, but only in the Wu-1 + BA4/5 boosted mice (Supp. Fig. 2F). Both IM mRNA-LNP and IN protein vaccinations elicited comparable IgG responses, which were detectable but not significantly higher than the PBS control group (Fig. 5B). Furthermore, while the 1 μg dose IN boost elicited detectable IgA levels in the nasal biofluid, these levels were not significantly higher in all IN boosted groups compared to the PBS control (Supp. Fig. 6A-B). Interestingly, we observed differential clustering in nasal biofluid compared to both serum and BALF, with IM boosted group clustering independently from both 1 ug dose and 10 ug dose IN boost in the PCA (Fig. 4E and Supp. Fig 6E). Furthermore, distinct clustering was observed based on the type of booster, which was primarily driven by antigen-specific IgA response.

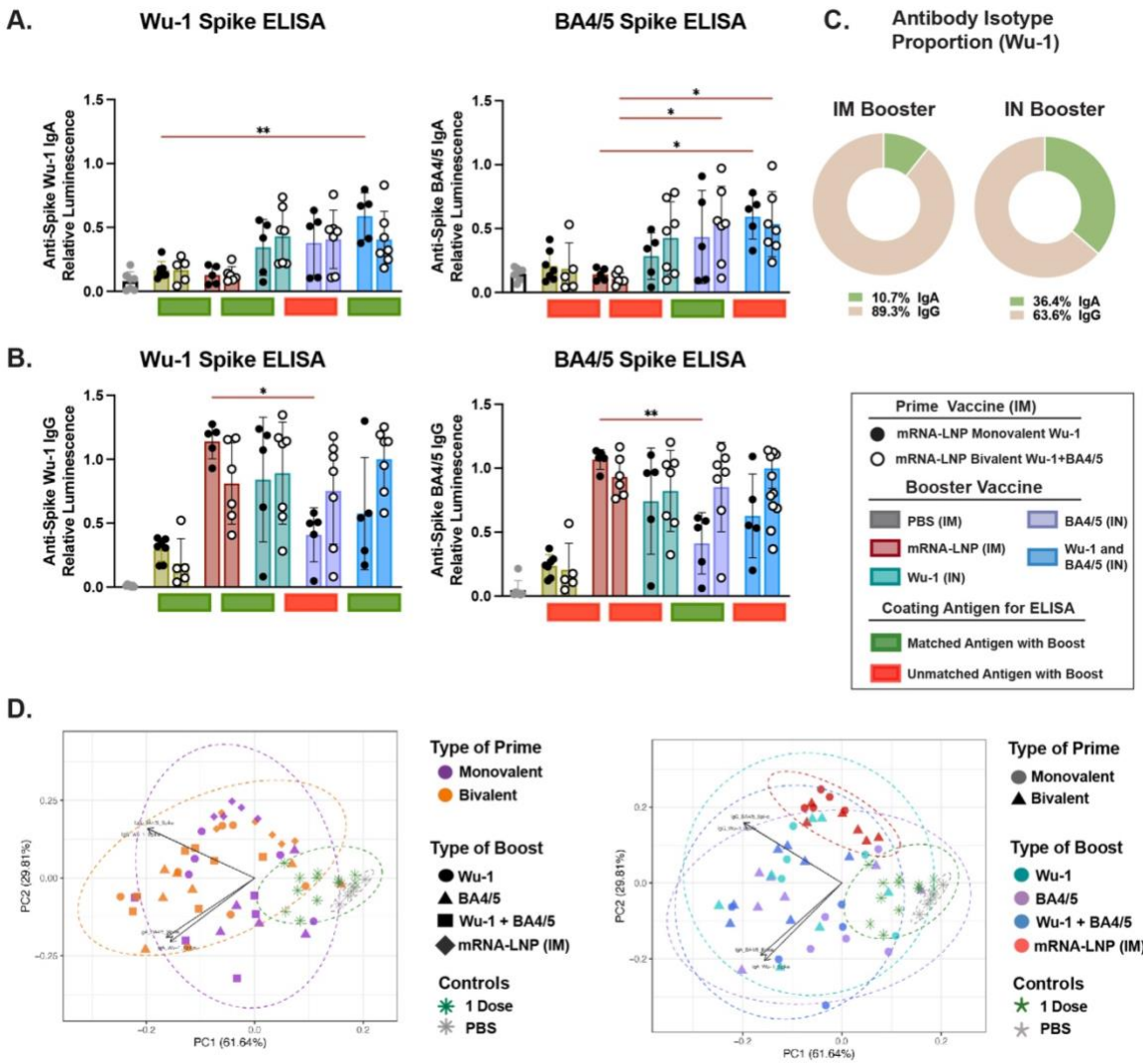

Figure 6.5 Characterization of mucosal immune responses in intestines following a heterologous systemic prime and mucosal boost vaccination.

A) Measurement of Wu-1 spike and BA4/5 spike specif IgA in intestinal fluid collected at end point. **B)** Measurement of Wu-1 spike and BA4/5 spike specific IgG titers and **C)** relative proportion of Wu-1 specific IgG and IgA isotypes in nasal wash. **D)** PCA of differentially expressed antibody responses intestines, PCA was applied to individual mice, where one point reflects all antibody response tested for an individual mouse as summarized in panels **A-B**. The PCA was colored on the basis of type of prime and type of boost to depict to differential trends of antibody clustering elicited by different vaccination regiments. Data reflects results obtained from one biological replicate and is representative as average of 2-3 technical replicates. Intestinal supernatant was diluted 1:2 for the measure of IgA specific titers. For statistical analysis, antibody titers were log- transformed and then analyzed by a one-way ANOVA with Tukey's multiple comparisons.

IM and IN vaccination induce potent IgG responses in the intestinal lumen

A single dose of mRNA-LNP administered IM induced detectable levels of IgG antibodies in the intestinal fluid (Fig. 6 and Supp. Fig. 7). While IN administration of a 10 μg dose of unadjuvanted protein boosted both IgG and IgA levels, the 1 μg dose or IM administration of the mRNA-LNP vaccine only boosted IgG responses (Fig. 5A and 5B; Supp. Fig. 7 and 7B). Notably, IM administration induced IgG levels that were either superior to or comparable with those elicited by the 10 μg IN boost. However, unlike in other mucosal compartments, both routes of administration elicited an IgG-predominant response in the intestinal fluid (Fig. 5C and Supp. Fig. 7C). Furthermore, no variant-specific IgG- or IgA- skewed response corresponding to the type of prime or boost vaccine formulation was observed, which contrasts to findings in other compartments (Supp. Fig. 2G). We observed differential clustering based on the administration route and number of vaccine doses received, which were primarily driven by both IgG and IgA responses (Fig. 5D and Supp. Fig. 7D)

Effect of Administration Route on Humoral Response Profiles and Antibody Correlations Across Compartments

Next, we sought to further dissect the relative influence of each administration route and vaccine formulation on the overall humoral response outcome. For this analysis, we included paired serological data from each distinct compartment across the various prime and boost groups. Notably, we observed 5 separate clusters primarily driving IgG and IgA responses (Fig. 6A). The mRNA-LNP IM boosted group clustered independently from the 10 μg and 1 μg protein IN boosted groups, and driving predominantly IgG responses, while the 1 μg dose groups clustered more closely to the 10 μg boosted groups, with the IgA response as the primary driver. Furthermore, we additionally note differential clustering based on the type of prime, similar to our observation in the serum. Several groups have previously reported strong to moderate IgG correlation between paired serum and saliva in convalescent COVID-19 patients, while IgA

responses exhibited weaker correlation highlighting possible compartmentalization of the IgA response[23,85-87].

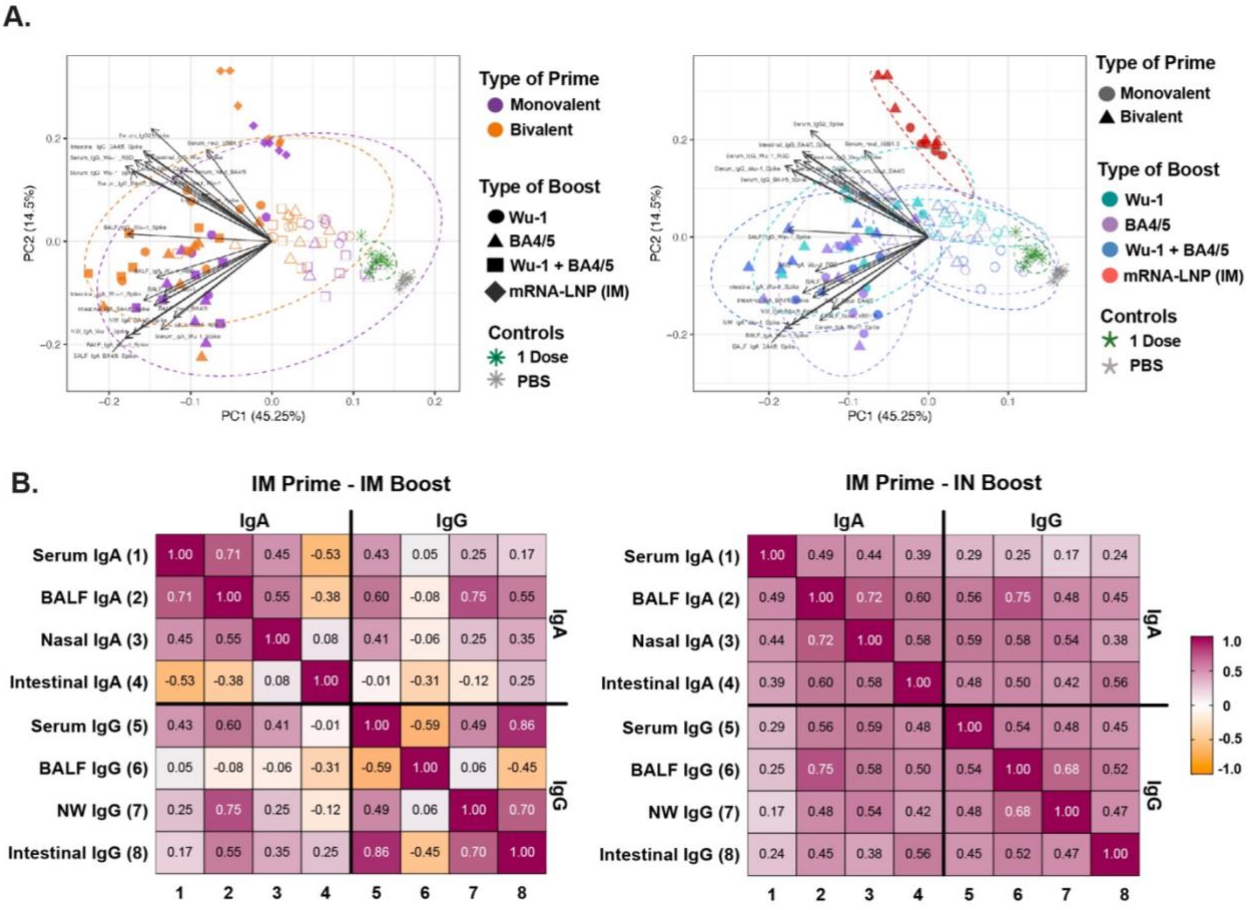

Figure 6.6 Humoral responses kinetics and analysis of IgA and IgG antibodies from different compartments.

Principal component analysis (PCA) of differentially expressed antibody responses elicited by different vaccination regiments in serum, BALF, nasal wash and intestines. PCA was applied to individual mice, where one point reflects all antibody response tested for an individual mouse in all compartments. The PCA was colored on the basis of **A)** type of prime and type of boost to depict to differential trends of antibody clustering. **B)** Correlation between IgG and IgA antibodies in serum, BALF, nasal and intestinal fluid applied to combined results from all mice, where each square reflects total antibody responses tested for all mice combined that received different IN boost formulation (1 and 10 ug dose) or mRNA-LNP IM boost.

Next, we analyzed the correlation between IgG and IgA responses across three anatomical compartments to better understand the distribution and coordination of the induced immune responses, determining whether they are compartmentalized or consistently aligned across the mucosal compartments (Fig. 6B). Paired serological data from each mouse were analyzed, with

antibody profiles stratified by administration route to reflect the distinct clustering observed between IN and IM boosted groups in Fig. 6A. Off the three mucosal compartments, we observed high IgA (r=0.72, P<0.0001) and IgG (r=0.68, P<0.0001) correlation between BALF and nasal wash in IN boosted mice only. While a positive correlation (r=0.75, P<0.0001) between IgG and IgA responses was observed in BALF in IN boosted mice, no correlation between these antibody isotypes in other biofluids was observed. While a positive IgA correlation (r=71, P=0.008) was observed between serum and BALF in IM boosted mice, it's likely confounded given the very low IgA titers detected in BALF following IM vaccination. Interestingly, we found a strong positive correlation (r=0.86, P=0.001) between serum and intestinal IgG antibody titers in IM boosted mice levels, which was not observed in IN boosted mice.

6.4 Discussion

In this study, we aimed to examine the effects of heterologous prime-boost regimens on humoral responses, focusing on IM and IN administration routes and variant-tailored vaccine formulations. Our findings indicate that the IM prime predominantly shapes systemic humoral responses, primarily driven by variant-specific neutralizing responses, while the IN boost further amplifies and refines them. Indeed, homologous prime and boost antigen vaccination resulted in Wu-1-skewed humoral responses. This effect was mitigated by heterologous IN boosting with the Omicron BA4/5 antigen, which significantly improved neutralization against antigenically distant VOCs compared to mice that received two doses of the monovalent mRNA-LNP IM vaccine, while retaining neutralization activity against the ancestral Wu-1 strain. Importantly, our results highlight the value of incorporating distinct antigenic variants in the prime vaccine, as the bivalent prime significantly enhanced the breadth of total and neutralizing responses against circulating VOCs in serum. The IN boost, rather than the IM prime, had a greater impact on mucosal responses, primarily driven by antigen-specific IgA responses in nasal wash and BALF. Higher IgA titers correlated more strongly with neutralizing activity than IgG, with the BA4/5 and BA4/5+Wu-1 boosted groups showing the highest neutralizing titers against BA4/5. Furthermore, we show differential induction of IgG and IgA antibody isotypes across distinct immune compartments following IM relative to IN boosting. Indeed, a strong IgA antibody correlation between mucosal compartments was observed only in IN vaccinated mice. Taken together, our findings highlight the merit of including distinct antigenic variants, if possible, in the prime

vaccine to enhance VOC neutralization and support the use of variant-tailored IN boosters, which simultaneously boost systemic responses and elicit mucosal responses at the viral point of entry.

Additionally, we demonstrate that IN was much superior to IM vaccination at driving a predominantly IgA-favored response in nasal, BAL and intestinal biofluids. This observation aligns with recent studies evaluating heterologous prime-boost regimens *in vivo*, which highlight the potent induction of cellular and humoral responses in BALF following IN or oral vaccination in mice with pre-existing immunity [22,69,71-74,78,79]. However, while variant-specific total and neutralizing responses after variant-tailored boosting are well documented in serum, the effects of heterologous boosting strategies on the induction of variant-specific responses in saliva, nasal, and BAL biofluids remain poorly characterized. Here, we demonstrate that variant-specific IgA responses in BALF and nasal wash were predominantly shaped by the vaccine antigens delivered via IN rather than IM immunization, highlighting the compartmentalization of mucosal responses as recently suggested [23,85-87]. Given that transmission of SARS-COV-2 primarily occurs via inhalation of aerosolized virus, local immune responses are uniquely positioned to act as rapid, first line of defense against infection. Initial mRNA-LNP IM vaccines were up to 90% effective against symptomatic infection following exposure to antigenically matched VOCs[15-17,29], likely due to potent induction of systemic IgG response, which could diffuse into the URT[55,88]. Our findings of robust IgG titers in BALG and nasal wash following the mRNA-LNP boost support this. However, Omicron and its sub-variants, evolved to preferentially replicate in the URT and have shorter incubation times and thereby reduce the immune recall response window[89-91]. This leads to increased viral transmissibility and emphasizes the need a persistent virus-neutralizing capacity at the initial replication site.

A growing body of literature highlights the importance of stimulating the respiratory mucosa and the role of sIgA in respiratory mucosa to protect against breakthrough infections[22,23,42,54-58,92]. We found that IgA responses in BALF correlated more strongly with neutralizing activity than the IgG isotype, consistent with studies showing sIgA's potent neutralization capacity against SARS-CoV-2 *in vitro* [23,65,72,75,79,84]. Notably, we observed comparable BA4/5 and XBB1.5 neutralizing activity in BALF, suggesting that IgA, abundant in dimeric or pentameric forms at the mucosal surface, it may be more effective than monomeric IgG at neutralizing variants with escape [84,93]. While

systemic neutralizing antibodies are an established correlate of vaccine protection[81], analogous correlates of mucosal immunity against viral infection and transmission have yet to be established. Identifying these will be key to assessing the efficacy of intranasal vaccines. Indeed, antibody kinetics at distinct mucosal sites in response to different vaccination regimens remain poorly characterized. In this study, we found a strong correlation between IgA in BAL and nasal compartments only in IN vaccinated mice, suggesting IgA compartmentalization, as observed in studies assessing IgA correlations in serum and saliva[23,85-87].

IgA is the predominant immunoglobulin at mucosal surfaces, while IgG, though less abundant, can constitute 15-20% of total immunoglobulins at certain sites[94,95] and plays a protective role in the lower respiratory tract through complement activation and antibody-dependent cellular cytotoxicity (ADCC)[88,96]. In serum, IgA exists primarily in monomeric form, accounting for approximately 15% of total immunoglobulins[97,98], contributing to immune defense via phagocytosis, ADCC, and, under specific conditions, complement activation[215,222]. Building on these observations, our study offers a comprehensive comparison of relative IgA and IgG levels in serum and across distinct anatomical compartments following IN or IM SARS-CoV-2 vaccination. This comparison is crucial for understanding how different vaccination routes shape antibody distribution across compartments and contribute to mucosal and systemic immunity, informing strategies for optimizing vaccine efficacy.

Interestingly, we observed IgG responses in the intestinal mucosa following both IM and IN immunization. While plasma cells can disseminate between distinct mucosal compartments after mucosal immunization[92,99,100], it remains unclear how IgG responses were generated after IM vaccination. Spike protein has been detected in plasma for up to five days following mRNA-LNP IM vaccination[101], suggesting that these antibody responses might be induced directly in Peyer's Patches, which are present in the intestinal tissue we analyzed. Notably, residual SARS-CoV-2 antigens have also been detected in intestinal mucosa and stool samples, even after viral clearance from the URT [102-104]. Thus, this potent induction of humoral responses in the intestinal lumen following IM vaccination with mRNA-LNP should be studies and potentially leveraged to reduce viral replication and transmission of gastrointestinal viruses.

We observed reduced BA4/5 and XBB.1.5 neutralization in mice primed with the monovalent Wu-1 vaccine and boosted with the BA4/5+Wu-1 combination, compared to those boosted with BA.4/5 antigen alone. In contrast, mice bivalently primed and boosted with either BA.4/5 alone or the BA.4/5+Wu-1 combination showed comparable neutralization activity across both formulations. These findings suggest that the BA4/5+Wu-1 boost in monovalent-primed mice primarily triggered cross-reactive recall responses to shared epitopes, rather than inducing BA.4/5-specific antibodies, indicating the presence of immune imprinting. This aligns with recent studies showing that variant-specific boosting primarily promoted recall responses, with the highest neutralizing titers against the ancestral strain[4,20,37,40,41,49-52]. This immune imprinting effect was further exacerbated by retaining the ancestral antigen in the bivalent vaccines. The generation of variant-specific *de novo* antibodies has been observed, although at low levels, with monovalent Omicron and XBB1.5-specific mRNA-LNP boosters, highlighting the benefits of updating vaccines to match circulating variants[40,41,105,106]. However, these findings highlight the influence of immune imprinting, which can be overcome by boosting with antigens that are sufficiently distinct from the priming antigen[105], through repeated boosting[107], or by incorporating adjuvants[108], as we have previously reviewed[47].

Our findings demonstrate that bivalent priming with two distinct variants significantly broadened the neutralization responses, which can be further enhanced by IN boosting. The strategic inclusion of multivalent viral strains or a highly conserved common antigen in vaccines, as proposed for some universal vaccines, can leverage immune imprinting, shaping a broadly reactive B cell repertoire and enhancing protection against both circulating and future VOCs. Understanding the impact of different vaccination strategies on immune responses across different anatomical compartments may aid in inducing protective mucosal responses against SARS-CoV-2 variants.

Limitation of the study

Early after SARS-Cov-2 infection, cellular immune responses are crucial in controlling infection severity and providing long-term protection, while vaccine-elicited total and neutralizing antibody responses are more closely associated with protection against infection and symptomatic disease [81,82]. Given that most T cell epitopes remain relatively unchanged in VOCs [109] , and that cellular responses were characterized in detail in the “Prime and Spike” vaccination approach by Mao *et*

al., this study focused exclusively on examining only the humoral antibody profiles across different anatomical compartments using monovalent and bivalent vaccines.

Another limitation is that we observed significantly lower relative antibody levels and neutralization potency in BALF, intestinal wash and nasal wash compared to serum. These compartments are anatomically very small in mice and required a 500-fold dilution of these samples with PBS to collect. This highlights that harvesting antibodies from various mucosal compartments in mice is very challenging, requires the addition of dilution buffer, and results are thereby prone to variations attributable to the technical procedures. The field would benefit from standardized methods. Similarly, neutralization assays were not performed for nasal and intestinal biofluids due to the very low amounts of antibodies recovered in these samples. Finally, in this study we measured IgA levels and not specifically mucosal sIgA due to the technical limitations of the assay to discriminate between the two types of this specific antibody isotype.

6.5 Material and methods

Mice immunization and sample collection

All animal experiments were conducted in accordance with the Ontario *Animals for Research Act* and approved by the University of Ottawa Animal Ethics Committee (protocol BMI-3649). Female, 8-week-old BALB/c mice were obtained from Charles River Laboratories (Saint-Constant, Canada). Prior to each immunization, mice were anesthetized with isoflurane and vaccinated either intramuscularly or intranasally. Intramuscular vaccinations were administered in the left quadriceps muscle using a 31-gauge syringe, delivering a final dose of 1 μg of Pfizer-Comirnaty monovalent Wuhan (Wu-1) or bivalent (Wu-1 + BA.4/5) vaccine in 20 μL of solution. As described previously in Maltseva et al., intranasal vaccinations involved administering 25 μL per nare, with a total dose of 10 μg of spike protein formulations consisting of Wu-1, BA.4/5, or Wu-1 + BA.4/5 variants, resuspended in endotoxin-free PBS (Sigma-Aldrich, USA). SARS-CoV-2 antigens, including full trimeric spike proteins for Wuhan (Wu-1) and Omicron (BA.4/5), were obtained from the Metrology Division of the National Research Council Canada. Control groups included mice vaccinated with phosphate-buffered saline (PBS), either a single or two-dose regimen of monovalent (Wu-1) or bivalent (Wu-1 + BA.4/5) mRNA vaccine administered intramuscularly. Additional groups included mice receiving two intranasal doses of Wu-1 protein, or a prime-boost regimen consisting of a monovalent (Wu-1) mRNA intramuscular prime followed by a boost with NL63 seasonal human coronavirus spike protein (Creative Diagnostics, DAGC133), as summarized in Table 1.

Plasma samples were collected periodically throughout the study via the submandibular vein, with terminal samples obtained by cardiac puncture. Two weeks after the booster dose, bronchoalveolar lavage fluid (BALF), nasal washes, and intestinal lumen contents were collected to assess mucosal humoral responses, following the method described in Maltseva *et al.*(269). Briefly, mucosal samples were collected using PBS supplemented with protease inhibitors (Complete Mini Protease Inhibitor Cocktail tablets, Cat. No.: 11836153001, Basel, Switzerland). A 10 cm section of the small intestine, free of fecal matter, was cut into 1–2 mm pieces and placed in an Eppendorf tube containing 200 µL PBS with protease inhibitors. The sample was incubated on a rocker at 4 °C overnight and centrifuged at 8,000 × *g* for 10 minutes at 4 °C, and the supernatants were stored at −80 °C for downstream ELISA analysis. Nasal wash and BALF samples were further concentrated using 50 kDa Pierce Protein Concentrator columns (Thermo Fisher Scientific, Waltham, MA, USA) following the manufacturer's instructions. Sample volumes were normalized before concentration, and the concentrates were stored at −80 °C until the ELISA assay was performed.

SARS-CoV-2 specific antibody measurements

SARS-CoV-2-specific antibody responses were evaluated as previously described in Maltseva *et al.*(269). Briefly, using trimeric spike proteins corresponding to the same variants used for immunizations, spike proteins were diluted to 4 µg/mL in sterile 1X PBS (Multicell, #311-010-CL) and coated onto 384-well immunoplates (ThermoFisher, #460372) at 10 µL per well, followed by overnight incubation at 4°C. Plates were washed three times with 100 µL of PBS-T (PBS + 0.05% Tween-20) to remove unbound antigen and blocked for 1 hour at room temperature with shaking using blocking buffer (PBS-T + 3% w/v non-fat milk powder). Following blocking, serum, BALF, nasal wash and intestinal supernatant samples were prepared and diluted in dilution buffer (PBS-T + 1% w/v non-fat milk powder). Serum was diluted 1:300 after the first immunization and 1:500 after the second immunization. BALF samples were diluted between 4- to 30-fold, while nasal wash and intestinal supernatant samples were diluted 4-fold and 2-fold, respectively. After washing the plates three times with PBS-T, 10 µL of the diluted samples were added to the respective wells. The plates were incubated for 2 hours at room temperature with shaking and washed three times with PBS-T. Next, 10 µL of the respective secondary-HRP antibody at specified dilutions 1:4000 secondary IgG Anti-Mouse, Human ads-HRP (#1030-05, Southern Biotech) and 1:1000 secondary anti-mouse IgA-HRP (#1040-05, Southern Biotech) were added. Plates were incubated for one hour on a shaker, washed thrice with PBS-T followed by the addition with 10 µL of the SuperSignal ELISA Pico Chemiluminescent Substrate (Thermo Scientific, #37069). Luminescence intensity was measured with BIO-TEK Synergy Neo2 plate reader for 20ms/well at a read height of 1.0 mm. Wells containing dilution buffer in place of sample served as negative controls to determine background luminescence. We expressed the SARS-CoV-2-specific antibody levels as relative luminescence values compared to a pooled sample from the Wu-1+BA.4/5 boosted group, with a pooled sample for each biofluid included as a standard control on every plate. This approach ensured plate-to-plate consistency aligned with results from normalization to the standard IgG and IgA controls (9A9C9 clone) (Genscript, USA).

Surrogate Neutralization ELISA (snELISA) assay to evaluate neutralization activity in serum and BALF samples

Surrogate neutralization ELISA was performed as previously described in Colwill *et al.* and Maltseva *et al.*, for the evaluation of the relative inhibition of neutralizing antibodies to spike protein from binding to soluble ACE2 (303-305). Briefly, SARS-CoV-2 proteins, including Wuhan (NRC Metrology, Canada), BA4/5 (NRC Metrology, Canada), and XBB1.5 (Abwiz, 2712), were diluted in sterile 1X PBS to 8 μg/mL and coated onto a 384-well Immuno plates (12.5 μL /well) overnight at 4°C. Plates were washed three times with PBS-T (PBS containing 0.05% Tween-20) and blocked for one hour while shaking. Plasma samples were 1:5 serially diluted in dilution buffer , while BALF samples were diluted 1:3. Diluted samples (20 μL/well) were applied to coated plates and incubated at room temperature for 2 hours while shaking. After incubation, plates were washed three times and biotinylated ACE2 (NRC Metrology, Canada), diluted to 0.35 ng/μL in a dilution buffer was added to the wells (20 μL/well). Plates were washed again three times with PBS-T followed and 20 μL per well of Streptavidin-Peroxidase polymer (Sigma, #S2438) diluted in dilution buffer to 1.25 ng/μL was added. Following one hour incubation at room temperature while shaking, plates were washed thrice with PBS-T and 20 μL per well of freshly prepared SuperSignal ELISA Pico Chemiluminescent Substrate (prepared by mixing a 1:1 ratio of components and further diluted with equal volume dH_2O) was applied. After 5 mins of incubation with shaking, luminescence intensity was measured with BIO-TEK Synergy Neo2 plate reader for 20ms/well at a read height of 1.0 mm. To determine the maximum binding signal, control wells were filled with dilution buffer in place of serum, followed by the addition of ACE2 under the same conditions. The relative percentage of inhibition was calculated using the following formula:

$$\%\ Inhibition = (1 - \frac{average\ mean\ of\ serum\ sample}{average\ mean\ of\ maxium\ signal}) \times 100$$

The serum and BALF dilutions required to achieve 50% inhibition of spike or RBD protein binding to the ACE2 receptor (half-maximal inhibitory dilution, ID50) were determined using a 4-parameter logistic (4PL) curve fitting analysis in GraphPad Prism 9.1.2 software. For samples where no neutralization activity was detected, the ID50 value was arbitrarily assigned as half of the lowest dilution tested.

Principal component analysis of neutralization and serology data

Principal component analysis (PCA) was performed on normalized serology and neutralization efficiency data from various prime and boost mouse groups. The analysis was conducted using the prcomp function in R 4.2.3, with scaling applied to ensure comparability across variables. Data visualization, including PCA plots and eigenvectors, was carried out using the ggplot2 package. During visualization, samples were annotated based on their prime and boost classifications. Animals with missing values in any measured parameter were excluded from the PCA analysis.

Data Availability:

The data generated and/or analysed in the current study are available from the corresponding authors on reasonable request.

ACKNOWLEDGEMENTS

Author contributions: M.M. and M-A.L. designed the study. M.M. developed the assays and conducted the in vitro experiments. Animal sample processing was carried out by M.M., P.M., Y.G., and N.C. C.C. provided the LNP-mRNA vaccines. Data analysis and curation were performed by M.M., Y.G., C.C. and M-A.L. M.M. prepared and wrote the original draft. M.M., C.C. and M-A.L. reviewed and edited the manuscript. M-A.L. supervised the project, managed funding, and oversaw project administration. All authors have read, revised, and approved the final manuscript.

Acknowledgements : We sincerely thank Anthony Carter and the uOttawa surgical ACVS core for their technical support with sample set up and acquisition.

Competing interest: The authors declare no conflict of financial or commercial interest relevant to the present manuscript.

Funding / Support : This work was supported by a Canadian Institute of Health Research (CIHR) grant (VR2-172722) and from a supplement by the COVID-19 Immunity Task Force (CITF) to M-A.L. M.M. holds the Queen Elizabeth II scholarship in Science and Technology. YG is supported by a Charles Best and Frederick Banting CGS-D from CIHR (476885). M.-A.L. holds a Faculty of Medicine Chair of Excellence in Pandemic Viruses and Preparedness Research.

6.6 Supplemental Figures

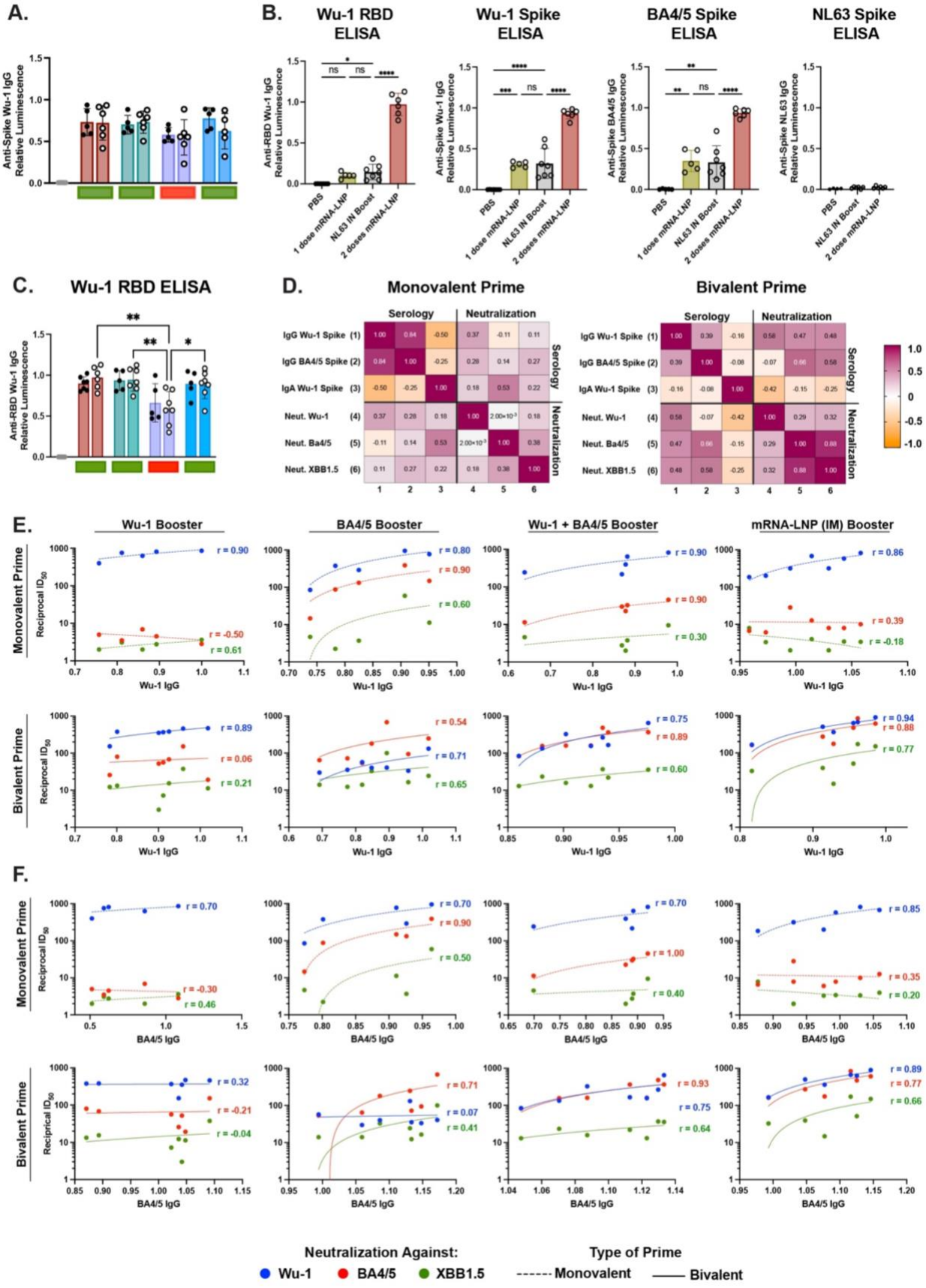

Supp. Figure 1: Prime vaccination drives differential humoral (total and neutralizing) responses in serum, while booster vaccination further refines these responses. A) Measurement of Wu-1 Spike relative titers in serum collected prior to second dose adminstration **B)** Measurement of Wu-1 Spike, BA4/5 spike and NL63 spike and **C)** Wu-1 RBD relative titers in serum collected at end point for mice intranasally boosted with 10 ug dose of NL63 seasonal coranavirus protein. **D)** Correlation between total and neutralizing antibodies in serum in mice who were monovalently primed or bivalently prime. Where each square reflects all respective antibody responses tested for all mice combined that received different IN boost formulation (10 ug dose) or different mRNA-LNP boost. **E)** Wu-1 specific IgG and Wu-1 (blue), BA4/5 (red) and XBB1.5 (green) neutralization ($ID_{50)}$ reciprocal titers elicited by different vaccination regiments in serum. **F)** BA4/5 specific IgG and Wu-1 (blue), BA4/5 (red) and XBB1.5 (green) neutralization (ID_{50}) reciprocal titer elicited by different vaccination regiments in serum. Data reflects results obtained from one biological replicate and is representative as average of 2-3 technical replicates. Serum was diluted 1:300 for pre-2^{nd} dose ebaluation and 1:500 for the the remaning measurements of IgG specific titers. For statistical analysis, antibody titers were log- transformed and then analyzed by a one-way ANOVA with Tukey's multiple comparisons test. ****$p < 0.0001$, **$p < 0.01$, *$p < 0.05$, n.s. no significant difference.

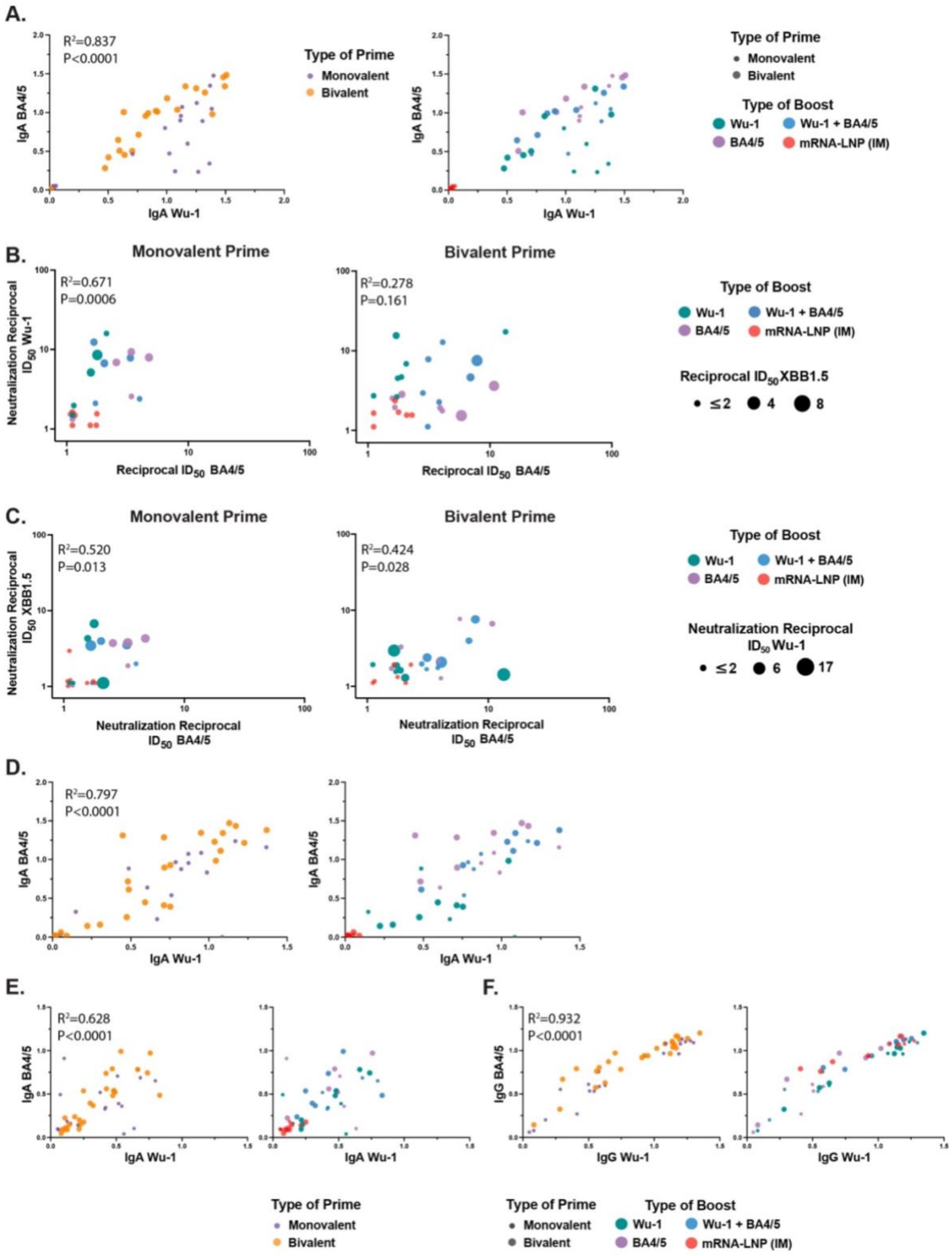

Supp. Figure 2: Dissection of mucosal immune responses in distinct biofluids.

A) Correlation of BA4/5 and Wu-1 specific IgA titers, colored on the basis of type of prime and type of boost in BALF. **B)** Correlation between BA4/5 and Wu-1 neutralization (ID_{50}) reciprocal titers, colored on the basis of type of boost and where the size of each appoint additionally reflects neutralization potency against XBB1.5

variant in BAL. **C)** Correlation between BA4/5 and XBB1.5 ID_{50} reciprocal titers, colored on the basis of type of boost and where the size of each appoint additionally reflects neutralization potency against Wu-1 strain in BAL. **E)** nasal and intestinal fluid correlation of BA4/5 and Wu-1 specific **F)** IgA and **G)** IgG titers.

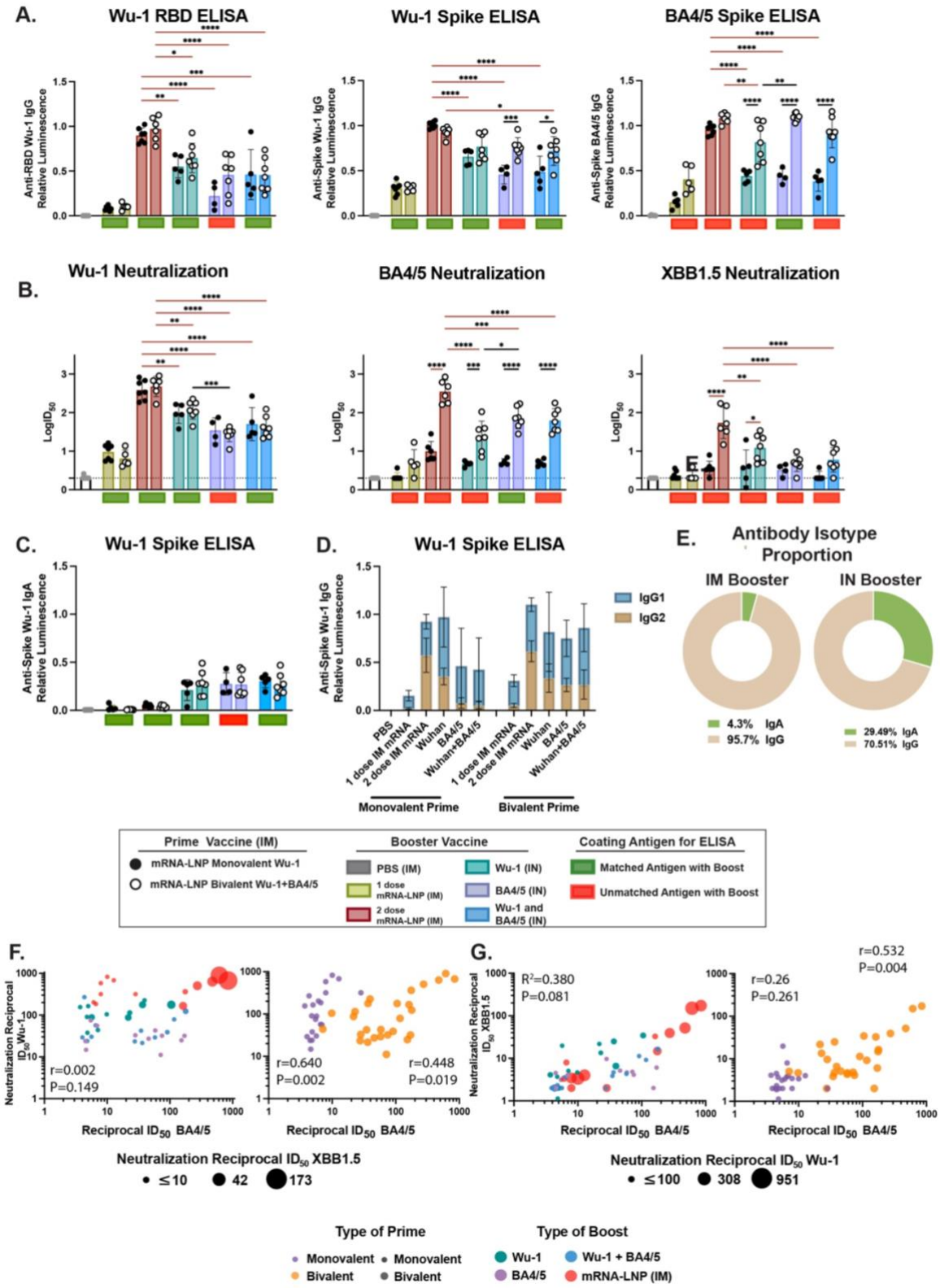

Supp. Figure 3: Characterization of systemic immune responses in serum following a heterologous systemic prime and 1 ug dose mucosal boost vaccination. A) Measurement of Wu-1 RBD, Wu-1 spike and BA4/5 spike specif IgG in serum collected at end point. **B)** Recipracal ID_{50} neutralization titers relative to inhibition of soluble ACE2 and immobilized Wu-1 spike, BA4/5 spike and XBB1.5 spike interaction. **C)**

Measurement of Wu-1 spike specific IgA and **D)** IgG1 and IgG2 in serum and relative proportion of Wu-1 specific IgG and IgA isotypes in serum. **E)** Correlation between BA4/5 and Wu-1 neutralization (ID_{50}) reciprocal titers, colored on the basis of type of boost and where the size of each appoint additionally reflects neutralization potency against XBB1.5 variant. Second graph reflect the same data but colored on the basis of the type of prime. **F)** Correlation between BA4/5 and **G)** XBB1.5 ID_{50} reciprocal titers, colored on the basis of type of boost and where the size of each appoint additionally reflects neutralization potency against Wu-1 variant. Second graph reflect the same data, but colored on the basis of the type of prime. Data reflect results obtained from one biological replicate and is representative as average of 3 technical replicates. For statistical analysis, antibody titers were log-transformed and then analyzed by a one-way ANOVA with Tukey's multiple comparisons test. ****$p < 0.0001$, **$p < 0.01$, *$p < 0.05$, n.s. no significant difference.

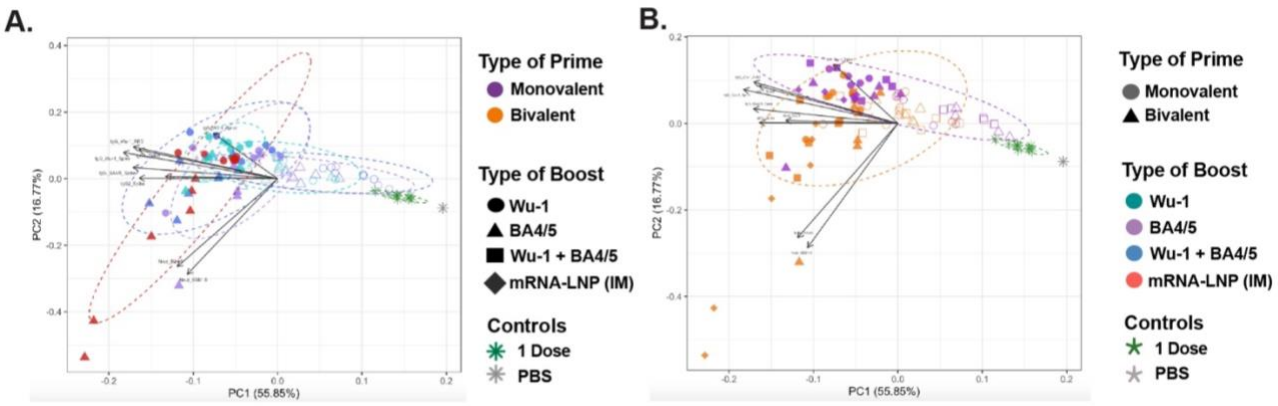

Supp Figure 4: Characterization of systemic immune kinetics in serum following a heterologous systemic prime and 1 ug dose mucosal boost vaccination.

PCA of differentially expressed antibody responses in serum following a 10 ug dose (filled points) or 1 ug dose (open points) boost. PCA was applied to individual mice, where one point reflects all antibody response tested for an individual mouse in serum as summarized in supp. figure 3. The PCA was colored on the basis of **A)** type of prime and **B)** type of boost to depict to differential trends of antibody clustering elicited by different vaccination regiments.

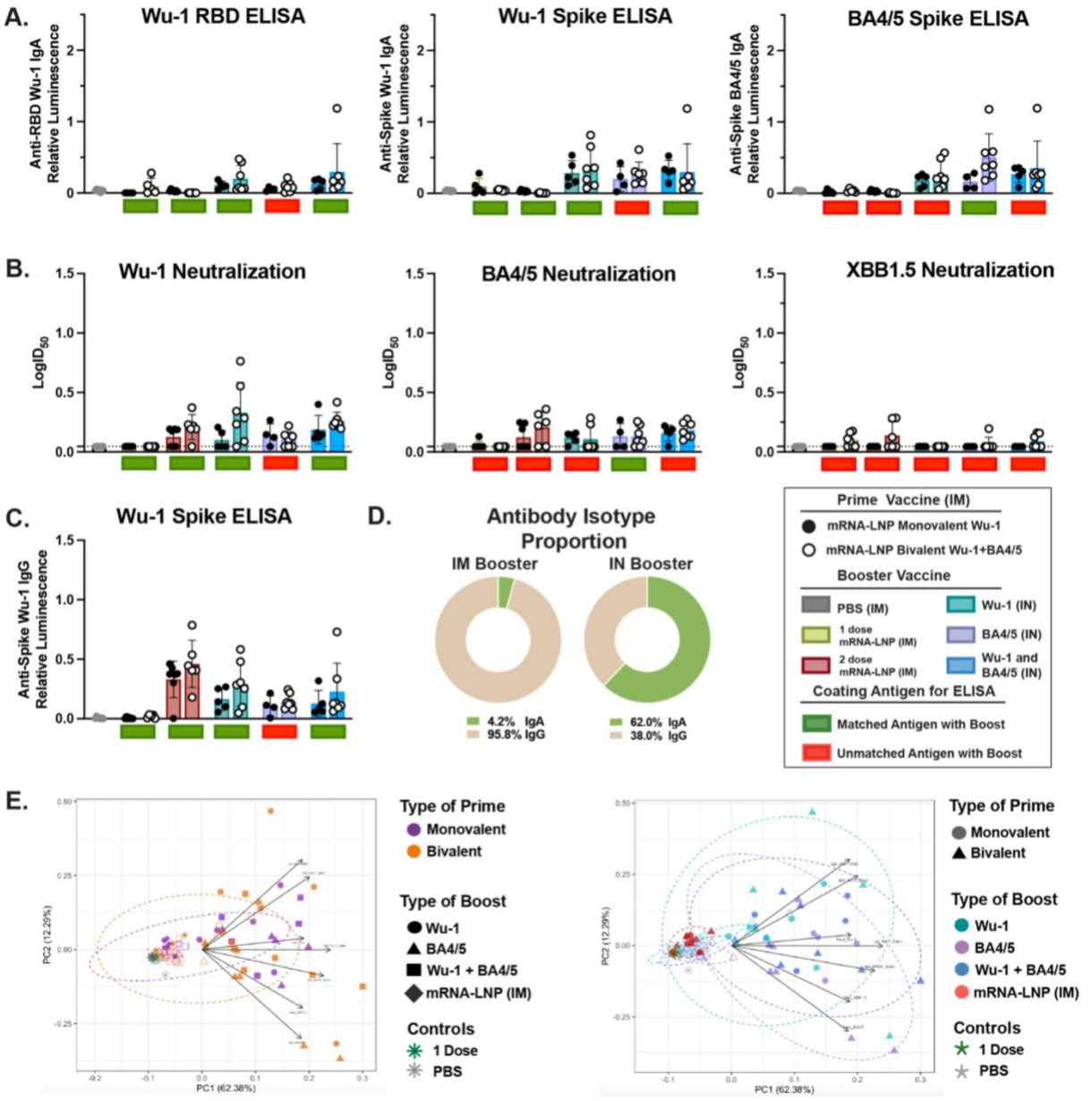

Supp. Figure 5: Characterization of mucosal immune responses in BALF following a heterologous systemic prime and 1 ug dose mucosal boost vaccination. A) Measurement of Wu-1 spike and BA4/5 spike specif IgA in serum collected at end point. **B)** Recipracal ID_{50} neutralization titers relative to inhibition of soluble ACE2 and immobilized Wu-1 spike, BA4/5 spike and XBB1.5 spike interaction. **C)** Measurement of Wu-1 spike specific IgG and **D)** relative proportion of Wu-1 specific IgG and IgA isotypes in serum. **E)** PCA of differentially expressed antibody responses in BALF following a 10 ug dose (filled points) or 1 ug dose (open points) boost. PCA was applied to individual mice, where one point reflects all antibody response tested for an individual mouse as summarized in panels A-C. The PCA was colored on the basis of type of prime and type of boost to depict to differential trends of antibody clustering elicited by different vaccination regiments. Data reflect results obtained from one biological replicate and is representative as average of 3 technical replicates. For statistical analysis, antibody titers were log- transformed and then analyzed by a one-way ANOVA with Tukey's multiple comparisons test. ****$p < 0.0001$, **$p < 0.01$, *$p < 0.05$, n.s. no significant difference.

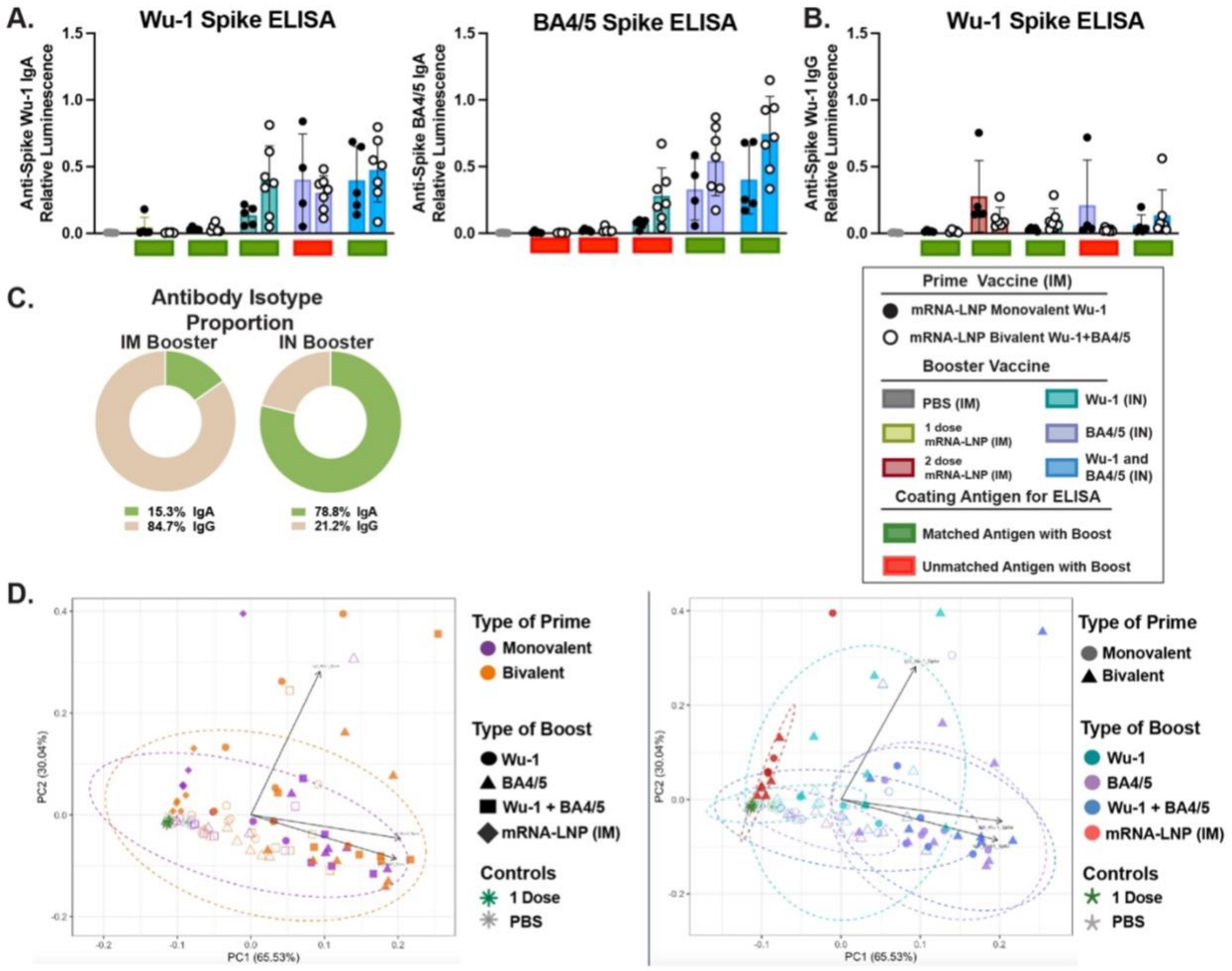

Supp. Figure 6: Characterization of mucosal immune responses in nasal fluid following a heterologous systemic prime and 1 ug dose mucosal boost vaccination. A) Measurement of Wu-1 spike and BA4/5 spike specif IgA in nasal wash collected at end point. **B)** Measurement of Wu-1 spike specific IgG and **C)** relative proportion of Wu-1 specific IgG and IgA isotypes in serum. **D)** PCA of differentially expressed antibody responses in nasal wash following a 10 ug dose (filled points) or 1 ug dose (open points) boost. PCA was applied to individual mice, where one point reflects all antibody response tested for an individual mouse as summarized in panels A-C. The PCA was colored on the basis of type of prime and type of boost to depict to differential trends of antibody clustering elicited by different vaccination regiments. Data reflect results obtained from one biological replicate and is representative as average of 3 technical replicates. For statistical analysis, antibody titers were log- transformed and then analyzed by a one-way ANOVA with Tukey's multiple comparisons test. ****$p < 0.0001$, **$p < 0.01$, *$p < 0.05$, n.s. no significant difference.

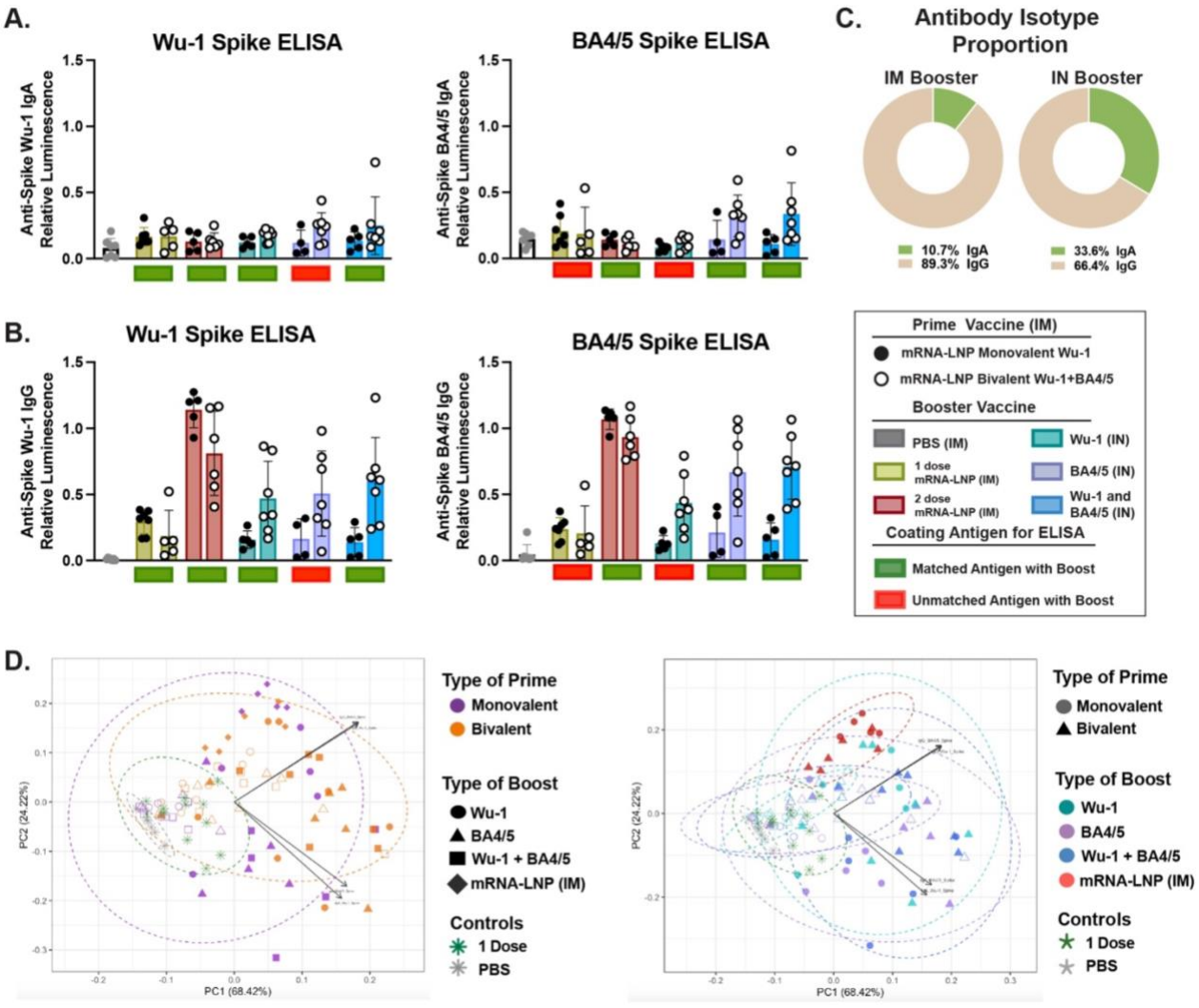

Supp. Figure 7: Characterization of mucosal immune responses in intestinal fluid following a heterologous systemic prime and 1 ug dose mucosal boost vaccination. A) Measurement of Wu-1 spike and BA4/5 spike specif **A)** IgA and **B)** IgG in intestines collected at end point. **C)** relative proportion of Wu-1 specific IgG and IgA isotypes in serum. **D)** PCA of differentially expressed antibody responses in intestines following a 10 ug dose (filled points) or 1 ug dose (open points) boost. PCA was applied to individual mice, where one point reflects all antibody response tested for an individual mouse as summarized in panels A-C. The PCA was colored on the basis of type of prime and type of boost to depict to differential trends of antibody clustering elicited by different vaccination regiments. Data reflect results obtained from one biological replicate and is representative as average of 3 technical replicates. For statistical analysis, antibody titers were log- transformed and then analyzed by a one-way ANOVA with Tukey's multiple comparisons test. ****$p < 0.0001$, **$p < 0.01$, *$p < 0.05$, n.s. no significant difference.

6.7 References

1 Cele, S. *et al.* SARS-CoV-2 Omicron has extensive but incomplete escape of Pfizer BNT162b2 elicited neutralization and requires ACE2 for infection. *medRxiv*, doi:10.1101/2021.12.08.21267417 (2021).

2 Chemaitelly, H. *et al.* Waning of BNT162b2 Vaccine Protection against SARS-CoV-2 Infection in Qatar. *N Engl J Med* **385**, e83, doi:10.1056/NEJMoa2114114 (2021).

3 Greaney, A. J. *et al.* Complete Mapping of Mutations to the SARS-CoV-2 Spike Receptor-Binding Domain that Escape Antibody Recognition. *Cell Host Microbe* **29**, 44-57 e49, doi:10.1016/j.chom.2020.11.007 (2021).

4 Tortorici, M. A. *et al.* Persistent immune imprinting occurs after vaccination with the COVID-19 XBB.1.5 mRNA booster in humans. *Immunity* **57**, 904-911 e904, doi:10.1016/j.immuni.2024.02.016 (2024).

5 Tan, S. T. *et al.* Infectiousness of SARS-CoV-2 breakthrough infections and reinfections during the Omicron wave. *Nat Med* **29**, 358-365, doi:10.1038/s41591-022-02138-x (2023).

6 Regenhardt, E. *et al.* SARS-CoV-2 Vaccine Breakthrough Infections of Omicron and Delta Variants in Healthcare Workers. *Vaccines (Basel)* **11**, doi:10.3390/vaccines11050958 (2023).

7 Singanayagam, A. *et al.* Community transmission and viral load kinetics of the SARS-CoV-2 delta (B.1.617.2) variant in vaccinated and unvaccinated individuals in the UK: a prospective, longitudinal, cohort study. *Lancet Infect Dis* **22**, 183-195, doi:10.1016/S1473-3099(21)00648-4 (2022).

8 Chu, L. *et al.* Immune response to SARS-CoV-2 after a booster of mRNA-1273: an open-label phase 2 trial. *Nat Med* **28**, 1042-1049, doi:10.1038/s41591-022-01739-w (2022).

9 Kaku, C. I. *et al.* Recall of preexisting cross-reactive B cell memory after Omicron BA.1 breakthrough infection. *Sci Immunol* **7**, eabq3511, doi:10.1126/sciimmunol.abq3511 (2022).

10 Kuhlmann, C. *et al.* Breakthrough infections with SARS-CoV-2 omicron despite mRNA vaccine booster dose. *Lancet* **399**, 625-626, doi:10.1016/S0140-6736(22)00090-3 (2022).

11 Lange, B., Gerigk, M. & Tenenbaum, T. Breakthrough Infections in BNT162b2-Vaccinated Health Care Workers. *N Engl J Med* **385**, 1145-1146, doi:10.1056/NEJMc2108076 (2021).

12 Kustin, T. *et al.* Evidence for increased breakthrough rates of SARS-CoV-2 variants of concern in BNT162b2-mRNA-vaccinated individuals. *Nat Med* **27**, 1379-1384, doi:10.1038/s41591-021-01413-7 (2021).

13 Bergwerk, M. *et al.* Covid-19 Breakthrough Infections in Vaccinated Health Care Workers. *N Engl J Med* **385**, 1474-1484, doi:10.1056/NEJMoa2109072 (2021).

14 Hager, K. J. *et al.* Efficacy and Safety of a Recombinant Plant-Based Adjuvanted Covid-19 Vaccine. *N Engl J Med* **386**, 2084-2096, doi:10.1056/NEJMoa2201300 (2022).

15 Thomas, S. J. *et al.* Safety and Efficacy of the BNT162b2 mRNA Covid-19 Vaccine through 6 Months. *N Engl J Med* **385**, 1761-1773, doi:10.1056/NEJMoa2110345 (2021).

16 Polack, F. P. *et al.* Safety and Efficacy of the BNT162b2 mRNA Covid-19 Vaccine. *N Engl J Med* **383**, 2603-2615, doi:10.1056/NEJMoa2034577 (2020).

17 Tenforde, M. W. *et al.* Association Between mRNA Vaccination and COVID-19 Hospitalization and Disease Severity. *JAMA* **326**, 2043-2054, doi:10.1001/jama.2021.19499 (2021).

18 Menni, C. *et al.* COVID-19 vaccine waning and effectiveness and side-effects of boosters: a prospective community study from the ZOE COVID Study. *Lancet Infect Dis*, doi:10.1016/S1473-3099(22)00146-3 (2022).

19 Lucas, C. *et al.* Impact of circulating SARS-CoV-2 variants on mRNA vaccine-induced immunity. *Nature* **600**, 523-529, doi:10.1038/s41586-021-04085-y (2021).

20 Weber, T. *et al.* Enhanced SARS-CoV-2 humoral immunity following breakthrough infection builds upon the preexisting memory B cell pool. *Sci Immunol* **8**, eadk5845, doi:10.1126/sciimmunol.adk5845 (2023).

21 Kemp, S. A. *et al.* Transmission of B.1.617.2 Delta variant between vaccinated healthcare workers. *Sci Rep* **12**, 10492, doi:10.1038/s41598-022-14411-7 (2022).

22 Tang, J. *et al.* Respiratory mucosal immunity against SARS-CoV-2 following mRNA vaccination. *Sci Immunol*, eadd4853, doi:10.1126/sciimmunol.add4853 (2022).

23 Sheikh-Mohamed, S. *et al.* Systemic and mucosal IgA responses are variably induced in response to SARS-CoV-2 mRNA vaccination and are associated with protection against subsequent infection. *Mucosal Immunol*, doi:10.1038/s41385-022-00511-0 (2022).

24 Krammer, F. SARS-CoV-2 vaccines in development. *Nature* **586**, 516-527, doi:10.1038/s41586-020-2798-3 (2020).

25 Brouwer, P. J. M. *et al.* Potent neutralizing antibodies from COVID-19 patients define multiple targets of vulnerability. *Science* **369**, 643-650, doi:10.1126/science.abc5902 (2020).
26 Liu, L. *et al.* Potent neutralizing antibodies against multiple epitopes on SARS-CoV-2 spike. *Nature* **584**, 450-456, doi:10.1038/s41586-020-2571-7 (2020).
27 Rogers, T. F. *et al.* Isolation of potent SARS-CoV-2 neutralizing antibodies and protection from disease in a small animal model. *Science* **369**, 956-963, doi:10.1126/science.abc7520 (2020).
28 Bartsch, Y. C. *et al.* Humoral signatures of protective and pathological SARS-CoV-2 infection in children. *Nat Med* **27**, 454-462, doi:10.1038/s41591-021-01263-3 (2021).
29 Baden, L. R. *et al.* Efficacy and Safety of the mRNA-1273 SARS-CoV-2 Vaccine. *N Engl J Med* **384**, 403-416, doi:10.1056/NEJMoa2035389 (2021).
30 Chalkias, S. *et al.* Original SARS-CoV-2 monovalent and Omicron BA.4/BA.5 bivalent COVID-19 mRNA vaccines: phase 2/3 trial interim results. *Nat Med* **29**, 2325-2333, doi:10.1038/s41591-023-02517-y (2023).
31 Kurhade, C. *et al.* Low neutralization of SARS-CoV-2 Omicron BA.2.75.2, BQ.1.1 and XBB.1 by parental mRNA vaccine or a BA.5 bivalent booster. *Nat Med* **29**, 344-347, doi:10.1038/s41591-022-02162-x (2023).
32 Chalkias, S. *et al.* A Bivalent Omicron-Containing Booster Vaccine against Covid-19. *N Engl J Med* **387**, 1279-1291, doi:10.1056/NEJMoa2208343 (2022).
33 Davis-Gardner, M. E. *et al.* Neutralization against BA.2.75.2, BQ.1.1, and XBB from mRNA Bivalent Booster. *N Engl J Med* **388**, 183-185, doi:10.1056/NEJMc2214293 (2023).
34 Zou, J. *et al.* Neutralization of BA.4-BA.5, BA.4.6, BA.2.75.2, BQ.1.1, and XBB.1 with Bivalent Vaccine. *N Engl J Med* **388**, 854-857, doi:10.1056/NEJMc2214916 (2023).
35 Collier, A. Y. *et al.* Immunogenicity of BA.5 Bivalent mRNA Vaccine Boosters. *N Engl J Med* **388**, 565-567, doi:10.1056/NEJMc2213948 (2023).
36 Wang, Q. *et al.* Antibody Response to Omicron BA.4-BA.5 Bivalent Booster. *N Engl J Med* **388**, 567-569, doi:10.1056/NEJMc2213907 (2023).
37 Wang, Q. *et al.* Deep immunological imprinting due to the ancestral spike in the current bivalent COVID-19 vaccine. *Cell Rep Med* **4**, 101258, doi:10.1016/j.xcrm.2023.101258 (2023).
38 Wang, Q. *et al.* SARS-CoV-2 neutralising antibodies after bivalent versus monovalent booster. *Lancet Infect Dis* **23**, 527-528, doi:10.1016/S1473-3099(23)00181-0 (2023).
39 Wang, Q. *et al.* SARS-CoV-2 neutralising antibodies after a second BA.5 bivalent booster. *Lancet* **402**, 1827-1828, doi:10.1016/S0140-6736(23)02278-X (2023).
40 Johnston, T. S. *et al.* Immunological imprinting shapes the specificity of human antibody responses against SARS-CoV-2 variants. *Immunity* **57**, 912-925 e914, doi:10.1016/j.immuni.2024.02.017 (2024).
41 Wang, Q. *et al.* XBB.1.5 monovalent mRNA vaccine booster elicits robust neutralizing antibodies against XBB subvariants and JN.1. *Cell Host Microbe* **32**, 315-321 e313, doi:10.1016/j.chom.2024.01.014 (2024).
42 Altarawneh, H. N. *et al.* Effects of previous infection, vaccination, and hybrid immunity against symptomatic Alpha, Beta, and Delta SARS-CoV-2 infections: an observational study. *EBioMedicine* **95**, 104734, doi:10.1016/j.ebiom.2023.104734 (2023).
43 Carabelli, A. M. *et al.* SARS-CoV-2 variant biology: immune escape, transmission and fitness. *Nat Rev Microbiol* **21**, 162-177, doi:10.1038/s41579-022-00841-7 (2023).
44 Aguilar-Bretones, M., Fouchier, R. A., Koopmans, M. P. & van Nierop, G. P. Impact of antigenic evolution and original antigenic sin on SARS-CoV-2 immunity. *J Clin Invest* **133**, doi:10.1172/JCI162192 (2023).
45 Lin, D. Y. *et al.* Durability of Bivalent Boosters against Omicron Subvariants. *N Engl J Med* **388**, 1818-1820, doi:10.1056/NEJMc2302462 (2023).
46 Han, A. X., de Jong, S. P. J. & Russell, C. A. Co-evolution of immunity and seasonal influenza viruses. *Nat Rev Microbiol* **21**, 805-817, doi:10.1038/s41579-023-00945-8 (2023).
47 Maltseva, M., Keeshan, A., Cooper, C. & Langlois, M. A. Immune imprinting: The persisting influence of the first antigenic encounter with rapidly evolving viruses. *Hum Vaccin Immunother* **20**, 2384192, doi:10.1080/21645515.2024.2384192 (2024).
48 Koutsakos, M. & Ellebedy, A. H. Immunological imprinting: Understanding COVID-19. *Immunity* **56**, 909-913, doi:10.1016/j.immuni.2023.04.012 (2023).
49 Huang, C. Q., Vishwanath, S., Carnell, G. W., Chan, A. C. Y. & Heeney, J. L. Immune imprinting and next-generation coronavirus vaccines. *Nat Microbiol* **8**, 1971-1985, doi:10.1038/s41564-023-01505-9 (2023).
50 Carreno, J. M., Singh, G., Simon, V., Krammer, F. & group, P. V. I. s. Bivalent COVID-19 booster vaccines and the absence of BA.5-specific antibodies. *Lancet Microbe* **4**, e569, doi:10.1016/S2666-5247(23)00118-0 (2023).

51 Park, Y. J. *et al.* Imprinted antibody responses against SARS-CoV-2 Omicron sublineages. *Science* **378**, 619-627, doi:10.1126/science.adc9127 (2022).

52 Roltgen, K. *et al.* Immune imprinting, breadth of variant recognition, and germinal center response in human SARS-CoV-2 infection and vaccination. *Cell* **185**, 1025-1040 e1014, doi:10.1016/j.cell.2022.01.018 (2022).

53 Aydillo, T. *et al.* Immunological imprinting of the antibody response in COVID-19 patients. *Nat Commun* **12**, 3781, doi:10.1038/s41467-021-23977-1 (2021).

54 Marking, U. *et al.* 7-month duration of SARS-CoV-2 mucosal immunoglobulin-A responses and protection. *Lancet Infect Dis* **23**, 150-152, doi:10.1016/S1473-3099(22)00834-9 (2023).

55 Sheikh-Mohamed, S., Sanders, E. C., Gommerman, J. L. & Tal, M. C. Guardians of the oral and nasopharyngeal galaxy: IgA and protection against SARS-CoV-2 infection. *Immunol Rev* **309**, 75-85, doi:10.1111/imr.13118 (2022).

56 Havervall, S. *et al.* Anti-Spike Mucosal IgA Protection against SARS-CoV-2 Omicron Infection. *N Engl J Med* **387**, 1333-1336, doi:10.1056/NEJMc2209651 (2022).

57 Sano, K. *et al.* SARS-CoV-2 vaccination induces mucosal antibody responses in previously infected individuals. *Nat Commun* **13**, 5135, doi:10.1038/s41467-022-32389-8 (2022).

58 Bhavsar, D. *et al.* Mucosal antibody responses to SARS-CoV-2 booster vaccination and breakthrough infection. *mBio* **14**, e0228023, doi:10.1128/mbio.02280-23 (2023).

59 Stark, F. C. *et al.* Intranasal immunization with a proteosome-adjuvanted SARS-CoV-2 spike protein-based vaccine is immunogenic and efficacious in mice and hamsters. *Sci Rep* **12**, 9772, doi:10.1038/s41598-022-13819-5 (2022).

60 Hassan, A. O. *et al.* A single intranasal dose of chimpanzee adenovirus-vectored vaccine protects against SARS-CoV-2 infection in rhesus macaques. *bioRxiv*, doi:10.1101/2021.01.26.428251 (2021).

61 Bricker, T. L. *et al.* A single intranasal or intramuscular immunization with chimpanzee adenovirus-vectored SARS-CoV-2 vaccine protects against pneumonia in hamsters. *Cell Rep* **36**, 109400, doi:10.1016/j.celrep.2021.109400 (2021).

62 Langel, S. N. *et al.* Adenovirus type 5 SARS-CoV-2 vaccines delivered orally or intranasally reduced disease severity and transmission in a hamster model. *Sci Transl Med*, eabn6868, doi:10.1126/scitranslmed.abn6868 (2022).

63 Afkhami, S. *et al.* Respiratory mucosal delivery of next-generation COVID-19 vaccine provides robust protection against both ancestral and variant strains of SARS-CoV-2. *Cell* **185**, 896-915 e819, doi:10.1016/j.cell.2022.02.005 (2022).

64 Du, Y. *et al.* Intranasal administration of a recombinant RBD vaccine induced protective immunity against SARS-CoV-2 in mouse. *Vaccine* **39**, 2280-2287, doi:10.1016/j.vaccine.2021.03.006 (2021).

65 Maltseva, M. *et al.* Characterization of Systemic and Mucosal Humoral Immune Responses to an Adjuvanted Intranasal SARS-CoV-2 Protein Subunit Vaccine Candidate in Mice. *Vaccines (Basel)* **11**, doi:10.3390/vaccines11010030 (2022).

66 Diaz, M. F. *et al.* Intranasal vaccination of hamsters with a Newcastle disease virus vector expressing the S1 subunit protects animals against SARS-CoV-2 disease. *Sci Rep* **12**, 10359, doi:10.1038/s41598-022-13560-z (2022).

67 van Doremalen, N. *et al.* Intranasal ChAdOx1 nCoV-19/AZD1222 vaccination reduces viral shedding after SARS-CoV-2 D614G challenge in preclinical models. *Sci Transl Med* **13**, doi:10.1126/scitranslmed.abh0755 (2021).

68 King, R. G. *et al.* Single-Dose Intranasal Administration of AdCOVID Elicits Systemic and Mucosal Immunity against SARS-CoV-2 and Fully Protects Mice from Lethal Challenge. *Vaccines (Basel)* **9**, doi:10.3390/vaccines9080881 (2021).

69 Lapuente, D. *et al.* Protective mucosal immunity against SARS-CoV-2 after heterologous systemic prime-mucosal boost immunization. *Nat Commun* **12**, 6871, doi:10.1038/s41467-021-27063-4 (2021).

70 Hassan, A. O. *et al.* A Single-Dose Intranasal ChAd Vaccine Protects Upper and Lower Respiratory Tracts against SARS-CoV-2. *Cell* **183**, 169-184 e113, doi:10.1016/j.cell.2020.08.026 (2020).

71 Agbayani, G. *et al.* Intranasal administration of unadjuvanted SARS-CoV-2 spike antigen boosts antigen-specific immune responses induced by parenteral protein subunit vaccine prime in mice and hamsters. *Eur J Immunol* **54**, e2350620, doi:10.1002/eji.202350620 (2024).

72 Mao, T. *et al.* Unadjuvanted intranasal spike vaccine booster elicits robust protective mucosal immunity against sarbecoviruses. *Science*, eabo2523, doi:10.1126/science.abo2523 (2022).

73 Christensen, D. *et al.* Protection against SARS-CoV-2 transmission by a parenteral prime-Intranasal boost vaccine strategy. *EBioMedicine* **84**, 104248, doi:10.1016/j.ebiom.2022.104248 (2022).

74 Beitari, S. *et al.* Effectiveness of VSV vectored SARS-CoV-2 spike when administered through intranasal, intramuscular or a combination of both. *Sci Rep* **13**, 21390, doi:10.1038/s41598-023-48397-7 (2023).

75 Gagne, M. *et al.* Mucosal Adenoviral-vectored Vaccine Boosting Durably Prevents XBB.1.16 Infection in Nonhuman Primates. *bioRxiv*, doi:10.1101/2023.11.06.565765 (2023).

76 Darling, T. L. *et al.* Mucosal immunization with ChAd-SARS-CoV-2-S prevents sequential transmission of SARS-CoV-2 to unvaccinated hamsters. *Sci Adv* **10**, eadp1290, doi:10.1126/sciadv.adp1290 (2024).

77 Braun, M. R. *et al.* Mucosal immunization with Ad5-based vaccines protects Syrian hamsters from challenge with omicron and delta variants of SARS-CoV-2. *Front Immunol* **14**, 1086035, doi:10.3389/fimmu.2023.1086035 (2023).

78 Laghlali, G. *et al.* Enhanced mucosal B- and T-cell responses against SARS-CoV-2 after heterologous intramuscular mRNA prime/intranasal protein boost vaccination with a combination adjuvant. *bioRxiv*, doi:10.1101/2024.03.28.587260 (2024).

79 Wang, Q. *et al.* Intranasal booster using an Omicron vaccine confers broad mucosal and systemic immunity against SARS-CoV-2 variants. *Signal Transduct Target Ther* **8**, 167, doi:10.1038/s41392-023-01423-6 (2023).

80 Lederer, K. *et al.* SARS-CoV-2 mRNA Vaccines Foster Potent Antigen-Specific Germinal Center Responses Associated with Neutralizing Antibody Generation. *Immunity* **53**, 1281-1295 e1285, doi:10.1016/j.immuni.2020.11.009 (2020).

81 Khoury, D. S. *et al.* Correlates of Protection, Thresholds of Protection, and Immunobridging among Persons with SARS-CoV-2 Infection. *Emerg Infect Dis* **29**, 381-388, doi:10.3201/eid2902.221422 (2023).

82 Khoury, D. S. *et al.* Neutralizing antibody levels are highly predictive of immune protection from symptomatic SARS-CoV-2 infection. *Nat Med* **27**, 1205-1211, doi:10.1038/s41591-021-01377-8 (2021).

83 Walls, A. C. *et al.* Elicitation of broadly protective sarbecovirus immunity by receptor-binding domain nanoparticle vaccines. *Cell* **184**, 5432-5447 e5416, doi:10.1016/j.cell.2021.09.015 (2021).

84 Wang, Z. *et al.* Enhanced SARS-CoV-2 neutralization by dimeric IgA. *Sci Transl Med* **13**, doi:10.1126/scitranslmed.abf1555 (2021).

85 Faustini, S. E. *et al.* Development of a high-sensitivity ELISA detecting IgG, IgA and IgM antibodies to the SARS-CoV-2 spike glycoprotein in serum and saliva. *Immunology* **164**, 135-147, doi:10.1111/imm.13349 (2021).

86 Isho, B. *et al.* Persistence of serum and saliva antibody responses to SARS-CoV-2 spike antigens in COVID-19 patients. *Sci Immunol* **5**, doi:10.1126/sciimmunol.abe5511 (2020).

87 Pisanic, N. *et al.* COVID-19 Serology at Population Scale: SARS-CoV-2-Specific Antibody Responses in Saliva. *J Clin Microbiol* **59**, doi:10.1128/JCM.02204-20 (2020).

88 Reynolds, H. Y. Immunoglobulin G and its function in the human respiratory tract. *Mayo Clin Proc* **63**, 161-174, doi:10.1016/s0025-6196(12)64949-0 (1988).

89 Wu, Y. *et al.* Incubation Period of COVID-19 Caused by Unique SARS-CoV-2 Strains: A Systematic Review and Meta-analysis. *JAMA Netw Open* **5**, e2228008, doi:10.1001/jamanetworkopen.2022.28008 (2022).

90 Hui, K. P. Y. *et al.* SARS-CoV-2 Omicron variant replication in human bronchus and lung ex vivo. *Nature* **603**, 715-720, doi:10.1038/s41586-022-04479-6 (2022).

91 Huang, N. *et al.* SARS-CoV-2 infection of the oral cavity and saliva. *Nat Med* **27**, 892-903, doi:10.1038/s41591-021-01296-8 (2021).

92 Iwasaki, A. Exploiting Mucosal Immunity for Antiviral Vaccines. *Annu Rev Immunol* **34**, 575-608, doi:10.1146/annurev-immunol-032414-112315 (2016).

93 Suzuki, T. *et al.* Relationship of the quaternary structure of human secretory IgA to neutralization of influenza virus. *Proc Natl Acad Sci U S A* **112**, 7809-7814, doi:10.1073/pnas.1503885112 (2015).

94 Schroeder, H. W., Jr. & Cavacini, L. Structure and function of immunoglobulins. *J Allergy Clin Immunol* **125**, S41-52, doi:10.1016/j.jaci.2009.09.046 (2010).

95 Corthesy, B. Multi-faceted functions of secretory IgA at mucosal surfaces. *Front Immunol* **4**, 185, doi:10.3389/fimmu.2013.00185 (2013).

96 Renegar, K. B., Small, P. A., Jr., Boykins, L. G. & Wright, P. F. Role of IgA versus IgG in the control of influenza viral infection in the murine respiratory tract. *J Immunol* **173**, 1978-1986, doi:10.4049/jimmunol.173.3.1978 (2004).

97 Woof, J. M. & Kerr, M. A. The function of immunoglobulin A in immunity. *J Pathol* **208**, 270-282, doi:10.1002/path.1877 (2006).
98 Kerr, M. A. The structure and function of human IgA. *Biochem J* **271**, 285-296, doi:10.1042/bj2710285 (1990).
99 Isho, B., Florescu, A., Wang, A. A. & Gommerman, J. L. Fantastic IgA plasma cells and where to find them. *Immunol Rev* **303**, 119-137, doi:10.1111/imr.12980 (2021).
100 Rojas, O. L. *et al.* Recirculating Intestinal IgA-Producing Cells Regulate Neuroinflammation via IL-10. *Cell* **177**, 492-493, doi:10.1016/j.cell.2019.03.037 (2019).
101 Nahass, G. R. *et al.* Intramuscular SARS-CoV-2 vaccines elicit varying degrees of plasma and salivary antibody responses as compared to natural infection. *Medrxiv*, 2021.2008. 2022.21262168 (2021).
102 Park, S. K. *et al.* Detection of SARS-CoV-2 in Fecal Samples From Patients With Asymptomatic and Mild COVID-19 in Korea. *Clin Gastroenterol Hepatol* **19**, 1387-1394 e1382, doi:10.1016/j.cgh.2020.06.005 (2021).
103 Gaebler, C. *et al.* Evolution of antibody immunity to SARS-CoV-2. *Nature* **591**, 639-644, doi:10.1038/s41586-021-03207-w (2021).
104 Morone, G. *et al.* Incidence and Persistence of Viral Shedding in COVID-19 Post-acute Patients With Negativized Pharyngeal Swab: A Systematic Review. *Front Med (Lausanne)* **7**, 562, doi:10.3389/fmed.2020.00562 (2020).
105 Schiepers, A. *et al.* Molecular fate-mapping of serum antibody responses to repeat immunization. *Nature* **615**, 482-489, doi:10.1038/s41586-023-05715-3 (2023).
106 Alsoussi, W. B. *et al.* SARS-CoV-2 Omicron boosting induces de novo B cell response in humans. *Nature* **617**, 592-598, doi:10.1038/s41586-023-06025-4 (2023).
107 Yisimayi, A. *et al.* Repeated Omicron exposures override ancestral SARS-CoV-2 immune imprinting. *Nature* **625**, 148-156, doi:10.1038/s41586-023-06753-7 (2024).
108 Kim, J. H., Davis, W. G., Sambhara, S. & Jacob, J. Strategies to alleviate original antigenic sin responses to influenza viruses. *Proc Natl Acad Sci U S A* **109**, 13751-13756, doi:10.1073/pnas.0912458109 (2012).
109 Grifoni, A. *et al.* SARS-CoV-2 human T cell epitopes: Adaptive immune response against COVID-19. *Cell Host Microbe* **30**, 1788, doi:10.1016/j.chom.2022.10.017 (2022).
110 Colwill, K. *et al.* A scalable serology solution for profiling humoral immune responses to SARS-CoV-2 infection and vaccination. *Clin Transl Immunology* **11**, e1380, doi:10.1002/cti2.1380 (2022).
111 Demone, J. *et al.* Scalable agroinfiltration-based production of SARS-CoV-2 antigens for use in diagnostic assays and subunit vaccines. *PLoS One* **17**, e0277668, doi:10.1371/journal.pone.0277668 (2022).

7 Chapter 7: Immune imprinting: The persisting influence of the first antigenic encounter with rapidly evolving viruses. *(Published)*

Preface: This chapter has been previously published as a review article.

Maltseva, M., Keeshan, A., Cooper, C., & Langlois, M. A. (2024). Immune imprinting: The persisting influence of the first antigenic encounter with rapidly evolving viruses. ***Human Vaccines & Immunotherapeutics,*** *20*(1), 2384192. DOI: 10.1080/21645515.2024.2384192

7.1 Abstract:

Immune imprinting is a phenomenon that stems from the fundamentals of immunological memory. Upon recurrent exposures to an evolving pathogen, the immune system must weigh the benefits of rapidly recalling established antibody repertoires with greater affinity to the initial variant or invest additional time and energy in producing de novo responses specific to the emerging variant. In this review, we delve into the mechanistic complexities of immune imprinting and its role in shaping subsequent immune responses, both *de novo* and recall, against rapidly evolving respiratory viruses such as influenza and coronaviruses. By exploring the duality of immune imprinting, we examine its potential to both enhance or hinder immune protection against disease, while emphasizing the role of host and viral factors. Finally, we explore how different vaccine platforms may affect immune imprinting and we comment on vaccine strategies that can favor *de novo* variant-specific antibody responses.

7.2 Immune imprinting

Constant exposure to evolving microbes represents a lifelong battle between the host and pathogen, beginning in childhood and continuing into old age. The cornerstone of adaptive humoral immunity relies on the induction of progressively compounding and efficient antibody responses following recurrent antigenic exposures, an effective mechanism exploited by seasonal or booster vaccinations[1]. Yet, this prompts the question: To what degree does our first exposure to a virus, through either natural infection or vaccination, shape subsequent immune responses to later encounters with antigenically related variants? This query has perplexed immunologists since a series of pivotal studies in the 1950s examined humoral response dynamics across distinct age ranges before and after infection or vaccination with different influenza strains[2-4]. Key observations were: 1) potent recall antibody responses induced against viral antigens not included in the vaccine formulation, and 2) the dominant antibody responses were against influenza strains encountered earliest in life. Consequently, Thomas Francis postulated the doctrine of original antigenic sin (OAS), describing an immune "imprint established by the original virus infection [that] governs the antibody response thereafter" [5].

Although OAS or immune imprinting has primarily been observed with influenza due to its recurrent seasonality and high mutability, it has also been noted in other viral infections, including dengue virus, norovirus, hepatitis C (HCV), respiratory syncytial virus (RSV), and more recently, Severe Acute Respiratory Syndrome Coronavirus 2 (SARS-CoV-2) 6-[11]. Evidence for imprinting in non-respiratory viruses includes the induction of antibody recall responses to the initially encountered antigen and the production of cross-reactive antibodies following reinfection with heterologous noroviruses genotypes or HCV subtypes. Differential infection risks and worsened clinical outcomes have been observed following sequential exposures to heterologous viral strains. For instance, increased hemorrhagic fever risk has been noted in individuals following secondary dengue infections with a heterologous serotype to the primary infecting serotype, suggesting immune imprinting effects [12]. However, antibody-dependent enhancement (ADE) has also been observed where pre-existing antibodies form complexes that facilitate viral entry into target immune cells via Fc receptor binding[6]. Enhanced RSV disease severity was observed among children vaccinated against RSV that were subsequently infected. Thus, differential humoral responses following heterologous viral exposures along with specific evidence of immune

imprinting in recurrent influenza infections and from recurrent SARS-CoV-2 infections or vaccinations, highlight the critical need for ongoing research on immune imprinting.

7.3 Mechanistic intricacies of immune imprinting

Circulating antibodies offer a unique snapshot of an individual's distinctive history of infection. Following infection, the host's B cells can directly recognize native (unprocessed) antigens in secondary lymphoid organs via their binding to the B cell receptor (BCR), and processed antigens that are displayed on MHC class II molecules on the surface of antigen-presenting cells (APC) [13,14]. Interactions with the antigen in both of these scenarios initiates B cell activation through receptor-induced signaling, which can be considerably enhanced by cross-linking multiple BCRs with multivalent antigens or repeating epitopes[13,14]. Although most soluble protein antigens do not contain repetitive epitopes, particulate antigens like viruses or viral-like particles (VLP) often have repetitive arrays of antigen on their surface and can promote BCR cross-linking through higher affinity binding that enhances priming of B cells prior to receiving T cell help[14]. Efficient interactions with the T cell receptor (TCR) and CD40 ligand (CD40L) expressed on antigen-specific helper T cells lead to further B cell activation, proliferation, and differentiation. In the early phase of the humoral response, following the first antigenic exposure, a portion of activated B cells differentiate into plasmablasts and provide an immediate but short-lived source of low-affinity antibodies to eliminate acute infections (Fig.1A). As the humoral response develops, more specialized responses are induced. Remaining activated B cells will differentiate into memory B cells (MBC) or migrate to secondary lymphoid tissues to form germinal centers (GC), where they will undergo isotype class switching, somatic hypermutation, and affinity maturation[15]. Selected B cells with high affinity for the antigen can differentiate into plasma cells (LLPC), which are long-lived and continuous secretors of antibodies, or into MBCs, which will rapidly respond upon reencountering the viral antigen. These become the dominant source of antibodies in subsequent exposures to the antigen (Fig. 1A). Thus, both LLPCs and MBCs are desirable cell types to elicit by vaccination, as they can rapidly respond following re-exposure. Therefore, with each new exposure to an antigenically distant viral variant, the induced humoral response may comprise both recall and de novo antibody responses, depending on the antigenic similarity between prior and subsequent antigens (Fig. 1C).

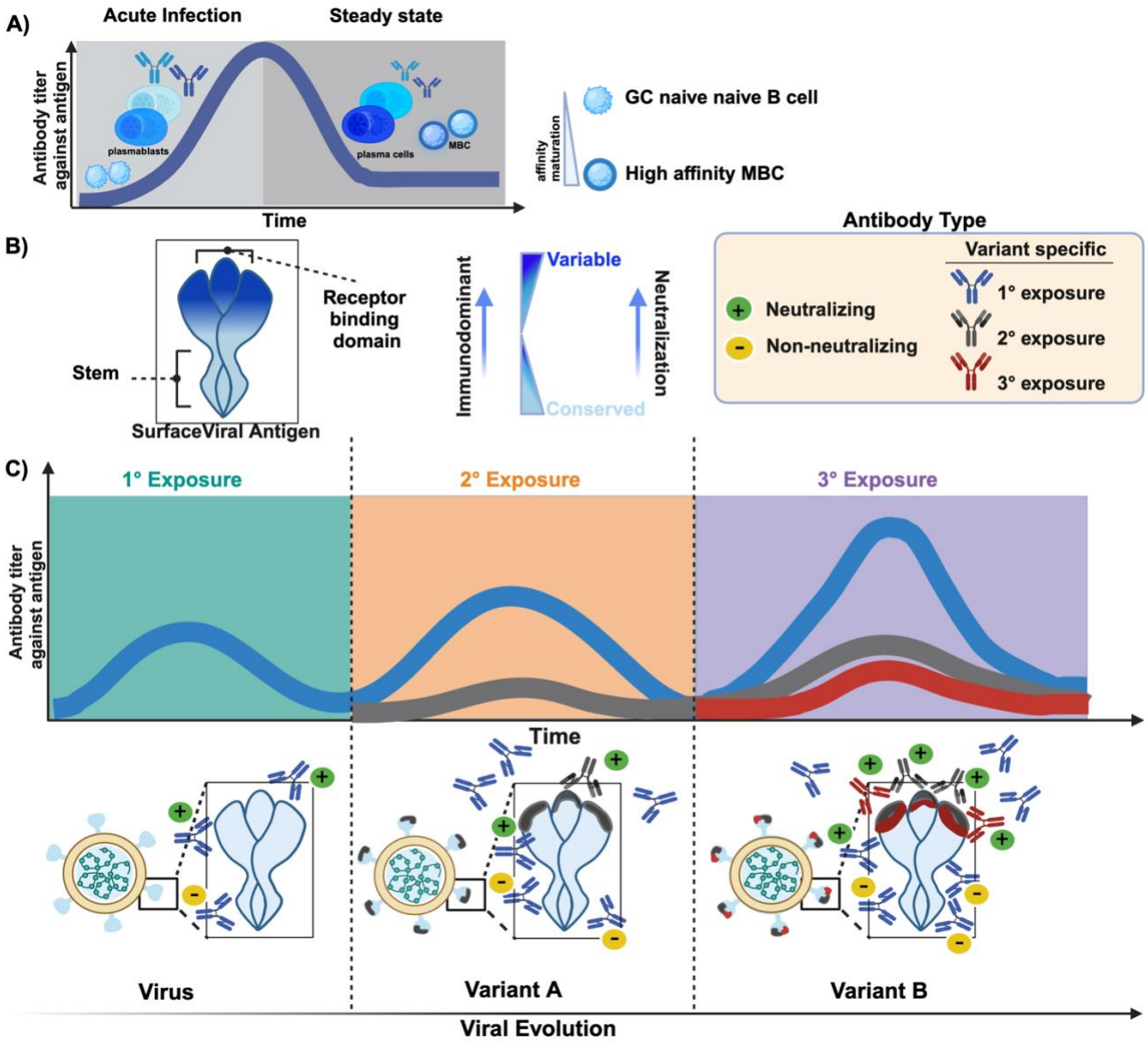

Figure 7.1 The dynamics of antibody responses following primary and subsequent infections with antigenically distant viruses.

A) Schematic illustration depicts the dynamics of the humoral response following infection or vaccination. Initially, after the first exposure, a portion of activated B cells differentiate into plasmablasts, which provide an immediate but short-lived source of low-affinity antibodies to limit acute infections. As the humoral response progresses, more specialized responses generate long-lived plasma cells and memory B cells (MBC) which persist at steady state. These cells will rapidly proliferate upon a reencounter with the antigen and become the dominant source of antibodies for subsequent exposures. **B)** Schematic illustration of SARS-CoV-2 and influenza surface viral proteins highlighting the receptor-binding domain (RBD) and/or the receptor-binding site (RBS) as well as the stem and stalk domain, respectively. The gradient represents the more variable, immunodominant domain (dark blue) relative to the more conserved domain (light blue) of the surface viral protein. The RBD/RBS contains numerous immunodominant epitopes and is an important neutralization target given its role in cell-mediated entry. C) The kinetics of antibody responses following primary and subsequent infections with antigenically distant viruses are depicted. The induced humoral response may compromise both recall and de novo responses, depending on the antigenic similarity and cross-reactivity between the infecting variant and previously encountered variants. Primary exposure to an antigen elicits a polyclonal antibody response consisting of both neutralizing and non-neutralizing antibodies. Each subsequent exposure to an

antigenically distant viral variant significantly boosts antibodies targeting conserved epitopes while also inducing de novo variant-specific neutralizing responses, albeit at much lower magnitudes. Exposure to an antigenically distinct antigen (Variant B) alleviates immunological imprinting and promotes de novo responses targeted to variant-specific epitopes.

The emergence of SARS-CoV-2 and the characterization of population immunity following repeated infections and vaccine boosters offer a unique opportunity to disentangle immune imprinting. Most infections and vaccines induce antibodies targeting the immunodominant spike protein, an envelope glycoprotein involved in viral fusion and entry into permissive cells. Influenza's hemagglutinin (HA) protein serves a similar role. Both are trimeric proteins composed of a variable receptor-binding domain (RBD) or receptor-binding site (RBS) and a more conserved stem or stalk, respectively (Fig. 1B). Given the roles of the RBD or RBS in receptor binding and cell entry, these regions contain the majority of antigenic sites where antibody binding can directly inhibit infection, leading to virus neutralization. Neutralizing antibodies are considered a strong correlate of protection against SARS-CoV-2 and influenza infection[16,17]. Epitopes within the RBD or RBS that are critical for virus binding are also, generally, highly immunogenic and attract the humoral response towards them. This targeted immunodominance creates a strong selection pressure that favors the emergence of mutations, also called antigenic drift. In new viral variants, immune escape mutations commonly arise at these immunodominant epitopes targeted by neutralizing antibodies (Fig. 1C)[18-20]. However, some neutralizing antibodies can target epitopes within the stem or stalk regions, which are relatively conserved between viral variants, are less susceptible to immune escape, and can be broadly protective [19,21]. Non-neutralizing antibodies that target subdominant epitopes or regions in the stem or stalk play an important role in recruiting innate and cellular antiviral immunity, and for some viral pathogens, this can occur through the effector functions of Fc-receptors [22,23].The accumulation of mutations, largely detected in the RBD of recent SARS-CoV-2 variants, further demonstrates the immunodominance of this domain and its significant role in humoral responses. This suggests that SARS-CoV-2 antigen evolution is strongly influenced by the selective pressures exerted by neutralizing responses, similar to influenza's antigenic drift [19,20].

Since the 1950s, the term OAS has been used interchangeably with other terminologies such as antigen imprinting, immunological imprinting, and immune imprinting to describe the lifelong

biased reactivity towards the original antigen. Importantly, the intended terminology stemmed from epidemiological observations of differential antibody reactivity shaped by both exposure history and age, as highlighted in several excellent reviews [24-28]. Several additional concepts are complementary and peripheral to immune imprinting. For instance, antigenic seniority denotes the quantitative hierarchal nature of antibody induction, wherein the highest titers are observed against antigens encountered earlier in life with progressively lower titers against subsequent exposures to antigenically related viruses (Fig. 1C). Similarly, the term back-boosting describes an increase or "bosting" of cross-reactive recall responses to conserved epitopes between the ancestral and latest viral exposure, rather than the induction of de novo antibody synthesis towards variant-specific epitopes (Fig. 1C). Conversely, back-boosting reflects the immune system's propensity for inducing cross-reactive antibodies with each infection. Indeed, recall responses can be favored over de novo antibody production, as MBCs can be activated with significantly lower antigen concentrations compared to naïve B cells, despite the latter having higher affinity for the immunizing antigen, underlying the basis of immune imprinting effects[29-32]. Furthermore, antibody feedback mechanisms can steer the antibody response and restrict the generation of de novo responses with similar specificities. This can occur through antigen sequestering (clearance) by established cellular or humoral responses following exposure to closely related strains[29,31,33-38]. One example is epitope masking, where existing antibodies bind to conserved but non-neutralizing epitopes, promoting antigen clearance. This mechanism restricts novel antigen interactions with memory or naïve B cells and hinders the induction of de novo antibody synthesis against similar epitopes [33-35,39-41].

While much attention for deciphering the mechanisms that drive immune imprinting has focused on humoral immunity, T cell-mediated immunity also plays a crucial role. Indeed, recent evidence highlights the role of T cells in shaping antibody responses. Richards et al. show that reduced CD4+ T cell responses in individuals with recurrent exposures to influenza can lead to diminished protective antibody responses[36]. Regulatory T cells induced by the initial exposure can reduce the amount of available antigen for presentation to APCs, thereby suppressing activation of naïve B cells and the synthesis of variant-specific de novo antibodies[37]. Moreover, Schiepers et al. show that memory T cells assist B cells in targeting subdominant epitopes to access secondary germinal centers (GCs) following boosting with a homologous antigen, even in the presence of pre-existing

antibodies[38]. Thus, this evidence highlights the interplay between humoral and cellular compartments in favoring imprinting responses, which can further be exacerbated by limiting the amount of antigen available following recurrent exposures to antigenically similar variants.

7.4 Immune imprinting in recurrent exposures to influenza

The skewing of memory recall responses to a restricted range of epitopes from the earliest infections has been shown to suppress the induction of variant-specific de novo responses, thereby increasing an individual's susceptibility to new infection with antigenically distant viruses[42,43]. This phenomenon of immune imprinting has been described in detail for influenza[24-28]. Multiple studies have shown that the immune response is biased towards influenza strains encountered earlier in life and that during ensuing exposures to antigenically related strains, antibody production toward the ancestral strain predominates. Lessler et al. observed antigenic seniority for influenza in a cross-sectional study where individuals had higher antibody titers against strains encountered earlier in life rather than against strains from recent infections[43]. Back-boosting of neutralizing antibodies against preceding influenza strains following subsequent influenza exposures was observed in a longitudinal analysis of the Framingham Heart Study data[42]. Other studies have also confirmed these findings, reporting an increase in antibodies against previously encountered antigenically related strains following both influenza infection and vaccination[19,29,42,44-49].

In immune imprinting, back-boosting coincides with a reduction in the de novo response to newer strains, with much of the recent evidence arising after the 2009 H1N1 pandemic. Choi et al. determined that vaccination for the 2009 pandemic H1N1 influenza virus induced relatively lower antibody titers among individuals who were vaccinated with the seasonal H1N1 vaccine three months prior [50]. Recalled cross-reactive antibodies against seasonal H1N1 strains were shown by Andrews et al. to block the development of broadly neutralizing antibodies against the HA stalk following vaccination against the 2009 pandemic strain through epitope masking[19]. Imprinting was shown to decrease protection against antigenically related influenza strains and worsen disease outcomes. During the 1918 Spanish flu and 2009 H1N1 pandemics, the mortality rate was higher for those exposed to discordant subtypes in early childhood[25]. Mortality rates varied similarly according to age (and therefore exposure profile) in the 1957 H2N2 pandemic [51]. Similarly, vaccine

effectiveness against H1N1 was impaired for middle-aged and older adults during the 2015–2016 flu season when the circulating H1N1 influenza strain acquired a new glycosylation site[52]. Furthermore, reduced protection from vaccination in the 2018/2019 H3N2 epidemic was associated with age and prior exposure to a mutated H3N2 strain during the 1968 pandemic [53].

Although much attention has been focused on the detrimental impacts of imprinting, it does not solely impair immune function[24]. Indeed, older individuals may benefit from increased protection and lower mortality rates compared to immunologically naive individuals due to immune imprinting[54]. These beneficial impacts of immune imprinting, acquired from infections encountered several decades earlier, can persist throughout an individual's lifetime. Birth cohort studies reporting increased titers against influenza strains encountered earlier in life suggest that imprinting reinforces immune memory against earlier strains upon exposure to antigenically related strains throughout life[25]. A multi-country study by Gostic et al. found that individuals initially infected with influenza A group 1 (H1, H2, and H5 seasonal subtypes) or group 2 (H3 and H7 seasonal subtypes) had a relatively low risk of mortality and severe illness from subsequent infections with the corresponding HA subtypes[24,25,45]. This protection likely results from antigenic seniority and the back-boosting of cross-reactive antibodies targeting conserved regions between the initial and infecting virus of the same HA subtype. In accordance with this evidence, epidemiological studies have reported lower mortality rates in the 2009 H1N1pandemic for older generations exposed to the 1918 H1N1 Spanish flu compared to younger generations[55]. For example, in China, 92% of hospitalizations and 77% of deaths resulting from 2009 H1N1 infections occurred in individuals under the age of 50. Similarly, during the 1918 pandemic, older individuals had lower mortality rates relative to younger individuals [45]. These observations indicate that imprinting induces a strong recall response towards the initial viral exposures and the induction of cross-reactive antibodies through back-boosting. This may confer improved protection for older individuals as they are exposed to antigenically similar viruses across their lifetime, thereby strengthening immunity against the initial virus.

7.5 Effect of previous HCoV infections on the induction of SARS-CoV-2 humoral responses

Early in the SARS-CoV-2 pandemic, some studies suggested that prior exposure to human seasonal coronaviruses (HCoVs) 229E, HKU-1, NL63, or OC43 could negatively impact the development of humoral responses specific to SARS-CoV-2[56-59]. The shared sequence homology

between HCoVs and SARS-CoV-2 hinted at the potential for immune imprinting. Indeed, back-boosting of antibodies cross-reactive to spike proteins of HCoVs has been observed following SARS-CoV-2 infection and vaccination[56,57,59,60]. For example, Yin et al. determined that COVID-19 vaccination was associated with increased titers against OC43 and HKU-1. Other studies report that SARS-CoV-2 infection also stimulated the production of antibodies against OC43 and HKU-1[59,61,62]. However, the literature on the clinical implications of immune imprinting from prior exposure to HCoVs on SARS-CoV-2 immunity is nuanced. Some evidence indicates that such imprinting may worsen clinical outcomes of SARS-CoV-2 infection[56-59]. Indeed, Aguilar-Bretones et al. reported an expansion of MBCs specific for HCoV-OC43 with limited cross-reactivity to SARS-CoV-2 in severely ill SARS-CoV-2 patients, but not in mildly ill patients [56]. Furthermore, they showed relatively low IgG antibody reactivity and neutralization to SARS-CoV-2 in these patients with severe COVID-19 [56]. In contrast, Guo et al. observed that disease severity correlated with a greater induction of back-boosting antibodies against HCoV-OC43, which were also cross-reactive with SARS-CoV-2 [57].

Additionally, some researchers have demonstrated a link between immune imprinting and post-acute sequelae, also called post-COVID-19 condition (PCC)[58]. In convalescent SARS-CoV-2 patients with underlying rheumatic disease, those who developed PCC had reduced antibody reactivity to SARS-CoV-2 and increased reactivity to HCoV-OC43 compared to those who did not develop PCC[58]. In turn, Galipeau et al. suggest that the relative ratio of prior antibody responses against all four HCoVs, rather than the absolute titer against a specific HCoV, correlated with increased SARS-CoV-2 neutralization[63]. However, some studies did not observe a correlation between back-boosting of HCoV antibodies upon infection with SARS-CoV-2 and more severe disease[59,60]. This contrasts with some influenza studies that reported the potential detrimental effect of immune imprinting [24,25,42,43,50]. In particular, Anderson et al. and Aydillo et al. report back-boosting of antibodies against HCoVs following SARS-CoV-2 infection in hospitalized adult patients, but this had no bearing on disease severity[59,60]. However, Aydillo et al. noted a delay in de novo antibody production against SARS-CoV-2 in severely ill patients[59]. Although these findings reveal conflicting perspectives on the impact of prior seasonal HCoV infections on disease severity following SARS-CoV-2 infection, they suggest the involvement of complex immune imprinting influences through the induction of back-boosting antibodies to these HCoVs.

7.6 The dynamics of serum antibody responses and the antigenic distance hypothesis

The extent of immune imprinting and antibody reactivity towards subsequent infections appears to be fundamentally dependent on the antigenic relatedness between the primary and subsequent antigens, as first postulated by Smith et al. [64]. Antigenic distance between two antigenically similar viruses can either enhance or hinder immune protection against disease[64]. When the level of relatedness between the primary and secondary strains is high, significant back-boosting of antibodies can occur (Fig. 1B). Although this could still protect from infection when back-boosted antibodies still effectively neutralized the circulating variant strain. Indeed, Hensley et al. eloquently demonstrated that mice heterologously boosted with an antigenically related influenza variant, which differed by 13 amino acid substitutions relative to the priming variant, preferentially induced recall antibody responses[65]. Although approximately 55% of isolated monoclonal antibodies were specific to the priming antigen, adoptive transfer of serum antibodies following boosting still protected mice from infectious challenge with the secondary strain[65]. In contrast, when circulating variants acquire immune escape mutations but are still sufficiently antigenically similar to the primary exposure, recall responses are favored at the expense of de novo antibody synthesis and to the detriment of protection as discussed above [19,29,42,44-49]. However, immune imprinting can be overcome by boosting with more distantly related viral antigens, as shown in several mouse studies [40,66-68].

The proportion of de novo serum antibodies synthesized relative to those produced through recall responses, and the compounding effect of subsequent antigen re-exposures have been challenging to study (Fig. 1C). Recently, Schiepers and colleagues employed an eloquent molecular fate-mapping technique to decipher antibody kinetics and their cellular origins following repeated antigen exposures[40]. In transgenic mice primed either by infection or vaccination with messenger RNA-Lipid Nanoparticle (mRNA-LNP), they distinguished antibodies generated from initially primed MBCs and those from de novo synthesis. In a prime vaccination followed by a two-dose boost regimen with the ancestral SARS-CoV-2 spike vaccine (homologous boosting), Schiepers et al. observed a 55-fold suppression of de novo B cell responses as a result of dominant recall responses. However, a heterologous boost with the Omicron BA.1 spike mRNA vaccine, Omicron BA.1 being a variant of SARS-CoV-2 that shares 91% sequence in the RBD with the ancestral strain, resulted in a partial alleviation of immune imprinting. In particular, they observed only a

3.6-fold suppression of de novo antibody responses with the heterologous boost. Following the heterologous boost, Schiepers et al. detected new BA.1-specific B cell clones that are not cross-reactive with the ancestral strain and that showed greater neutralization against the BA.1 variant specifically. Furthermore, by varying the amino acid sequence of influenza boosting antigens, they experimentally demonstrated that immune imprinting is a function of antigenic distance between the primary and subsequently encountered antigens[40,66,67]. Collectively, these findings suggest that immune imprinting can be alleviated when the boosting antigen is sufficiently distinct from the priming antigen.

7.7 B cell activation outcomes and the dynamics of germinal center reactions

Given the role of GC reactions in shaping the diversity of the humoral response, understanding B cell clonal selection and expansion following primary or repeated antigen exposures is critical for dissecting the fundamentals of immune imprinting (Fig. 2). In GCs, activated B cells will undergo iterative rounds of somatic hypermutation, where only the clones expressing the highest affinity receptors to the antigen are selected for clonal expansion by receiving survival signals from T follicular helper cells[69]. Some of these affinity-matured clones make their way into circulation, serving as a source of antibodies or as MBCs (Fig. 2B). However, a portion of MBC clones will undergo further affinity maturation, leading to inter-clonal competition and a progressive loss of MBC clonal diversity given that selection favors clones with the highest antigen affinity to immunodominant epitopes (Fig. 2B). Immunodominant epitopes for SARS-CoV-2 and influenza viruses are frequently detected in the RBD and RBS, compared to the relatively immuno-subdominant stem or stalk, respectively (Fig. 1B). This immunogenicity could result from their increased epitope exposure compared to the more sheltered regions of the stem or stalk, repetitive epitope display, or specific amino acid sequences leading to improved B cell receptor cross-linking [19,20,70]. Nevertheless, GC reactions concurrently lead to the breadth of the humoral response. Through lineage tracing experiments, Hagglof et al. demonstrated that ongoing GCs continuously recruit activated B cells and up to 30% of late-stage GCs can consist of clones with limited rounds of mutations and low antigen affinity[71]. Their findings suggest that as the GC reactions develop, antibody-mediated feedback can favor the entry and expansion of B cells specific for non-dominant epitopes, thereby contributing to the maintenance of antibody diversity. Indeed, following primary COVID-19 mRNA vaccination in humans, Weber et al. detected early exported

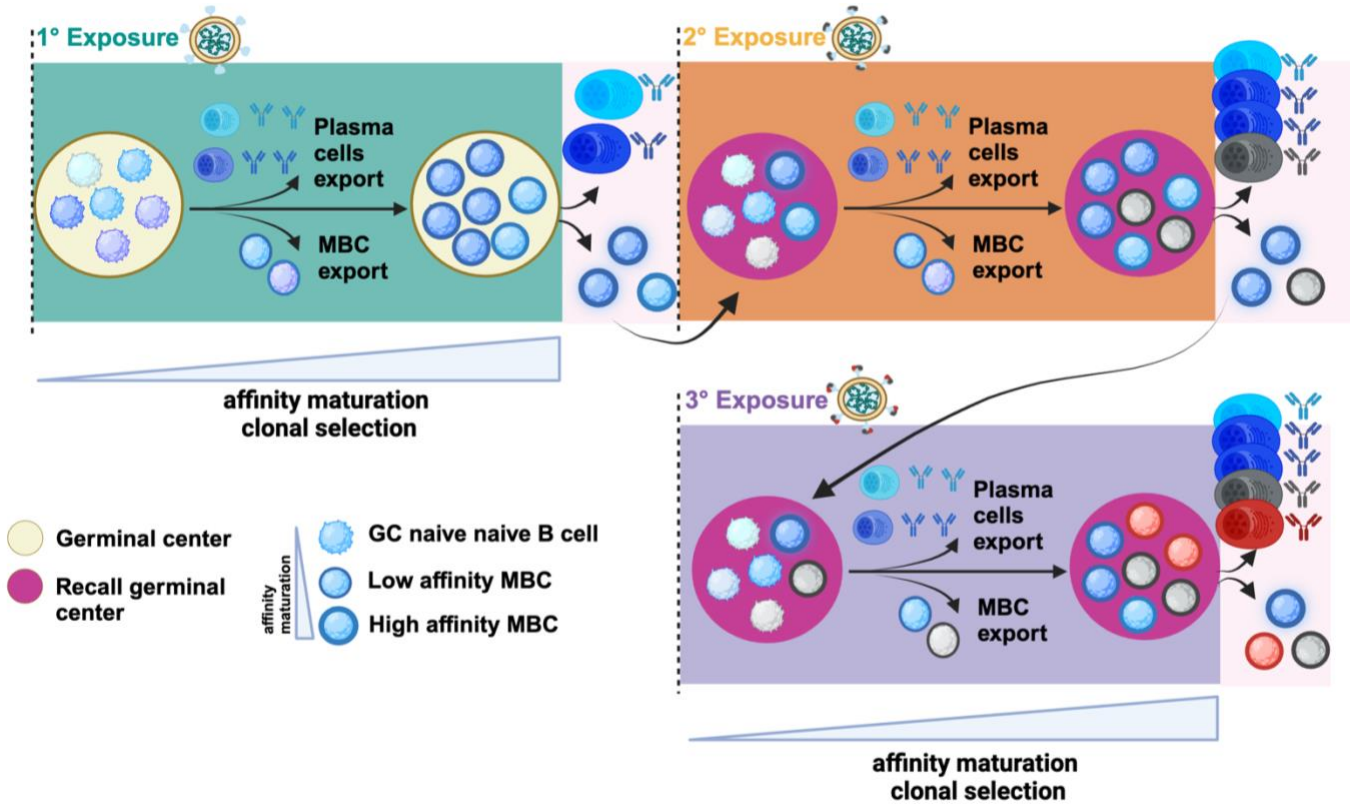

Figure 7.2 B cell activation outcomes and dynamics of germinal center (GC) reactions following primary and secondary infections with antigenically distant viruses.
The schematic illustration depicts the dynamics of GC reactions following primary and secondary infections with antigenically distant viruses. Activated B cells form GCs where they undergo isotype switching, somatic hypermutation, and affinity maturation. Only clones expressing the highest affinity receptors to the antigen are selected for clonal expansion by receiving survival signals from T follicular helper cells. Some of these affinity-matured clones make their way into circulation, serving as a source of antibodies or as low-affinity MBCs. However, a portion of MBC clones will undergo further affinity maturation, leading to a progressive loss of clonal diversity as selection favors clones with the highest antigen affinity to immunodominant epitopes. These high-affinity B cells can differentiate into plasma cells or into MBCs. Following re-exposure through subsequent infection or vaccine boosting, recall GCs are mostly composed of activated B cells without prior GC experience (GC-naïve B cells) and a limited subset of dominant affinity-matured MBCs.

MBCs with limited clonal affinity maturation[72]. These MBCs exhibited broad neutralization against currently circulating viral variants, emphasizing the diversity of the early humoral repertoire.

Recent evidence highlights that mRNA-LNP vaccines induce potent GC responses in both mice and humans, which have important implications for vaccine design[15,73-81]. However, the mechanisms by which the distinct mRNA and LNP components of mRNA-LNP vaccines promote robust GC reactions remain largely undefined. Recent findings by Bettini et al. and others suggest that both components promote the differentiation of T follicular helper cells and dendritic cells,

thereby enhancing the overall magnitude of GC reactions compared to protein-subunit vaccines adjuvanted with LNP[73,79,80,82]. Moreover, studies from several groups suggest that prolonged antigen expression and availability following mRNA-LNP vaccination may contribute to enhanced and sustained GC reactions [76,79,81,83-86]. Indeed, comparisons between mRNA-LNP vaccines and protein subunit vaccines adjuvanted with LNP or other adjuvants highlight the potent adjuvant properties of LNP, which likely significantly contribute to the impressive immunogenicity of the mRNA-LNP vaccine platform[73,78-80,82,85,87,88]. Overall these findings suggest that the LNP component of vaccines has intrinsic adjuvant activity and is a major driver in promoting durable and protective antibodies through the combined induction of T follicular helper cells, long-lived plasma cells, MBC and prolonged GC reactions[15,73-81]. Although ongoing GCs have been detected over varying periods following SARS-CoV-2 exposure from natural infection or vaccination, these GC reactions are to shown drive clonal diversification through antibody-mediated feedback to produce antibodies with sufficient breadth to neutralize a range of genetic variants [35,76,86,89,90].

Two alternative models exist to explain GC dynamics following re-exposure through subsequent infection or boosting. First, in the conventional model, affinity-matured MBCs can readily enter secondary or recall GCs for further affinity maturation to finetune their affinity for antigenically drifted viruses[15]. However, recent evidence highlights another potential model of GC dynamics and demonstrates a bottleneck in the recruitment of the diverse, affinity-matured MBCs into recall GCs, restricting entry to only a small portion of high-affinity immunodominant clones in mice and humans[33,38,91] (Fig. 2B). Certainly, Mesin et al. demonstrate that recall GCs are mostly composed of activated B cells without prior GC experience (GC-naïve B cells) and a limited subset of dominant affinity-matured MBCs regardless of re-infection or boosting in mouse models. Their findings suggest that antibody-mediated feedback suppresses the recruitment of these affinity-matured MBCs, promoting the recruitment and diversification of GC-naïve B cells in recall GCs, thereby circumventing immune imprinting (Fig. 2B). Similarly, human lymph node analysis by Turner et al. showed substantial recruitment of GC-naïve B cells to recall GCs following vaccination with influenza despite prior exposures[92]. However, their results suggest a higher propensity for humans, relative to mice, for MBC entry into recall GCs, highlighting a greater potential for immune imprinting to occur. Yet, despite the large diversity of MBCs generated by each exposure, recall antibodies seem to consistently derive from a subset of dominant MBCs

generated by the original exposure (Fig. 2A) 8,[40,72,93]. In a longitudinal analysis of the B cell repertoire in humans following both vaccination and subsequent Omicron infection, Weber et al. found that a substantial proportion of humoral responses stemmed from recall of the original cohort of MBCs produced following the primary vaccination series [72]. Thus, understanding dynamics of germinal center reactions and their role in the humoral response can have important implications for alleviating immune imprinting in the context of recurrent exposures to antigenically distinct viruses.

7.8 Influence of the vaccination platform in promoting or overriding immune imprinting

Secondary viral infection and vaccination can result in varying intensities of immune imprinting. The immune system often favours recall responses over of de novo synthesis given that MBCs can be activated with much lower antigen concentrations than naïve B cells. Indeed, these effects can be further exacerbated when the amount of antigen available during the secondary exposure is limited, favoring recall responses[29,31,33-38]. Several studies demonstrate this phenomenon by reducing the dose of protein subunit vaccines or infectious viruses. In the case of the latter, the humoral and cellular memory responses established during the initial exposure can suppress viral replication, thereby limiting the amount of viral antigens available to stimulate new responses[29-32,83,84]. In the case of protein subunit vaccination, the amount of administered antigen may be more susceptible to antibody feedback mechanisms, potentially exacerbating the detrimental effects of immune imprinting. In contrast, vaccine platforms that are self-replicating, such as some DNA or mRNA vaccines, may bypass pre-existing antibodies and effectively overcome the constraints of immune imprinting mechanisms[26,67].

Indeed, intramuscular administration of mRNA-LNP vaccines leads to uptake and synthesis of encoded antigens primarily by local cells at the injection site and the draining lymph node, with limited spread to other tissues[81,94,95]. APCs, such as monocytes, macrophages, dendritic cells, play a critical role in mRNA-LNP uptake, antigen production, and subsequent antigen presentation for robust induction of humoral and cellular responses[73,81,85,94,96]. Indeed, monocytes, macrophages and dendritic cells can directly uptake and efficiently translate the mRNA of encoded antigens, thereby driving the immune response through presentation of processed antigen on MHC class I and MHC class II molecules to produce both cellular and humoral responses, respectively. Muscle

cells can also uptake and produce antigens and depending on the mRNA design, the synthesized antigen will either be membrane-anchored or secreted[97,98]. Additionally, mRNA-LNP can be passively transported to draining lymph nodes, although this seems to depend on particle size and composition and needs further investigation[85]. While B cells have the potential to directly uptake and synthesize the encoded antigens, this appears to be less common compared to the direct uptake by macrophages, monocytes and dendritic cells[73,94,96,99]. Instead, B cells will likely interact with either secreted soluble antigens or processed antigens presented on the surface of APCs, which may influence the strength of receptor induced signalling, based on the degree of cross-linking[14,15,100]. In fact, membrane-bound antigens have been shown to be more efficiently recognized compared to soluble antigens[14,101-103].

Anderson et al. demonstrate through absorption assays, that a first SARS-CoV-2 exposure through natural infection induced back-boosted antibodies with high cross-reactivity to the stem region of sCoV spike protein, contrasting with mRNA-LNP vaccination, which predominantly produced antibodies with higher affinity to the RBD of SARS-CoV-2[62]. Furthermore, studies by England et al. and Willis et al. demonstrated that mRNA-LNP vaccines against SARS-CoV-2 or influenza effectively overcame maternal antibody inhibition of de novo humoral responses in vaccinated mouse pups[78,82]. Although Willis et al. showed limited de novo responses following a live attenuated influenza vaccine (LAIV) or inactivated vaccine immunization in presence of maternal antibodies, England et al. demonstrated that adjuvanted protein subunit vaccines effectively evoked de novo responses despite the presence of the maternal antibodies, with mRNA-LNP vaccines inducing the highest neutralizing titers[78,82]. Indeed, the inclusion of adjuvants during initial or secondary vaccination has been shown to alleviate the effects of immune imprinting. Kim et al. showed that adjuvants which preferentially stimulate dendritic cells, such as CpG ODN, Bordetella pertussis toxin, or squalene-based oil-in-water, elicit strain-specific de novo total and neutralizing antibody responses[67].

In contrast, viruses and VLPs can bind to B cells with high affinity and avidity by crosslinking BCRs with repetitive antigens displayed on their surfaces, thereby enhancing B cell responses and retention in the lymph nodes[99,104]. Cohen et al., as well as others groups, have demonstrated that immunization with heterotypic VLPs, which simultaneously display RBDs from eight different SARS-like beta coronaviruses (sarbecovirus), promote crosslinking interactions with high avidity

to subdominant, conserved regions of the adjacent RBD antigens[105-109]. This leads to the induction of broadly cross-reactive and neutralizing responses compared to homotypic VLPs that display only one type of RBD antigen. Furthermore, through fate mapping experiments discussed above, Cohen et al. demonstrate that boosting with heterotypic VLPs induces de novo antibody synthesis in mice and non-human primates previously primed with two to four doses of DNA, mRNA, or viral vectored SARS-CoV-2 vaccines[106]. Additionally, serum antibody epitope mapping using deep mutational scanning revealed that boosting with heterotypic VLPs, relative to the homotypic VLPs, elicit antibodies with preferential binding to conserved epitopes of the RBD. These epitopes exhibit low variability among sarbecoviruses and SARS-CoV-2 variants. In contrast, antibodies induced by homotypic VLPs vaccination primarily targeted epitopes on the apex of the antigen. Although more accessible, these epitopes of the RBD are more variable likely due to greater selective pressures, consistent with findings by several groups[106,107,110-113]. This highlights the potential of immunization with heterotypic VLPs or "universal vaccines" as a strategy to mitigate the effects of immune imprinting following recurrent infections with antigenically distinct variants.

7.9 Immune imprinting following recurrent exposures to SARS-CoV-2 antigens through natural infection or vaccination

The extensive characterization of population immunity following recurrent exposures to SARS-CoV-2 through booster vaccinations or breakthrough infections has provided immunologists with a unique opportunity to dissect the effects of immune imprinting in the context of SARS-CoV-2. The continuous circulation and transmission of SARS-CoV-2 has led to the emergence of variants of concern (VOC), characterized by substantial antigenic variation, evolved fitness advantages and distinguished from other viral variants by their increased risk of causing severe COVID-19 disease. These changes are primarily driven by selective pressures arising from recurrent vaccinations and infections [19,20,114,115]. Notably, the efficacy of ancestral SARS-CoV-2 mRNA-LNP and viral vector vaccines was reduced against the Beta variant, showing more than a ten-fold reduction in neutralizing titers in sera from vaccinated donors[116-118]. Breakthrough infections with the Alpha or Delta variants resulted in a greater increase in antibody titers against the ancestral strain compared to the VOC strain in individuals vaccinated with three doses of ancestral mRNA-LNP, highlighting the effects of immune imprinting[86,119]. Meanwhile Zar et al. show antibody back-boosting to

ancestral, Beta, Delta or Omicron variants without a clear hierarchical order[120]. Efforts to enhance vaccine efficacy by updating vaccines have led to improved VOC neutralization. However, individuals previously vaccinated with the ancestral mRNA vaccines showed dominant recall antibody responses following monovalent Beta or Delta boosters, or bivalent ancestral and Beta/Delta boosters[8,121,122]. In contrast, boosting with a bivalent ancestral and Beta mRNA vaccine, relative to boosting with the ancestral vaccine, led to a reduction in symptomatic infection from 10.7% to 3.4%[122].

Following the emergence of Omicron and its sub-variants, which possess a greater number of immune escape mutations over earlier variants, varying effects of immune imprinting have been observed[114]. Omicron breakthrough infections predominantly promoted recall responses, leading to reduced neutralization of Omicron variants. Although some de novo antibody synthesis has been observed, it remains at a low level[8,123,124]. Vaccination with an Omicron-specific mRNA-LNP booster has been shown to produce de novo antibody responses and superior neutralization against Omicron variants compared to individuals boosted with the ancestral vaccine, which demonstrates the benefits of updating the vaccine to match circulating variants [122,125-128]. However, conflicting evidence reported from some studies indicate no significant differences in neutralizing antibody titers between those boosted with the Omicron bivalent vaccine or the ancestral vaccine, highlighting potential effects of immune imprinting[129-133]. Whereas, Alsoussi et al. demonstrated that in individuals previously vaccinated with the ancestral SARS-CoV-2 mRNA vaccine, variant-specific de novo B cell responses were only induced with Omicron-specific boosting, and not with the ancestral or bivalent Beta/Delta variant boosters (which shared 98.7% and 99.1% sequence conservation with the ancestral RBD, respectively)8. Although being of low frequency, these clones targeting BA.1 variant-specific epitopes were derived from GC-naïve B cells recruited into recall GCs of the draining lymph nodes following heterologous boosting. Yisimayi et al. demonstrate that boosting with two doses of Omicron protein subunit or mRNA vaccines induced robust variant-specific *de novo* humoral responses in both mice and individuals previously immunize with ancestral SARS-CoV-2 viral vector vaccines[66]. These findings suggest that priming with inactivated viral vector vaccines may lead to a reduced degree of immune imprinting compared to mRNA vaccines, potentially due the stronger immune response elicited by initial mRNA vaccination. Interestingly, breakthrough infections in individuals with diverse exposure

histories from vaccination and infection, have been shown to increase the breadth of neutralizing antibody responses against previous and circulating VOCs, as well as elicit *de novo* responses[119,120,123,124]. In fact, Hoffman et al. demonstrated that boosting with ancestral and BA4.5 bivalent vaccines produced enhanced neutralizing responses against circulating Omicron variant in individuals who had previously received two doses of ancestral mRNA-LNP vaccines and subsequently experienced a breakthrough infection. However, the highest neutralizing titers were observed against the ancestral strain, highlighting the effects of immune imprinting[123]. These findings collectively suggest that Omicron-specific booster vaccinations may partially alleviate the effects of immune imprinting caused by repeated exposures to early SARS-CoV-2 variants. However, their findings also highlight that maintaining the ancestral antigen in the bivalent booster vaccine may favor immune imprinting, supporting the collective decision to proceed with monovalent SARS-CoV-2 variant specific booster roll-out. Indeed, monovalent XBB.1.5 boosters administered to individuals with a prior vaccination history markedly increased serum neutralizing antibody titers against the XBB.1.5 variant, as well as against the more recently emerged EG.5.1 and JN.1 variants[134,135].

However, these studies emphasize the persistence of immune imprinting, given that the highest neutralizing responses were observed against the ancestral variant. Notably, Tortorici et al. showed that depletion of antibodies that are cross-reactive with the ancestral antigen abrogated the observed neutralization of XBB1.5, suggesting that mRNA vaccination with the XBB1.5 booster primarily induces recall responses[136]. However, Johnston et al. demonstrated the development of variant-specific de novo humoral responses, albeit at a low frequency, following boosting with the XBB1.5 monovalent mRNA vaccine in individuals who were previously vaccinated with ancestral mRNA vaccines and experienced breakthrough infections[134]. Indeed, these studies evaluating neutralizing responses following vaccination with updated booster vaccines highlight the persistence of immune imprinting, which can be reduced when the boosting antigen is sufficiently distinct from ancestral SARS-CoV-2 . Therefore, comprehensive evaluations of antigenic distance scores between primary and subsequent viral variants, while comparing various vaccine platforms, may help predict their ability to promote recall or *de novo* antibody responses. When interpreting these studies, it is crucial to consider variables such as 1) differences in antigen presentation by different vaccine platforms (and therefore their recognition by the immune system), 2) antigenic

distance between primary and subsequent antigens, and 3) the nature of primary exposure and subsequent re-exposures (natural infection or vaccination).

While several comparisons between influenza and SARS-CoV-2 studies regarding immune imprinting have been discussed, it is important to approach these interpretations with caution due to inherent differences in their virology, epidemiology, and vaccination approaches. Furthermore, this review highlights the importance of investigating whether different vaccine platforms induce varying degrees of immune imprinting following repeated exposures. Collectively, these findings suggest that boosting with a significantly distinct antigen is paramount in steering the humoral immune response away from favoring recall and towards de novo responses that target variant-specific epitopes.

7.10 Conclusion

Given the role of immune imprinting in shaping humoral responses following recurrent exposures to antigenically distant viruses, its impact should be thoroughly considered when designing vaccination strategies. The evolving landscape of SARS-CoV-2 and the emergence of variants with immune escape mutations have prompted multiple updates to COVID-19 vaccines. These updates aim to improve vaccine efficacy against circulating variants, similar to seasonal updates for influenza vaccines. Recent studies on SARS-CoV-2 and influenza have shown that boosting with sufficiently antigenically distinct vaccine promotes the induction of variant-specific de novo responses that are less cross-reactive with previously encountered antigens. Indeed, some of the next-generation vaccine strategies focus on developing universal vaccines, which induce both variant-specific and broadly protective cross-reactive responses by simultaneously expressing multiple surface glycoproteins from distinct influenza subtypes or coronaviruses [106,137]. Ultimately, the effectiveness of these vaccines will depend on their capacity to overcome the constraints of immune imprinting and address age-related differences in disease risk, which are ultimately shaped by individual's distinct infection histories. A comprehensive understanding of immune imprinting is essential for guiding vaccine design and maximizing vaccine effectiveness against both current and future viral infections.

Acknowledgements

M.M. holds an Ontario Graduate Scholarship. M.-A.L. holds a Faculty of Medicine Chair of Excellence in Pandemic Viruses and Preparedness Research. M.-A.L. and C.C. are members of and have received research funding from the Coronavirus Variants Rapid Response Network (CoVaRR-Net). Figures were created with BioRender.com.

Conflict of Interest

The authors declare no conflict of interest relevant to the present manuscript.

Author contributions

M.M., A.K., C.C., and M.-A.L. designed the study. M.M. and M.-A.L. designed the figures. M.M., A.K., and M.A.L wrote the manuscript. All authors edited the final version of the manuscript.

7.11 References

1 Plotkin, S. A. Correlates of protection induced by vaccination. *Clin Vaccine Immunol* **17**, 1055-1065, doi:10.1128/CVI.00131-10 (2010).

2 Jensen, K. E., Davenport, F. M., Hennessy, A. V. & Francis, T., Jr. Characterization of influenza antibodies by serum absorption. *J Exp Med* **104**, 199-209, doi:10.1084/jem.104.2.199 (1956).

3 Davenport, F. M., Hennessy, A. V. & Francis, T., Jr. Epidemiologic and immunologic significance of age distribution of antibody to antigenic variants of influenza virus. *J Exp Med* **98**, 641-656, doi:10.1084/jem.98.6.641 (1953).

4 Davenport, F. M. & Hennessy, A. V. A serologic recapitulation of past experiences with influenza A; antibody response to monovalent vaccine. *J Exp Med* **104**, 85-97, doi:10.1084/jem.104.1.85 (1956).

5 Francis, T. On the Doctrine of Original Antigenic Sin. *Proceedings of the American Philosophical Society* **vol. 104, no. 6**, pp. 572–578 (1960).

6 Katzelnick, L. C. *et al.* Antibody-dependent enhancement of severe dengue disease in humans. *Science* **358**, 929-932, doi:10.1126/science.aan6836 (2017).

7 Kim, H. W. *et al.* Respiratory syncytial virus disease in infants despite prior administration of antigenic inactivated vaccine. *Am J Epidemiol* **89**, 422-434, doi:10.1093/oxfordjournals.aje.a120955 (1969).

8 Alsoussi, W. B. *et al.* SARS-CoV-2 Omicron boosting induces de novo B cell response in humans. *Nature* **617**, 592-598, doi:10.1038/s41586-023-06025-4 (2023).

9 Underwood, A. P. *et al.* B-cell characteristics define HCV reinfection outcome. *J Hepatol*, doi:10.1016/j.jhep.2024.04.004 (2024).

10 Lindesmith, L. C. *et al.* Immune Imprinting Drives Human Norovirus Potential for Global Spread. *mBio* **13**, e0186122, doi:10.1128/mbio.01861-22 (2022).

11 Lindesmith, L. C. *et al.* Heterotypic humoral and cellular immune responses following Norwalk virus infection. *J Virol* **84**, 1800-1815, doi:10.1128/JVI.02179-09 (2010).

12 Midgley, C. M. *et al.* An in-depth analysis of original antigenic sin in dengue virus infection. *J Virol* **85**, 410-421, doi:10.1128/JVI.01826-10 (2011).

13 Pierce, S. K. & Liu, W. The tipping points in the initiation of B cell signalling: how small changes make big differences. *Nat Rev Immunol* **10**, 767-777, doi:10.1038/nri2853 (2010).

14 Harwood, N. E. & Batista, F. D. Early events in B cell activation. *Annu Rev Immunol* **28**, 185-210, doi:10.1146/annurev-immunol-030409-101216 (2010).

15 Victora, G. D. & Nussenzweig, M. C. Germinal Centers. *Annu Rev Immunol* **40**, 413-442, doi:10.1146/annurev-immunol-120419-022408 (2022).

16 Khoury, D. S. *et al.* Correlates of Protection, Thresholds of Protection, and Immunobridging among Persons with SARS-CoV-2 Infection. *Emerg Infect Dis* **29**, 381-388, doi:10.3201/eid2902.221422 (2023).

17 Hobson, D., Curry, R. L., Beare, A. S. & Ward-Gardner, A. The role of serum haemagglutination-inhibiting antibody in protection against challenge infection with influenza A2 and B viruses. *J Hyg (Lond)* **70**, 767-777, doi:10.1017/s0022172400022610 (1972).

18 Willett, B. J. *et al.* SARS-CoV-2 Omicron is an immune escape variant with an altered cell entry pathway. *Nat Microbiol* **7**, 1161-1179, doi:10.1038/s41564-022-01143-7 (2022).

19 Andrews, S. F. *et al.* Immune history profoundly affects broadly protective B cell responses to influenza. *Sci Transl Med* **7**, 316ra192, doi:10.1126/scitranslmed.aad0522 (2015).

20 Han, A. X., de Jong, S. P. J. & Russell, C. A. Co-evolution of immunity and seasonal influenza viruses. *Nat Rev Microbiol* **21**, 805-817, doi:10.1038/s41579-023-00945-8 (2023).

21 Ng, K. W. *et al.* SARS-CoV-2 S2-targeted vaccination elicits broadly neutralizing antibodies. *Sci Transl Med* **14**, eabn3715, doi:10.1126/scitranslmed.abn3715 (2022).

22 Watanabe, A. *et al.* Antibodies to a Conserved Influenza Head Interface Epitope Protect by an IgG Subtype-Dependent Mechanism. *Cell* **177**, 1124-1135 e1116, doi:10.1016/j.cell.2019.03.048 (2019).

23 He, W. *et al.* Epitope specificity plays a critical role in regulating antibody-dependent cell-mediated cytotoxicity against influenza A virus. *Proc Natl Acad Sci U S A* **113**, 11931-11936, doi:10.1073/pnas.1609316113 (2016).
24 Koutsakos, M. & Ellebedy, A. H. Immunological imprinting: Understanding COVID-19. *Immunity* **56**, 909-913, doi:10.1016/j.immuni.2023.04.012 (2023).
25 Zhang, A., Stacey, H. D., Mullarkey, C. E. & Miller, M. S. Original Antigenic Sin: How First Exposure Shapes Lifelong Anti-Influenza Virus Immune Responses. *J Immunol* **202**, 335-340, doi:10.4049/jimmunol.1801149 (2019).
26 Yewdell, J. W. & Santos, J. J. S. Original Antigenic Sin: How Original? How Sinful? *Cold Spring Harb Perspect Med* **11**, doi:10.1101/cshperspect.a038786 (2021).
27 Huang, C. Q., Vishwanath, S., Carnell, G. W., Chan, A. C. Y. & Heeney, J. L. Immune imprinting and next-generation coronavirus vaccines. *Nat Microbiol* **8**, 1971-1985, doi:10.1038/s41564-023-01505-9 (2023).
28 Gouma, S., Anderson, E. M. & Hensley, S. E. Challenges of Making Effective Influenza Vaccines. *Annu Rev Virol* **7**, 495-512, doi:10.1146/annurev-virology-010320-044746 (2020).
29 Kim, J. H., Skountzou, I., Compans, R. & Jacob, J. Original antigenic sin responses to influenza viruses. *J Immunol* **183**, 3294-3301, doi:10.4049/jimmunol.0900398 (2009).
30 Webster, R. G., Kasel, J. A., Couch, R. B. & Laver, W. G. Influenza virus subunit vaccines. II. Immunogenicity and original antigenic sin in humans. *J Infect Dis* **134**, 48-58, doi:10.1093/infdis/134.1.48 (1976).
31 Fazekas de St, G. & Webster, R. G. Disquisitions on Original Antigenic Sin. II. Proof in lower creatures. *J Exp Med* **124**, 347-361, doi:10.1084/jem.124.3.347 (1966).
32 Braciale, T. J., Gerhard, W. & Klinman, N. R. Analysis of the humoral immune response to influenza virus in vitro. *J Immunol* **116**, 827-834 (1976).
33 Tas, J. M. J. *et al.* Antibodies from primary humoral responses modulate the recruitment of naive B cells during secondary responses. *Immunity* **55**, 1856-1871 e1856, doi:10.1016/j.immuni.2022.07.020 (2022).
34 Zhang, Y. *et al.* Germinal center B cells govern their own fate via antibody feedback. *J Exp Med* **210**, 457-464, doi:10.1084/jem.20120150 (2013).
35 Inoue, T. *et al.* Antibody feedback contributes to facilitating the development of Omicron-reactive memory B cells in SARS-CoV-2 mRNA vaccinees. *J Exp Med* **220**, doi:10.1084/jem.20221786 (2023).
36 Richards, K. A. *et al.* Evidence That Blunted CD4 T-Cell Responses Underlie Deficient Protective Antibody Responses to Influenza Vaccines in Repeatedly Vaccinated Human Subjects. *J Infect Dis* **222**, 273-277, doi:10.1093/infdis/jiz433 (2020).
37 Ndifon, W. A simple mechanistic explanation for original antigenic sin and its alleviation by adjuvants. *J R Soc Interface* **12**, doi:10.1098/rsif.2015.0627 (2015).
38 Schiepers, A., van 't Wout, M. F. L., Hobbs, A., Mesin, L. & Victora, G. D. Opposing effects of pre-existing antibody and memory T cell help on the dynamics of recall germinal centers. *bioRxiv*, doi:10.1101/2023.12.15.571936 (2023).
39 Schaefer-Babajew, D. *et al.* Antibody feedback regulates immune memory after SARS-CoV-2 mRNA vaccination. *Nature* **613**, 735-742, doi:10.1038/s41586-022-05609-w (2023).
40 Schiepers, A. *et al.* Molecular fate-mapping of serum antibody responses to repeat immunization. *Nature* **615**, 482-489, doi:10.1038/s41586-023-05715-3 (2023).
41 Zarnitsyna, V. I. *et al.* Masking of antigenic epitopes by antibodies shapes the humoral immune response to influenza. *Philos Trans R Soc Lond B Biol Sci* **370**, doi:10.1098/rstb.2014.0248 (2015).
42 Miller, M. S. *et al.* Neutralizing antibodies against previously encountered influenza virus strains increase over time: a longitudinal analysis. *Sci Transl Med* **5**, 198ra107, doi:10.1126/scitranslmed.3006637 (2013).
43 Lessler, J. *et al.* Evidence for antigenic seniority in influenza A (H3N2) antibody responses in southern China. *PLoS Pathog* **8**, e1002802, doi:10.1371/journal.ppat.1002802 (2012).

44 Nunez, I. A. *et al.* Impact of age and pre-existing influenza immune responses in humans receiving split inactivated influenza vaccine on the induction of the breadth of antibodies to influenza A strains. *PLoS One* **12**, e0185666, doi:10.1371/journal.pone.0185666 (2017).
45 Gostic, K. M., Ambrose, M., Worobey, M. & Lloyd-Smith, J. O. Potent protection against H5N1 and H7N9 influenza via childhood hemagglutinin imprinting. *Science* **354**, 722-726, doi:10.1126/science.aag1322 (2016).
46 Fonville, J. M. *et al.* Antibody landscapes after influenza virus infection or vaccination. *Science* **346**, 996-1000, doi:10.1126/science.1256427 (2014).
47 Carter, D. M. *et al.* Complex patterns of human antisera reactivity to novel 2009 H1N1 and historical H1N1 influenza strains. *PLoS One* **7**, e39435, doi:10.1371/journal.pone.0039435 (2012).
48 Lee, J. *et al.* Molecular-level analysis of the serum antibody repertoire in young adults before and after seasonal influenza vaccination. *Nat Med* **22**, 1456-1464, doi:10.1038/nm.4224 (2016).
49 Skowronski, D. M. *et al.* Immuno-epidemiologic correlates of pandemic H1N1 surveillance observations: higher antibody and lower cell-mediated immune responses with advanced age. *J Infect Dis* **203**, 158-167, doi:10.1093/infdis/jiq039 (2011).
50 Choi, Y. S. *et al.* Reduced antibody responses to the pandemic (H1N1) 2009 vaccine after recent seasonal influenza vaccination. *Clin Vaccine Immunol* **18**, 1519-1523, doi:10.1128/CVI.05053-11 (2011).
51 Gagnon, A. *et al.* Pandemic Paradox: Early Life H2N2 Pandemic Influenza Infection Enhanced Susceptibility to Death during the 2009 H1N1 Pandemic. *mBio* **9**, doi:10.1128/mBio.02091-17 (2018).
52 Lewnard, J. A. & Cobey, S. Immune History and Influenza Vaccine Effectiveness. *Vaccines (Basel)* **6**, doi:10.3390/vaccines6020028 (2018).
53 Skowronski, D. M. *et al.* Paradoxical clade- and age-specific vaccine effectiveness during the 2018/19 influenza A(H3N2) epidemic in Canada: potential imprint-regulated effect of vaccine (I-REV). *Euro Surveill* **24**, doi:10.2807/1560-7917.ES.2019.24.46.1900585 (2019).
54 Ma, J., Dushoff, J. & Earn, D. J. Age-specific mortality risk from pandemic influenza. *J Theor Biol* **288**, 29-34, doi:10.1016/j.jtbi.2011.08.003 (2011).
55 Simonsen, L. *et al.* Global mortality estimates for the 2009 Influenza Pandemic from the GLaMOR project: a modeling study. *PLoS Med* **10**, e1001558, doi:10.1371/journal.pmed.1001558 (2013).
56 Aguilar-Bretones, M. *et al.* Seasonal coronavirus-specific B cells with limited SARS-CoV-2 cross-reactivity dominate the IgG response in severe COVID-19. *J Clin Invest* **131**, doi:10.1172/JCI150613 (2021).
57 Guo, L. *et al.* Cross-reactive antibody against human coronavirus OC43 spike protein correlates with disease severity in COVID-19 patients: a retrospective study. *Emerg Microbes Infect* **10**, 664-676, doi:10.1080/22221751.2021.1905488 (2021).
58 Herman, J. D. *et al.* Humoral immunity to an endemic coronavirus is associated with postacute sequelae of COVID-19 in individuals with rheumatic diseases. *Sci Transl Med* **15**, eadf6598, doi:10.1126/scitranslmed.adf6598 (2023).
59 Aydillo, T. *et al.* Immunological imprinting of the antibody response in COVID-19 patients. *Nat Commun* **12**, 3781, doi:10.1038/s41467-021-23977-1 (2021).
60 Anderson, E. M. *et al.* Seasonal human coronavirus antibodies are boosted upon SARS-CoV-2 infection but not associated with protection. *Cell* **184**, 1858-1864 e1810, doi:10.1016/j.cell.2021.02.010 (2021).
61 Yin, D. *et al.* Effect of seasonal coronavirus immune imprinting on the immunogenicity of inactivated COVID-19 vaccination. *Front Immunol* **14**, 1195533, doi:10.3389/fimmu.2023.1195533 (2023).
62 Anderson, E. M. *et al.* SARS-CoV-2 infections elicit higher levels of original antigenic sin antibodies compared with SARS-CoV-2 mRNA vaccinations. *Cell Rep* **41**, 111496, doi:10.1016/j.celrep.2022.111496 (2022).
63 Galipeau, Y. *et al.* Relative Ratios of Human Seasonal Coronavirus Antibodies Predict the Efficiency of Cross-Neutralization of SARS-CoV-2 Spike Binding to ACE2. *EBioMedicine* **74**, 103700, doi:10.1016/j.ebiom.2021.103700 (2021).

64 Smith, D. J., Forrest, S., Ackley, D. H. & Perelson, A. S. Variable efficacy of repeated annual influenza vaccination. *Proc Natl Acad Sci U S A* **96**, 14001-14006, doi:10.1073/pnas.96.24.14001 (1999).
65 Linderman, S. L. & Hensley, S. E. Antibodies with 'Original Antigenic Sin' Properties Are Valuable Components of Secondary Immune Responses to Influenza Viruses. *PLoS Pathog* **12**, e1005806, doi:10.1371/journal.ppat.1005806 (2016).
66 Yisimayi, A. *et al.* Repeated Omicron exposures override ancestral SARS-CoV-2 immune imprinting. *Nature* **625**, 148-156, doi:10.1038/s41586-023-06753-7 (2024).
67 Kim, J. H., Davis, W. G., Sambhara, S. & Jacob, J. Strategies to alleviate original antigenic sin responses to influenza viruses. *Proc Natl Acad Sci U S A* **109**, 13751-13756, doi:10.1073/pnas.0912458109 (2012).
68 Ramsay, L. C. *et al.* The impact of repeated vaccination on influenza vaccine effectiveness: a systematic review and meta-analysis. *BMC Med* **17**, 9, doi:10.1186/s12916-018-1239-8 (2019).
69 Crotty, S. T Follicular Helper Cell Biology: A Decade of Discovery and Diseases. *Immunity* **50**, 1132-1148, doi:10.1016/j.immuni.2019.04.011 (2019).
70 Victora, G. D. & Wilson, P. C. Germinal center selection and the antibody response to influenza. *Cell* **163**, 545-548, doi:10.1016/j.cell.2015.10.004 (2015).
71 Hagglof, T. *et al.* Continuous germinal center invasion contributes to the diversity of the immune response. *Cell* **186**, 147-161 e115, doi:10.1016/j.cell.2022.11.032 (2023).
72 Weber, T. *et al.* Enhanced SARS-CoV-2 humoral immunity following breakthrough infection builds upon the preexisting memory B cell pool. *Sci Immunol* **8**, eadk5845, doi:10.1126/sciimmunol.adk5845 (2023).
73 Bettini, E. *et al.* Distinct components of nucleoside-modified messenger RNA vaccines cooperate to instruct efficient germinal center responses. *bioRxiv*, doi:10.1101/2024.05.17.594726 (2024).
74 Lederer, K. *et al.* Germinal center responses to SARS-CoV-2 mRNA vaccines in healthy and immunocompromised individuals. *Cell* **185**, 1008-1024 e1015, doi:10.1016/j.cell.2022.01.027 (2022).
75 Tan, H. X. *et al.* Immunogenicity of prime-boost protein subunit vaccine strategies against SARS-CoV-2 in mice and macaques. *Nat Commun* **12**, 1403, doi:10.1038/s41467-021-21665-8 (2021).
76 Turner, J. S. *et al.* SARS-CoV-2 mRNA vaccines induce persistent human germinal centre responses. *Nature* **596**, 109-113, doi:10.1038/s41586-021-03738-2 (2021).
77 Lederer, K. *et al.* SARS-CoV-2 mRNA Vaccines Foster Potent Antigen-Specific Germinal Center Responses Associated with Neutralizing Antibody Generation. *Immunity* **53**, 1281-1295 e1285, doi:10.1016/j.immuni.2020.11.009 (2020).
78 Willis, E. *et al.* Nucleoside-modified mRNA vaccination partially overcomes maternal antibody inhibition of de novo immune responses in mice. *Sci Transl Med* **12**, doi:10.1126/scitranslmed.aav5701 (2020).
79 Pardi, N. *et al.* Nucleoside-modified mRNA vaccines induce potent T follicular helper and germinal center B cell responses. *J Exp Med* **215**, 1571-1588, doi:10.1084/jem.20171450 (2018).
80 Alameh, M. G. *et al.* Lipid nanoparticles enhance the efficacy of mRNA and protein subunit vaccines by inducing robust T follicular helper cell and humoral responses. *Immunity* **55**, 1136-1138, doi:10.1016/j.immuni.2022.05.007 (2022).
81 Pardi, N. *et al.* Expression kinetics of nucleoside-modified mRNA delivered in lipid nanoparticles to mice by various routes. *J Control Release* **217**, 345-351, doi:10.1016/j.jconrel.2015.08.007 (2015).
82 England, R. N. *et al.* Evaluation of mRNA-LNP and adjuvanted protein SARS-CoV-2 vaccines in a maternal antibody mouse model. *NPJ Vaccines* **9**, 110, doi:10.1038/s41541-024-00901-4 (2024).
83 Cirelli, K. M. & Crotty, S. Germinal center enhancement by extended antigen availability. *Curr Opin Immunol* **47**, 64-69, doi:10.1016/j.coi.2017.06.008 (2017).
84 Tam, H. H. *et al.* Sustained antigen availability during germinal center initiation enhances antibody responses to vaccination. *Proc Natl Acad Sci U S A* **113**, E6639-E6648, doi:10.1073/pnas.1606050113 (2016).
85 Verbeke, R., Hogan, M. J., Lore, K. & Pardi, N. Innate immune mechanisms of mRNA vaccines. *Immunity* **55**, 1993-2005, doi:10.1016/j.immuni.2022.10.014 (2022).

86 Roltgen, K. *et al.* Immune imprinting, breadth of variant recognition, and germinal center response in human SARS-CoV-2 infection and vaccination. *Cell* **185**, 1025-1040 e1014, doi:10.1016/j.cell.2022.01.018 (2022).
87 Shirai, S. *et al.* Lipid Nanoparticle Acts as a Potential Adjuvant for Influenza Split Vaccine without Inducing Inflammatory Responses. *Vaccines (Basel)* **8**, doi:10.3390/vaccines8030433 (2020).
88 Awasthi, S. *et al.* Antibody responses to crucial functional epitopes as a novel approach to assess immunogenicity of vaccine adjuvants. *Vaccine* **37**, 3770-3778, doi:10.1016/j.vaccine.2019.05.068 (2019).
89 Robbiani, D. F. *et al.* Convergent antibody responses to SARS-CoV-2 in convalescent individuals. *Nature* **584**, 437-442, doi:10.1038/s41586-020-2456-9 (2020).
90 Wang, Z. *et al.* Naturally enhanced neutralizing breadth against SARS-CoV-2 one year after infection. *Nature* **595**, 426-431, doi:10.1038/s41586-021-03696-9 (2021).
91 Mesin, L. *et al.* Restricted Clonality and Limited Germinal Center Reentry Characterize Memory B Cell Reactivation by Boosting. *Cell* **180**, 92-106 e111, doi:10.1016/j.cell.2019.11.032 (2020).
92 Turner, J. S. *et al.* Human germinal centres engage memory and naive B cells after influenza vaccination. *Nature* **586**, 127-132, doi:10.1038/s41586-020-2711-0 (2020).
93 Carreno, J. M., Singh, G., Simon, V., Krammer, F. & group, P. V. I. s. Bivalent COVID-19 booster vaccines and the absence of BA.5-specific antibodies. *Lancet Microbe* **4**, e569, doi:10.1016/S2666-5247(23)00118-0 (2023).
94 Li, C. *et al.* Mechanisms of innate and adaptive immunity to the Pfizer-BioNTech BNT162b2 vaccine. *Nat Immunol* **23**, 543-555, doi:10.1038/s41590-022-01163-9 (2022).
95 Hassett, K. J. *et al.* Optimization of Lipid Nanoparticles for Intramuscular Administration of mRNA Vaccines. *Mol Ther Nucleic Acids* **15**, 1-11, doi:10.1016/j.omtn.2019.01.013 (2019).
96 Liang, F. *et al.* Efficient Targeting and Activation of Antigen-Presenting Cells In Vivo after Modified mRNA Vaccine Administration in Rhesus Macaques. *Mol Ther* **25**, 2635-2647, doi:10.1016/j.ymthe.2017.08.006 (2017).
97 Lazzaro, S. *et al.* CD8 T-cell priming upon mRNA vaccination is restricted to bone-marrow-derived antigen-presenting cells and may involve antigen transfer from myocytes. *Immunology* **146**, 312-326, doi:10.1111/imm.12505 (2015).
98 McNamara, M. A., Nair, S. K. & Holl, E. K. RNA-Based Vaccines in Cancer Immunotherapy. *J Immunol Res* **2015**, 794528, doi:10.1155/2015/794528 (2015).
99 Bachmann, M. F. & Jennings, G. T. Vaccine delivery: a matter of size, geometry, kinetics and molecular patterns. *Nat Rev Immunol* **10**, 787-796, doi:10.1038/nri2868 (2010).
100 Heesters, B. A., van der Poel, C. E., Das, A. & Carroll, M. C. Antigen Presentation to B Cells. *Trends Immunol* **37**, 844-854, doi:10.1016/j.it.2016.10.003 (2016).
101 Tolar, P., Hanna, J., Krueger, P. D. & Pierce, S. K. The constant region of the membrane immunoglobulin mediates B cell-receptor clustering and signaling in response to membrane antigens. *Immunity* **30**, 44-55, doi:10.1016/j.immuni.2008.11.007 (2009).
102 Depoil, D. *et al.* CD19 is essential for B cell activation by promoting B cell receptor-antigen microcluster formation in response to membrane-bound ligand. *Nat Immunol* **9**, 63-72, doi:10.1038/ni1547 (2008).
103 Carrasco, Y. R. & Batista, F. D. B cell recognition of membrane-bound antigen: an exquisite way of sensing ligands. *Curr Opin Immunol* **18**, 286-291, doi:10.1016/j.coi.2006.03.013 (2006).
104 Lainscek, D. *et al.* A Nanoscaffolded Spike-RBD Vaccine Provides Protection against SARS-CoV-2 with Minimal Anti-Scaffold Response. *Vaccines (Basel)* **9**, doi:10.3390/vaccines9050431 (2021).
105 Cohen, A. A. *et al.* Mosaic nanoparticles elicit cross-reactive immune responses to zoonotic coronaviruses in mice. *Science* **371**, 735-741, doi:10.1126/science.abf6840 (2021).
106 Cohen, A. A. *et al.* Mosaic sarbecovirus vaccination elicits cross-reactive responses in pre-immunized animals. *bioRxiv*, doi:10.1101/2024.02.08.576722 (2024).
107 Cohen, A. A. *et al.* Mosaic RBD nanoparticles protect against multiple sarbecovirus challenges in animal models. *bioRxiv*, doi:10.1101/2022.03.25.485875 (2022).

108 Burnett, D. L. *et al.* Immunizations with diverse sarbecovirus receptor-binding domains elicit SARS-CoV-2 neutralizing antibodies against a conserved site of vulnerability. *Immunity* **54**, 2908-2921 e2906, doi:10.1016/j.immuni.2021.10.019 (2021).
109 Walls, A. C. *et al.* Elicitation of broadly protective sarbecovirus immunity by receptor-binding domain nanoparticle vaccines. *Cell* **184**, 5432-5447 e5416, doi:10.1016/j.cell.2021.09.015 (2021).
110 Greaney, A. J. *et al.* Complete Mapping of Mutations to the SARS-CoV-2 Spike Receptor-Binding Domain that Escape Antibody Recognition. *Cell Host Microbe* **29**, 44-57 e49, doi:10.1016/j.chom.2020.11.007 (2021).
111 Barnes, C. O. *et al.* SARS-CoV-2 neutralizing antibody structures inform therapeutic strategies. *Nature* **588**, 682-687, doi:10.1038/s41586-020-2852-1 (2020).
112 Greaney, A. J. *et al.* Mapping mutations to the SARS-CoV-2 RBD that escape binding by different classes of antibodies. *Nat Commun* **12**, 4196, doi:10.1038/s41467-021-24435-8 (2021).
113 Piccoli, L. *et al.* Mapping Neutralizing and Immunodominant Sites on the SARS-CoV-2 Spike Receptor-Binding Domain by Structure-Guided High-Resolution Serology. *Cell* **183**, 1024-1042 e1021, doi:10.1016/j.cell.2020.09.037 (2020).
114 Carabelli, A. M. *et al.* SARS-CoV-2 variant biology: immune escape, transmission and fitness. *Nat Rev Microbiol* **21**, 162-177, doi:10.1038/s41579-022-00841-7 (2023).
115 Telenti, A. *et al.* After the pandemic: perspectives on the future trajectory of COVID-19. *Nature* **596**, 495-504, doi:10.1038/s41586-021-03792-w (2021).
116 Li, T. *et al.* Potent SARS-CoV-2 neutralizing antibodies with protective efficacy against newly emerged mutational variants. *Nat Commun* **12**, 6304, doi:10.1038/s41467-021-26539-7 (2021).
117 Madhi, S. A. *et al.* Efficacy of the ChAdOx1 nCoV-19 Covid-19 Vaccine against the B.1.351 Variant. *N Engl J Med* **384**, 1885-1898, doi:10.1056/NEJMoa2102214 (2021).
118 Kustin, T. *et al.* Evidence for increased breakthrough rates of SARS-CoV-2 variants of concern in BNT162b2-mRNA-vaccinated individuals. *Nat Med* **27**, 1379-1384, doi:10.1038/s41591-021-01413-7 (2021).
119 Goel, R. R. *et al.* Efficient recall of Omicron-reactive B cell memory after a third dose of SARS-CoV-2 mRNA vaccine. *Cell* **185**, 1875-1887 e1878, doi:10.1016/j.cell.2022.04.009 (2022).
120 Zar, H. J. *et al.* Natural and hybrid immunity following four COVID-19 waves: A prospective cohort study of mothers in South Africa. *EClinicalMedicine* **53**, 101655, doi:10.1016/j.eclinm.2022.101655 (2022).
121 Chu, L. *et al.* Immune response to SARS-CoV-2 after a booster of mRNA-1273: an open-label phase 2 trial. *Nat Med* **28**, 1042-1049, doi:10.1038/s41591-022-01739-w (2022).
122 Chalkias, S. *et al.* A Bivalent Omicron-Containing Booster Vaccine against Covid-19. *N Engl J Med* **387**, 1279-1291, doi:10.1056/NEJMoa2208343 (2022).
123 Hoffmann, M. *et al.* Effect of hybrid immunity and bivalent booster vaccination on omicron sublineage neutralisation. *Lancet Infect Dis* **23**, 25-28, doi:10.1016/S1473-3099(22)00792-7 (2023).
124 Kaku, C. I. *et al.* Recall of preexisting cross-reactive B cell memory after Omicron BA.1 breakthrough infection. *Sci Immunol* **7**, eabq3511, doi:10.1126/sciimmunol.abq3511 (2022).
125 Chalkias, S. *et al.* Original SARS-CoV-2 monovalent and Omicron BA.4/BA.5 bivalent COVID-19 mRNA vaccines: phase 2/3 trial interim results. *Nat Med* **29**, 2325-2333, doi:10.1038/s41591-023-02517-y (2023).
126 Kurhade, C. *et al.* Low neutralization of SARS-CoV-2 Omicron BA.2.75.2, BQ.1.1 and XBB.1 by parental mRNA vaccine or a BA.5 bivalent booster. *Nat Med* **29**, 344-347, doi:10.1038/s41591-022-02162-x (2023).
127 Davis-Gardner, M. E. *et al.* Neutralization against BA.2.75.2, BQ.1.1, and XBB from mRNA Bivalent Booster. *N Engl J Med* **388**, 183-185, doi:10.1056/NEJMc2214293 (2023).
128 Zou, J. *et al.* Neutralization of BA.4-BA.5, BA.4.6, BA.2.75.2, BQ.1.1, and XBB.1 with Bivalent Vaccine. *N Engl J Med* **388**, 854-857, doi:10.1056/NEJMc2214916 (2023).
129 Collier, A. Y. *et al.* Immunogenicity of BA.5 Bivalent mRNA Vaccine Boosters. *N Engl J Med* **388**, 565-567, doi:10.1056/NEJMc2213948 (2023).
130 Wang, Q. *et al.* Antibody Response to Omicron BA.4-BA.5 Bivalent Booster. *N Engl J Med* **388**, 567-569, doi:10.1056/NEJMc2213907 (2023).

131 Wang, Q. *et al.* Deep immunological imprinting due to the ancestral spike in the current bivalent COVID-19 vaccine. *Cell Rep Med* **4**, 101258, doi:10.1016/j.xcrm.2023.101258 (2023).
132 Wang, Q. *et al.* SARS-CoV-2 neutralising antibodies after bivalent versus monovalent booster. *Lancet Infect Dis* **23**, 527-528, doi:10.1016/S1473-3099(23)00181-0 (2023).
133 Wang, Q. *et al.* SARS-CoV-2 neutralising antibodies after a second BA.5 bivalent booster. *Lancet* **402**, 1827-1828, doi:10.1016/S0140-6736(23)02278-X (2023).
134 Johnston, T. S. *et al.* Immunological imprinting shapes the specificity of human antibody responses against SARS-CoV-2 variants. *Immunity* **57**, 912-925 e914, doi:10.1016/j.immuni.2024.02.017 (2024).
135 Wang, Q. *et al.* XBB.1.5 monovalent mRNA vaccine booster elicits robust neutralizing antibodies against XBB subvariants and JN.1. *Cell Host Microbe* **32**, 315-321 e313, doi:10.1016/j.chom.2024.01.014 (2024).
136 Tortorici, M. A. *et al.* Persistent immune imprinting occurs after vaccination with the COVID-19 XBB.1.5 mRNA booster in humans. *Immunity* **57**, 904-911 e904, doi:10.1016/j.immuni.2024.02.016 (2024).
137 Arevalo, C. P. *et al.* A multivalent nucleoside-modified mRNA vaccine against all known influenza virus subtypes. *Science* **378**, 899-904, doi:10.1126/science.abm0271 (2022).

8 Chapter 8: Plant-based production of SARS-CoV-2 antigens for use in a subunit vaccine. *(Published)*

Preface: This chapter has been previously published as a research article.

Demone J*, Maltseva M*, Nourimand M,Nasr-Sharif M, Galipeau Y, Alarcon EI, et al. (2022) Scalable agroinfiltration-based production of SARS-CoV-2 antigens for use in diagnostic assays and subunit vaccines. PLoS ONE 17(12): e0277668. https://doi.org/10.1371/journal.pone.0277668

8.1 Abstract

Agroinfiltration is a method used in biopharming to support plant-based biosynthesis of therapeutic proteins such as antibodies and viral antigens involved in vaccines. Major advantages of generating proteins in plants is the low cost, massive scalability and the rapid yield of the technology. Herein, we report the agroinfiltration-based production of glycosylated SARS-CoV-2 Spike receptor-binding domain (RBD) protein. We show that it exhibits highaffinity binding to the SARS-CoV-2 receptor angiotensin-converting enzyme 2 (ACE2) and displays folding similar to antigen produced in mammalian expression systems. Moreover, our plant-expressed RBD was readily detected by IgM, IgA, and IgG antibodies from the serum of SARS-CoV-2 infected and vaccinated individuals. We further demonstrate that binding of plant-expressed RBD to ACE2 is efficiently neutralized by these antibodies. Collectively, these findings demonstrate that recombinant RBD produced via agroinfiltration exhibits suitable biochemical and antigenic features for use in serological and neutralization assays, and in subunit vaccine platforms.

8.2 Introduction

Agroinfiltration is a well-established method used frequently in plant biology in which a strain of the Gram-negative alpha-Proteobacterial species *Agrobacterium tumefaciens* is 'injected' with a needleless syringe into plant leaves. This bacterial plant pathogen then employs a specialized secretion system to genetically transform plant host nuclei by transferring genes of interest into recipient host cells with a high degree of efficiency. The transient transformation of *Nicotiana benthamiana* via agroinfiltration is one of the most rapid methods to efficiently express recombinant proteins in any eukaryotic system [1]. Unlike traditional stably transformed transgenic plants that may require many months to generate, we can transiently transform the leaves of *N. benthamiana* to (co-)express one or multiple proteins simultaneously, observing high levels of protein expression in 3–4 days. This system is highly responsive and flexible. It is well-suited for supporting the rapid development of viral antigen-based diagnostic tests, such as serological assays to detect antibodies in blood, and vaccines against diseases such as COVID-19 in real time where the occurrence of viral variants represent an ever-evolving target.

In this work, we describe the development of a rapid and flexible agroinfiltration-based platform for the production of recombinant SARS-CoV-2 Spike Receptor-Binding Domain (RBD) in the plant *Nicotiana benthamiana*. This platform is simple, massively scalable, costeffective and easily adaptable to reflect rapid changes in circulating viral sequences. The RBD of the viral spike is the region primarily involved in binding to the cell surface receptor of the virus, the angiotensin converting enzyme 2 (ACE2) receptor [2]. Most neutralizing antibodies against SARS-CoV-2 are directed to RBD [3–5]. A number of studies have already demonstrated the feasibility of plant-based RBD antigen development: histidine-tagged RBD has been expressed at levels as high as 8 ug/g leaf biomass [6], and similar RBD antigens exhibit effective neutralizing responses in mice [7] and non-human primates [8].

The system we describe here utilizes *Agrobacterium tumefaciens*-mediated transient transformation of *N. benthamiana* (Fig 1), to enable the biosynthesis of high-quality SARS-CoV-2 RBD antigen *in planta*. This accessible and cost-effective process requires approximately only six weeks, encompassing seed germination to delivery of the tandem-purified antigen. We demonstrate in this study that plant expressed RBD displays similar biochemical, structural and antigenic properties as RBD produced in classical mammalian cell expression systems, thereby indicating its suitability for use in diagnostic tests.

Aside from diagnostics assays, SARS-CoV-2 antigens can also be utilized in adjuvanted subunit vaccines [9–11], as well as unadjuvanted vaccines when used as a booster shot [12]. While most SARS-CoV-2 vaccines focus on intramuscular delivery systems, development of a subunit nasal spray vaccine offers a complementary method to increase mucosal immunity to SARS-CoV-2 variants and provide vaccine-hesitant and needle-phobic individuals with alternative immunization options [13]. Protein subunit vaccine platforms have been extensively characterized and have an established safety and efficacy profile against multiple pathogens such as Shingles, Hepatitis B and Meningitis B [14]. The effectiveness of plant-expressed proteins in vaccines has been demonstrated in animal models where they induced potent mucosal immune responses and protection following intranasal immunization [15, 16]. Vaccines produced in plants offer several advantages over traditional manufacturing processes, including significantly lower production costs, increased scalability, and a negligible risk of contamination with human pathogens [17]. These advantages are critical parameters towards facilitating equitable vaccine access to the world's population.

8.3 Materials and methods

Plant materials and growth conditions

Wild-type *Nicotiana benthamiana* plants were grown in a greenhouse equipped with 400-Watt high pressure sodium (HPS) light bulbs set at a 20h light/4h dark photoperiod at 25˚C for five weeks prior to infiltration. Plants were fertilized once per week using Miracle-Gro (24-8-16) at a concentration of 1.1 g/L. Seeds were germinated on a weekly basis and 56 two-week-old seedlings were transplanted to individual pots once a week.

Gene synthesis

The RBD sequence was obtained from the Wuhan strain (NC_045512) Spike sequence spanning amino acids 319 to 540. The sequence designed for expression in *N. benthamiana* had a C-terminal thrombin cleavage site, 8xhis tag, a Twin-Strep-tag[1], and a KDEL sequence for ER-retention. An endoplasmic reticulum targeting signal peptide derived from *Nicotiana tabacum* PR-1a signal peptide (amino acids 1 to 31) was added to the N-terminal side of the RBD sequence. The construct was codon-optimized for *N. benthamiana* expression and was synthesized by GenScript into the pHREAC vector [18] via BsaI sites. Lectin-binding human chaperone calreticulin (NP_004334.1) was codon-optimized for *N. benthamiana* and synthesized in the pHRE vector [18].

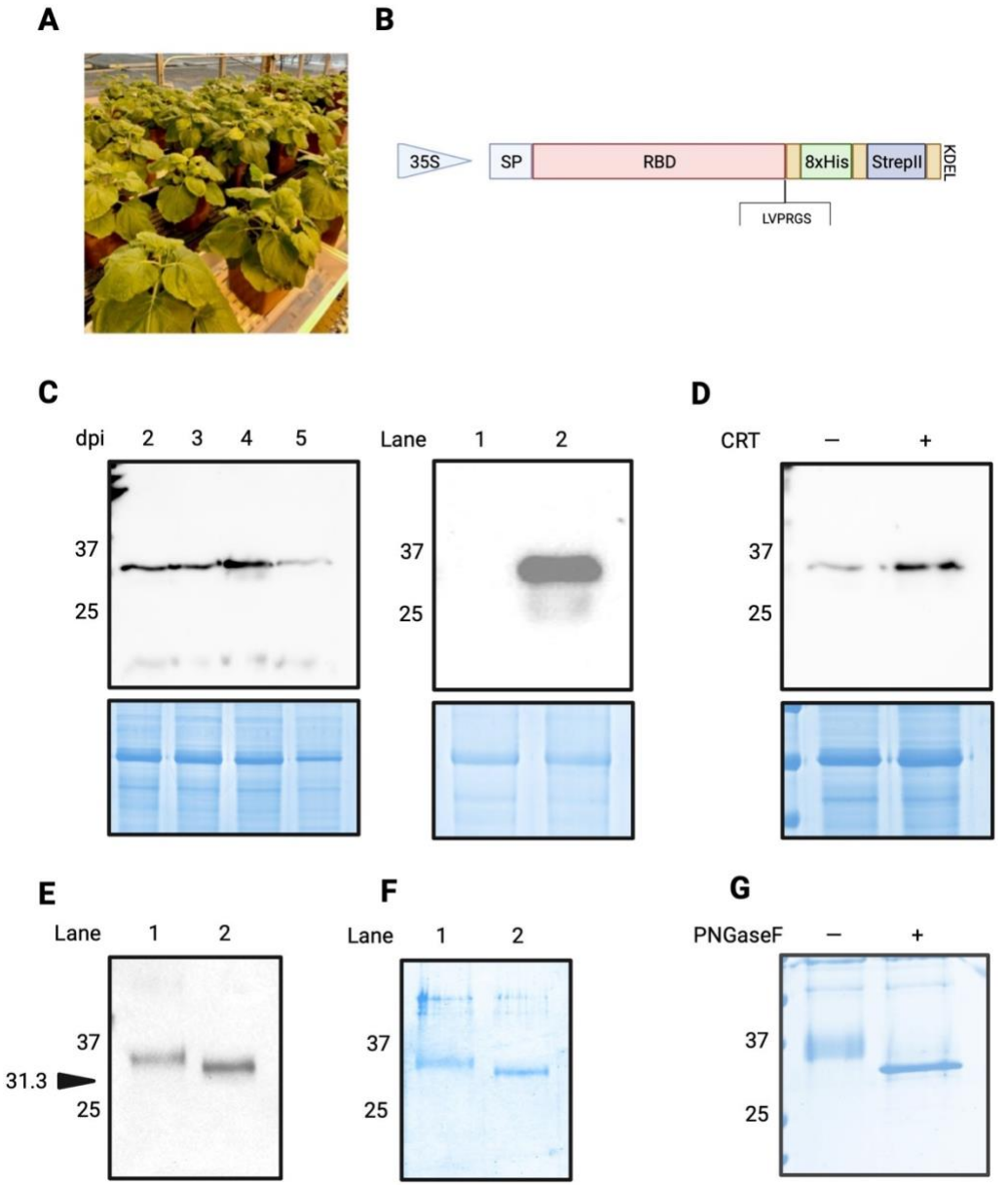

Figure 8.1 Expression and purification of SARS-CoV-2 RBD in Nicotiana benthamiana.

(A) Agroinfiltrated *Nicotiana benthamiana* growing in greenhouse. (B) Schematic representation of genetic construct used to express SARS-CoV-2 RBD *in planta*. The SARS-CoV-2 sequence was expressed as a recombinant protein with a dual 8xHis and Twin-Strep II tag, interspersed with Gly-Ser linkers (gold boxes). An ER-retention KDEL sequence was positioned at the C-terminus, and a Thrombin cleavage site (LVPRGS) was included for tag removal. (C) Left panel: Anti-His IB of samples obtained from *N. benthamiana* 2 to 5 days post-infiltration (dpi) with RBD construct in B. Loading control at 5 dpi reproducibly demonstrates reduced abundance of protein due to initiation of tissue necrosis at this time. Right panel: NT control (lane 1) compared to RBD expressed in *N. benthamiana* with calreticulin (lane 2). Anti-his IB. (D) Co-infiltration of human calreticulin (CRT) increases expression levels of RBD in *N. benthamiana*. Samples collected 4dpi. Anti-his IB. (E) AntiS1 IB of purified RBD expressed in *N. benthamiana* (lane 1) and control RBD expressed in mammalian 293F cells (lane2). Arrow indicates expected migration of a protein corresponding to 31.3 kDa. (F) CBB-stained SDS-PAGE of purified RBD expressed in *N. benthamiana* (lane 1) and control RBD expressed in mammalian 293F cells (lane 2). (G) CBBstained SDS-PAGE of plant-derived RBD treated with (+) and without (-) the amidase Peptide-N-Glycosidase F (PNGaseF), an enzyme that cleaves *N*-linked glycan chains. SP, signal peptide. IB, immunoblot. CBB, Coomassie Brilliant Blue. NT, non-transformed.

Transient expression in Nicotiana benthamiana

Prior to infiltration, pHREAC-RBD and pHRE-calreticulin were freshly transformed into *Agrobacterium tumefaciens* strains AGL1 and Gv2260, respectively, via electroporation. A single colony was used to inoculate each 5 mL starter culture, and each culture was sub-cultured once in two litres of LB broth containing 50 mg/L ampicillin and 50 mg/L kanamycin at 28˚C. The final cultures were grown to an optical density at 600nm (OD600) of 0.6 and were centrifuged and resuspended in MMA buffer (10 mM MES, 10 mM $MgCl_2$, 200 μM acetosyringone, pH 5.6). Unless otherwise indicated, *Agrobacterium* containing the pHREAC-RBD and pHRE-calreticulin constructs were combined and incubated at room temperature for one hour prior to infiltration, to a final OD600 of 0.25 (pHREAC-RBD) and 0.1 (pHRE-CRT). Small-scale infiltration was performed by using 1 mL needleless syringes to inject *Agrobacterium* into the abaxial side of the leaves. Large-scale infiltration was performed via vacuum infiltration using three litres of infiltration solution. Leaves were gently scored, and individual plants were inverted and placed into the vacuum chamber for 2–3 minutes at a pressure of 5 bar. The vacuum was repeatedly applied until the plant was fully infiltrated. Infiltrated leaves were marked and plants were returned to the greenhouse until collection. Twenty-five plants were typically infiltrated per large-scale infiltration, equating to approximately 200 grams of fresh leaf biomass.

Total soluble protein extraction

Leaves co-infiltrated with pHREAC-RBD and pHRE-calreticulin were collected 4–5 dpi (days post-infiltration). Leaf spines were removed, and tissue was homogenized in liquid nitrogen with mortar and pestle. Protein extracts were prepared under native conditions. For each FPLC run: 60 grams of ground tissue were resuspended in 270 mL of ice-cold buffer (PBS (20 mM NaH_2PO_4, 280 mM NaCl, 6 mM KCl), 10 mM imidazole, pH 7.4) and vortexed for five minutes. Ten microlitres of Lysonase Bioprocessing Reagent (Sigma Aldrich Canada Ltd; Etobicoke, Ontario) was added and the lysate was incubated at 4˚C for 15 minutes while gently shaking. Lysate were vortexed again and sonicated three times for 1 minute using a Kontes micro ultrasonic cell disruptor set at 70 output. Lysate was centrifuged for 45 minutes at 20,442 x *g* at 4˚C to pellet cell debris. Supernatants were filtered using several layers of cheesecloth and subsequently filtered using Corning one liter 0.22 μM polyethersulfone (PES) sterilizing low-binding filters (Corning, Incorporated; Corning, NY, USA).

Purification of RBD using HisPur™ Ni-NTA resin

Clarified total protein extract was passed through a HisPur Ni-NTA resin column (5 mL bed volume; Cytiva, Marlborough, US), pre-equilibrated with five volumes of imidazole binding buffer (PBS, 10 mM imidazole buffer, pH 7.4) using a fast protein liquid chromatography (FPLC) system (AKTA Pure; GE Healthcare systems). The column was washed with twenty bed volumes of binding buffer (PBS, 10 mM imidazole, pH 7.4) at a flow rate of 5 mL/minute. Protein was eluted using five bed volumes of elution buffer (PBS, 500 mM imidazole, pH 7.4) at a flow rate of 2 mL/minute. Samples were collected as 2 mL fractions. In initial experiments, aliquots of each fraction were visualized via immunoblotting (anti-His antibody; Cat: SAB2702218, Sigma Aldrich Canada, Oakville, Canada) to identify fractions enriched for RBD, which we found to consistently correspond to a visible peak eluting from the column in fractions 25 to 35.

Purification of RBD using Strep-Tactin resin

Fractions corresponding to the protein peak from the HisPur Ni-NTA resin were pooled and protein was further purified using a Strep-Tactin resin column (5 mL bed volume; Cytiva, Marlborough, US) using the AKTA Pure system. The Strep-Tactin column was pre-equilibrated with five bed volumes of binding buffer (PBS, pH 7.4) prior to sample loading, and the column was then washed with 10 bed volumes of binding buffer (PBS, pH 7.4). Protein was eluted using six bed volumes of StrepTrap elution buffer (PBS, 5 mM *d*-Desthiobiotin, pH 7.4) at a flow rate of 2 mL/minute. Samples were collected as 0.5 mL fractions. In initial experiments, aliquots of each fraction were immunoblotted (probed with anti-His antibody) and protein was also visualized via SDS-PAGE gels stained with Coomassie blue staining solution. We reproducibly detected RBD within fractions 22 to 33, which corresponded to the visible peak eluting from the column. Peak samples were collected, pooled, and concentrated to 500 µL using a Vivaspin 20 column (GE Healthcare; Mississauga, Canada). Plant and mammalian RBD were run on an SDS-PAGE gel and Coomassie-stained for analysis. Both proteins were also immunoblotted with anti-S1 (1: 2000) antibody (Cat: PA5-81795, Invitrogen) and a goat anti-rabbit secondary antibody (1: 10 000).

Further processing of RBD protein

Thrombin cleavage was performed to remove the tag from purified RBD protein. Ten microlitres of thrombin (1U/µL) were added to the 500 µL sample of purified RBD protein and incubated at

22˚C for 20 hours. To remove the cleaved 3 kDa tag from the final product, the reaction was passed through a Strep-Tactin resin column (5 mL bed volume) as described above. Flowthrough fractions corresponding to the peak were collected and concentrated to 500 µL using a Vivaspin 20 column (GE Healthcare, Mississauga, Canada). Protein concentration was quantified using the Bio-Rad Protein Assay and used BSA for standard curve preparation. Protein purity was analyzed using SDS-PAGE and protein was visualized using Coomassie blue staining solution.

PNGase F assay

PNGase F, an amidase, is an enzyme used to cleave *N*-linked glycans from glycoproteins and was used to assess the glycosylation status of plant-expressed RBD. Briefly, 20 µg of partially purified plant RBD protein (following elution from the StrepTrap column) was incubated with denaturation buffer at 100˚C for 10 minutes. The sample was chilled to halt the denaturation process and GlycoBuffer 2 (New England Biolabs), NP-40, and PNGase F were added to the sample. The sample was incubated at 37˚C for one hour and analyzed on an SDS-PAGE gel. Bands were visualized using a Coomassie blue staining solution.

Circular dichroism (CD) spectra and secondary structure calculations

CD spectra were recorded in a J-810 CD spectrophotometer from Jasco analytical instruments equipped with a temperature-controlled Peltier system at 37±0.2˚C. Spectra were measured in 0.2 mm path length cuvettes (50 µL of sample) and recorded using a scan rate of 100 nm/min, in high sensitivity mode between 200–250 nm (1.0 nm intervals). Total number of accumulations per spectra was set as five. The equipment is routinely calibrated with camphorsulfonic acid. A mammalian RBD standard was used as a reference protein for the CD analysis and secondary structure calculation (Cat: Pro1151-3, National Research Council, Ottawa, Canada). Secondary structural analyses were carried out using the BeStSel analysis server [19].

Indirect ELISA to assess ACE2 binding (Kd measurement)

To evaluate protein binding, an indirect ELISA was carried out. Plant or mammalian produced SARS-CoV-2 RBD protein were diluted in sterile 1X PBS (Multicell #311-010-CL) to 4 µg/mL and coated onto a 384-well Immuno plates (Thermofisher, #460372) (12.5 µL/well) overnight at 4˚C. Plates were washed three times with 100 µL of PBS-T (PBS, 1% Tween-20) using a BIOTEK plate washer (model ELX405) and blocked for one hour with blocking buffer (PBS-T

+ 3% non-fat milk powder, w/v) while shaking (700rpm) at room temperature. Biotinylated ACE2 as produced in Abe et al., was diluted in dilution buffer (PBS-T + 1% non-fat milk powder, w/v) to 258 ng/µL and subsequently 1:2 serially diluted [20]. Plates were washed thrice with PBS-T, followed by addition of 20 µL per well of titrated soluble ACE2 and incubated for one hour while shaking at room temperature. Plates were again washed thrice with PBS-T followed by the addition of 20 µL per well of Streptavidin-Peroxidase polymer (Sigma #S2438) diluted in dilution buffer to 1.25 ng/µL. After a one hour incubation with shaking, plates were washed thrice with PBS-T and 20 µL of freshly prepared SuperSignal ELISA Pico Chemiluminescent Substrate (Thermo Scientific, #37069) (mixed 1:1 ratio and diluted in equal volume with dH_2O, (V:V)) was added to each well. Following 5 mins of incubation on a shaker, the luminescence signal (relative light units; RLU) was measured with BIO-TEK Synergy Neo2 plate reader at 20 ms/well at a read height of 1.0 mm. Wells filled with dilution buffer in place of ACE2 accounted for background luminescence and were subtracted from the titrated ACE2 values. Dissociation constant (K_D) was determined using 4-parameter curve fitting with GraphPad Prism 9.1.2 software.

Indirect ELISA to evaluate anti-SARS-CoV-2 immunoreactivity in serum samples (serology)

Plant or mammalian produced SARS-CoV-2 RBD protein were diluted in sterile 1X PBS to 2 µg/mL and coated onto a 96-well plates (VWR #62402–959) (50 µL/well) overnight at 4˚C. Plates were washed three times with 200 µL of PBS-T and blocked for one hour with a blocking buffer (PBS-T + 3% non-fat milk powder, w/v) on a shaker at room temperature. Serum samples were diluted 1:50 in dilution buffer (PBS-T + 1% non-fat milk powder, w/v). In conjunction, titration curves of conformation-dependent monoclonal IgM (Absolute Antibody, Ab01680-15.0), IgA (Absolute Antibody, Ab01680-16.0), and IgG (Absolute Antibody, Ab01680-10.0) CR3022 antibodies were used as reference material to assess protein folding. CR3022 antibodies were diluted 1:2000, followed by 1:2 serial dilution to establish a calibration curve. After blocking, plates were washed thrice with PBS-T, and followed by addition of 100 µL of the respective diluted serum samples and CR3022 antibodies. The plates were incubated for two hours on a shaker at room temperature, washed thrice with PBS-T followed by the addition of 50 µL of the respective secondary-HRP antibody at specified dilutions (1:4000 secondary anti-human IgG-HRP (NRC anti-hIgG#5-HRP fusion), anti- human 1:8000 IgA-HRP (Jackson ImmunoResearch, 109-035-011) or 1:9600 anti- human IgM-HRP (Jackson ImmunoResearch,

109-035-129)). Plates were incubated for one hour on a shaker, washed thrice with PBS-T followed by the addition with 100 µL of the diluted SuperSignal ELISA Pico Chemiluminescent Substrate. Luminescence intensity was measured with BIO-TEK Synergy Neo2 plate reader for 20ms/well at a read height of 1.0 mm. Wells filled with dilution buffer in place of serum accounted for background luminescence and were subtracted from the patient serum values.

Surrogate neutralization ELISA (snELISA) assay to evaluate neutralization activity in serum samples

The described methodology was adapted from the surrogate neutralization ELISA assay as shown in Abe *et al*. (2020) for the evaluation of the relative inhibition of neutralizing antibodies to RBD protein from binding to soluble ACE2 [20, 21]. Briefly, plant or mammalian produced SARS-CoV-2 RBD protein were diluted in sterile 1X PBS to 8 µg/mL and coated onto a 384-well Immuno plates (12.5 µL/well) overnight at 4˚C. Plates were washed three times with PBS-T and blocked for one hour while shaking. Serum samples were 1:5 serially diluted in a dilution buffer, applied to wells (20 µL/well) and incubated for 2 hours while shaking at room temperature. Plates were washed thrice, followed by the addition of biotinylated ACE2 diluted to 0.35 ng/µL in a dilution buffer (20 µL/well). Plates were washed thrice with PBS-T followed by the addition of 20 µL per well of Streptavidin-Peroxidase polymer diluted in dilution buffer to 1.25 ng/µL. Following one hour incubation, plates were washed thrice with PBS-T and freshly prepared SuperSignal ELISA Pico Chemiluminescent Substrate was applied (20 µL/ well). Following 5 mins of incubation while shaking, luminescence intensity was measured with BIO-TEK Synergy Neo2 plate reader for 20ms/well at a read height of 1.0 mm. Control wells were filled with a dilution buffer in place of serum followed by the addition of ACE2 to assess maximum binding signal. Relative percent inhibition was calculated as follows:

$$\%\ Inhibition = (1 - \frac{average\ mean\ of\ serum\ sample}{average\ mean\ of\ maxium\ signal}) \times 100$$

Serum dilution resulting in a 50% inhibition (half-maximal inhibitory dilution (ID_{50})) of RBD protein from binding ACE2 receptor was determined using 4-parameter fitting with GraphPad Prism 9.1.2 software.

RBD production in mammalian cells

For comparison, a mammalian RBD was produced in HEK 293F cells and purified. Briefly, a plasmid generously provided by Dr Florian Krammer (Mount Sinai, NYC) encoding the Whuhan-Hu-1 RBD (MN908947) sequence coding for the amino acid 319–541 and fused with the N-terminal SARS-CoV-2 spike secretory signal and a C-terminal hexa-histidine tag was transfected into 293F cells cultivated in Freestyle 293 expression media (Thermo Fisher, #12338018) at 37˚C, 7% CO_2, while shaking (125rpm). A total of 600 million cells resuspended in 200 mL were transfected with 200 μg of plasmid using ExpiFectamine (Thermo Fisher, 14525). Three days post-transfection, cell supernatant was harvested by centrifugation (4000xg for 20 mins at 4˚C) and filtered through a low binding 0.22 μm stericup vacuum filter (Millipore Sigma, S2GPU10RE). The filtered supernatant was incubated for 2 hours at room temperature with 6ml of Ni-NTA resin (Qiagen, 30210). The column containing the mix of supernatant and resin was washed four times with a washing buffer containing 20mM imidazole, 300mM NaCl and 57.5mM of $NaH_2PO_4H_2O$. The RBD protein was then eluted with three column volumes of the elution buffer containing 234mM of imidazole, 300mM NaCl and 57.5mM of $NaH_2PO_4H_2O$. The eluted solution was concentrated and the buffer was replaced with PBS using a 10kDa Amicon filter (Millipore Sigma, UFC901008). RBD protein integrity was verified by SDS-PAGE, aliquoted to minimize freeze-thaw cycles and stored at -80˚C. RBD used for CD analysis was produced by the National Research Council of Canada and was a gift from Yves Durocher. RBD production details are published elsewhere [21].

Patient samples and collection

Use of human samples for this study was approved by the University of Ottawa Ethics Review Board: Certificates H-04-20-5727, H-04-21-6643 and H-07-20-6009. All participants gave informed written consent to participate in the study. The negative sample was taken from an individual with no history of SARS-CoV-2 infection and tested with PCR. Pooled negative samples were obtained from individuals negative for SARS-CoV-2 as tested by PCR and serology assay. Serum samples from convalescent or vaccinated patients enrolled in surveillance studies from different research studies post-2019. Samples were collected using standard phlebotomy procedures. Samples were de-identified and held at 4˚C for short term handling and testing at University of Ottawa CL2+ biocontainment facility. All research was performed in accordance with current guidelines and regulations.

8.4 Results

A codon-optimized RBD sequence corresponding to the Wuhan-Hu-1 isolate of SARS-CoV-2 was cloned into the pHREAC vector backbone [18] a plant-specific expression platform that has been demonstrated to achieve among the highest levels of *in vivo* protein expression reported in *N. benthamiana* (Fig 1B). The RBD sequence was flanked on the N-terminal side by an endoplasmic reticulum targeting signal peptide derived from *Nicotiana tabacum* PR-1a signal peptide (amino acids 1–31), and on the C-terminal side by a tandem affinity tag consisting of an 8xHis (OctoHis) tag and a Twin-Strep-tag (Fig 1B). The dual affinity tags were separated by a glycine-serine linker, flanked by a thrombin cleavage site (LVPRGS) that was positioned directly upstream of the affinity tags, and an ER retention signal (KDEL) located downstream and adjacent to two tandem stop codons. For an initial assessment of expression, samples were flash frozen in liquid nitrogen, ground, and resuspended in SDS-PAGE loading buffer. These crude samples were next analyzed using immunoblot analysis (Fig 1C & 1D) prior to purification.

Initial screening of the sequence validated expression vector demonstrated that the greatest expression was achieved using *Agrobacterium tumefaciens* strain AGL1 when infiltrated into five-to-six-week-old *N. benthamiana* leaves that were collected four days post-infiltration (dpi) (Fig 1C, left panel), with lower levels of protein expression also observed at 2-, 3-, and 5 dpi. At 3dpi leaves began to develop chlorosis and subsequently reduced photosynthesis, becoming increasingly necrotic 5dpi onward. We did not observe a signal in NT (non-transformed) plants when crude extracts were immunoblotted with anti-His (Fig 1C, right panel). Margolin et al. (2019) had previously demonstrated much enhanced expression of a trimeric Spike mimetic protein in *N. benthamiana* when co-expressed in the presence of human calreticulin [22] thus we assessed expression of RBD in the presence and absence of this chaperone. Coinfiltrating with calreticulin (CRT) produced a noticeable increase in RBD expression levels (Fig 1D) and we thus opted to co-express calreticulin with RBD in subsequent infiltrations, with the assumption that the human chaperone may promote proper RBD folding. All RBD samples revealed a band that migrated slightly above the expected molecular weight of 31.3 kDa. Plant-expressed RBD migrates slightly above the mammalian-expressed RBD control (Fig 1E & 1F), possibly due to differences in glycosylation profiles. Immunoblot analysis using an antibody raised against the SARS-CoV-2 S1 region of the Spike protein confirmed the identity of both plant and mammalian RBD. The S1

antibody also recognized a band at ~75 kDa for the plant RBD sample only, suggesting homodimer formation.

To scale up purification, we agroinfiltrated production batches of 25–30 five-to-six-week old plants (Fig 1A) equivalent to approximately 200 grams fresh biomass) under a vacuum. As described in the methods, protein was partially purified by passing lysate through a Ni-NTA column, corresponding to purification of the 8xHis moiety of the tag. Fractions corresponding to the peak detected at 280 nm were visualized using immunoblot analysis to confirm presence and integrity of protein and were then loaded onto a StrepTrap column. Peak fractions were visualized via immunoblot, pooled, concentrated, and digested overnight with thrombin to remove the 8xHis-Twin-Strep-tag. The digested sample was passed through the StrepTrap column a second time to remove the cleaved tag, and aliquots of the purified protein were analyzed on a Coomassie gel (Fig 1F). A band on the Coomassie gel was visualized migrating at approximately 35 kDa, corresponding to the band recognized on the RBD immunoblot by an anti-S1 antibody (Fig 1E). We next assessed the glycosylation status of the plant and mammalian RBD antigens: the Spike protein of SARS-CoV-2 has 22 *N*-linked glycosylation sites, two of which are located within RBD [23]. Peptide-*N*-glycosidase F (PNGase F) digestion of the plant-expressed RBD protein confirmed that it was glycosylated by a shift in band size (Fig 1G). We estimate the purification yield of RBD at up to 10 ug per gram of fresh leaf mass, in line with other *in planta* production systems that also utilize a histidine-tag [6, 24].

We next performed a comprehensive functional assessment of the RBD produced in *N. benthamiana* in comparison to RBD produced in mammalian cells. Appropriate folding of the RBD antigen is critical for its interaction with the human ACE2 receptor and for the development of antibodies that will target and neutralize native virus and viral variants. We characterized the biochemical properties of the plant-expressed RBD by circular dichroism spectra (CD). More specifically we compared the folding of plant RBD to mammalian expressed RBD standard. We show that the spectral profile of plant-expressed RBD is largely similar to the mammalian expressed RBD, both displaying a single minimum at ~206 nm, consistent with previously reported profiles [25, 26] (Fig 2A). This is further reflected in the analysis of the secondary structure composition by BeStSel analysis server, which shows an overall similar distribution with small differences in α-helical content estimation, which could be due to different post-translational modifications between plant and mammalian cells (Fig 2B).

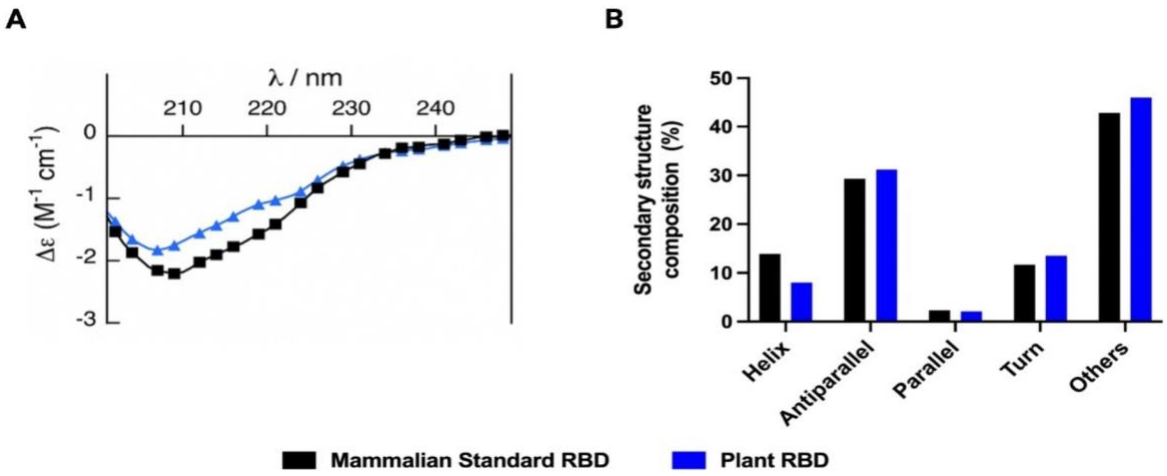

Figure 8.2 Biochemical evaluation of plant-expressed RBD by circular dichroism (CD).
A) Spectral profiles of mammalian standard (black) and plant (blue) expressed RBD in PBS buffer pH 7.4 at 37˚C (200–250 nm). Data expressed in molar circular dichroism (Δε) calculated from averaging 5 independent spectra of each sample. B) Secondary structure content in percentage calculated for mammalian and plant-derived RBD in PBS buffer pH 7.4 at 37˚C (200–250 nm). Content was calculated using BeStSel analysis server by direct analysis of the raw data (mDeg) from the CD system. Molecular weights for both proteins were considered as 35 kDa.

To evaluate plant-expressed RBD receptor binding kinetics, we first examined its interaction with ACE2. Fig 3 summarizes the three types of ELISA-based assays that were conducted for the functional assessment of the RBD antigens. For this purpose, binding kinetics between soluble and serially titrated ACE2 protein and immobilized plant- and mammalian-RBD were evaluated by indirect enzyme-linked immunosorbent assay (ELISA) (Fig 3A). We found that plant-expressed RBD readily binds to ACE2 with high affinity (K_D = 8.21 nM, R^2 = 0.993), and at a comparable level to RBD expressed in mammalian 293F cells (K_D = 6.90 nM, R^2 = 0.981) (Fig 4A).

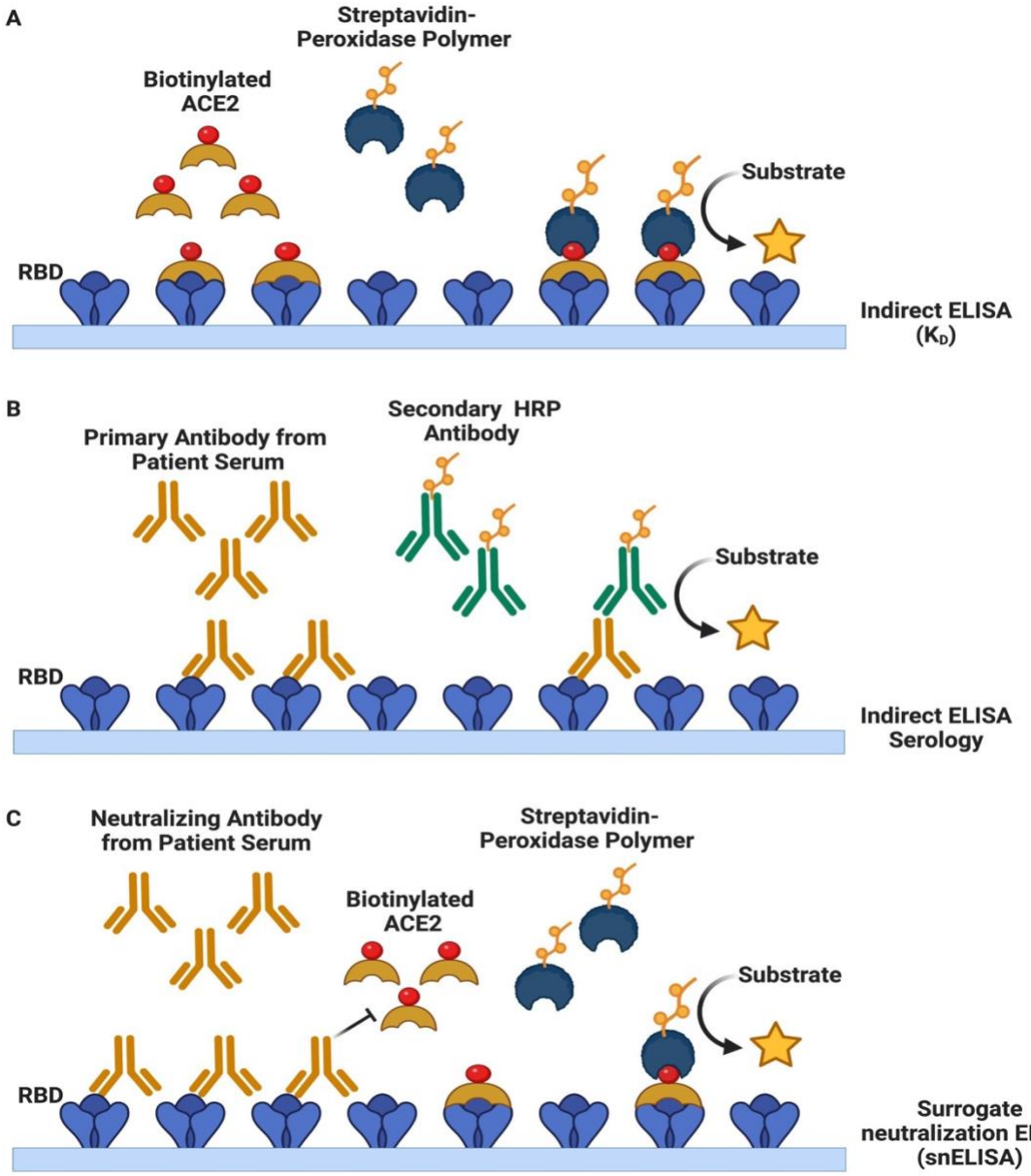

Figure 8.3 Schematic representations of the different types of ELISA used to characterize plant-expressed RBD.

(A) Indirect ELISA (Kd) set up for the evaluation of binding kinetics of soluble human ACE2 to immobilized RBD. (B) Indirect ELISA (serology) set up for the evaluation of binding and recognition of commercial monoclonal and serum IgG, IgM and IgA antibodies to immobilized RBD. (C) Surrogate neutralization ELISA (snELISA) set up to evaluate relative inhibition of anti-SARS-CoV-2 neutralizing antibodies in blocking immobilized RBD from binding soluble ACE2.

Similar binding kinetics have been reported by other studies, however the slightly lower value of the plant derived equilibrium dissociation constant (K_D) could be attributed to minor differences in glycosylation and other post-translational modifications as a result of the different expression platforms [27–30].

Next, we examined whether plant-expressed RBD was recognized by sera from COVID-19 convalescent, partially and fully vaccinated individuals. To this effect, human sera was added to immobilized plant RBD and we probed for the binding of three classes of antibodies (IgG, IgM, and IgA) by ELISA (Figs 3B and 4B). Here, we show that plant RBD was readily detected by IgM, IgA, and IgG antibodies from naturally infected convalescent, vaccinated or convalescent and vaccinated individuals (Fig 4B). We reveal detection and high titers of IgG antibodies comparable to the mammalian-expressed RBD across all samples tested. We also report that IgM and IgA immunoreactivity to plant-expressed RBD was comparable but slightly less efficient in comparison to mammalian-derived RBD. Non-specific binding of antibodies to antigen-naïve individuals was minimal for both RBD antigens tested (Fig 4B). In contrast to previously published results [31, 32], our plant-expressed RBD was bound by conformationdependent monoclonal IgM, IgA, and IgG CR3022 antibodies (Fig 4C). This constitutes a further indirect indication that the plant RBD antigen is folded similarly to the mammalian counterpart and exposes the conformational epitope for this antibody. While we note comparable half-maximal inhibitory dilution (ID_{50}) values for IgG CR3022 (plant $ID_{50} = 1.8x10^{-5}$, mammalian $ID_{50} = 1.2x10^{-5}$), we did observe slightly reduced binding of the IgA CR3022 antibody to plant-derived RBD ($6.9x10^{-5}$) compared to mammalian-expressed RBD ($3.4x10^{-5}$), respectively (Fig 4C and 4D). Post-translational modifications such as glycosylation may also explain these small differences in IgA and IgM binding [27], although we also cannot exclude the possibility of minor unfavourable folding motifs that could contribute to these observations.

Lastly, we investigated the relative efficacy of human serum neutralizing antibodies in blocking the immobilized plant RBD's interaction with soluble ACE2 by surrogate neutralization ELISA (snELISA) (Fig 3C) [20, 33]. As mentioned previously, most neutralizing antibodies produced by natural infection or vaccine immunity are directed to the RBD of the spike protein [3–5]. Neutralization of plant RBD-ACE2 interactions by human serum antibodies is therefore an additional indicator of adequate and functional protein folding and of neutralizing epitope

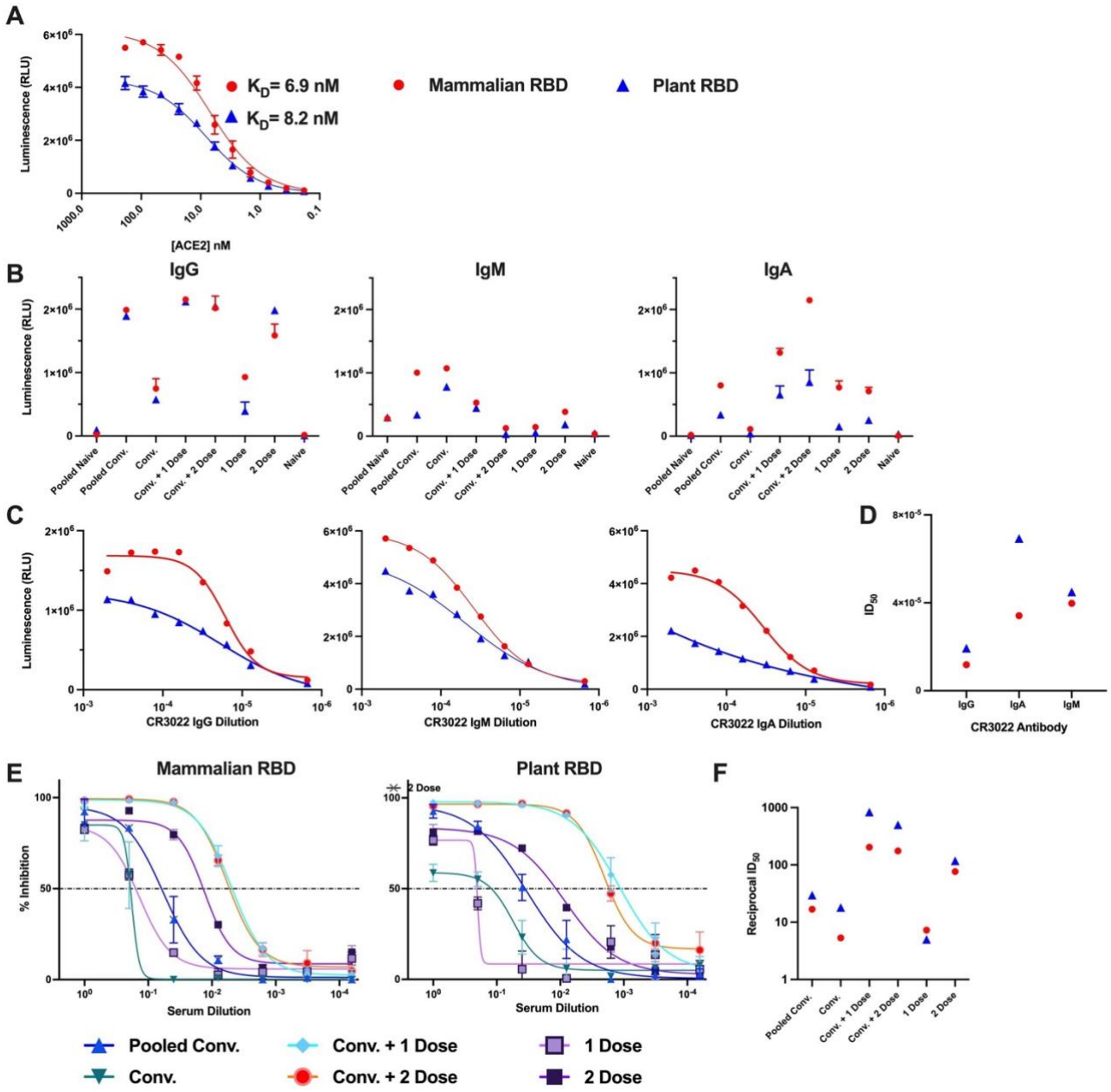

Figure 8.4 Evaluation of plant-expressed RBD protein functionality, folding and binding kinetics.

A comprehensive assessment of protein function of the RBD produced in *N. benthamiana* as it pertains to protein folding and binding to ACE2 receptor, recognition and neutralization by antibodies in sera from SARS-CoV-2 exposed individuals. (A) Indirect ELISA demonstrating binding kinetics of soluble human ACE2 to immobilized mammalian RBD (red circle) and plant RBD (blue triangle). (B) Binding and recognition of immobilized mammalian and plant produced RBD by IgG, IgM and IgA polyclonal antibodies in sera of pooled naïve (unvaccinated, uninfected individuals; n>100), pooled convalescent (pooled Conv.) (n>100), convalescent and vaccinated with one dose (Conv. + 1 dose), convalescent and vaccinated with two doses (Conv. + 2 dose), vaccinated with one dose (1 dose), vaccinated with 2 doses (2 doses) of Pfizer (BNT162b2) and naïve (PCR negative confirmed). Pooled sera are samples pooled from a surveillance study of 100 individuals with (pooled convalescent) or without (pooled naïve) prior SARS-CoV-2 infection. While the rest of the samples were collected from single individuals from each category described above. (C) Binding and recognition of immobilized mammalian and plant produced RBD by conformation dependant monoclonal IgG, IgM, and IgA CR3022 antibodies and (D) their half-maximal inhibitory dilution (ID_{50}) values. (E) Relative inhibition percentage of anti-SARS-CoV-2 neutralizing antibodies in blocking immobilized mammalian and plant produced RBD from binding to soluble ACE2 by snELISA. This assay is representative of technical triplicates

or quadruplicates and presented as mean ± standard deviation. (F) Reciprocal ID_{50} values from (E) for mammalian- and plant-expressed RBD.

accessibility on plant RBD. Serum was added to immobilized plant-expressed RBD and then binding to soluble biotinylated ACE2 receptor was evaluated (Fig 4E). We then measured the inhibition of the binding as a function of the serum dilution. Our observations indicate that human antibodies were able to bind plant-expressed RBD and neutralize its binding to the ACE2 receptor with similar kinetics to the mammalian-expressed RBD (Fig 4F). In fact, we observed generally greater ID_{50} values for the plant-expressed RBD, thereby indicating that its interactions with the ACE2 receptor were more efficiently disrupted by neutralizing antibodies.

8.5 Discussion

We have demonstrated that plant-expressed RBD retains folding and functionality comparable to mammalian produced RBD as evaluated by CD analysis, binding to host cell receptor ACE2, recognition by the conformation-dependant monoclonal CR3022 antibody directed to RBD, and binding of polyclonal antibodies from sera of SARS-CoV-2-infected and vaccinated individuals. Although we did note a reduced ability of human IgM and IgA antibodies to bind plant-expressed RBD as compared to mammalian-expressed RBD, similar binding of IgG, which have high affinity to the target antigen, was observed. Additionally, binding of plant-expressed RBD to the ACE2 receptor was efficiently neutralized by antibodies from sera of convalescent, partially and fully vaccinated individuals. Collectively, these findings demonstrate that recombinant RBD produced in *N. benthamiana* exhibits suitable biochemical, structural, and antigenic features for testing as antigen in a subunit vaccine platform.

There are many advantages in developing a plant-based platform for viral antigen production, one of which is its flexibility to rapidly pivot to express antigens for emerging SARSCoV-2 variants of concern. In six weeks, it is possible to produce the purified RBD of a new variant from an expression plasmid. The amount produced is directly linked to the number of plants grown, which can be cost-effectively scaled up to meet any laboratory requirements; growing of *N. benthamiana* does not require sophisticated or costly installations, making this technology broadly accessible worldwide. SARS-CoV-2 antigens are required in serological assays to measure antibodies in blood raised against the virus from exposure or induced by vaccines. Viral RBD and Spike proteins

are also an integral part of ELISA-based antibody neutralization assays, as the one used in this study [20]. These types of assays are critical for measuring the potential of new variants of concern to evade vaccine immunity. Furthermore, purification yields of this RBD antigen could conceivably be doubled simply by changing the tagging system, i.e. switching out of the standard 8xhistidine tag for a FLAG-tag, a phenomenon observed in a comparative study [24]. Such a modification may also negate the cost-effectiveness of the procedure proposed in our study, however, and so further analysis is required. The expression system used to drive recombinant protein production also has a dramatic effect on purification yield, as demonstrated by the use of the potato virus X-based pEff vector [34]. Incorporating this vector into our protocol in the future could easily fast-track the scaling-up process.

As variants continue to emerge, the viral targets of vaccines and vaccination technology also need to evolve to match the pathogen's evolutionary pace. Vaccines targeting the Spike or RBD of several variants, called multivalent vaccines, will be important to help immune responses focus on specific mutations [35, 36]. Different vaccine technologies will also have a major role to play to diversify cellular and humoral immune responses to help combat disease severity and transmission. For instance, new vaccines based on different technologies to the original mRNA and adenovirus-based vaccines are now entering and emerging from clinical trials. Protein subunit, viral vector and virus-like particle (VLP) vaccines are but a few, including a new plant-based adjuvanted VLP vaccine by Medicago [37–39]. Delivery methods such as oral and intranasal vaccine technologies that stimulate mucosal immunity specialized in reducing transmissions will also become critical for moving out of the acute stage of this pandemic [40, 41]. As customizing vaccines to new variants will be critical in keeping SARS-CoV-2 infections and transmissions in check, so will be the rapid biomanufacturing of viral antigens that are critical components for some of these vaccine technologies.

The data presented in this study therefore sets the stage for further investigating the use of cost-effective and massively scalable plant-based viral antigen in protein subunit vaccines given its comparable properties to its animal cell-expressed counterpart. Such protein antigens have already shown great promise in various research studies and clinical trials [9, 10, 42].

Limitations of the study

The degree to which the native glycosylation profile of viral antigen is reconstituted is an important consideration to the selection of an expression system, and the expression of a heterologous (glyco)protein in a plant-based platform will yield a glycosylation profile that is distinct from that of mammalian systems [43]. Plants and animals differ in terms of both *N*- and *O*-linked glycosylation, with plants producing highly specific glycans that are absent in other eukaryotes (for example, β(1,2)-xylose and α(1,3)-fucose), and lacking others such as sialic acid [44]. Moreover, there is increasing evidence that heterologous glycoproteins may be under-glycosylated (i.e., display reduced glycan occupancy) when expressed in plants [45]. Importantly, plant-manufactured VLP-based vaccines against both influenza and SARS-CoV2 have been demonstrated to be safe and effective in humans, despite containing plant-specific glycan structures [39, 46, 47] and ongoing initiatives to humanize the glycosylation systems of plants offer great potential [48]. In this study, it is also worth noting that the RBD of the SARS-CoV-2 Spike protein is not subject to extensive post-translational modifications and glycosylation, particularly in comparison to other heavily decorated viral proteins that are more challenging to produce in plants. Ultimately, it is yet unknown whether different glycosylation patterns are a caveat to producing our plant-derived antigen for diagnostics and subunit vaccines. Currently ongoing studies in animals will reveal the potential and efficacy of plantexpressed antigen as a subunit vaccine for SARS-CoV-2.

Supporting information

S1 Fig.

S1 Data.

S1 Raw images.

Acknowledgments

We are grateful for helpful discussions and advice from Rima Menassa and colleagues at Agriculture and Agri-Food Canada, London Research and Development Centre, Canada, Emmanuel Margolin, Edward Rybicki and colleagues from Biopharming Research Unit,

University of Cape Town, South Africa, and Dominique Michaud, Universite´ Laval, Canada. We gratefully acknowledge the excellent support of Michelle Brazeau, University of Ottawa, in her management of our greenhouse.

Author Contributions

Conceptualization: Marc-André Langlois, Allyson M. MacLean. **Funding acquisition:** Marc-André Langlois, Allyson M. MacLean. **Investigation:** Jordan Demone, Mariam Maltseva, Maryam Nourimand, Mina Nasr-Sharif, Yannick Galipeau, Emilio I. Alarcon. **Methodology:** Allyson M. MacLean. **Resources:** Marc-André Langlois, Allyson M. MacLean. **Supervision:** Marc-Andre´ Langlois, Allyson M. MacLean. **Validation:** Jordan Demone, Mariam Maltseva, Maryam Nourimand, Emilio I. Alarcon, Marc-André Langlois. **Writing – original draft:** Jordan Demone, Mariam Maltseva, Maryam Nourimand, Marc-André Langlois, Allyson M. MacLean. **Writing – review & editing:** Mariam Maltseva, Emilio I. Alarcon, Marc-André Langlois, Allyson M. MacLean.

8.6 References

1. Bally J, Jung H, Mortimer C, Naim F, Philips JG, Hellens R, et al. The rise and rise of Nicotiana benthamiana: A plant for all reasons. Annual Review of Phytopathology 2018. https://doi.org/10.1146/annurev-phyto-080417-050141 PMID: 30149789
2. Hoffmann M, Kleine-Weber H, Schroeder S, Kru¨ger N, Herrler T, Erichsen S, et al. SARS-CoV-2 Cell Entry Depends on ACE2 and TMPRSS2 and Is Blocked by a Clinically Proven Protease Inhibitor. Cell 2020; 181. https://doi.org/10.1016/j.cell.2020.02.052 PMID: 32142651
3. Piccoli L, Park YJ, Tortorici MA, Czudnochowski N, Walls AC, Beltramello M, et al. Mapping Neutralizing and Immunodominant Sites on the SARS-CoV-2 Spike Receptor-Binding Domain by Structure-Guided High-Resolution Serology. Cell 2020. https://doi.org/10.1016/j.cell.2020.09.037 PMID: 32991844
4. Yang J, Wang W, Chen Z, Lu S, Yang F, Bi Z, et al. A vaccine targeting the RBD of the S protein of SARS-CoV-2 induces protective immunity. Nature 2020. https://doi.org/10.1038/s41586-020-2599-8 PMID: 32726802
5. Garcia-Beltran WF, Lam EC, Astudillo MG, Yang D, Miller TE, Feldman J, et al. COVID-19-neutralizing antibodies predict disease severity and survival. Cell 2021. https://doi.org/10.1016/j.cell.2020.12.015 PMID: 33412089
6. Rattanapisit K, Shanmugaraj B, Manopwisedjaroen S, Purwono PB, Siriwattananon K, Khorattanakulchai N, et al. Rapid production of SARS-CoV-2 receptor binding domain (RBD) and spike specific monoclonal antibody CR3022 in Nicotiana benthamiana. Scientific Reports 2020. https://doi.org/10.1038/s41598-020-74904-1 PMID: 33077899
7. Royal JM, Simpson CA, McCormick AA, Phillips A, Hume S, Morton J, et al. Development of a SARSCoV-2 vaccine candidate using plant-based manufacturing and a tobacco mosaic virus-like nano-particle. Vaccines (Basel) 2021; 9(11):1347. https://doi.org/10.3390/vaccines9111347 PMID: 34835278
8. Siriwattananon K, Manopwisedjaroen S, Shanmugaraj B, Rattanapisit K, Phumiamorn S, Sapsutthipas S, et al. Plant-produced receptor-binding domain of SARS-CoV-2 elicits potent neutralizing responses in mice and non-human primates. Frontiers in Plant Science 2021; 12. https://doi.org/10.3389/fpls.2021.682953 PMID: 34054909
9. Akache B, Renner TM, Tran A, Deschatelets L, Dudani R, Harrison BA, et al. Immunogenic and efficacious SARS-CoV-2 vaccine based on resistin-trimerized spike antigen SmT1 and SLA archaeosome adjuvant. Scientific Reports 2021; 11. https://doi.org/10.1038/s41598-021-01363-7 PMID: 34750472
10. Tabynov K, Turebekov N, Babayeva M, Fomin G, Yerubayev T, Yespolov T, et al. An adjuvanted subunit SARS-CoV-2 spike protein vaccine provides protection against Covid-19 infection and transmission. Npj Vaccines 2022; 7. https://doi.org/10.1038/s41541-022-00450-8 PMID: 35197485
11. Wu Y, Huang X, Yuan L, Wang S, Zhang Y, Xiong H, et al. A recombinant spike protein subunit vaccine confers protective immunity against SARS-CoV-2 infection and transmission in hamsters. Science Translational Medicine 2021; 13. https://doi.org/10.1126/scitranslmed.abg1143 PMID: 34285130
12. Mao T, Goldman-Israelow B, Suberi A, Zhou L, Reschke M, Pena-hernandez M, et al. Unadjuvanted intranasal spike vaccine booster elicits robust protective mucosal immunity against sarbecoviruses. BioRxiv 2022. https://doi.org/10.1101/2022.01.24.477597 PMID: 35118464
13. Alu A, Chen L, Lei H, Wei Y, Tian X, Wei X. Intranasal COVID-19 vaccines: From bench to bed. EBioMedicine 2022; 76. https://doi.org/10.1016/j.ebiom.2022.103841 PMID: 35085851

14. di Pasquale A, Preiss S, da Silva FT, Garc¸on N. Vaccine adjuvants: From 1920 to 2015 and beyond. Vaccines (Basel) 2015; 3. https://doi.org/10.3390/vaccines3020320 PMID: 26343190
15. Wang SH, Smith D, Cao Z, Chen J, Acosta H, Chichester JA, et al. Recombinant H5 hemagglutinin adjuvanted with nanoemulsion protects ferrets against pathogenic avian influenza virus challenge. Vaccine 2019; 37. https://doi.org/10.1016/j.vaccine.2019.02.002 PMID: 30795941
16. Smith D, Streatfield SJ, Acosta H, Ganesan S, Fattom A. A nanoemulsion-adjuvanted intranasal H5N1 influenza vaccine protects ferrets against homologous and heterologous H5N1 lethal challenge. Vaccine 2019; 37. https://doi.org/10.1016/j.vaccine.2019.08.071 PMID: 31495593
17. Yao J, Weng Y, Dickey A, Wang KY. Plants as factories for human pharmaceuticals: Applications and challenges. International Journal of Molecular Sciences 2015; 16. https://doi.org/10.3390/ ijms161226122 PMID: 26633378
18. Peyret H, Brown JKM, Lomonossoff GP. Improving plant transient expression through the rational design of synthetic 5^0 and 3^0 untranslated regions. Plant Methods 2019. https://doi.org/10.1186/s13007019-0494-9 PMID: 31548848
19. Micsonai A, Wien F, Kernya L, Lee YH, Goto Y, Re´fre´giers M, et al. Accurate secondary structure prediction and fold recognition for circular dichroism spectroscopy. Proc Natl Acad Sci U S A 2015; 112. https://doi.org/10.1073/pnas.1500851112 PMID: 26038575
20. Abe KT, Li Z, Samson R, Samavarchi-Tehrani P, Valcourt EJ, Wood H, et al. A simple protein-based surrogate neutralization assay for SARS-CoV-2. JCI Insight 2020; 5. https://doi.org/10.1172/jci.insight.142362 PMID: 32870820
21. Colwill K, Galipeau Y, Stuible M, Gervais C, Arnold C, Rathod B, et al. A scalable serology solution for profiling humoral immune responses to SARS-CoV-2 infection and vaccination. Clinical and Translational Immunology 2022; 11. https://doi.org/10.1002/cti2.1380 PMID: 35356067
22. Margolin E.; Verbeek M.; Meyers A.; Chapman R.; Williamson A.L.; Rybicki EP. Calreticulin co-expression supports high level production of a recombinant SARS-CoV-2 spike mimetic in Nicotiana benthamiana. BioRxiv 2020. https://doi.org/10.1101/2020.06.14.150458
23. Zhou D, Tian X, Qi R, Peng C, Zhang W. Identification of 22 N-glycosites on spike glycoprotein of SARS-CoV-2 and accessible surface glycopeptide motifs: Implications for vaccination and antibody therapeutics. Glycobiology 2021; 31. https://doi.org/10.1093/glycob/cwaa052 PMID: 32518941
24. Mamedov T, Yuksel D, Ilgın M, Gu¨rbu¨zaslan I, Gulec B, Mammadova G, et al. Production and characterization of nucleocapsid and RBD cocktail antigens of SARS-CoV-2 in Nicotiana benthamiana plant as a vaccine candidate against COVID-19. Vaccines (Basel). 2021; 9(11). Epub 2021/11/28. https://doi. org/10.3390/vaccines9111337 PMID: 34835268
25. Maffei M, Montemiglio LC, Vitagliano G, Fedele L, Sellathurai S, Bucci F, et al. The nuts and bolts of SARS-CoV-2 spike receptor-binding domain heterologous expression. Biomolecules 2021; 11. https://doi.org/10.3390/biom11121812 PMID: 34944456
26. Consortium AA. Structural and functional comparison of SARS-CoV-2-spike receptor binding domain produced in Pichia pastoris and mammalian cells. Sci Rep 2020; 10. https://doi.org/10.1038/s41598020-78711-6 PMID: 33311634
27. Gong Y, Qin S, Dai L, Tian Z. The glycosylation in SARS-CoV-2 and its receptor ACE2. Signal Transduction and Targeted Therapy 2021; 6. https://doi.org/10.1038/s41392-021-00809-8 PMID: 34782609
28. Lan J, Ge J, Yu J, Shan S, Zhou H, Fan S, et al. Structure of the SARS-CoV-2 spike receptor-binding domain bound to the ACE2 receptor. Nature 2020; 581. https://doi.org/10.1038/s41586-020-2180-5 PMID: 32225176

29. Tian X, Li C, Huang A, Xia S, Lu S, Shi Z, et al. Potent binding of 2019 novel coronavirus spike protein by a SARS coronavirus-specific human monoclonal antibody. Emerging Microbes and Infections 2020; 9. https://doi.org/10.1080/22221751.2020.1729069 PMID: 32065055
30. Walls AC, Park YJ, Tortorici MA, Wall A, McGuire AT, Veesler D. Structure, Function, and Antigenicity of the SARS-CoV-2 Spike Glycoprotein. Cell 2020. https://doi.org/10.1016/j.cell.2020.02.058 PMID: 32155444
31. Shin Y-J, Ko¨nig-Beihammer J, Vavra U, Schwestka J, Kienzl NF, Klausberger M, et al. N-Glycosylation of the SARS-CoV-2 Receptor Binding Domain Is Important for Functional Expression in Plants. Frontiers in Plant Science 2021; 12. https://doi.org/10.3389/fpls.2021.689104 PMID: 34211491
32. Klausberger M, Duerkop M, Haslacher H, Wozniak-Knopp G, Cserjan-Puschmann M, Perkmann T, et al. A comprehensive antigen production and characterisation study for easy-to-implement, specific and quantitative SARS-CoV-2 serotests. EBioMedicine 2021; 67. https://doi.org/10.1016/j.ebiom.2021.103348 PMID: 33906067
33. Anderson DE, Tan CW, Chia WN, Young BE, Linster M, Low JGH, et al. Lack of cross-neutralization by SARS patient sera towards SARS-CoV-2. Emerging Microbes and Infections 2020; 9. https://doi.org/10.1080/22221751.2020.1761267 PMID: 32380903
34. Mardanova ES, Kotlyarov RY, Ravin NV. High-yield production of receptor binding domain of SARSCoV-2 linked to bacterial flagellin in plants using self-replicating viral vector pEff. Plants (Basel) 2021;
10(12). Epub 2021/12/29. https://doi.org/10.3390/plants10122682 PMID: 34961153
35. Callaway E, Ledford H. How to redesign COVID vaccines so they protect against variants. Nature 2021; 590. https://doi.org/10.1038/d41586-021-00241-6 PMID: 33514888
36. Stokel-Walker C. How are vaccines being adapted to meet the changing face of SARS-CoV-2? BMJ 2022; 377:o1257. https://doi.org/10.1136/bmj.o1257 PMID: 35649582
37. Dunkle LM, Kotloff KL, Gay CL, A´ ñez G, Adelglass JM, Barrat Herna´ndez AQ, et al. Efficacy and Safety of NVX-CoV2373 in Adults in the United States and Mexico. New England Journal of Medicine 2022;
386. https://doi.org/10.1056/NEJMoa2116185 PMID: 34910859
38. Afkhami S, D'Agostino MR, Zhang A, Stacey HD, Marzok A, Kang A, et al. Respiratory mucosal delivery of next-generation COVID-19 vaccine provides robust protection against both ancestral and variant strains of SARS-CoV-2. Cell 2022; 185. https://doi.org/10.1016/j.cell.2022.02.005 PMID: 35180381
39. Hager KJ, et al. Efficacy and Safety of a Recombinant Plant-Based Adjuvanted Covid-19 Vaccine. The New England Journal of Medicine 2022; 386:2084–96. https://doi.org/10.1056/NEJMoa2201300 PMID: 35507508
40. Mouro V, Fischer A. Dealing with a mucosal viral pandemic: lessons from COVID-19 vaccines. Mucosal Immunology 2022; 15:584–94. https://doi.org/10.1038/s41385-022-00517-8 PMID: 35505121
41. Lavelle EC, Ward RW. Mucosal vaccines—fortifying the frontiers. Nature Reviews Immunology 2022; 22. https://doi.org/10.1038/s41577-021-00583-2 PMID: 34312520
42. Zhang R, Li D, Xu K, Yang C, Luo T, Zhao X, et al. A protein subunit vaccine booster following two doses of inactivated SARS-CoV-2 vaccine provides high neutralisation of SARS-CoV-2 and its variants in mice. The Lancet Microbe 2022; 3. https://doi.org/10.1016/S2666-5247(21)00331-1 PMID: 34977828
43. Margolin E, Crispin M, Meyers A, Chapman R, Rybicki EP. A roadmap for the molecular farming of viral glycoprotein vaccines: engineering glycosylation and glycosylation-directed folding. Frontiers in Plant Science 2020. https://doi.org/10.3389/fpls.2020.609207 PMID: 33343609

44. Margolin E, Chapman R, Williamson AL, Rybicki EP, Meyers AE. Production of complex viral glycoproteins in plants as vaccine immunogens. Plant Biotechnology Journal 2018. https://doi.org/10.1111/pbi. 12963 PMID: 29890031
45. Margolin E, Allen JD, Verbeek M, van Diepen M, Ximba P, Chapman R, et al. Site-Specific Glycosylation of Recombinant Viral Glycoproteins Produced in Nicotiana benthamiana. Frontiers in Plant Science
2021; 12. https://doi.org/10.3389/fpls.2021.709344 PMID: 34367227
46. Ward BJ, Makarkov A, Se´guin A, Pillet S, Tre´panier S, Dhaliwall J, et al. Efficacy, immunogenicity, and safety of a plant-derived, quadrivalent, virus-like particle influenza vaccine in adults (18–64 years) and older adults (65 years): two multicentre, randomised phase 3 trials. The Lancet 2020. https://doi.org/10.1016/S0140-6736(20)32014-6
47. Ward BJ, Landry N, Tre´panier S, Mercier G, Dargis M, Couture M, et al. Human antibody response to N-glycans present on plant-made influenza virus-like particle (VLP) vaccines. Vaccine 2014; 32. https://doi.org/10.1016/j.vaccine.2014.08.079 PMID: 25240757
48. Jansing J, Sack M, Augustine SM, Fischer R, Bortesi L. CRISPR/Cas9-mediated knockout of six glycosyltransferase genes in Nicotiana benthamiana for the production of recombinant proteins lacking β1,2-xylose and core α-1,3-fucose. Plant Biotechnology Journal 2019. https://doi.org/10.1111/pbi.12981 PMID: 29969180

9 Conclusion

The impact of respiratory viruses on public health and economies demand innovative strategies in disease prevention and control, with vaccine development relying on a thorough understanding of pathogen phenotypes, infection dynamics, and pathogenesis. This dissertation explores the challenges posed by circulating and emerging respiratory viruses through the development of rapid diagnostic tools, characterization of virus-host interactions, and evaluation of next-generation vaccine strategies. These strategies include optimal antigen selection, routes of administration, and the role of mucosal immunity in reducing infection and transmission. The goal of this work is to provide insights that guide the design of vaccines capable of mitigating SARS-CoV-2 transmission and strengthening preparedness for future pandemics.

9.1 Leveraging Flow Virometry for Rapid Virus Detection and Characterization

FVM has emerged as a versatile analytical tool for characterizing viruses at the single-particle level, offering detailed insights beyond what traditional bulk analysis techniques can provide. Its ability to analyze viral particles individually, along with the potential to sort infectious viral particles for downstream analysis, allows researchers to study viral heterogeneity—including differences in glycoprotein expression, maturation stages, and interactions with host proteins (14, 22-31). FVM's application has recently expanded into vaccine development and manufacturing as a rapid, high-throughput tool for evaluating viral vector-based vaccine candidates (19-21). These applications highlight FVM's value as an analytical tool capable of meeting the rapid characterization needs during emerging health crises.

A key challenge in effectively characterizing viral populations lies in accurately differentiating them from EVs and other background elements. Given that traditional flow cytometers were

originally designed to detect particles larger than 500 nm, making it difficult to analyze smaller particles, such as retroviruses, which often fall at or below the detection threshold. Even advanced cytometers struggle to reliably detect particles under 300 nm, as forward scatter alone is insufficient to differentiate viral particles from background noise and contaminants(32). The proximity in size range between viral particles and background noise complicates their differentiation, necessitating more sensitive and specific techniques for accurate viral characterization. Recent advancements, such as the Beckman Coulter CytoFLEX, offer hardware modifications tailored for nanoscale particle analysis, further improving detection capabilities (306). To further improve detection, viral structural components—such as capsid, matrix/tegument, or envelope glycoproteins—can be genetically modified with fluorescent tags to enhance discrimination (14, 22, 25, 26, 29, 30, 307). Alternatively, some groups directly target viral nucleic acids to resolve fluorescently labeled particles from background noise (29-31)

In **Chapter 2,** we delineated a workflow for instrument setup and calibration using reference materials to ensure effective detection and resolution of viruses at the single-particle level. This methodology optimized the sensitivity and standardization of FVM. By calibrating the flow cytometer, we accurately measured the concentration of intact viral particles, quantified the abundance of target antigens on the viral surface, and determined the relative diameter of the virus(33). We provided a comprehensive overview of procedures for staining, detecting, and quantifying viral and host-derived proteins on viral surfaces. These protocols outlined the essential steps for experimental design, with a focus on practical considerations for FVM, virus staining, and best practices for data reporting and instrument calibration.

9.2 Virus- Host Interactions

Employing the optimized techniques and instrument setup established in **Chapter 2**, we utilized FVM in **Chapter 3** to study the role of the accessory protein Glycogag of MLV**,** which plays a significant role in viral assembly and host modulation. GlycoGag is considered an accessory protein of MLV because, while not essential for viral replication *in vitro,* it enhances MLV replication and pathogenesis *in vivo*. Similar to HIV-1 accessory proteins, GlycoGag is believed to contribute to MLV pathogenesis and resistance to host restriction factors, facilitating efficient replication (92, 93, 96, 97, 117–120). Additionally, GlycoGag is thought to influence viral budding by directing virion assembly and release at lipid rafts, which are enriched in cholesterol and lipids (92, 93).

We hypothesized that GlycoGag modulates the incorporation of host proteins into the viral envelope during assembly and budding. Our FVM analysis revealed that glycoGag is associated with increased incorporation of host-derived tetraspanins CD81 and CD63, along with the lipid raft marker Thy1.2, during the assembly and release of viral particles from physiologically distinct cell types. Notably, we observed these differences in host protein uptake between MLV viruses with and without glycoGag, along with heterogeneity in host-derived antigen expression at the individual viral particle level. Certain cellular antigens were either enriched or excluded from the viral envelope depending on glycoGag expression, suggesting that glycoGag mediates the selective incorporation of host proteins into the viral envelope (34). Indeed, various cellular and viral factors influence the type and abundance of host proteins at the site of viral egress, and our results suggest that glycoGag plays a role in this selective host protein incorporation process.

Human sCoVs are major contributors to the common cold, generally causing mild upper respiratory tract infections but can lead to severe complications in vulnerable populations. Although the replication and pathogenesis of highly pathogenic coronaviruses, such as SARS-CoV-2, are well-studied, less is known about the replication kinetics of sCoVs in permissive cell lines and their effects on host cells. In **Chapter 4**, we identified permissive cell lines susceptible to OC43, 229E, and NL63 infection and characterized viral replication by tracking vRNA transcripts coding for N and SPG proteins. Human lung, colon cancer, and rhesus monkey kidney cell line such as MRC-5, HCT-8, and LLC-MK2, proved most suitable under our experimental conditions for assessing viral kinetics, cytopathic effects (CPE) and cell surface marker expression. Notably, not all permissive cell types showed CPE using standard characterization methods, consistent with previous studies (26, 30), while some displayed severe CPE, limiting our ability to perform flow cytometry. Viral spread and CPE are influenced by antiviral responses and intrinsic host factors. For instance, interferon production, restriction factors like tetherin and APOBEC can inhibit viral replication and release by disrupting key processes such as viral budding, egress, and genome stability (114, 308).

We also investigated the modulation of key cellular receptors following viral infection and observed significant modulation of viral entry receptors. Notably, we observed a significant downregulation, GD3 expression and CD13 expression after OC43 and 229E infection, respectively. This is similar to mechanisms seen in HIV, where CD4 downregulation in infected lymphocytes reduces co-infections or superinfections (28). Interestingly, ACE2 expression significantly increased after infection with NL63 and OC43. This upregulation could raise potential concerns about co-infections with other coronaviruses that also utilize the ACE2 receptor for viral entry. Though antiviral responses from the primary infection antiviral responses should

limit secondary infections, increased ACE2 expression may promote co-infection and raise the risk of recombination events, as observed with the emergence of the XBB variant of SARS-CoV-2, which arose from recombination between distinct Omicron variants (136, 164).

Given the potential of monoclonal anti-ACE2 antibody treatments and the varied efficacy of polyclonal antibodies and soluble ACE2 in reducing SARS-CoV-2 replication(104, 309, 310), we evaluated their effects on blocking NL63 infection. LLC-MK2 cells treated in a dose-dependent manner with soluble ACE2 and anti-ACE2 monoclonal antibodies showed a significant reduction in N and S viral RNA expression. In contrast, polyclonal anti-ACE2 antibodies did not significantly reduce infection. In **Chapter 4**, we provide insights into the infection kinetics of sCoVs in permissive cell models and reveal entry receptor modulation that may facilitate co-infections with multiple coronaviruses, while also presenting potential antiviral treatments for sCoV infections.

9.3 Next-generation vaccine development

The COVID-19 pandemic has highlighted the critical role that vaccines play in protecting global health and preventing the spread of infectious diseases. As the virus continues to evolve, the emergence of variants with immune-escape mutations poses ongoing challenges to the effectiveness of current vaccine strategies. The development of next-generation vaccines that can provide broad and durable protection against both current and future variants is essential to controlling the spread of SARS-CoV-2. Mucosal immunity, particularly through the actions of sIgA and tissue-resident memory cells, is a critical component of the immune system's defense against respiratory pathogens like SARS-CoV-2 and influenza. By targeting the mucosal immune system, these mucosal vaccines have the potential to reduce infection at the site of viral entry,

which could significantly reduce viral transmission and control outbreak. However, mucosal humoral and tissue-resident memory cells are typically induced by local antigen stimulation, further underscoring the importance of mucosal-targeted vaccines and treatments in enhancing protection against respiratory viruses (285, 294).

A key objective of my thesis is to elucidate immunogenic targets for intranasal vaccine design. By characterizing the associated humoral mucosal and systemic immune responses in distinct biological compartments. In **Chapter 5**, we demonstrated that an adjuvanted subunit vaccine platform induced robust mucosal and systemic total and neutralizing antibody responses against rapidly emerging SARS-CoV-2 variants (269). We conducted a direct comparison of the immunogenic profiles following intranasal administration of a protein subunit vaccine expressing either the full SARS-CoV-2 SPG or RBD, each adjuvanted with two different adjuvants. While the immunogenicity of these antigens has been extensively studied following intramuscular administration in preclinical models, their relative immunogenicity as intranasal vaccine candidates against emerging VOC remains unclear.

Adjuvants enhance immune responses by overcoming mucosal tolerance, which limits immune activation when antigens are administered alone [7, 37, 38]. Mucosal adjuvants must withstand low pH and mucociliary clearance while penetrating mucus layers to induce immunity [39, 40]. Currently, no mucosal adjuvants are approved for IN vaccines. We demonstrated robust IgG and IgA induction in plasma, nasal wash, and BALF in mice vaccinated with SPG or RBD adjuvanted with cholera toxin (CT) or AMVAD. Two doses of adjuvanted vaccines elicited stronger responses than protein or adjuvant alone. Our data suggest that combining antigens with CT or AMVAD enhances both mucosal and systemic neutralizing responses, with systemic neutralization capacity

equal to or greater than antibodies from SARS-CoV-2 infection or mRNA vaccination in humans, respectively. While CT elicited more potent responses, safety concerns such as neuroinflammation and Bell's palsy limit its use (311-313). In contrast, Patel et al. showed that AMVAD-adjuvanted ovalbumin induced strong mucosal and systemic IgA responses, suggesting it as a safer alternative (314, 315).

Notably, we highlighted the added benefit of additional epitopes from the full SPG protein, which enhanced immunogenicity at the respiratory mucosa and neutralizing activity against VOCs. While RBD immunization induced strong neutralizing antibodies against the ancestral and Delta variants, we observed reduced neutralization against the Omicron BA.1 variant, which harbors over 15 mutations within the RBD. This suggests that the induced antibodies likely targeted immunodominant epitopes that are more susceptible to antigenic drift (136, 137). The spike's superior immunogenicity likely stems from its larger, stabilized trimeric structure, which enhances B cell activation and IgA responses through repetitive antigen presentation (85,86). Furthermore, its broader T cell epitope repertoire also recruits more T follicular helper cells, boosting the humoral response, as shown by Tan et al. (200). **Chapter 5** provides valuable insights for selecting optimal immunogenic targets and adjuvants in the development of IN vaccines against current and future VOCs.

Despite progress in vaccine research, there remains limited understanding regarding the concentration, isotype distribution, and kinetics of antibodies generated at distinct mucosal sites following various vaccination regimens. While systemic neutralizing antibodies serve as established correlates of protective efficacy, the corresponding markers of mucosal immunity

against viral infection and transmission have yet to be fully elucidated (108, 109, 235). Identifying such correlates will be essential for evaluating the effectiveness of intranasal vaccines.

In **Chapter 6**, we investigated the impact of heterologous prime-boost regimens on humoral responses across different anatomical compartments, focusing on varying administration routes and variant-tailored vaccine formulations. We found that IM priming predominantly shaped systemic humoral responses, particularly through variant-specific neutralizing antibodies, while IN boost further refined them. We demonstrated that IN, but not IM, vaccination drive a predominantly IgA-favored response in nasal, BAL and intestinal biofluids. This observation aligns with recent studies evaluating heterologous prime-boost regimens *in vivo*, which highlight the potent induction of cellular and humoral responses in BAL fluid following IN or oral vaccination in mice with pre-existing immunity (233, 266, 268, 284, 316-319).

Interestingly, we observed IgG responses in the intestinal mucosa following both IM and IN immunization. Notably, residual SARS-CoV-2 antigens have also been detected in intestinal mucosa and stool samples, even after viral clearance from the URT (320-322). Thus, this potent induction of humoral responses in the intestinal lumen following IM vaccination with mRNA-LNP should be further evaluated and potentially leveraged to reduce viral replication of gastrointestinal viruses. Overall, our data revealed distinct IgG and IgA profiles across different biofluids, with a clear correlation between IgA levels in BAL and nasal biofluids in IN-vaccinated mice, demonstrating the compartmentalization of mucosal responses following IN vaccination as noted in studies assessing IgA correlations in serum and saliva (235, 323-325).

Recent studies have explored several prime-boost approaches, including different vaccine platforms and IN boosting strategies, in the context of pre-existing systemic immunity (233, 266,

268, 284, 316-319). However, a gap remains in understanding how intranasal boosting strategies tailored to circulating variants affect humoral responses in mice with pre-existing immunity induced by an antigenically distant strain. Importantly, our results highlight the value of incorporating distinct antigenic variants in the prime vaccine, as the bivalent prime significantly enhanced the breadth of total and neutralizing responses against circulating VOCs in serum.

While total and neutralizing responses after variant-tailored boosting are well-characterized in serum, our study provides new insights into IgA induction in BAL and nasal biofluids following heterologous boosting. Variant-specific IN vaccines induced distinct variant-specific IgA responses in nasal and BAL biofluid, with stronger correlation to neutralization in BAL compared to IgG. Furthermore, mice primed with the monovalent Wu-1 vaccine and boosted with BA4/5+Wu-1 showed reduced neutralization of BA4/5 and XBB1.5 compared to groups boosted with BA4/5 alone or primed bivalently. This suggests the BA4/5+Wu-1 boost elicited cross-reactive recall to shared epitopes rather than generating BA4/5-specific antibodies, indicating immune imprinting. This aligns with studies showing that variant-specific boosts mostly promote recall responses to the ancestral strain (165, 166, 326-332). Incorporating multivalent strains in priming vaccines, as proposed for universal vaccines, can leverage immune imprinting to shape a broadly reactive B cell repertoire, enhancing protection against current and future VOCs. With increasing recognition of long COVID, a condition characterized by health complications that can arise after the initial acute infection has cleared, effective prevention of recurrent respiratory infections is crucial(85, 86). Mucosal vaccination offers a strategic advantage by targeting the virus at its entry point, thereby reducing early viral replication and limiting transmission. By controlling infection at the respiratory mucosa, IN vaccines may help mitigate the risk of long COVID by minimizing prolonged viral presence, tissue damage, and persistent inflammation,

factors which may contribute to its development (85, 86). Furthermore, reducing community transmission can limit the emergence of new variants that may exacerbate long-term health impacts, underscoring the vital role of mucosal vaccines in both individual protection and public health. **Chapter 6** highlights how heterologous vaccination strategies affect immune responses across distinct mucosal compartments to induce protective immunity against respiratory viruses.

In addition to their immunological advantages, intranasal vaccines offer several practical benefits, including needle-free administration, which could improve vaccine uptake, particularly in populations with high levels of vaccine hesitancy or needle phobia. The potential for self-administration also reduces the burden on healthcare systems during mass vaccination campaigns and allows for more rapid and widespread deployment in the event of future pandemic. The development of novel vaccine platforms, such as cost-effective plant-based expression systems, is also likely to play a significant role in future vaccine strategies.

Despite their potential, mucosal vaccines face several challenges in development. One of the primary obstacles is ensuring that the vaccine antigens are delivered effectively to the appropriate mucosal sites and remain stable in the mucosal environment. The mucosa contains enzymes that can degrade vaccine antigens before they trigger an immune response, so optimizing the formulation and delivery method is crucial for the success of intranasal vaccine (239, 247-249). Another challenge is ensuring the safety of IN vaccines, particularly regarding the risk of vaccine components crossing the blood-brain barrier via the olfactory nerve (107, 247, 248, 311, 333). This concern is particularly relevant for live-attenuated or viral vector vaccines delivered intranasally.

Additionally, the durability of the mucosal immune responses elicited by IN vaccines remains an area of active research, with some studies suggesting that frequent booster doses may be necessary

to maintain optimal levels of mucosal immunity and to ensure long-term protection. In Canada, among the 10 authorized influenza vaccines for human use, FluMist, a live attenuated influenza vaccine (LAIV), is the only IN vaccine available and is recommended for individuals aged 2-17(334). This vaccine is attenuated to allow replication in the URT and combines HA and NA genes from the WHO-recommended strains with a cold-adapted viral backbone(335). In children, FluMist induces both systemic and mucosal immune responses, along with cross-reactive T cell responses, providing immunity for up to a year(336, 337). LAIVs have shown superior cross-protective immunity against heterosubtypic influenza strains compared to IM vaccines. Although effective in children, LAIV have generally shown comparable or lower efficacy to IM vaccines in adults, and during 2013 to 2016 seasons, their performance was notably inferior(338, 339). However, some studies on IN vaccines against influenza have demonstrated that mucosal vaccination, compared to the IM route, induces stronger cross-protective immunity against heterosubtypic influenza strains and promotes long-term immune responses (129, 274).

The suboptimal efficacy of LAIV is thought to result from challenges in viral production relating to antigenic drift and pre-existing immunity, especially in older individuals, who may clear the vaccine too quickly to mount a strong response. Similarly, the ongoing occurrence of SARS-CoV-2 breakthrough infections may be driven by 1) antigenically mismatched variants with immune escape mutations, 2) poor induction of mucosal immunity, and 3) the persisting influence of immune imprinting to the priming antigen. Immune imprinting, first observed with influenza, occurs when initial exposure to a virus—through infection or vaccination—shapes future immune responses to related variants. This phenomenon has now been noted in SARS-CoV-2 infections as well, where immune imprinting may limit the effectiveness of variant-specific booster(165, 166, 326-332).

Thus, both influenza and SARS-CoV-2 illustrate how repeated exposure to evolving viruses can lead to immune responses dominated by prior immunological memory, which may hinder the ability to generate variant-specific immunity against new strains. In **Chapter 7,** we review the mechanistic complexities of immune imprinting and its influence on *de novo* and recall immune responses against rapidly evolving respiratory viruses like influenza and coronaviruses. By examining the duality of immune imprinting, we assess its potential to both enhance and hinder protection, with a focus on host and viral factors. Lastly, we discuss how different vaccine platforms may shape immune imprinting and consider strategies to promote de novo variant-specific antibody responses.

Plant-based vaccines offer significant advantages, such as rapid scalability, low production costs, and the ability to produce glycosylated proteins that closely mimic native viral antigens produced in mammalian cells. In **Chapter 8**, we compared plant-produced antigens to their mammalian-produced counterparts using various *in vitro* ELISA-based kinetic assays. Notably, the plant-produced RBD was similarly recognized by commercial monoclonal antibodies and polyclonal antibodies from convalescent individuals, demonstrating that plant-based RBD retains key biochemical and antigenic properties essential for serological and neutralization assays, as well as for subunit vaccine platforms. These findings underscore the potential of plant-based platforms to produce high-quality antigens rapidly and cost-effectively, making them ideal for addressing emerging pathogens and responding swiftly to future pandemics. Plant-based vaccines, such as Medicago's COVID-19 vaccine and quadrivalent influenza vaccine, have shown promising efficacy and safety in clinical trials, highlighting the growing role of this technology in global vaccine production (220, 340). Leveraging plant-based vaccine systems can significantly improve access and strengthen our preparedness for future viral threats.

Final Remarks

The persistent impact of circulating and emerging respiratory viruses on global health, healthcare systems, and economies highlights the urgent need for innovative solutions. A comprehensive understanding of pathogen biology, infection dynamics, and pathogenesis is critical for designing effective vaccines. This PhD thesis addresses key areas including the development of rapid viral diagnostics, the characterization of virus-host interactions, and the exploration of next-generation vaccine strategies—such as optimized antigen selection, alternative delivery routes, and the crucial role of mucosal immunity in reducing viral infection and transmission. By integrating these elements, this work aims to guide the design of next-generation vaccines to halt the spread respiratory viruses such as SARS-CoV-2 and enhance preparedness for future pandemics.

References

1. Johnson NP, Mueller J. Updating the accounts: global mortality of the 1918-1920 "Spanish" influenza pandemic. Bull Hist Med. 2002;76(1):105-15.
2. WHO. Seasonsal Influenza. October 3rd, 2023.
3. Simonsen L, Spreeuwenberg P, Lustig R, Taylor RJ, Fleming DM, Kroneman M, et al. Global mortality estimates for the 2009 Influenza Pandemic from the GLaMOR project: a modeling study. PLoS Med. 2013;10(11):e1001558.
4. WHO. WHO COVID-19 Dashboard: Cumulatative confirmed case load of COVID-19 reported worldwide.
5. WHO. WHO COVID-19 Dashboard: Cumulatative number of COVID-19 deaths reported worldwide.
6. Cutler DM, Summers LH. The COVID-19 Pandemic and the $16 Trillion Virus. JAMA. 2020;324(15):1495-6.
7. Putri W, Muscatello DJ, Stockwell MS, Newall AT. Economic burden of seasonal influenza in the United States. Vaccine. 2018;36(27):3960-6.
8. Pollard AJ, Bijker EM. A guide to vaccinology: from basic principles to new developments. Nat Rev Immunol. 2021;21(2):83-100.
9. Watson OJ, Barnsley G, Toor J, Hogan AB, Winskill P, Ghani AC. Global impact of the first year of COVID-19 vaccination: a mathematical modelling study. Lancet Infect Dis. 2022;22(9):1293-302.
10. Mesle MMI, Brown J, Mook P, Katz MA, Hagan J, Pastore R, et al. Estimated number of lives directly saved by COVID-19 vaccination programmes in the WHO European Region from December, 2020, to March, 2023: a retrospective surveillance study. Lancet Respir Med. 2024;12(9):714-27.
11. Klasse PJ. Molecular determinants of the ratio of inert to infectious virus particles. Prog Mol Biol Transl Sci. 2015;129:285-326.
12. Ackermann HW. The first phage electron micrographs. Bacteriophage. 2011;1(4):225-7.
13. Doan M, Vorobjev I, Rees P, Filby A, Wolkenhauer O, Goldfeld AE, et al. Diagnostic Potential of Imaging Flow Cytometry. Trends Biotechnol. 2018;36(7):649-52.
14. Lippe R. Flow Virometry: a Powerful Tool To Functionally Characterize Viruses. J Virol. 2018;92(3).
15. Hercher M, Mueller W, Shapiro HM. Detection and discrimination of individual viruses by flow cytometry. J Histochem Cytochem. 1979;27(1):350-2.
16. Chen F, Lu JR, Binder BJ, Liu YC, Hodson RE. Application of digital image analysis and flow cytometry to enumerate marine viruses stained with SYBR gold. Appl Environ Microbiol. 2001;67(2):539-45.
17. Brussaard CP, Marie D, Bratbak G. Flow cytometric detection of viruses. J Virol Methods. 2000;85(1-2):175-82.
18. Nolte-'t Hoen E, Cremer T, Gallo RC, Margolis LB. Extracellular vesicles and viruses: Are they close relatives? Proc Natl Acad Sci U S A. 2016;113(33):9155-61.
19. Ricci G, Minsker K, Kapish A, Osborn J, Ha S, Davide J, et al. Flow virometry for process monitoring of live virus vaccines-lessons learned from ERVEBO. Sci Rep. 2021;11(1):7432.

20. Tang VA, Renner TM, Varette O, Le Boeuf F, Wang J, Diallo JS, et al. Single-particle characterization of oncolytic vaccinia virus by flow virometry. Vaccine. 2016;34(42):5082-9.
21. Prout A, Rustandi RR, Tubbs C, Winters MA, McKenna P, Vlasak J. Functional profiling of Covid 19 vaccine candidate by flow virometry. Vaccine. 2022;40(37):5529-36.
22. Renner TM, Tang VA, Burger D, Langlois MA. Intact Viral Particle Counts Measured by Flow Virometry Provide Insight into the Infectivity and Genome Packaging Efficiency of Moloney Murine Leukemia Virus. J Virol. 2020;94(2).
23. Burnie J, Guzzo C. The Incorporation of Host Proteins into the External HIV-1 Envelope. Viruses. 2019;11(1).
24. Zicari S, Arakelyan A, Fitzgerald W, Zaitseva E, Chernomordik LV, Margolis L, et al. Evaluation of the maturation of individual Dengue virions with flow virometry. Virology. 2016;488:20-7.
25. Gaudin R, Barteneva NS. Sorting of small infectious virus particles by flow virometry reveals distinct infectivity profiles. Nat Commun. 2015;6:6022.
26. Landowski M, Dabundo J, Liu Q, Nicola AV, Aguilar HC. Nipah virion entry kinetics, composition, and conformational changes determined by enzymatic virus-like particles and new flow virometry tools. J Virol. 2014;88(24):14197-206.
27. Arakelyan A, Fitzgerald W, Margolis L, Grivel JC. Nanoparticle-based flow virometry for the analysis of individual virions. J Clin Invest. 2013;123(9):3716-27.
28. Chaudhuri R, Lindwasser OW, Smith WJ, Hurley JH, Bonifacino JS. Downregulation of CD4 by human immunodeficiency virus type 1 Nef is dependent on clathrin and involves direct interaction of Nef with the AP2 clathrin adaptor. J Virol. 2007;81(8):3877-90.
29. Khadivjam B, El Bilali N, Lippe R. Analysis and Sorting of Individual HSV-1 Particles by Flow Virometry. Methods Mol Biol. 2020;2060:289-303.
30. El Bilali N, Duron J, Gingras D, Lippe R. Quantitative Evaluation of Protein Heterogeneity within Herpes Simplex Virus 1 Particles. J Virol. 2017;91(10).
31. Loret S, El Bilali N, Lippe R. Analysis of herpes simplex virus type I nuclear particles by flow cytometry. Cytometry A. 2012;81(11):950-9.
32. Bonar MM, Tilton JC. High sensitivity detection and sorting of infectious human immunodeficiency virus (HIV-1) particles by flow virometry. Virology. 2017;505:80-90.
33. Maltseva M, Langlois MA. Flow Virometry for Characterizing the Size, Concentration, and Surface Antigens of Viruses. Curr Protoc. 2022;2(2):e368.
34. Maltseva M, Langlois M-A. Influence of GlycoGag on the Incorporation of Host Membrane Proteins into the Envelope of the Moloney Murine Leukemia Virus. Frontiers in Virology. 2021;1:747253.
35. Renner TM, Belanger K, Goodwin LR, Campbell M, Langlois MA. Characterization of molecular attributes that influence LINE-1 restriction by all seven human APOBEC3 proteins. Virology. 2018;520:127-36.
36. Renner TM, Belanger K, Lam C, Gerpe MCR, McBane JE, Langlois MA. Full-Length Glycosylated Gag of Murine Leukemia Virus Can Associate with the Viral Envelope as a Type I Integral Membrane Protein. J Virol. 2018;92(6).
37. Tang VA, Renner TM, Fritzsche AK, Burger D, Langlois MA. Single-Particle Discrimination of Retroviruses from Extracellular Vesicles by Nanoscale Flow Cytometry. Sci Rep. 2017;7(1):17769.

38. Belanger K, Savoie M, Aydin H, Renner TM, Montazeri Z, Langlois MA. Deamination intensity profiling of human APOBEC3 protein activity along the near full-length genomes of HIV-1 and MoMLV by HyperHRM analysis. Virology. 2014;448:168-75.
39. Rein A. Murine leukemia viruses: objects and organisms. Adv Virol. 2011;2011:403419.
40. Opstelten DJ, Wallin M, Garoff H. Moloney murine leukemia virus envelope protein subunits, gp70 and Pr15E, form a stable disulfide-linked complex. J Virol. 1998;72(8):6537-45.
41. Kuznetsov YG, Low A, Fan H, McPherson A. Atomic force microscopy investigation of wild-type Moloney murine leukemia virus particles and virus particles lacking the envelope protein. Virology. 2004;323(2):189-96.
42. Stano A, Leaman DP, Kim AS, Zhang L, Autin L, Ingale J, et al. Dense Array of Spikes on HIV-1 Virion Particles. J Virol. 2017;91(14).
43. Zhu P, Liu J, Bess J, Jr., Chertova E, Lifson JD, Grise H, et al. Distribution and three-dimensional structure of AIDS virus envelope spikes. Nature. 2006;441(7095):847-52.
44. Butan C, Winkler DC, Heymann JB, Craven RC, Steven AC. RSV capsid polymorphism correlates with polymerization efficiency and envelope glycoprotein content: implications that nucleation controls morphogenesis. J Mol Biol. 2008;376(4):1168-81.
45. Tang VA, Fritzsche AK, Renner TM, Burger D, Lannigan JA, Brittain GC, et al. Engineered Retroviruses as Fluorescent Biological Reference Particles for Nanoscale Flow Cytometry. bioRxiv. 2019:614461.
46. Corman VM, Muth D, Niemeyer D, Drosten C. Hosts and Sources of Endemic Human Coronaviruses. Adv Virus Res. 2018;100:163-88.
47. Su S, Wong G, Shi W, Liu J, Lai ACK, Zhou J, et al. Epidemiology, Genetic Recombination, and Pathogenesis of Coronaviruses. Trends Microbiol. 2016;24(6):490-502.
48. Cui J, Li F, Shi ZL. Origin and evolution of pathogenic coronaviruses. Nat Rev Microbiol. 2019;17(3):181-92.
49. Ye ZW, Yuan S, Yuen KS, Fung SY, Chan CP, Jin DY. Zoonotic origins of human coronaviruses. Int J Biol Sci. 2020;16(10):1686-97.
50. Shah MM, Winn A, Dahl RM, Kniss KL, Silk BJ, Killerby ME. Seasonality of Common Human Coronaviruses, United States, 2014-2021(1). Emerg Infect Dis. 2022;28(10):1970-6.
51. Nickbakhsh S, Ho A, Marques DFP, McMenamin J, Gunson RN, Murcia PR. Epidemiology of Seasonal Coronaviruses: Establishing the Context for the Emergence of Coronavirus Disease 2019. J Infect Dis. 2020;222(1):17-25.
52. Saunders N, Fernandez I, Planchais C, Michel V, Rajah MM, Baquero Salazar E, et al. TMPRSS2 is a functional receptor for human coronavirus HKU1. Nature. 2023;624(7990):207-14.
53. Woo PC, Lau SK, Chu CM, Chan KH, Tsoi HW, Huang Y, et al. Characterization and complete genome sequence of a novel coronavirus, coronavirus HKU1, from patients with pneumonia. J Virol. 2005;79(2):884-95.
54. Skowronski DM, Astell C, Brunham RC, Low DE, Petric M, Roper RL, et al. Severe acute respiratory syndrome (SARS): a year in review. Annu Rev Med. 2005;56:357-81.
55. Menachery VD, Yount BL, Jr., Debbink K, Agnihothram S, Gralinski LE, Plante JA, et al. A SARS-like cluster of circulating bat coronaviruses shows potential for human emergence. Nat Med. 2015;21(12):1508-13.
56. Wang LF, Shi Z, Zhang S, Field H, Daszak P, Eaton BT. Review of bats and SARS. Emerg Infect Dis. 2006;12(12):1834-40.

57. Wang LF, Eaton BT. Bats, civets and the emergence of SARS. Curr Top Microbiol Immunol. 2007;315:325-44.
58. Zumla A, Hui DS, Perlman S. Middle East respiratory syndrome. Lancet. 2015;386(9997):995-1007.
59. Memish ZA, Perlman S, Van Kerkhove MD, Zumla A. Middle East respiratory syndrome. Lancet. 2020;395(10229):1063-77.
60. Kim KH, Tandi TE, Choi JW, Moon JM, Kim MS. Middle East respiratory syndrome coronavirus (MERS-CoV) outbreak in South Korea, 2015: epidemiology, characteristics and public health implications. J Hosp Infect. 2017;95(2):207-13.
61. WHO. Pathogens prioritization: a scientific framework for epidemic and pandemic research preparedness. 2024(R&D Blue Print (RDB)).
62. Zhu N, Zhang D, Wang W, Li X, Yang B, Song J, et al. A Novel Coronavirus from Patients with Pneumonia in China, 2019. N Engl J Med. 2020;382(8):727-33.
63. Zhou P, Yang XL, Wang XG, Hu B, Zhang L, Zhang W, et al. A pneumonia outbreak associated with a new coronavirus of probable bat origin. Nature. 2020;579(7798):270-3.
64. Holmes EC. The Emergence and Evolution of SARS-CoV-2. Annu Rev Virol. 2024.
65. Wang X, Allen S, Blake JF, Bowcut V, Briere DM, Calinisan A, et al. Identification of MRTX1133, a Noncovalent, Potent, and Selective KRAS(G12D) Inhibitor. J Med Chem. 2022;65(4):3123-33.
66. The Novel Coronavirus Pneumonia Emergency Response Epidemiology T. The Epidemiological Characteristics of an Outbreak of 2019 Novel Coronavirus Diseases (COVID-19) - China, 2020. China CDC Wkly. 2020;2(8):113-22.
67. Hoehl S, Rabenau H, Berger A, Kortenbusch M, Cinatl J, Bojkova D, et al. Evidence of SARS-CoV-2 Infection in Returning Travelers from Wuhan, China. N Engl J Med. 2020;382(13):1278-80.
68. Li Q, Guan X, Wu P, Wang X, Zhou L, Tong Y, et al. Early Transmission Dynamics in Wuhan, China, of Novel Coronavirus-Infected Pneumonia. N Engl J Med. 2020;382(13):1199-207.
69. Wang L, Didelot X, Yang J, Wong G, Shi Y, Liu W, et al. Inference of person-to-person transmission of COVID-19 reveals hidden super-spreading events during the early outbreak phase. Nat Commun. 2020;11(1):5006.
70. Riou J, Althaus CL. Pattern of early human-to-human transmission of Wuhan 2019 novel coronavirus (2019-nCoV), December 2019 to January 2020. Euro Surveill. 2020;25(4).
71. Kucharski AJ, Russell TW, Diamond C, Liu Y, Edmunds J, Funk S, et al. Early dynamics of transmission and control of COVID-19: a mathematical modelling study. Lancet Infect Dis. 2020;20(5):553-8.
72. Liu Y, Morgenstern C, Kelly J, Lowe R, Group CC-W, Jit M. The impact of non-pharmaceutical interventions on SARS-CoV-2 transmission across 130 countries and territories. BMC Med. 2021;19(1):40.
73. Sanche S, Lin YT, Xu C, Romero-Severson E, Hengartner N, Ke R. High Contagiousness and Rapid Spread of Severe Acute Respiratory Syndrome Coronavirus 2. Emerg Infect Dis. 2020;26(7):1470-7.
74. Killingley B, Mann AJ, Kalinova M, Boyers A, Goonawardane N, Zhou J, et al. Safety, tolerability and viral kinetics during SARS-CoV-2 human challenge in young adults. Nat Med. 2022;28(5):1031-41.

75. Wu Y, Kang L, Guo Z, Liu J, Liu M, Liang W. Incubation Period of COVID-19 Caused by Unique SARS-CoV-2 Strains: A Systematic Review and Meta-analysis. JAMA Netw Open. 2022;5(8):e2228008.
76. He X, Lau EHY, Wu P, Deng X, Wang J, Hao X, et al. Temporal dynamics in viral shedding and transmissibility of COVID-19. Nat Med. 2020;26(5):672-5.
77. Byambasuren O, Cardona M, Bell K, Clark J, McLaws ML, Glasziou P. Estimating the extent of asymptomatic COVID-19 and its potential for community transmission: Systematic review and meta-analysis. J Assoc Med Microbiol Infect Dis Can. 2020;5(4):223-34.
78. Ganyani T, Kremer C, Chen D, Torneri A, Faes C, Wallinga J, et al. Estimating the generation interval for coronavirus disease (COVID-19) based on symptom onset data, March 2020. Euro Surveill. 2020;25(17).
79. Hawks SA, Prussin AJ, 2nd, Kuchinsky SC, Pan J, Marr LC, Duggal NK. Infectious SARS-CoV-2 Is Emitted in Aerosol Particles. mBio. 2021;12(5):e0252721.
80. Cascella M, Rajnik M, Aleem A, Dulebohn SC, Di Napoli R. Features, Evaluation, and Treatment of Coronavirus (COVID-19). StatPearls. Treasure Island (FL) ineligible companies. Disclosure: Michael Rajnik declares no relevant financial relationships with ineligible companies. Disclosure: Abdul Aleem declares no relevant financial relationships with ineligible companies. Disclosure: Scott Dulebohn declares no relevant financial relationships with ineligible companies. Disclosure: Raffaela Di Napoli declares no relevant financial relationships with ineligible companies.2024.
81. Wiersinga WJ, Rhodes A, Cheng AC, Peacock SJ, Prescott HC. Pathophysiology, Transmission, Diagnosis, and Treatment of Coronavirus Disease 2019 (COVID-19): A Review. JAMA. 2020;324(8):782-93.
82. Docherty AB, Harrison EM, Green CA, Hardwick HE, Pius R, Norman L, et al. Features of 20 133 UK patients in hospital with covid-19 using the ISARIC WHO Clinical Characterisation Protocol: prospective observational cohort study. BMJ. 2020;369:m1985.
83. Mehta P, McAuley DF, Brown M, Sanchez E, Tattersall RS, Manson JJ, et al. COVID-19: consider cytokine storm syndromes and immunosuppression. Lancet. 2020;395(10229):1033-4.
84. Kwok KO, Huang Y, Tsoi MTF, Tang A, Wong SYS, Wei WI, et al. Epidemiology, clinical spectrum, viral kinetics and impact of COVID-19 in the Asia-Pacific region. Respirology. 2021;26(4):322-33.
85. Klein J, Wood J, Jaycox JR, Dhodapkar RM, Lu P, Gehlhausen JR, et al. Distinguishing features of long COVID identified through immune profiling. Nature. 2023;623(7985):139-48.
86. Davis HE, McCorkell L, Vogel JM, Topol EJ. Long COVID: major findings, mechanisms and recommendations. Nat Rev Microbiol. 2023;21(3):133-46.
87. Verity R, Okell LC, Dorigatti I, Winskill P, Whittaker C, Imai N, et al. Estimates of the severity of coronavirus disease 2019: a model-based analysis. Lancet Infect Dis. 2020;20(6):669-77.
88. Richardson S, Hirsch JS, Narasimhan M, Crawford JM, McGinn T, Davidson KW, et al. Presenting Characteristics, Comorbidities, and Outcomes Among 5700 Patients Hospitalized With COVID-19 in the New York City Area. JAMA. 2020;323(20):2052-9.
89. Krammer F. The role of vaccines in the COVID-19 pandemic: what have we learned? Semin Immunopathol. 2024;45(4-6):451-68.
90. Masters PS. The molecular biology of coronaviruses. Adv Virus Res. 2006;66:193-292.

91. Sturman LS, Holmes KV. The molecular biology of coronaviruses. Adv Virus Res. 1983;28:35-112.
92. Letko M, Marzi A, Munster V. Functional assessment of cell entry and receptor usage for SARS-CoV-2 and other lineage B betacoronaviruses. Nat Microbiol. 2020;5(4):562-9.
93. Tortorici MA, Veesler D. Structural insights into coronavirus entry. Adv Virus Res. 2019;105:93-116.
94. Lu R, Zhao X, Li J, Niu P, Yang B, Wu H, et al. Genomic characterisation and epidemiology of 2019 novel coronavirus: implications for virus origins and receptor binding. Lancet. 2020;395(10224):565-74.
95. Plotkin SA. Correlates of protection induced by vaccination. Clin Vaccine Immunol. 2010;17(7):1055-65.
96. Zhong X, Yang H, Guo ZF, Sin WY, Chen W, Xu J, et al. B-cell responses in patients who have recovered from severe acute respiratory syndrome target a dominant site in the S2 domain of the surface spike glycoprotein. J Virol. 2005;79(6):3401-8.
97. Qiu M, Shi Y, Guo Z, Chen Z, He R, Chen R, et al. Antibody responses to individual proteins of SARS coronavirus and their neutralization activities. Microbes Infect. 2005;7(5-6):882-9.
98. Tang XC, Agnihothram SS, Jiao Y, Stanhope J, Graham RL, Peterson EC, et al. Identification of human neutralizing antibodies against MERS-CoV and their role in virus adaptive evolution. Proc Natl Acad Sci U S A. 2014;111(19):E2018-26.
99. Garcia-Beltran WF, Lam EC, Astudillo MG, Yang D, Miller TE, Feldman J, et al. COVID-19-neutralizing antibodies predict disease severity and survival. Cell. 2021;184(2):476-88 e11.
100. Brouwer PJM, Caniels TG, van der Straten K, Snitselaar JL, Aldon Y, Bangaru S, et al. Potent neutralizing antibodies from COVID-19 patients define multiple targets of vulnerability. Science. 2020;369(6504):643-50.
101. Rogers TF, Zhao F, Huang D, Beutler N, Burns A, He WT, et al. Isolation of potent SARS-CoV-2 neutralizing antibodies and protection from disease in a small animal model. Science. 2020;369(6506):956-63.
102. Zost SJ, Gilchuk P, Case JB, Binshtein E, Chen RE, Nkolola JP, et al. Potently neutralizing and protective human antibodies against SARS-CoV-2. Nature. 2020;584(7821):443-9.
103. Pinto D, Park YJ, Beltramello M, Walls AC, Tortorici MA, Bianchi S, et al. Cross-neutralization of SARS-CoV-2 by a human monoclonal SARS-CoV antibody. Nature. 2020;583(7815):290-5.
104. Barnes CO, Jette CA, Abernathy ME, Dam KA, Esswein SR, Gristick HB, et al. SARS-CoV-2 neutralizing antibody structures inform therapeutic strategies. Nature. 2020;588(7839):682-7.
105. Piccoli L, Park YJ, Tortorici MA, Czudnochowski N, Walls AC, Beltramello M, et al. Mapping Neutralizing and Immunodominant Sites on the SARS-CoV-2 Spike Receptor-Binding Domain by Structure-Guided High-Resolution Serology. Cell. 2020;183(4):1024-42 e21.
106. Burton DR, Walker LM. Rational Vaccine Design in the Time of COVID-19. Cell Host Microbe. 2020;27(5):695-8.
107. Krammer F. SARS-CoV-2 vaccines in development. Nature. 2020;586(7830):516-27.
108. Khoury DS, Schlub TE, Cromer D, Steain M, Fong Y, Gilbert PB, et al. Correlates of Protection, Thresholds of Protection, and Immunobridging among Persons with SARS-CoV-2 Infection. Emerg Infect Dis. 2023;29(2):381-8.

109. Khoury DS, Cromer D, Reynaldi A, Schlub TE, Wheatley AK, Juno JA, et al. Neutralizing antibody levels are highly predictive of immune protection from symptomatic SARS-CoV-2 infection. Nat Med. 2021;27(7):1205-11.
110. Cromer D, Steain M, Reynaldi A, Schlub TE, Wheatley AK, Juno JA, et al. Neutralising antibody titres as predictors of protection against SARS-CoV-2 variants and the impact of boosting: a meta-analysis. Lancet Microbe. 2022;3(1):e52-e61.
111. Diamond MS, Kanneganti TD. Innate immunity: the first line of defense against SARS-CoV-2. Nat Immunol. 2022;23(2):165-76.
112. Li D, Wu M. Pattern recognition receptors in health and diseases. Signal Transduct Target Ther. 2021;6(1):291.
113. Takeuchi O, Akira S. Pattern recognition receptors and inflammation. Cell. 2010;140(6):805-20.
114. Duggal NK, Emerman M. Evolutionary conflicts between viruses and restriction factors shape immunity. Nat Rev Immunol. 2012;12(10):687-95.
115. Eisenbarth SC. Dendritic cell subsets in T cell programming: location dictates function. Nat Rev Immunol. 2019;19(2):89-103.
116. Iwasaki A. Mucosal dendritic cells. Annu Rev Immunol. 2007;25:381-418.
117. Randall TD, Mebius RE. The development and function of mucosal lymphoid tissues: a balancing act with micro-organisms. Mucosal Immunol. 2014;7(3):455-66.
118. Randolph GJ, Ochando J, Partida-Sanchez S. Migration of dendritic cell subsets and their precursors. Annu Rev Immunol. 2008;26:293-316.
119. Neutra MR, Pringault E, Kraehenbuhl JP. Antigen sampling across epithelial barriers and induction of mucosal immune responses. Annu Rev Immunol. 1996;14:275-300.
120. Brandtzaeg P. Mucosal immunity: induction, dissemination, and effector functions. Scand J Immunol. 2009;70(6):505-15.
121. Brandtzaeg P. Molecular and cellular aspects of the secretory immunoglobulin system. APMIS. 1995;103(1):1-19.
122. Zhu J, Tao P, Chopra AK, Rao VB. Bacteriophage T4 as a Protein-Based, Adjuvant- and Needle-Free, Mucosal Pandemic Vaccine Design Platform. Annu Rev Virol. 2024;11(1):395-420.
123. Blanco-Melo D, Nilsson-Payant BE, Liu WC, Uhl S, Hoagland D, Moller R, et al. Imbalanced Host Response to SARS-CoV-2 Drives Development of COVID-19. Cell. 2020;181(5):1036-45 e9.
124. Park A, Iwasaki A. Type I and Type III Interferons - Induction, Signaling, Evasion, and Application to Combat COVID-19. Cell Host Microbe. 2020;27(6):870-8.
125. Agerer B, Koblischke M, Gudipati V, Montano-Gutierrez LF, Smyth M, Popa A, et al. SARS-CoV-2 mutations in MHC-I-restricted epitopes evade CD8(+) T cell responses. Sci Immunol. 2021;6(57).
126. Yoo JS, Sasaki M, Cho SX, Kasuga Y, Zhu B, Ouda R, et al. SARS-CoV-2 inhibits induction of the MHC class I pathway by targeting the STAT1-IRF1-NLRC5 axis. Nat Commun. 2021;12(1):6602.
127. Grifoni A, Sidney J, Vita R, Peters B, Crotty S, Weiskopf D, et al. SARS-CoV-2 human T cell epitopes: Adaptive immune response against COVID-19. Cell Host Microbe. 2022;30(12):1788.
128. Lee S, Yeung KK, Watts TH. Tissue-resident memory T cells in protective immunity to influenza virus. Curr Opin Virol. 2024;65:101397.

129. Zens KD, Chen JK, Farber DL. Vaccine-generated lung tissue-resident memory T cells provide heterosubtypic protection to influenza infection. JCI Insight. 2016;1(10).
130. Hombrink P, Helbig C, Backer RA, Piet B, Oja AE, Stark R, et al. Programs for the persistence, vigilance and control of human CD8(+) lung-resident memory T cells. Nat Immunol. 2016;17(12):1467-78.
131. Sridhar S, Begom S, Bermingham A, Hoschler K, Adamson W, Carman W, et al. Cellular immune correlates of protection against symptomatic pandemic influenza. Nat Med. 2013;19(10):1305-12.
132. Wilkinson TM, Li CK, Chui CS, Huang AK, Perkins M, Liebner JC, et al. Preexisting influenza-specific CD4+ T cells correlate with disease protection against influenza challenge in humans. Nat Med. 2012;18(2):274-80.
133. Mueller SN, Gebhardt T, Carbone FR, Heath WR. Memory T cell subsets, migration patterns, and tissue residence. Annu Rev Immunol. 2013;31:137-61.
134. Inoue T, Kurosaki T. Memory B cells. Nat Rev Immunol. 2024;24(1):5-17.
135. Schenkel JM, Masopust D. Tissue-resident memory T cells. Immunity. 2014;41(6):886-97.
136. Markov PV, Ghafari M, Beer M, Lythgoe K, Simmonds P, Stilianakis NI, et al. The evolution of SARS-CoV-2. Nat Rev Microbiol. 2023;21(6):361-79.
137. Carabelli AM, Peacock TP, Thorne LG, Harvey WT, Hughes J, Consortium C-GU, et al. SARS-CoV-2 variant biology: immune escape, transmission and fitness. Nat Rev Microbiol. 2023;21(3):162-77.
138. Volz E, Hill V, McCrone JT, Price A, Jorgensen D, O'Toole A, et al. Evaluating the Effects of SARS-CoV-2 Spike Mutation D614G on Transmissibility and Pathogenicity. Cell. 2021;184(1):64-75 e11.
139. Korber B, Fischer WM, Gnanakaran S, Yoon H, Theiler J, Abfalterer W, et al. Tracking Changes in SARS-CoV-2 Spike: Evidence that D614G Increases Infectivity of the COVID-19 Virus. Cell. 2020;182(4):812-27 e19.
140. Yurkovetskiy L, Wang X, Pascal KE, Tomkins-Tinch C, Nyalile TP, Wang Y, et al. Structural and Functional Analysis of the D614G SARS-CoV-2 Spike Protein Variant. Cell. 2020;183(3):739-51 e8.
141. Robson F, Khan KS, Le TK, Paris C, Demirbag S, Barfuss P, et al. Coronavirus RNA Proofreading: Molecular Basis and Therapeutic Targeting. Mol Cell. 2020;80(6):1136-8.
142. Amicone M, Borges V, Alves MJ, Isidro J, Ze-Ze L, Duarte S, et al. Mutation rate of SARS-CoV-2 and emergence of mutators during experimental evolution. Evol Med Public Health. 2022;10(1):142-55.
143. Viana R, Moyo S, Amoako DG, Tegally H, Scheepers C, Althaus CL, et al. Rapid epidemic expansion of the SARS-CoV-2 Omicron variant in southern Africa. Nature. 2022;603(7902):679-86.
144. Burki TK. Omicron variant and booster COVID-19 vaccines. Lancet Respir Med. 2022;10(2):e17.
145. McCallum M, Czudnochowski N, Rosen LE, Zepeda SK, Bowen JE, Walls AC, et al. Structural basis of SARS-CoV-2 Omicron immune evasion and receptor engagement. Science. 2022;375(6583):864-8.
146. Vitiello A, Ferrara F, Auti AM, Di Domenico M, Boccellino M. Advances in the Omicron variant development. J Intern Med. 2022;292(1):81-90.

147. Kurhade C, Zou J, Xia H, Liu M, Chang HC, Ren P, et al. Low neutralization of SARS-CoV-2 Omicron BA.2.75.2, BQ.1.1 and XBB.1 by parental mRNA vaccine or a BA.5 bivalent booster. Nat Med. 2023;29(2):344-7.
148. Regenhardt E, Kirsten H, Weiss M, Lubbert C, Stehr SN, Remane Y, et al. SARS-CoV-2 Vaccine Breakthrough Infections of Omicron and Delta Variants in Healthcare Workers. Vaccines (Basel). 2023;11(5).
149. Lin DY, Xu Y, Gu Y, Zeng D, Sunny SK, Moore Z. Durability of Bivalent Boosters against Omicron Subvariants. N Engl J Med. 2023;388(19):1818-20.
150. Liu L, Iketani S, Guo Y, Chan JF, Wang M, Liu L, et al. Striking antibody evasion manifested by the Omicron variant of SARS-CoV-2. Nature. 2022;602(7898):676-81.
151. Yamasoba D, Kimura I, Nasser H, Morioka Y, Nao N, Ito J, et al. Virological characteristics of the SARS-CoV-2 Omicron BA.2 spike. Cell. 2022;185(12):2103-15 e19.
152. Cele S, Jackson L, Khoury DS, Khan K, Moyo-Gwete T, Tegally H, et al. Omicron extensively but incompletely escapes Pfizer BNT162b2 neutralization. Nature. 2022;602(7898):654-6.
153. Willett BJ, Grove J, MacLean OA, Wilkie C, De Lorenzo G, Furnon W, et al. SARS-CoV-2 Omicron is an immune escape variant with an altered cell entry pathway. Nat Microbiol. 2022;7(8):1161-79.
154. Kaku CI, Bergeron AJ, Ahlm C, Normark J, Sakharkar M, Forsell MNE, et al. Recall of preexisting cross-reactive B cell memory after Omicron BA.1 breakthrough infection. Sci Immunol. 2022;7(73):eabq3511.
155. Schmidt F, Muecksch F, Weisblum Y, Da Silva J, Bednarski E, Cho A, et al. Plasma Neutralization of the SARS-CoV-2 Omicron Variant. N Engl J Med. 2022;386(6):599-601.
156. Kuhlmann C, Mayer CK, Claassen M, Maponga T, Burgers WA, Keeton R, et al. Breakthrough infections with SARS-CoV-2 omicron despite mRNA vaccine booster dose. Lancet. 2022;399(10325):625-6.
157. Cao Y, Wang J, Jian F, Xiao T, Song W, Yisimayi A, et al. Omicron escapes the majority of existing SARS-CoV-2 neutralizing antibodies. Nature. 2022;602(7898):657-63.
158. Dejnirattisai W, Huo J, Zhou D, Zahradnik J, Supasa P, Liu C, et al. SARS-CoV-2 Omicron-B.1.1.529 leads to widespread escape from neutralizing antibody responses. Cell. 2022;185(3):467-84 e15.
159. Wang Q, Bowen A, Valdez R, Gherasim C, Gordon A, Liu L, et al. Antibody Response to Omicron BA.4-BA.5 Bivalent Booster. N Engl J Med. 2023;388(6):567-9.
160. Chalkias S, Whatley JL, Eder F, Essink B, Khetan S, Bradley P, et al. Original SARS-CoV-2 monovalent and Omicron BA.4/BA.5 bivalent COVID-19 mRNA vaccines: phase 2/3 trial interim results. Nat Med. 2023;29(9):2325-33.
161. Zou J, Kurhade C, Patel S, Kitchin N, Tompkins K, Cutler M, et al. Neutralization of BA.4-BA.5, BA.4.6, BA.2.75.2, BQ.1.1, and XBB.1 with Bivalent Vaccine. N Engl J Med. 2023;388(9):854-7.
162. Chalkias S, Harper C, Vrbicky K, Walsh SR, Essink B, Brosz A, et al. A Bivalent Omicron-Containing Booster Vaccine against Covid-19. N Engl J Med. 2022;387(14):1279-91.
163. Tuekprakhon A, Nutalai R, Dijokaite-Guraliuc A, Zhou D, Ginn HM, Selvaraj M, et al. Antibody escape of SARS-CoV-2 Omicron BA.4 and BA.5 from vaccine and BA.1 serum. Cell. 2022;185(14):2422-33 e13.

164. Tamura T, Ito J, Uriu K, Zahradnik J, Kida I, Anraku Y, et al. Virological characteristics of the SARS-CoV-2 XBB variant derived from recombination of two Omicron subvariants. Nat Commun. 2023;14(1):2800.
165. Wang Q, Guo Y, Bowen A, Mellis IA, Valdez R, Gherasim C, et al. XBB.1.5 monovalent mRNA vaccine booster elicits robust neutralizing antibodies against XBB subvariants and JN.1. Cell Host Microbe. 2024;32(3):315-21 e3.
166. Tortorici MA, Addetia A, Seo AJ, Brown J, Sprouse K, Logue J, et al. Persistent immune imprinting occurs after vaccination with the COVID-19 XBB.1.5 mRNA booster in humans. Immunity. 2024;57(4):904-11 e4.
167. Muhlemann B, Trimpert J, Walper F, Schmidt ML, Jansen J, Schroeder S, et al. Antigenic cartography using variant-specific hamster sera reveals substantial antigenic variation among Omicron subvariants. Proc Natl Acad Sci U S A. 2024;121(32):e2310917121.
168. Li P, Faraone JN, Hsu CC, Chamblee M, Zheng YM, Carlin C, et al. Neutralization escape, infectivity, and membrane fusion of JN.1-derived SARS-CoV-2 SLip, FLiRT, and KP.2 variants. Cell Rep. 2024;43(8):114520.
169. Davis-Gardner ME, Lai L, Wali B, Samaha H, Solis D, Lee M, et al. Neutralization against BA.2.75.2, BQ.1.1, and XBB from mRNA Bivalent Booster. N Engl J Med. 2023;388(2):183-5.
170. Yang S, Yu Y, Xu Y, Jian F, Song W, Yisimayi A, et al. Fast evolution of SARS-CoV-2 BA.2.86 to JN.1 under heavy immune pressure. Lancet Infect Dis. 2024;24(2):e70-e2.
171. Kaku Y, Okumura K, Padilla-Blanco M, Kosugi Y, Uriu K, Hinay AA, Jr., et al. Virological characteristics of the SARS-CoV-2 JN.1 variant. Lancet Infect Dis. 2024;24(2):e82.
172. Kaku Y, Uriu K, Kosugi Y, Okumura K, Yamasoba D, Uwamino Y, et al. Virological characteristics of the SARS-CoV-2 KP.2 variant. Lancet Infect Dis. 2024;24(7):e416.
173. CDC. Summary of Variant Surveillance. 2024.
174. Hui KPY, Ho JCW, Cheung MC, Ng KC, Ching RHH, Lai KL, et al. SARS-CoV-2 Omicron variant replication in human bronchus and lung ex vivo. Nature. 2022;603(7902):715-20.
175. Mohsin M, Mahmud S. Omicron SARS-CoV-2 variant of concern: A review on its transmissibility, immune evasion, reinfection, and severity. Medicine (Baltimore). 2022;101(19):e29165.
176. Hakki S, Zhou J, Jonnerby J, Singanayagam A, Barnett JL, Madon KJ, et al. Onset and window of SARS-CoV-2 infectiousness and temporal correlation with symptom onset: a prospective, longitudinal, community cohort study. Lancet Respir Med. 2022;10(11):1061-73.
177. Andrews SF, Huang Y, Kaur K, Popova LI, Ho IY, Pauli NT, et al. Immune history profoundly affects broadly protective B cell responses to influenza. Sci Transl Med. 2015;7(316):316ra192.
178. Han AX, de Jong SPJ, Russell CA. Co-evolution of immunity and seasonal influenza viruses. Nat Rev Microbiol. 2023;21(12):805-17.
179. Dolton G, Rius C, Hasan MS, Wall A, Szomolay B, Behiry E, et al. Emergence of immune escape at dominant SARS-CoV-2 killer T cell epitope. Cell. 2022;185(16):2936-51 e19.
180. Geers D, Shamier MC, Bogers S, den Hartog G, Gommers L, Nieuwkoop NN, et al. SARS-CoV-2 variants of concern partially escape humoral but not T-cell responses in COVID-19 convalescent donors and vaccinees. Sci Immunol. 2021;6(59).
181. Gao Y, Cai C, Grifoni A, Muller TR, Niessl J, Olofsson A, et al. Ancestral SARS-CoV-2-specific T cells cross-recognize the Omicron variant. Nat Med. 2022;28(3):472-6.

182. GeurtsvanKessel CH, Geers D, Schmitz KS, Mykytyn AZ, Lamers MM, Bogers S, et al. Divergent SARS-CoV-2 Omicron-reactive T and B cell responses in COVID-19 vaccine recipients. Sci Immunol. 2022;7(69):eabo2202.
183. Liu L, Wang P, Nair MS, Yu J, Rapp M, Wang Q, et al. Potent neutralizing antibodies against multiple epitopes on SARS-CoV-2 spike. Nature. 2020;584(7821):450-6.
184. Bartsch YC, Wang C, Zohar T, Fischinger S, Atyeo C, Burke JS, et al. Humoral signatures of protective and pathological SARS-CoV-2 infection in children. Nat Med. 2021;27(3):454-62.
185. Baden LR, El Sahly HM, Essink B, Kotloff K, Frey S, Novak R, et al. Efficacy and Safety of the mRNA-1273 SARS-CoV-2 Vaccine. N Engl J Med. 2021;384(5):403-16.
186. Li C, Lee A, Grigoryan L, Arunachalam PS, Scott MKD, Trisal M, et al. Mechanisms of innate and adaptive immunity to the Pfizer-BioNTech BNT162b2 vaccine. Nat Immunol. 2022;23(4):543-55.
187. Hassett KJ, Benenato KE, Jacquinet E, Lee A, Woods A, Yuzhakov O, et al. Optimization of Lipid Nanoparticles for Intramuscular Administration of mRNA Vaccines. Mol Ther Nucleic Acids. 2019;15:1-11.
188. Pardi N, Tuyishime S, Muramatsu H, Kariko K, Mui BL, Tam YK, et al. Expression kinetics of nucleoside-modified mRNA delivered in lipid nanoparticles to mice by various routes. J Control Release. 2015;217:345-51.
189. Bettini E, Chudnovskiy A, Protti G, Nakadakari-Higa S, Ceglia S, Castano D, et al. Distinct components of nucleoside-modified messenger RNA vaccines cooperate to instruct efficient germinal center responses. bioRxiv. 2024.
190. Verbeke R, Hogan MJ, Lore K, Pardi N. Innate immune mechanisms of mRNA vaccines. Immunity. 2022;55(11):1993-2005.
191. Liang F, Lindgren G, Lin A, Thompson EA, Ols S, Rohss J, et al. Efficient Targeting and Activation of Antigen-Presenting Cells In Vivo after Modified mRNA Vaccine Administration in Rhesus Macaques. Mol Ther. 2017;25(12):2635-47.
192. Lazzaro S, Giovani C, Mangiavacchi S, Magini D, Maione D, Baudner B, et al. CD8 T-cell priming upon mRNA vaccination is restricted to bone-marrow-derived antigen-presenting cells and may involve antigen transfer from myocytes. Immunology. 2015;146(2):312-26.
193. McNamara MA, Nair SK, Holl EK. RNA-Based Vaccines in Cancer Immunotherapy. J Immunol Res. 2015;2015:794528.
194. Thomas SJ, Moreira ED, Jr., Kitchin N, Absalon J, Gurtman A, Lockhart S, et al. Safety and Efficacy of the BNT162b2 mRNA Covid-19 Vaccine through 6 Months. N Engl J Med. 2021;385(19):1761-73.
195. El Sahly HM, Baden LR, Essink B, Doblecki-Lewis S, Martin JM, Anderson EJ, et al. Efficacy of the mRNA-1273 SARS-CoV-2 Vaccine at Completion of Blinded Phase. N Engl J Med. 2021;385(19):1774-85.
196. Polack FP, Thomas SJ, Kitchin N, Absalon J, Gurtman A, Lockhart S, et al. Safety and Efficacy of the BNT162b2 mRNA Covid-19 Vaccine. N Engl J Med. 2020;383(27):2603-15.
197. Tenforde MW, Self WH, Adams K, Gaglani M, Ginde AA, McNeal T, et al. Association Between mRNA Vaccination and COVID-19 Hospitalization and Disease Severity. JAMA. 2021;326(20):2043-54.
198. Victora GD, Nussenzweig MC. Germinal Centers. Annu Rev Immunol. 2022;40:413-42.

199. Lederer K, Bettini E, Parvathaneni K, Painter MM, Agarwal D, Lundgreen KA, et al. Germinal center responses to SARS-CoV-2 mRNA vaccines in healthy and immunocompromised individuals. Cell. 2022;185(6):1008-24 e15.
200. Tan HX, Juno JA, Lee WS, Barber-Axthelm I, Kelly HG, Wragg KM, et al. Immunogenicity of prime-boost protein subunit vaccine strategies against SARS-CoV-2 in mice and macaques. Nat Commun. 2021;12(1):1403.
201. Turner JS, O'Halloran JA, Kalaidina E, Kim W, Schmitz AJ, Zhou JQ, et al. SARS-CoV-2 mRNA vaccines induce persistent human germinal centre responses. Nature. 2021;596(7870):109-13.
202. Lederer K, Castano D, Gomez Atria D, Oguin TH, 3rd, Wang S, Manzoni TB, et al. SARS-CoV-2 mRNA Vaccines Foster Potent Antigen-Specific Germinal Center Responses Associated with Neutralizing Antibody Generation. Immunity. 2020;53(6):1281-95 e5.
203. Willis E, Pardi N, Parkhouse K, Mui BL, Tam YK, Weissman D, et al. Nucleoside-modified mRNA vaccination partially overcomes maternal antibody inhibition of de novo immune responses in mice. Sci Transl Med. 2020;12(525).
204. Pardi N, Hogan MJ, Naradikian MS, Parkhouse K, Cain DW, Jones L, et al. Nucleoside-modified mRNA vaccines induce potent T follicular helper and germinal center B cell responses. J Exp Med. 2018;215(6):1571-88.
205. Alameh MG, Tombacz I, Bettini E, Lederer K, Sittplangkoon C, Wilmore JR, et al. Lipid nanoparticles enhance the efficacy of mRNA and protein subunit vaccines by inducing robust T follicular helper cell and humoral responses. Immunity. 2022;55(6):1136-8.
206. England RN, Drapeau EM, Alameh MG, Hosseinzadeh R, Weissman D, Hensley SE. Evaluation of mRNA-LNP and adjuvanted protein SARS-CoV-2 vaccines in a maternal antibody mouse model. NPJ Vaccines. 2024;9(1):110.
207. Shirai S, Kawai A, Shibuya M, Munakata L, Omata D, Suzuki R, et al. Lipid Nanoparticle Acts as a Potential Adjuvant for Influenza Split Vaccine without Inducing Inflammatory Responses. Vaccines (Basel). 2020;8(3).
208. Awasthi S, Hook LM, Swaminathan G, Cairns TM, Brooks B, Smith JS, et al. Antibody responses to crucial functional epitopes as a novel approach to assess immunogenicity of vaccine adjuvants. Vaccine. 2019;37(29):3770-8.
209. Durand J, Dogne JM, Cohet C, Browne K, Gordillo-Maranon M, Piccolo L, et al. Safety Monitoring of COVID-19 Vaccines: Perspective from the European Medicines Agency. Clin Pharmacol Ther. 2023;113(6):1223-34.
210. Kracalik I, Oster ME, Broder KR, Cortese MM, Glover M, Shields K, et al. Outcomes at least 90 days since onset of myocarditis after mRNA COVID-19 vaccination in adolescents and young adults in the USA: a follow-up surveillance study. Lancet Child Adolesc Health. 2022;6(11):788-98.
211. Karlstad O, Hovi P, Husby A, Harkanen T, Selmer RM, Pihlstrom N, et al. SARS-CoV-2 Vaccination and Myocarditis in a Nordic Cohort Study of 23 Million Residents. JAMA Cardiol. 2022;7(6):600-12.
212. Patone M, Mei XW, Handunnetthi L, Dixon S, Zaccardi F, Shankar-Hari M, et al. Risks of myocarditis, pericarditis, and cardiac arrhythmias associated with COVID-19 vaccination or SARS-CoV-2 infection. Nat Med. 2022;28(2):410-22.

213. Falsey AR, Sobieszczyk ME, Hirsch I, Sproule S, Robb ML, Corey L, et al. Phase 3 Safety and Efficacy of AZD1222 (ChAdOx1 nCoV-19) Covid-19 Vaccine. N Engl J Med. 2021;385(25):2348-60.
214. Hardt K, Vandebosch A, Sadoff J, Le Gars M, Truyers C, Lowson D, et al. Efficacy, safety, and immunogenicity of a booster regimen of Ad26.COV2.S vaccine against COVID-19 (ENSEMBLE2): results of a randomised, double-blind, placebo-controlled, phase 3 trial. Lancet Infect Dis. 2022;22(12):1703-15.
215. Greinacher A, Thiele T, Warkentin TE, Weisser K, Kyrle PA, Eichinger S. Thrombotic Thrombocytopenia after ChAdOx1 nCov-19 Vaccination. N Engl J Med. 2021;384(22):2092-101.
216. Marquez-Martinez S, Khan S, Lubbe JV, Solforosi L, Costes LMM, Choi Y, et al. The Biodistribution of the Spike Protein after Ad26.COV2.S Vaccination Is Unlikely to Play a Role in Vaccine-Induced Immune Thrombotic Thrombocytopenia. Vaccines (Basel). 2024;12(5).
217. Muir KL, Kallam A, Koepsell SA, Gundabolu K. Thrombotic Thrombocytopenia after Ad26.COV2.S Vaccination. N Engl J Med. 2021;384(20):1964-5.
218. Pavord S, Scully M, Hunt BJ, Lester W, Bagot C, Craven B, et al. Clinical Features of Vaccine-Induced Immune Thrombocytopenia and Thrombosis. N Engl J Med. 2021;385(18):1680-9.
219. Heath PT, Galiza EP, Baxter DN, Boffito M, Browne D, Burns F, et al. Safety and Efficacy of NVX-CoV2373 Covid-19 Vaccine. N Engl J Med. 2021;385(13):1172-83.
220. Hager KJ, Perez Marc G, Gobeil P, Diaz RS, Heizer G, Llapur C, et al. Efficacy and Safety of a Recombinant Plant-Based Adjuvanted Covid-19 Vaccine. N Engl J Med. 2022;386(22):2084-96.
221. Liang Z, Zhu H, Wang X, Jing B, Li Z, Xia X, et al. Adjuvants for Coronavirus Vaccines. Front Immunol. 2020;11:589833.
222. Fujkuyama Y, Tokuhara D, Kataoka K, Gilbert RS, McGhee JR, Yuki Y, et al. Novel vaccine development strategies for inducing mucosal immunity. Expert Rev Vaccines. 2012;11(3):367-79.
223. Bally J, Jung H, Mortimer C, Naim F, Philips JG, Hellens R, et al. The Rise and Rise of Nicotiana benthamiana: A Plant for All Reasons. Annu Rev Phytopathol. 2018;56:405-26.
224. Dunkle LM, Kotloff KL, Gay CL, Anez G, Adelglass JM, Barrat Hernandez AQ, et al. Efficacy and Safety of NVX-CoV2373 in Adults in the United States and Mexico. N Engl J Med. 2022;386(6):531-43.
225. Kemp SA, Cheng MTK, Hamilton WL, Kamelian K, Indian S-C-GC, Singh S, et al. Transmission of B.1.617.2 Delta variant between vaccinated healthcare workers. Sci Rep. 2022;12(1):10492.
226. Chia PY, Ong SWX, Chiew CJ, Ang LW, Chavatte JM, Mak TM, et al. Virological and serological kinetics of SARS-CoV-2 Delta variant vaccine breakthrough infections: a multicentre cohort study. Clin Microbiol Infect. 2022;28(4):612 e1- e7.
227. Lange B, Gerigk M, Tenenbaum T. Breakthrough Infections in BNT162b2-Vaccinated Health Care Workers. N Engl J Med. 2021;385(12):1145-6.
228. Marking U, Bladh O, Havervall S, Svensson J, Greilert-Norin N, Aguilera K, et al. 7-month duration of SARS-CoV-2 mucosal immunoglobulin-A responses and protection. Lancet Infect Dis. 2023;23(2):150-2.

229. Sheikh-Mohamed S, Sanders EC, Gommerman JL, Tal MC. Guardians of the oral and nasopharyngeal galaxy: IgA and protection against SARS-CoV-2 infection. Immunol Rev. 2022;309(1):75-85.
230. Havervall S, Marking U, Svensson J, Greilert-Norin N, Bacchus P, Nilsson P, et al. Anti-Spike Mucosal IgA Protection against SARS-CoV-2 Omicron Infection. N Engl J Med. 2022;387(14):1333-6.
231. Sano K, Bhavsar D, Singh G, Floda D, Srivastava K, Gleason C, et al. SARS-CoV-2 vaccination induces mucosal antibody responses in previously infected individuals. Nat Commun. 2022;13(1):5135.
232. Altarawneh HN, Chemaitelly H, Ayoub HH, Tang P, Hasan MR, Yassine HM, et al. Effects of previous infection, vaccination, and hybrid immunity against symptomatic Alpha, Beta, and Delta SARS-CoV-2 infections: an observational study. EBioMedicine. 2023;95:104734.
233. Tang J, Zeng C, Cox TM, Li C, Son YM, Cheon IS, et al. Respiratory mucosal immunity against SARS-CoV-2 following mRNA vaccination. Sci Immunol. 2022:eadd4853.
234. Bhavsar D, Singh G, Sano K, Gleason C, Srivastava K, Group PS, et al. Mucosal antibody responses to SARS-CoV-2 booster vaccination and breakthrough infection. mBio. 2023;14(6):e0228023.
235. Sheikh-Mohamed S, Isho B, Chao GYC, Zuo M, Cohen C, Lustig Y, et al. Systemic and mucosal IgA responses are variably induced in response to SARS-CoV-2 mRNA vaccination and are associated with protection against subsequent infection. Mucosal Immunol. 2022.
236. Wilkie BN. Respiratory tract immune response to microbial pathogens. J Am Vet Med Assoc. 1982;181(10):1074-9.
237. Brandtzaeg P. Induction of secretory immunity and memory at mucosal surfaces. Vaccine. 2007;25(30):5467-84.
238. Kaetzel CS. The polymeric immunoglobulin receptor: bridging innate and adaptive immune responses at mucosal surfaces. Immunol Rev. 2005;206:83-99.
239. Woodrow KA, Bennett KM, Lo DD. Mucosal vaccine design and delivery. Annu Rev Biomed Eng. 2012;14:17-46.
240. Jang MH, Kweon MN, Iwatani K, Yamamoto M, Terahara K, Sasakawa C, et al. Intestinal villous M cells: an antigen entry site in the mucosal epithelium. Proc Natl Acad Sci U S A. 2004;101(16):6110-5.
241. Rescigno M, Urbano M, Valzasina B, Francolini M, Rotta G, Bonasio R, et al. Dendritic cells express tight junction proteins and penetrate gut epithelial monolayers to sample bacteria. Nat Immunol. 2001;2(4):361-7.
242. Macpherson AJ, McCoy KD, Johansen FE, Brandtzaeg P. The immune geography of IgA induction and function. Mucosal Immunol. 2008;1(1):11-22.
243. Shikina T, Hiroi T, Iwatani K, Jang MH, Fukuyama S, Tamura M, et al. IgA class switch occurs in the organized nasopharynx- and gut-associated lymphoid tissue, but not in the diffuse lamina propria of airways and gut. J Immunol. 2004;172(10):6259-64.
244. Brandtzaeg P, Johansen FE. Mucosal B cells: phenotypic characteristics, transcriptional regulation, and homing properties. Immunol Rev. 2005;206:32-63.
245. Mestecky J. The common mucosal immune system and current strategies for induction of immune responses in external secretions. J Clin Immunol. 1987;7(4):265-76.

246. Hand TW, Reboldi A. Production and Function of Immunoglobulin A. Annu Rev Immunol. 2021;39:695-718.
247. Lavelle EC, Ward RW. Mucosal vaccines - fortifying the frontiers. Nat Rev Immunol. 2022;22(4):236-50.
248. Iwasaki A. Exploiting Mucosal Immunity for Antiviral Vaccines. Annu Rev Immunol. 2016;34:575-608.
249. Brandtzaeg P. Secretory IgA: Designed for Anti-Microbial Defense. Front Immunol. 2013;4:222.
250. Kerr MA. The structure and function of human IgA. Biochem J. 1990;271(2):285-96.
251. Woof JM, Kerr MA. The function of immunoglobulin A in immunity. J Pathol. 2006;208(2):270-82.
252. Schroeder HW, Jr., Cavacini L. Structure and function of immunoglobulins. J Allergy Clin Immunol. 2010;125(2 Suppl 2):S41-52.
253. Matsumoto ML. Molecular Mechanisms of Multimeric Assembly of IgM and IgA. Annu Rev Immunol. 2022;40:221-47.
254. Halpern MS, Koshland ME. The stoichiometry of J chain in human secretory IgA. J Immunol. 1973;111(6):1653-60.
255. Hauptman SP, Tomasi TB, Jr. Mechanism of immunoglobulin A polymerization. J Biol Chem. 1975;250(10):3891-6.
256. Mostov KE, Blobel G. A transmembrane precursor of secretory component. The receptor for transcellular transport of polymeric immunoglobulins. J Biol Chem. 1982;257(19):11816-21.
257. Lindh E. Increased risistance of immunoglobulin A dimers to proteolytic degradation after binding of secretory component. J Immunol. 1975;114(1 Pt 2):284-6.
258. Rath T, Baker K, Pyzik M, Blumberg RS. Regulation of immune responses by the neonatal fc receptor and its therapeutic implications. Front Immunol. 2014;5:664.
259. Corthesy B. Multi-faceted functions of secretory IgA at mucosal surfaces. Front Immunol. 2013;4:185.
260. Renegar KB, Small PA, Jr., Boykins LG, Wright PF. Role of IgA versus IgG in the control of influenza viral infection in the murine respiratory tract. J Immunol. 2004;173(3):1978-86.
261. Reynolds HY. Immunoglobulin G and its function in the human respiratory tract. Mayo Clin Proc. 1988;63(2):161-74.
262. Mestecky J, Russell MW, Elson CO. Intestinal IgA: novel views on its function in the defence of the largest mucosal surface. Gut. 1999;44(1):2-5.
263. Suzuki T, Kawaguchi A, Ainai A, Tamura S, Ito R, Multihartina P, et al. Relationship of the quaternary structure of human secretory IgA to neutralization of influenza virus. Proc Natl Acad Sci U S A. 2015;112(25):7809-14.
264. Mantis NJ, Rol N, Corthesy B. Secretory IgA's complex roles in immunity and mucosal homeostasis in the gut. Mucosal Immunol. 2011;4(6):603-11.
265. Brandtzaeg P. Function of mucosa-associated lymphoid tissue in antibody formation. Immunol Invest. 2010;39(4-5):303-55.
266. Wang Q, Yang C, Yin L, Sun J, Wang W, Li H, et al. Intranasal booster using an Omicron vaccine confers broad mucosal and systemic immunity against SARS-CoV-2 variants. Signal Transduct Target Ther. 2023;8(1):167.

267. Gagne M, Flynn BJ, Andrew SF, Flebbe DR, Mychalowych A, Lamb E, et al. Mucosal Adenoviral-vectored Vaccine Boosting Durably Prevents XBB.1.16 Infection in Nonhuman Primates. bioRxiv. 2023.
268. Mao T, Israelow B, Suberi A, Zhou L, Reschke M, Pena-Hernandez MA, et al. Unadjuvanted intranasal spike vaccine booster elicits robust protective mucosal immunity against sarbecoviruses. Science. 2022:eabo2523.
269. Maltseva M, Galipeau Y, Renner TM, Deschatelets L, Durocher Y, Akache B, et al. Characterization of Systemic and Mucosal Humoral Immune Responses to an Adjuvanted Intranasal SARS-CoV-2 Protein Subunit Vaccine Candidate in Mice. Vaccines (Basel). 2022;11(1).
270. Wang Z, Lorenzi JCC, Muecksch F, Finkin S, Viant C, Gaebler C, et al. Enhanced SARS-CoV-2 neutralization by dimeric IgA. Sci Transl Med. 2021;13(577).
271. Stubbe H, Berdoz J, Kraehenbuhl JP, Corthesy B. Polymeric IgA is superior to monomeric IgA and IgG carrying the same variable domain in preventing Clostridium difficile toxin A damaging of T84 monolayers. J Immunol. 2000;164(4):1952-60.
272. Lindley RA, Steele EJ. Analysis of SARS-CoV-2 haplotypes and genomic sequences during 2020 in Victoria, Australia, in the context of putative deficits in innate immune deaminase anti-viral responses. Scand J Immunol. 2021;94(5):e13100.
273. Gorczynski RM, Lindley RA, Steele EJ, Wickramasinghe NC. Nature of Acquired Immune Responses, Epitope Specificity and Resultant Protection from SARS-CoV-2. J Pers Med. 2021;11(12).
274. Oh JE, Song E, Moriyama M, Wong P, Zhang S, Jiang R, et al. Intranasal priming induces local lung-resident B cell populations that secrete protective mucosal antiviral IgA. Sci Immunol. 2021;6(66):eabj5129.
275. Afkhami S, D'Agostino MR, Zhang A, Stacey HD, Marzok A, Kang A, et al. Respiratory mucosal delivery of next-generation COVID-19 vaccine provides robust protection against both ancestral and variant strains of SARS-CoV-2. Cell. 2022;185(5):896-915 e19.
276. Langel SN, Johnson S, Martinez CI, Tedjakusuma SN, Peinovich N, Dora EG, et al. Adenovirus type 5 SARS-CoV-2 vaccines delivered orally or intranasally reduced disease severity and transmission in a hamster model. Sci Transl Med. 2022:eabn6868.
277. Stark FC, Akache B, Deschatelets L, Tran A, Stuible M, Durocher Y, et al. Intranasal immunization with a proteosome-adjuvanted SARS-CoV-2 spike protein-based vaccine is immunogenic and efficacious in mice and hamsters. Sci Rep. 2022;12(1):9772.
278. Cervia C, Nilsson J, Zurbuchen Y, Valaperti A, Schreiner J, Wolfensberger A, et al. Systemic and mucosal antibody responses specific to SARS-CoV-2 during mild versus severe COVID-19. J Allergy Clin Immunol. 2021;147(2):545-57 e9.
279. King RG, Silva-Sanchez A, Peel JN, Botta D, Dickson AM, Pinto AK, et al. Single-Dose Intranasal Administration of AdCOVID Elicits Systemic and Mucosal Immunity against SARS-CoV-2 and Fully Protects Mice from Lethal Challenge. Vaccines (Basel). 2021;9(8).
280. Hassan AO, Feldmann F, Zhao H, Curiel DT, Okumura A, Tang-Huau TL, et al. A single intranasal dose of chimpanzee adenovirus-vectored vaccine protects against SARS-CoV-2 infection in rhesus macaques. Cell Rep Med. 2021;2(4):100230.
281. An X, Martinez-Paniagua M, Rezvan A, Sefat SR, Fathi M, Singh S, et al. Single-dose intranasal vaccination elicits systemic and mucosal immunity against SARS-CoV-2. iScience. 2021;24(9):103037.

282. Du Y, Xu Y, Feng J, Hu L, Zhang Y, Zhang B, et al. Intranasal administration of a recombinant RBD vaccine induced protective immunity against SARS-CoV-2 in mouse. Vaccine. 2021;39(16):2280-7.
283. Sterlin D, Mathian A, Miyara M, Mohr A, Anna F, Claer L, et al. IgA dominates the early neutralizing antibody response to SARS-CoV-2. Sci Transl Med. 2021;13(577).
284. Lapuente D, Fuchs J, Willar J, Vieira Antao A, Eberlein V, Uhlig N, et al. Protective mucosal immunity against SARS-CoV-2 after heterologous systemic prime-mucosal boost immunization. Nat Commun. 2021;12(1):6871.
285. Allie SR, Bradley JE, Mudunuru U, Schultz MD, Graf BA, Lund FE, et al. The establishment of resident memory B cells in the lung requires local antigen encounter. Nat Immunol. 2019;20(1):97-108.
286. Oja AE, Piet B, Helbig C, Stark R, van der Zwan D, Blaauwgeers H, et al. Trigger-happy resident memory CD4(+) T cells inhabit the human lungs. Mucosal Immunol. 2018;11(3):654-67.
287. Kumar BV, Ma W, Miron M, Granot T, Guyer RS, Carpenter DJ, et al. Human Tissue-Resident Memory T Cells Are Defined by Core Transcriptional and Functional Signatures in Lymphoid and Mucosal Sites. Cell Rep. 2017;20(12):2921-34.
288. Sallusto F, Lenig D, Forster R, Lipp M, Lanzavecchia A. Two subsets of memory T lymphocytes with distinct homing potentials and effector functions. Nature. 1999;401(6754):708-12.
289. Ariotti S, Hogenbirk MA, Dijkgraaf FE, Visser LL, Hoekstra ME, Song JY, et al. T cell memory. Skin-resident memory CD8(+) T cells trigger a state of tissue-wide pathogen alert. Science. 2014;346(6205):101-5.
290. Schenkel JM, Fraser KA, Beura LK, Pauken KE, Vezys V, Masopust D. T cell memory. Resident memory CD8 T cells trigger protective innate and adaptive immune responses. Science. 2014;346(6205):98-101.
291. McMaster SR, Wilson JJ, Wang H, Kohlmeier JE. Airway-Resident Memory CD8 T Cells Provide Antigen-Specific Protection against Respiratory Virus Challenge through Rapid IFN-gamma Production. J Immunol. 2015;195(1):203-9.
292. Altmann DM, Boyton RJ. SARS-CoV-2 T cell immunity: Specificity, function, durability, and role in protection. Sci Immunol. 2020;5(49).
293. Miller MS, Gardner TJ, Krammer F, Aguado LC, Tortorella D, Basler CF, et al. Neutralizing antibodies against previously encountered influenza virus strains increase over time: a longitudinal analysis. Sci Transl Med. 2013;5(198):198ra07.
294. Cheng L, Becattini S. Local antigen encounter promotes generation of tissue-resident memory T cells in the large intestine. Mucosal Immunol. 2024.
295. Hassan AO, Feldmann F, Zhao H, Curiel DT, Okumura A, Tang-Huau TL, et al. A single intranasal dose of chimpanzee adenovirus-vectored vaccine protects against SARS-CoV-2 infection in rhesus macaques. bioRxiv. 2021.
296. Bricker TL, Darling TL, Hassan AO, Harastani HH, Soung A, Jiang X, et al. A single intranasal or intramuscular immunization with chimpanzee adenovirus-vectored SARS-CoV-2 vaccine protects against pneumonia in hamsters. Cell Rep. 2021;36(3):109400.
297. Diaz MF, Calderon K, Rojas-Neyra A, Vakharia VN, Choque-Guevara R, Montalvan-Avalos A, et al. Intranasal vaccination of hamsters with a Newcastle disease virus vector expressing the S1 subunit protects animals against SARS-CoV-2 disease. Sci Rep. 2022;12(1):10359.

298. van Doremalen N, Purushotham JN, Schulz JE, Holbrook MG, Bushmaker T, Carmody A, et al. Intranasal ChAdOx1 nCoV-19/AZD1222 vaccination reduces viral shedding after SARS-CoV-2 D614G challenge in preclinical models. Sci Transl Med. 2021;13(607).
299. Darling TL, Harastani HH, Joshi A, Bricker TL, Soudani N, Seehra K, et al. Mucosal immunization with ChAd-SARS-CoV-2-S prevents sequential transmission of SARS-CoV-2 to unvaccinated hamsters. Sci Adv. 2024;10(31):eadp1290.
300. Koolaparambil Mukesh R, Yinda CK, Munster VJ, van Doremalen N. Beyond COVID-19: the promise of next-generation coronavirus vaccines. npj Viruses. 2024;2(1):39.
301. WHO. COVID-19 vaccine tracker and landscape. 2023.
302. NIH. Phase 1 Trial of ChAd68 and Ad5 Adenovirus COVID-19 Vaccines Delivered by Aerosol
.
303. Colwill K, Galipeau Y, Stuible M, Gervais C, Arnold C, Rathod B, et al. A scalable serology solution for profiling humoral immune responses to SARS-CoV-2 infection and vaccination. Clin Transl Immunology. 2022;11(3):e1380.
304. Maltseva M, Keeshan A, Cooper C, Langlois MA. Immune imprinting: The persisting influence of the first antigenic encounter with rapidly evolving viruses. Hum Vaccin Immunother. 2024;20(1):2384192.
305. Demone J, Maltseva M, Nourimand M, Nasr-Sharif M, Galipeau Y, Alarcon EI, et al. Scalable agroinfiltration-based production of SARS-CoV-2 antigens for use in diagnostic assays and subunit vaccines. PLoS One. 2022;17(12):e0277668.
306. Brittain GCt, Chen YQ, Martinez E, Tang VA, Renner TM, Langlois MA, et al. A Novel Semiconductor-Based Flow Cytometer with Enhanced Light-Scatter Sensitivity for the Analysis of Biological Nanoparticles. Sci Rep. 2019;9(1):16039.
307. Welsh JA, Jones JC, Tang VA. Fluorescence and Light Scatter Calibration Allow Comparisons of Small Particle Data in Standard Units across Different Flow Cytometry Platforms and Detector Settings. Cytometry A. 2020;97(6):592-601.
308. Conticello SG, Langlois MA, Neuberger MS. Insights into DNA deaminases. Nat Struct Mol Biol. 2007;14(1):7-9.
309. Monteil V, Kwon H, Prado P, Hagelkruys A, Wimmer RA, Stahl M, et al. Inhibition of SARS-CoV-2 Infections in Engineered Human Tissues Using Clinical-Grade Soluble Human ACE2. Cell. 2020;181(4):905-13 e7.
310. Chan KK, Dorosky D, Sharma P, Abbasi SA, Dye JM, Kranz DM, et al. Engineering human ACE2 to optimize binding to the spike protein of SARS coronavirus 2. Science. 2020;369(6508):1261-5.
311. Freytag LC, Clements JD. Mucosal adjuvants. Vaccine. 2005;23(15):1804-13.
312. Lewis DJ, Huo Z, Barnett S, Kromann I, Giemza R, Galiza E, et al. Transient facial nerve paralysis (Bell's palsy) following intranasal delivery of a genetically detoxified mutant of Escherichia coli heat labile toxin. PLoS One. 2009;4(9):e6999.
313. Mutsch M, Zhou W, Rhodes P, Bopp M, Chen RT, Linder T, et al. Use of the inactivated intranasal influenza vaccine and the risk of Bell's palsy in Switzerland. N Engl J Med. 2004;350(9):896-903.

314. Patel GB, Zhou H, Ponce A, Harris G, Chen W. Intranasal immunization with an archaeal lipid mucosal vaccine adjuvant and delivery formulation protects against a respiratory pathogen challenge. PLoS One. 2010;5(12):e15574.
315. Patel GB, Chen W. Archaeal lipid mucosal vaccine adjuvant and delivery system. Expert Rev Vaccines. 2010;9(4):431-40.
316. Agbayani G, Akache B, Renner TM, Tran A, Stuible M, Dudani R, et al. Intranasal administration of unadjuvanted SARS-CoV-2 spike antigen boosts antigen-specific immune responses induced by parenteral protein subunit vaccine prime in mice and hamsters. Eur J Immunol. 2024;54(6):e2350620.
317. Beitari S, Agbayani G, Hewitt M, Duque D, Bavananthasivam J, Sandhu JK, et al. Effectiveness of VSV vectored SARS-CoV-2 spike when administered through intranasal, intramuscular or a combination of both. Sci Rep. 2023;13(1):21390.
318. Christensen D, Polacek C, Sheward DJ, Hanke L, Moliner-Morro A, McInerney G, et al. Protection against SARS-CoV-2 transmission by a parenteral prime-Intranasal boost vaccine strategy. EBioMedicine. 2022;84:104248.
319. Laghlali G, Wiest MJ, Karadag D, Warang P, O'Konek JJ, Chang LA, et al. Enhanced mucosal B- and T-cell responses against SARS-CoV-2 after heterologous intramuscular mRNA prime/intranasal protein boost vaccination with a combination adjuvant. bioRxiv. 2024.
320. Park SK, Lee CW, Park DI, Woo HY, Cheong HS, Shin HC, et al. Detection of SARS-CoV-2 in Fecal Samples From Patients With Asymptomatic and Mild COVID-19 in Korea. Clin Gastroenterol Hepatol. 2021;19(7):1387-94 e2.
321. Gaebler C, Wang Z, Lorenzi JCC, Muecksch F, Finkin S, Tokuyama M, et al. Evolution of antibody immunity to SARS-CoV-2. Nature. 2021;591(7851):639-44.
322. Morone G, Palomba A, Iosa M, Caporaso T, De Angelis D, Venturiero V, et al. Incidence and Persistence of Viral Shedding in COVID-19 Post-acute Patients With Negativized Pharyngeal Swab: A Systematic Review. Front Med (Lausanne). 2020;7:562.
323. Faustini SE, Jossi SE, Perez-Toledo M, Shields AM, Allen JD, Watanabe Y, et al. Development of a high-sensitivity ELISA detecting IgG, IgA and IgM antibodies to the SARS-CoV-2 spike glycoprotein in serum and saliva. Immunology. 2021;164(1):135-47.
324. Isho B, Abe KT, Zuo M, Jamal AJ, Rathod B, Wang JH, et al. Persistence of serum and saliva antibody responses to SARS-CoV-2 spike antigens in COVID-19 patients. Sci Immunol. 2020;5(52).
325. Pisanic N, Randad PR, Kruczynski K, Manabe YC, Thomas DL, Pekosz A, et al. COVID-19 Serology at Population Scale: SARS-CoV-2-Specific Antibody Responses in Saliva. J Clin Microbiol. 2020;59(1).
326. Johnston TS, Li SH, Painter MM, Atkinson RK, Douek NR, Reeg DB, et al. Immunological imprinting shapes the specificity of human antibody responses against SARS-CoV-2 variants. Immunity. 2024;57(4):912-25 e4.
327. Weber T, Dahling S, Rose S, Affeldt P, Vanshylla K, Ullrich L, et al. Enhanced SARS-CoV-2 humoral immunity following breakthrough infection builds upon the preexisting memory B cell pool. Sci Immunol. 2023;8(89):eadk5845.
328. Huang CQ, Vishwanath S, Carnell GW, Chan ACY, Heeney JL. Immune imprinting and next-generation coronavirus vaccines. Nat Microbiol. 2023;8(11):1971-85.

329. Wang Q, Guo Y, Tam AR, Valdez R, Gordon A, Liu L, et al. Deep immunological imprinting due to the ancestral spike in the current bivalent COVID-19 vaccine. Cell Rep Med. 2023;4(11):101258.
330. Carreno JM, Singh G, Simon V, Krammer F, group PVIs. Bivalent COVID-19 booster vaccines and the absence of BA.5-specific antibodies. Lancet Microbe. 2023;4(8):e569.
331. Park YJ, Pinto D, Walls AC, Liu Z, De Marco A, Benigni F, et al. Imprinted antibody responses against SARS-CoV-2 Omicron sublineages. Science. 2022;378(6620):619-27.
332. Roltgen K, Nielsen SCA, Silva O, Younes SF, Zaslavsky M, Costales C, et al. Immune imprinting, breadth of variant recognition, and germinal center response in human SARS-CoV-2 infection and vaccination. Cell. 2022;185(6):1025-40 e14.
333. Lycke N, Bemark M. Mucosal adjuvants and long-term memory development with special focus on CTA1-DD and other ADP-ribosylating toxins. Mucosal Immunol. 2010;3(6):556-66.
334. Canada H. Influenza vaccines: Canadian Immunization Guide.
335. Maassab HF. Adaptation and growth characteristics of influenza virus at 25 degrees c. Nature. 1967;213(5076):612-4.
336. Wright PF, Hoen AG, Ilyushina NA, Brown EP, Ackerman ME, Wieland-Alter W, et al. Correlates of Immunity to Influenza as Determined by Challenge of Children with Live, Attenuated Influenza Vaccine. Open Forum Infect Dis. 2016;3(2):ofw108.
337. Hoft DF, Babusis E, Worku S, Spencer CT, Lottenbach K, Truscott SM, et al. Live and inactivated influenza vaccines induce similar humoral responses, but only live vaccines induce diverse T-cell responses in young children. J Infect Dis. 2011;204(6):845-53.
338. Pilapitiya D, Wheatley AK, Tan HX. Mucosal vaccines for SARS-CoV-2: triumph of hope over experience. EBioMedicine. 2023;92:104585.
339. CDC. Past Seasons' Vaccine Effectiveness Estimates.
340. Ward BJ, Makarkov A, Seguin A, Pillet S, Trepanier S, Dhaliwall J, et al. Efficacy, immunogenicity, and safety of a plant-derived, quadrivalent, virus-like particle influenza vaccine in adults (18-64 years) and older adults (>/=65 years): two multicentre, randomised phase 3 trials. Lancet. 2020;396(10261):1491-503.

10 Appendix